GRAPHITE NANOREINFORCEMENTS IN POLYMER NANOCOMPOSITES

By

Hiroyuki Fukushima

A DISSERTATION

Submitted to
Michigan State University
in partial fulfillment of the requirements
for the degree of

DOCTOR OF PHILOSOPHY

Department of Chemical Engineering & Materials Science

2003

ABSTRACT

GRAPHITE NANOREINFORCEMENTS IN POLYMER NANOCOMPOSITES

By

Hiroyuki Fukushima

Nanocomposites composed of polymer matrices with clay reinforcements of less than 100 nm in size, are being considered for applications such as interior and exterior accessories for automobiles, structural components for portable electronic devices, and films for food packaging. While most nanocomposite research has focused on exfoliated clay platelets, the same nanoreinforcement concept can be applied to another layered material, graphite, to produce nanoplatelets and nanocomposites. Graphite is the stiffest material found in nature (Young's Modulus = 1060 GPa), having a modulus several times that of clay, but also with excellent electrical and thermal conductivity. The key to utilizing graphite as a platelet nanoreinforcement is in the ability to exfoliate this material. Also, if the appropriate surface treatment can be found for graphite, its exfoliation and dispersion in a polymer matrix will result in a composite with not only excellent mechanical properties but electrical properties as well, opening up many new structural applications as well as non-structural ones where electromagnetic shielding and high thermal conductivity are requirements.

In this research, a new process to fabricate exfoliated nano-scale graphite platelets was established (Patent pending). The size of the resulted graphite platelets was less than 1 um in diameter and 10 nm in thickness, and the surface area of the material was around 100 m^2/g. The reduction of size showed positive effect on mechanical properties of

composites because of the increased edge area and more functional groups attached with it. Also various surface treatment techniques were applied to the graphite nanoplatelets to improve the surface condition. As a result, acrylamide grafting treatment was found to enhance the dispersion and adhesion of graphite flakes in epoxy matrices. The resulted composites showed better mechanical properties than those with commercially available carbon fibers, vapor grown carbon fibers, or carbon blacks. The exfoliated graphite flakes reached the percolation threshold at 1.93 wt% (1.13 vol%) in an epoxy system and the resistivity of the composite showed 39 ohm•cm with 7 wt% of exfoliated graphite, which is comparable to the high-grade carbon black based systems. The vapor grown carbon fiber based composites showed higher resistivity at the same filler contents while the conventional carbon fiber composites showed much higher resistivity and percolation threshold. Stress distribution analysis by Finite Element Method revealed the stress concentration condition of composite systems is affected by factors such as shape of the reinforcements, aspect ratio, and geological arrangements. Based on these results, an optimal morphology design of nanocomposite system was proposed. Market research revealed that there is a realistic possibility for applying the new process and material in commercial products and a venture business plan was proposed based on this new technology. The venture plan won "The Most Innovative Design" award at the 2002 Michigan Collegiate Entrepreneur's Conference.

TO MY PARENTS

YOSHIHIKO & AKIKO FUKUSHIMA

ACKNOWLEDGEMENT

First of all, I would like to thank my advisor Prof. Lawrence T. Drzal for his guidance and support throughout my graduate research. Without his patience and assistance, this research project has not been successfully accomplished. I also want to thank Prof. Phillip M. Duxbury, Prof. Krishnamurthy Jayaraman, Prof. Andre Y. Lee, Prof. Dashin Liu, and Prof. Thomas J. Pinnavaia for accepting to be my committee members and providing valuable advices, information, and comments. Also special thanks go to Prof. Ramani Narayan for his guidance in engineering entrepreneurship.

In addition, I would like to thank Mike Rich, Brian Rook, Phil Culcasi, and Kelby Thayer for their help and guidance in learning and operating the equipment in Composite Materials and Structures Center. Also my special thanks go to Dr. Richard Schalek for his support in operating Environmental Scanning Electron Microscopy, Dr. Per Askeland for his experimental and analytical support on X-ray Photoelectron Spectroscopes, Dr. Ahmed Al-Ostaz for his guidance in Finite Element Analysis Method, and Dr. Xudong Fan for his help in operating Transmission Electron Microscopy. Many thanks go to all members in Composite Materials and Structures Center for their friendship and help.

I thank my parents for their encouragement and support. It is clear that this accomplishment wouldn't have been achieved without their sincere support throughout my life. Finally I would like to give my deepest appreciation to my wife, Kana, for her tremendous patience and support during my graduate research.

TABLE OF CONTENTS

TABLE OF CONTENTS

TABLE OF CONTENTS

TABLE OF CONTENTS

TABLE OF CONTENTS

LIST OF TABLES

Page

CHAPTER 1

CHAPTER 2

LIST OF TABLES

Page

CHAPTER 3

CHAPTER 4

LIST OF TABLES

LIST OF FIGURES

Page

CHAPTER 1

CHAPTER 2

LIST OF FIGURES

CHAPTER 3

LIST OF FIGURES

CHAPTER 4

LIST OF FIGURES

LIST OF FIGURES

Page

LIST OF FIGURES

Page

CHAPTER 5

LIST OF FIGURES

Page

CHAPTER 6

ABBREBIATION

AFM: Atomic Force Microscopy

ASTM: American Society for Testing Materials

BET: Brunauer-Emmerr-Teller

CTE: Coefficient of Thermal Expansion

DGEBA: Diglycidyl ether of bisphenol A

DSC: Differential Scanning Calorimeter

EMI: Electromagnetic Interference

EHI: Equivalent Homogeneous Inclusion

ESCA: Electron Spectroscopy for Chemical Analysis

ESEM: Environmental Scanning Electron Microscopy

FT-IR: Fourier-Transform Infrared Spectroscopy

GIC: Graphite-Intercalated Compounds

GSED: Gaseous Secondary Electron Detector

HDT: Heat Distortion Temperature

IFSS: Interfacial Shear Strength

LRO: Long Range Ordering

NMR: Nuclear Magnetic Resonance

PAN: Polyacrylonotrile

PDA: Personal Digital Assistant

PES: Polyethersulfone

PET: Polyethylene terephthalate

PMMA: Polymethylmethacrylate

PP: Polypropylene

PPS: Polyphenylene sulfonate

SEM: Scanning Electron Microscope

TEM: Transmission Electron Microscope

TEPA: Tetraethylenepentamine

TGA: Thermogravimetric Analysis

TMA: Thermal Mechanical Analysis

UHMWPE: Ultra High Molecular Weight Polyethylene

UV: Ultraviolet

VGCF: Vapor Grown Carbon Fiber

VOC: Volatile Organic Compounds

XRD: X-Ray Diffraction

XPS: X-Ray Photoelectroscopy

CHAPTER 1.

INTRODUCTION --- LITERATURE REVIEW

1.1. Introduction

Recent advancement in synthesizing, controlling, and characterizing materials on an atomic scale has attracted many attention to nano-size materials. Polymer nanocomposites are new type of composites that have been developed recently. Among these, polymer-exfoliated clay composite are most widely investigated nanocomposites that show considerable improvement in mechanical properties such as strength, modulus, and/or toughness with significantly lower reinforcement content than their conventional counterparts. The exfoliated clay nanocomposites can also provide other unique properties such as high temperature resistance and reduced permeability. Because of these advantages, clay-polymer nanocomposites are considered to be useful in applications such as interior and exterior accessories for automobiles and aircrafts, structural components for portable electronic devices, and films for food packaging.

The same nanoreinforcement concept could be applied to graphite platelet reinforced polymer composites, since graphite also has layered structures. Graphite flakes have been known as host materials for intercalated compounds for many years. Some of the graphite-intercalated compounds (GICs) can be expanded by rapid heating and show significant volume increase of 100 times or more. These expanded graphite flakes have been used as reinforcements for polymer composites, primarily for adding electrical conductivity to polymer systems. But most of the researches have shown relatively poor mechanical properties because of insufficient separation of the exfoliated graphite sheets, lack of good interaction between graphite and matrix, and the existence of many voids trapped in the composites. Graphite has excellent mechanical properties as well as electrical and thermal conductivity. If the appropriate exfoliation condition and surface

treatment can be found for graphite material, its dispersion in a polymer matrix will result in a composite with excellent mechanical properties. Also composites with good electrical and thermal properties could be achieved, which opens up many applications such as electromagnetic shielding and thermal conductors. The graphite nanocomposite is a new research filed that has many possibilities in the future, yet the area hasn't been fully investigated and still lots of important knowledge is missing such as:

- The efficient exfoliation techniques to process graphite flakes into nano-scale layers
- Systematic knowledge to design optimal surface condition of graphite nanoflakes for better nanocomposite systems
- The total design method to control properties of graphite nanocomposites to fit many applications.

To provide valuable information to fulfill this missing knowledge, it is necessary to understand the basic background of graphite nanocomposite field. This introduction explains:

1. The reason why nano-size materials are good reinforcements.
2. The background of clay nanocomposite systems.
3. The background of graphite flake reinforced composites.
4. Matrix System
5. Adhesion --- Key factor for better composite.
6. Models and theories of nanocomposite properties
7. Summary of introduction

and provides goals and objectives of this research project.

1.2. The Effect of Nano-scale Materials as Reinforcements for Composite Systems

1.1.1. Size Effect on Strength of Solid Materials

In the 1920's, Griffith found the fact that the strength of glass fibers depends on its size. The smaller the material is, the stronger it becomes [1]. Now this phenomenon is called Griffith's law, and is confirmed for different brittle materials by many researchers [2, 3]. One example of this theory is shown in **Figure 1.1**.

Griffith proposed that weakness of larger material is due to the existence of more defects such as cracks. He assumed that the work on creating new crack surface is equal to the strain energy released, or the total amount of relaxation of material upon crack propagation [4]. If the energy required for creating new crack surface is larger than the strain energy that would be released, the crack doesn't grow. Based on his assumptions, Griffith

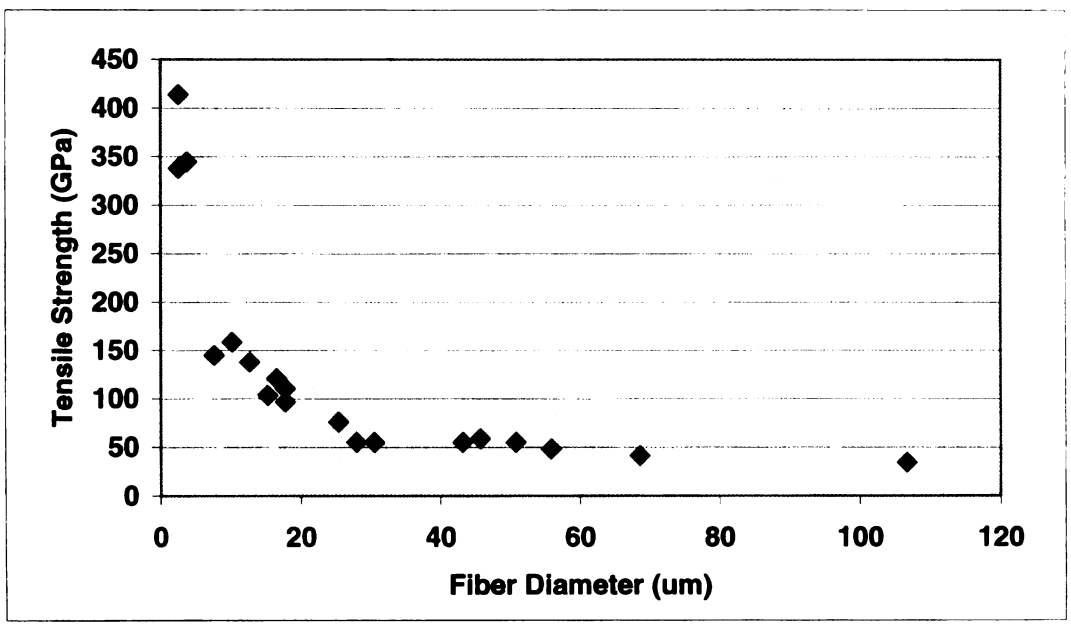

Figure 1.1 Tensile Strength of Glass Fibers in terms of Fiber Diameter (An example of Griffith's Law. Ref. 2)

proposed the existence of a critical crack length at any given stress condition on a material. Griffith crack length is described as follows **[Appendix A1]**

$$\sigma = \sqrt{\frac{2E\gamma}{\pi a}} \quad \text{or} \quad a = \frac{2E\gamma}{\pi\sigma^2} \tag{1-1}$$

where σ is the applied stress, E is the Young's Modulus, γ is the surface tension, and a is the half of the crack length. Cracks longer than this length lead to catastrophic failure of the material. If the material is smaller than the critical crack length, it will not fail and reach its theoretical maximum strength.

In the 1950's, Weibull suggested that the failure of fibers was controlled by the random distribution of defects and thus required a statistical analysis. [5, 6] According to his model, the probability of failure of a material with volume V can be expressed as follows **[Appendix A2]**

$$P_V = 1 - \exp\left[-\left(\frac{\sigma - \sigma_u}{\sigma_0}\right)^m V\right] \tag{1-2}$$

where σ is the Applied stress, σ_u is the critical stress below which no failure occurs, σ_0 is a material constant which relates to the density and the flaw size distribution of the material, m is called Weibull modulus or Weibull shape parameter which is an empirically obtained material constant.

Now consider two specimens made of the same material but have different volumes V_1 and V_2. Assume the material's critical stress, σ_u, is 0 and the median failure stresses (the stress at which 50% of the material fails, which means Pv = 0.5) for the two specimens are σ_1 and σ_2, respectively. Applying equation (1-2) leads the following relation.

$$\frac{V_2}{V_1} = \left(\frac{\sigma_1}{\sigma_2}\right)^m \qquad (1\text{-}3)$$

This equation shows that if V_1 is larger than V_2, σ_1 is smaller than σ_2. In other words, the smaller the material is, the stronger it becomes. This result agrees with the Griffith's law and indicates that the smaller materials can be better reinforcements in composite systems in terms of strength. This relation is experimentally well established with many fiber materials such as glass [7], carbon/graphite [8, 9], boron [10, 11], Kevlar [12, 13], and ultrahigh molecular weight polyethylene [UHMWPE, 14, 15].

1.1.2. Critical Reinforcement Volume

If a very small amount of reinforcements are added to a matrix, the material will be weakened rather than strengthened. But if sufficient reinforcement materials are added, the composite will be stronger than the matrix itself. Thus, there should be a critical filler volume fraction necessary to achieve reinforcement. Piggott explained this theoretically [16, **Appendix A3**]

$$V_{f.\min} = \frac{E_f \sigma_{mu} - E_m \sigma_{fu}}{(x_1 E_f - E_m)\sigma_{fu}} \qquad (1\text{-}4)$$

where $V_{f.min}$ is the Critical Volume Fraction, σ_m and σ_{fu} are the tensile strength of matrix and reinforcements, *Em* and *Ef* is the Young's modulus of matrix and reinforcements, x_1 is a factor which relates to the orientation of reinforcements, and has a value in the range $0<x_1<1$.

This equation shows that the critical volume is decreased when stronger fillers are used. This indicates that a reinforced composite can be achieved with less amount of

fillers if smaller materials are used as reinforcements. Thus, using nanoscale material as reinforcements could lead to composites with easy processability, lightweight, and lower overall cost.

1.1.3. Average Dispersion Distances of Reinforcements in Matrix

Assume fillers are spherical and packed in face center cubic structure in a matrix. The average dispersion distance between particles can be written as: [**Appendix A4**]

$$d = \left[\left(\frac{4\sqrt{2}\pi}{V_f} \right)^{\frac{1}{3}} - 2 \right] \times r \qquad (1\text{-}5)$$

where d is the average dispersion distance, V_f is the volume fraction of reinforcement, r is the radius of reinforcement (assuming as spherical form). The calculated results are illustrated in **Figure 1.2.** As shown, the average dispersion distance becomes smaller

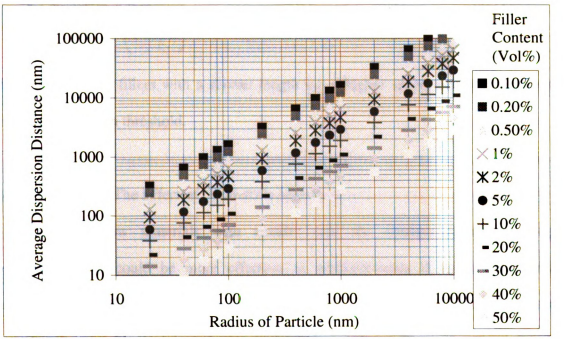

Figure 1.2. Average Dispersion Distance between Particles in a Matrix

for smaller fillers, which means the composite system can achieve a lower percolation threshold with smaller spherical fillers.

This is also true in the case of platelet fillers [**Appendix A5**]. Suppose platelet fillers are embedded in a matrix and aligned in one direction, the volume fraction of fillers can be written as:

$$V_f = \frac{1}{\left(1+\frac{d}{l}\right)^2\left(1+\frac{d}{t}\right)} \qquad (1\text{-}6)$$

where V_f is the volume fraction of fillers, d is the average dispersion distance, l and t are the diameter and thickness of platelet filler. If d is fixed at a distance where tunneling occurs, say 10 nm at room temperature, the volume fraction becomes smaller when l and/or t is smaller. Now define aspect ratio as $a = l / t$, then the equation becomes:

$$V_f = \frac{1}{\left(1+\frac{d}{l}\right)^2\left(1+\frac{d}{l}a\right)} \qquad (1\text{-}7)$$

which implies that fillers with a shorter length but a higher aspect ratio could give the smallest percolation threshold.

1.1.4. Summary of The Effect of Nano-scale Materials

Theories show materials with smaller size are stronger than their larger counterparts, and could be more effective as reinforcements if appropriate surface condition was applied. Also materials with a smaller size but a higher aspect ratio are very effective to add special properties such as electrical and thermal conductivity. The barrier property can be improved if the fillers have flake shape.

1.3. Clay-Polymer Nanocomposites

1.3.1. Background of Clay-Polymer Nanocomposites

Nanocomposites are new materials, which have been developed since the late 1980's. These materials are a combination of matrix and reinforcements with dimensions in nanometer size. Compared to the conventional inorganic-organic hybrid composites, which typically used micrometer size reinforcements, the nanocomposites contain reinforcements of the size of nanometers, such as layered silicates, carbon whiskers, metal fillers, and ceramics made by sol-gel processes. The most widely investigated and developed system among them is the layered silicate-polymer systems.

Layered silicates are a family of phylosilicates that have closely stacked layered structures comprising silica and alumina or magnesium sheets joined together. They have high aspect ratio and good mechanical properties, which make them possible reinforcements for polymer composites. However, their intrinsic tendency to stack together to form tactoids and hydrophilicity that cause incompatibility with most of the engineering polymers prevent them from being exfoliated and dispersed in polymer matrices.

On the other hand, clay minerals have been known as host materials for many cations since the 1930's [17]. This swelling phenomenon was investigated intensively by the end of 1960's including organic cation exchange reaction [18]. Based on this knowledge, a research group at Toyota first reported a polymer intercalated clay composite in 1987 [19, 20]. In the process, they exchanged the inorganic cations inside the layers of silicates by alkylammonium ions and then ε-caprolactam was introduced into the galleries. This process became possible because of the compatibility between

alkyl chains and monomers. Once the monomers are intercalated into the galleries, a polymerization process made it possible to exfoliate the clay layers and disperse them in polymer matrix. Since then, a variety of polymer systems have been investigated including nylon-6, epoxies, polyimide, poly(ε-caprolacton), polysiloxane, polypropylene, polystylene, polyethyleneoxide and rubbers [21, 22, 23,24, 25, 26].

1.3.2. Classification of Clay-Polymer Nanocomposites

In general, clay-polymer composites are classified into four types: conventional, intercalated, long range ordering (LRO) and disordered composites [27, 28] (**Figure 1.3**). In a conventional composite, clays exist as aggregated layers without any intercalation or exfoliation. The size of clay reinforcements is the order of micrometers. This type of composite shows better rigidity than pristine polymers, but the effect is usually limited and often sacrifices other properties such as strength and toughness. In an intercalated composite, polymer chains are introduced into the clay galleries, but clays still keep their layered structures. The distance between layers is in the range of 10~30Å. This type of composite shows considerable advantages in barrier properties and heat resistance ability [29], but still the improvement in mechanical properties is limited.

Exfoliated composites have exfoliated and dispersed clay platelets with few-nanometer thickness and several hundred-nanometer diameter [27]. This type of composites can be divided into two groups, LRO and disordered composites. LRO composite has intercalated and separated clay platelets (30~100Å) so that the adjacent platelets cannot interact with each other. This allows the comparable reinforcing effect to

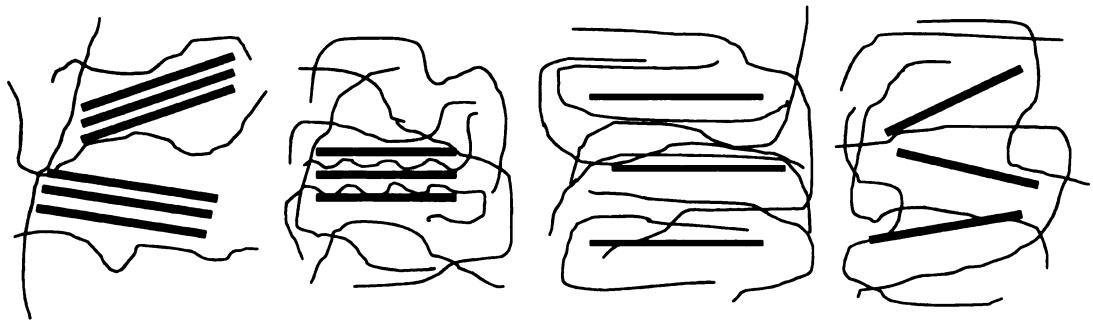

Figure 1.3. Schematic Illustration of Clay-Polymer Nanocomposite Types

that of disordered composites. This structure can be detected by the XRD diffraction of clay 001 plane. In a disordered composite, clays are intercalated and exfoliated. They show no 001 peak in XRD measurement. Because of their structure, both of them show superior mechanical properties with relatively low reinforcements content in addition to the advantages of intercalated composites [28].

1.3.3. Fabrication Methods of Clay Nanocomposites

Conventional clay-polymer composite fabrication includes simple mixing of clays with a matrix polymer. Appropriate surface treatments can be applied on the clay surfaces such as silane coupling, titanate coupling, and polymer grafting. These treatments improve dispersion of the reinforcements in a matrix. But they do not cause intercalation or exfoliation [30, 31, 32]. Clay nanocomposite fabrication methods can be classified into three categories, (1) *in-situ* polymerization, (2) polymer melts intercalation, and (3) compatibilizer intercalation.

(1) *In-situ* polymerization

This method includes monomer intercalation into clay galleries followed by polymerization. During the polymerization process, clays are exfoliated into nano-size platelets. At first, the cations in the clay galleries are exchanged by alkyl ammonium ions, and then polar monomers are intercalated and polymerized by heating. This method leads to either intercalated or exfoliated composites depending on the kinds of monomers and polymerization conditions. In the case of ε-caprolactam [33, 34, 35, 36, 37, 38, 39], epoxy resins [27, 28, 40, 41, 42, 43, 44, 45, 46], and ε-caprolactone [47, 48], intercalation has been done in solutions and exfoliated composites have been produced. In the case of aniline [49] and pyrrole [50], vaporized monomers are applied and intercalated composites have been achieved. This method is limited only for polar monomers and nonpolar monomers such as olefins cannot be used.

(2) Polymer melts intercalation

This method includes direct intercalation of melted polymer chains into clay galleries. At first, alkyl ammonium ions are introduced into clay galleries by using ion exchange reaction to improve the affinity of clay to organic molecules. Then polymers such as poly (amic acid), which causes imidization upon heating [51, 52, 53, 54], poly (ethylene oxide) [55], polystyrene [56, 57], and acrylonitrile-butadiene rubber [58] are intercalated by mixing polymer melts with the clays. Usually these processes produce intercalated composites but in some cases long range ordering exfoliated composites can be achieved.

(3) Compatibilizer intercalation

The Compatibilizer intercalation method was developed to fabricate clay-nonpolar polymer nanocomposites. After intercalating alkyl ammonium ions, compatibilizers such

as functionalized oligomers or copolymers are introduced inside the clay layers. The key point is to choose compatibilizers that have enough polar segments to cause intercalation into clays and also have enough nonpolar segments to make them miscible with a nonpolar polymer matrix. During the mixing process of compatibilizer intercalated clays and nonpolar polymers, shear stress causes exfoliation and dispersion of clays. Nonpolar polymers like polypropylene have been used in this method [60, 61].

1.3.4. Properties of Clay-Polymer Nanocomposites

Once silicates layers are exfoliated and dispersed in a polymer matrix, the hybrid shows unique and preferred properties. Unlike conventional composites, which usually improve rigidity (modulus) but sacrifice strength, elongation, and/or toughness, these nanocomposites can improve not only these mechanical properties, but also other properties such as gas permeability, chemical stability, and thermal stability.

Table 1.1., **1.2.**, and **1.3.** show properties of some conventional silicate-polymer composites, which are mica/nylon 66 [61], mica/polypropylene [62], and mica/epoxy systems [63, 64]. **Table 1.4, 1.5, 1.6,** and **1.7** show properties of clay/nylon 6 [37, 39], clay/polypropylene [59, 60], and clay/epoxy [45, 46] nanocomposites.

In the above Tg condition, the moduli of conventional composites were improved by 300 to 500% with 30 to 40 wt% of fillers while those of nanocomposites were improved by 100 to 300% with only 5 to 10 wt% of reinforcements. In the case of below Tg condition, the moduli of conventional composites were improved typically by 50 to 100%, while those of nanocomposites were improved by 20 to 80% with much less reinforcements. The tensile, flexural, and impact strength of conventional composites

could be improved, but often decreased by 20 to 40%, while those of nanocomposites were often improved by 10 to 40%.

The heat distortion temperature of conventional composites was improved by 20 to 140°C, while that of nanocomposites was improved by 20 to 80°C. The mold shrinkage and coefficient of thermal expansion (CTE) of conventional composites were improved by 50 to 80%, while CTE of nanocomposites was improved by 20 to 50%. Water absorption of conventional composites was improved by about 70%, while water and other solvents absorption of nanocomposites was improved by 40 to 80%. Considering the fact that nanocomposites have much less reinforcements, these accomplishments make nanocomposites excellent materials for many applications.

Table 1.1. Properties of Mica/Nylon 66 Conventional Composites (Ref. 61)

		Nylon 66	Mica (%Change)	Glass Beads (%Change)	Clay (%Change)
Filler Content	Wt%	0	40	40	40
Tensile Strength	x 10^3 psi	13.70	15.26 (+11.4%)	9.78 (-28.6%)	10.85 (-21.5%)
Elongation	%	15.0	2.7 (-82.0%)	3.2 (-78.7%)	2.5 (-83.3%)
Flexural Strength	x 10^3 psi	17.0	26.0 (+52.9%)	15.8 (-7.1%)	23.7 (+39.4%)
Flexural Modulus	x 10^6 psi	0.45	1.54 (+242%)	0.62 (+48.9%)	1.01 (+124%)
Impact Strength	ft*lb/in	0.55	0.6 (+9.1%)	0.4 (-27.3%)	0.3 (-45.5%)
HDT* @264 psi	°C	93.3	237.8 (+144.5°C)	208.3 (+115.0°C)	199.4 (+106.5°C)
Mold Shrinkage	%	1.5	0.31 (-79.3%)	1.1 (-26.7%)	0.4 (-73.3%)
Specific gravity		1.10	1.50 (+36.4%)	1.46 (+32.7%)	1.47 (+33.6%)
Water Absorption	Wt% (24hr)	1.8	0.6 (-66.7%)	0.6 (-66.7%)	0.4 (-77.8%)
CTE**	X 10^5 /°C	8.0	2.2 (-72.5%)	2.8 (-65.0%)	3.9 (-51.3%)

* Heat Distortion Temperature ** Coefficient of Thermal Expansion

Table 1.2. Properties of Mica/Polypropylene Conventional Composites (Ref. 62)

		PP	Mica (%Change)	Silane-Mica (%Change)	Talc (%Change)	Glass Fiber (%Change)
Filler Content	Wt%	0	40	40	40	30
Tg	°C	~0				
Tensile Strength	x 10^3 psi	4.7	4.1 (-12.7%)	6.2 (+31.9%)	4.3 (-8.5%)	6.3 (+34.0%)
Flexural Strength	x 10^3 psi	4.5	6.5 (+44.4%)	9.5 (+111%)	6.4 (+42.2%)	10.1 (+124%)
Flexural Modulus	x 10^6 psi	0.18	0.93 (+417%)	1.10 (+511%)	0.68 (+278%)	0.93 (+417%)
Impact Strength	ft*lb /in	0.45	0.60 (+33.3%)	0.65 (+44.4%)	0.45 (0%)	1.40 (+211%)
HDT* @264 psi	°C	56	89 (+33°C)	108 (+42°C)	78 (+22°C)	125 (+69°C)
Mold Shrinkage	%	2	0.8 (-60%)	0.8 (-60%)	1.2 (-40%)	0.3 (-85%)

* Heat Distortion Temperature

Table 1.3. Properties of Mica/Glassy Epoxy Conventional Composites (Ref. 63, 64)

		Epoxy	Untreated Mica (%Change)			Silane Treated Mica (%Change)		
Filler Content	Wt%	0	10	20	30	10	20	30
Tg	°C	172.8	170.8 (-2.0°C)	167.4 (-5.4°C)	168.7 (-4.1°C)			
Tensile Strength	MPa	76.4	52.9 (-31%)	52.2 (-32%)	48.3 (-37%)	53.5 (-30%)	53.7 (-30%)	48.4 (-37%)
Tensile Modulus	GPa	1.73	2.06 (+19%)	2.38 (+38%)	2.67 (+54%)	2.45 (+42%)	2.70 (+56%)	3.51 (+103%)
Elongation	%	11.48	4.60 (-60%)	3.69 (-68%)	2.77 (-76%)	4.55 (-60%)	3.45 (-70%)	2.58 (-78%)
Flexural Strength	MPa	128.9	132.2 (+2.5%)	90.3 (-30%)	84.9 (-34%)	137.3 (+6.5%)	114.4 (-11%)	102.2 (-21%)
Flexural Modulus	GPa	3.03	3.57 (+18%)	4.60 (+51%)	5.22 (+72%)	3.45 (+14%)	5.40 (+78%)	5.78 (+91%)
CTE ** (30-50°C)	x 10^5 /°C	8.65	5.89 (-32%)	5.15 (-41%)	4.48 (-48%)	4.70 (-46%)	4.83 (-44%)	4.36 (-50%)
CTE ** (200-220°C)	x 10^5 /°C	53.70	14.30 (-73%)	11.70 (-78%)	10.90 (-80%)	13.00 (-75%)	11.20 (-79%)	10.10 (-81%)

** Coefficient of Thermal Expansion

Table 1.4. Properties of Clay/Nylon 6 Nanocomposites (Ref. 37, 39)

		Nylon 6	Montmo-rillonite (%Change)	Mica (%Change)	Saponite (%Change)	Hectorite (%Change)
Filler Content	Wt%	0	5	5	5	5
Tg	°C	~70				
Tensile Strength	@23°C MPa	68.6	97.2 (+43.9%)	93.1 (+35.7%)	84.7 (+23.5%)	89.5 (+30.5%)
	@120°C MPa	26.6	32.3 (+21.4%)	30.2 (+13.5%)	29.0 (+9.0%)	26.4 (-0.8%)
Elongation	%	>100	7.3	7.2	>100	>100
Tensile Modulus	@23°C GPa	1.11	1.87 (+68.5%)	2.02 (+82.0%)	1.59 (+43.2%)	1.65 (+48.6%)
	@120°C GPa	0.19	0.61 (+221%)	0.52 (+174%)	0.29 (+52.6%)	0.29 (+52.6%)
Flexural Strength	@23°C MPa	89.3	143 (+60.1%)			
	@120°C MPa	12.5	32.7 (+162%)			
Flexural Modulus	@23°C GPa	1.94	4.34 (+124%)			
	@120°C GPa	0.29	1.16 (+300%)			
Impact Strength	kJ/m^2	20.6	18.1 (-12.4%)			
HDT* @1.82 MPa	°C	65	152 (+87°C)	145 (+80°C)	107 (+42°C)	93 (+28°C)
Water Absorption	%	0.87	0.51 (-41.4%)			
CTE**	$x\ 10^{-5}$ /°C	13.0	6.3 (-51.5%)			

* Heat Distortion Temperature

** Coefficient of Thermal Expansion

Table 1.5. Properties of Clay/Polypropylene Nanocomposites (Ref. 59, 60)

		PP	Montmorillonite (%Change)
Filler Content	Wt%	0	5
Tg	°C	13	13
Tensile Strength	MPa	32.5	31.7 (-2.5%)
Tensile Modulus	GPa	0.78	1.01 (+29.5%)
Storage Modulus	@-40°C, GPa	3.92	5.06 (+29.1%)
	@20°C, GPa	1.98	2.98(+50.5%)
	@80°C, GPa	0.648	1.14(+75.9%)

Table 1.6 Properties of Clay/Glassy Epoxy Nanocomposites (Ref. 45)

		Glassy Epoxy (DGEBA/ D230)	Synthetic Montmorillonite (%Change)		Natural Montmorillonite (%Change)	
Filler Content	Wt%	0	5	10	5	10
Tg	°C	81.6	83.1 (+1.5°C)	80.2 (-1.2°C)	80.6 (-1.0°C)	79.9 (-1.7°C)
Yield Strength	MPa	75.3	80.0 (+6.2%)	87.5 (+16.2%)	80.5 (+6.9%)	83.0 (+10.2%)
Compressive Modulus	GPa	1.40	1.51 (+7.9%)	1.77 (+26.4%)	1.56 (+11.4%)	1.70 (+21.4%)
CTE** below Tg	x 10^{-5} /°C	8.0	6.4 (-20.0%)	6.0 (-25.0%)		
CTE** above Tg	x 10^{-5} /°C	15.0	14.4 (-4.0%)	13.5 (-10.0%)		
Solvent Uptake (Propanol)	@50days wt%	18.0		7.0 (-61.1%)		
Solvent Uptake (Toluene)	@50days wt%	12.0		2.5 (-79.2%)		

** Coefficient of Thermal Expansion

Table 1.7 Properties of Clay/Rubbery Epoxy Nanocomposites (Ref. 46)

	Rubbery Epoxy (DGEBA/ D2000)	Montmorillonite			Magadiite		
Filler Content [Wt%]	0	1.4	3.6	7.4	2.6	5.4	10.8
Tensile Strength [MPa]	0.6	0.8 (+33%)	1.55 (+158%)	3.60 (+500%)	1.50 (+150%)	2.50 (+317%)	3.40 (+467%)
Tensile Modulus [GPa]	3.5	4.5 (+29%)	7.5 (+114%)	14.5 (+314%)	6.5 (+85.7%)	7.7 (+120%)	9.2 (+163%)
Elongation [%]	24				31 (+29.2%)	43 (+79.2%)	48 (+100%)

1.3.5. Applications of Clay-Polymer Nanocomposites

The clay-nylon 6 system was the first nanocomposite used in commercial applications and is still the most advanced and successfully applied nanocomposite. Because of its increased stiffness, strength, thermal stability, and flame retardancy, the material was first applied in timing belt cover. Although the material is not used for this application any more, since the cover did not require the improved performance of the nanocomposite, this trial provided the background to apply this material to other automobile parts, such as engine and valve covers, underhood connectors, fuel system components, and coolant system components. Another main application for this material is food packaging. Because of the improved oxygen barrier performance as a film, the nanocomposite is used in food packaging primarily for meats and cheese. The material reduces the thickness of a film that lowers the cost and/or increases the shelf life of the package.

The clay-polypropylene (PP) system is considered to be the next most important nanocomposite material since PP has the largest range of applications. The applications include automobile components such as: interior and exterior trim and air ducting; and packaging of snacks, meats, cheeses and baked goods.

The clay-polyethylenetelephthalate (PET) system is another important nanocomposite. Because of its improved barrier properties, the material is considered to be used in PET bottle application, especially the plastic beer bottle market which requires to maintain the freshness and flavor of the beer. Industrial fiber application such as tire cord is another possible market for this nanocomposite.

The clay-epoxy system is also a well developed nanocomposite, which is expected to be used in metal coating application for appliance housings, automobile components, industrial machinery, and equipment panels. The nanocomposite can provide improved scratch and corrosion resistance.

Many other clay-polymer systems are under development and expected to be used in many applications [65, 66, 67, 68]. The applications for clay nanocomposite systems are summarized below.

- Films for food and/or pharmaceutical packaging
- Automobile parts (fuel tanks, brake parts, engine components, interior and exterior trim)
- PET bottles
- Housings for electronic devices (TVs, stereos, refrigerators, vacuum cleaners, and kitchen electronics)
- Window sidings
- Wire and cable covers

1.4. Graphite-Polymer Nanocomposites

1.4.1. Background of Graphite Reinforced Polymer Nanocomposites

While many researches have focused on exfoliated clay platelets reinforced nanocomposite systems, the same nanoreinforcement concept can be applied to graphite platelet. Graphite is one of the stiffest materials found in nature (Young's Modulus=1060 GPa) and also has excellent electrical and thermal conductivity. Compared to clay minerals, graphite has better mechanical, electrical, and thermal properties while the density is lower than that of clays (**Table 1.8**) [69, 70]. Since the chemical structures of these materials are totally different [**Figure 1.4**.], the fabrication method to achieve graphite nanocomposites should be also different.

Table 1.8. Properties of Clay and Graphite (Ref. 69, 70)

	Clay	Graphite
Physical Structure	Layer	Layer
Chemical Structure	SiO2, Al2O3, MgO, K2O, Fe2O3	Carbon
Interactions between Layers	Hydrogen bond Dipole-Dipole	$\pi - \pi$
Tensile Modulus	172 GPa	1060 GPa
Tensile Strength	0.3-0.9 GPa	20 GPa
Resistivity	$10^{10} - 10^{16}$ Ω cm	50×10^{-6} Ω cm
Thermal Conductivity	6.7×10^{-3} W/cm K	30 W/cm K
Coefficient of Thermal Expansion	$8 - 16 \times 10^{-6}$ /K	-1×10^{-6} /K
Density	2.75 – 3.00 g/cm^3	1.80-2.00 g/cm^3

Carbon and graphite materials have been used as fillers for a long time. Carbon black is one of the most widely used carbon materials as fillers because of its cost effectiveness (less than $0.5/lb). Carbon black is especially important in elastomer systems such as automobile tire application. The material can provide useful properties such as UV and thermal protection, electrical conductivity, and improved compound

processability. Carbon black is also used in many thermoplastic and thermoset resin systems to add adequate conductivity at lower costs. Because of its relatively poor mechanical properties and insufficient interactions with matrix polymers, the carbon black is not used as reinforcement but used as filler for economy, moderate conductivity, coloring, or opacifying polymers [71].

In the late 1950's, Bacon succeeded in fabricating graphite whiskers by applying DC arc discharging process to graphite electrode under high temperature and pressure [72]. The resulted material showed excellent mechanical properties (**Table 1.9**) and attracted much attention. However, the difficulty of large-scale fabrication prevents it from being used in commercial applications.

At the same time, research efforts to produce continuous carbon fibers were under way. First, the carbonization process of rayon fibers was developed, and then polyacrylonitrile fibers were found to be useful as the starting material. Later, the melt-spinning method of mesophase pitch was discovered. By the end of 1960's, some carbon fibers were commercially available and used in military grade aerospace applications. Because of constant improvements in properties and decreased price, carbon fibers have found many applications such as commercial jet planes, sporting goods, and automobiles. Now the tensile strength of some carbon fibers reach 5 to 7 GPa, while the moduli of other fibers show 600 to 800 GPa [73]. Now it is obvious that carbon fibers become some of the most important reinforcement materials. However, relatively high cost of carbon fibers has prevented them from being used in some large-scale applications. Just recently some of the carbon fiber manufactures began providing low cost carbon fibers at the price

range of $5-6/lb. These products could open new applications for the carbon fiber reinforced composites such as commercial automobile body parts.

Since the 1970's, a new fabrication method of carbon fibers called vapor-grown carbon fiber (VGCF) has been investigated. The process includes pyrolysis of hydrocarbon in the presence of catalyst. The resulted fiber has a unique morphology. The graphene planes are more circumpherentially oriented around the fiber axis and have higher purity in carbon, which leads to excellent mechanical, electrical, and thermal properties. However, highly pure graphene planes cause poor interaction with polymer matrices. The early stage process used fixed catalyst method, which could produce only small amount of discontinuous fibers at once. Recent introduction of floating catalyst method improves productivity, but resulting fibers with tangled fibril like shape. Although the expected cost would be $10/lb or less, the price is still much higher than that of melt-spun carbon fibers at this point. The current price of VGCFs is $40-50/lb.

In 1985, a new structure of carbon material is found and named as fullerene (or buckyball) [74]. It has a spherical shape, comprised of 60 carbons. These carbons form five or six-membered rings, which construct a sphere just like a soccer ball. Following this discovery, another new structure of carbon was reported in 1991 [75]. Because of its nano-scale size and tubular shape, the material is called carbon nanotubes. Because researchers predicted that the material has the highest available mechanical and electrical properties among carbon materials, a lot of researchers in a variety of fields including advanced composite area are now working with this material. But its low productivity and very high cost make it difficult to apply this material to commercial applications in the near future.

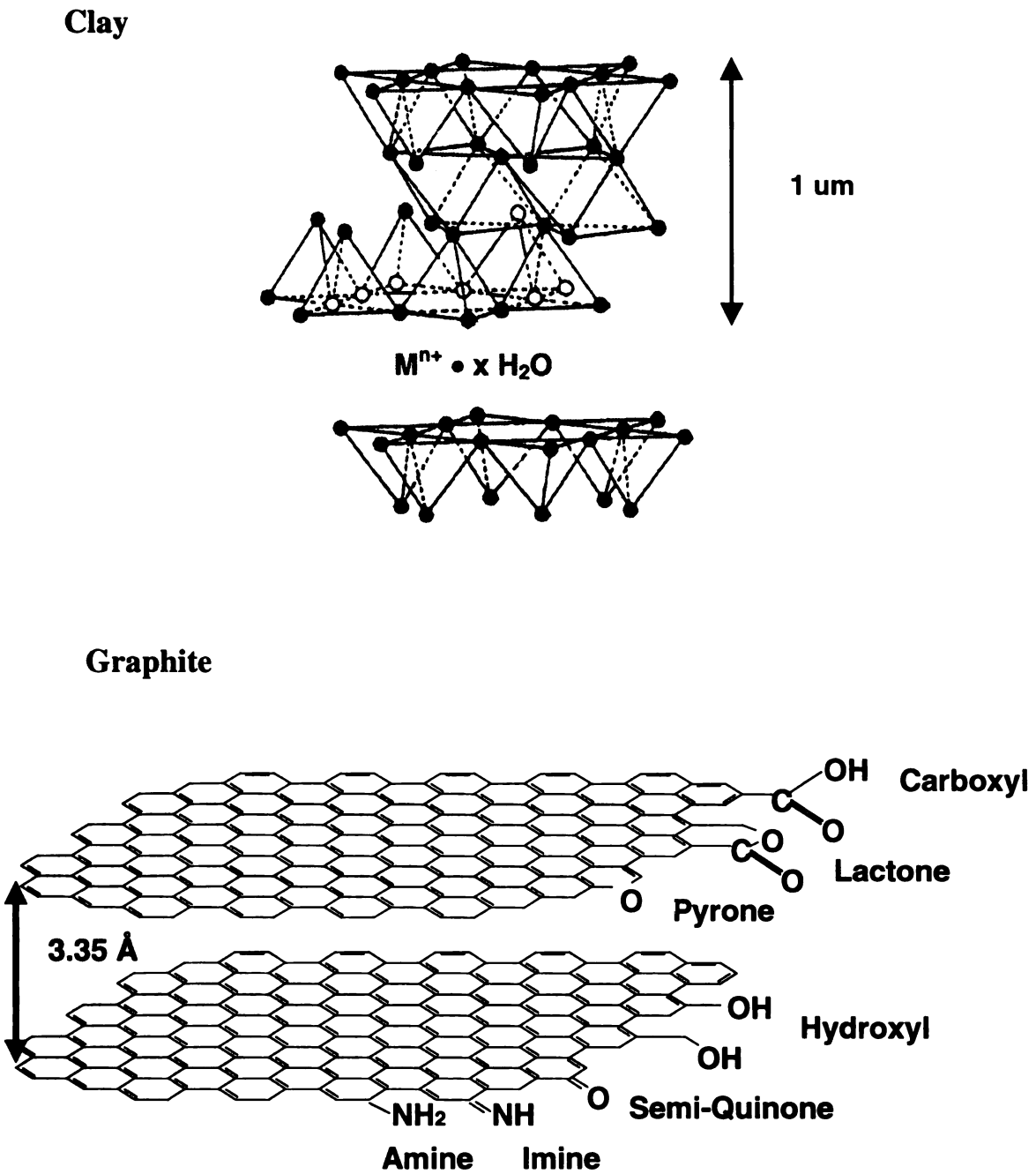

Figure 1.4. Structures of Clay and Graphite

Table 1.9. Properties of Carbon/Graphite Materials

	Diameter [um]	Length [um]	Tensile Modulus [GPa]	Tensile Strength [GPa]	Electrical Resistivity [Ω cm]	Thermal Conductivity [W/m*K]	Cost [$/lb]
Carbon Black	10-300	10-300			10^{-1} - 10^{2}		< 0.4
High Strength CF	4.5-7.2	Continuous	250- 300	5 - 7	6.8 x 10^{-3}		<15
High Modulus CF	4.3-8.4	Continuous	400-800	2.5 – 4.0	1.7 x 10^{-3}		15-25
Chopped CF	6-8	100 - 7500	150-250	1.5-3			5 -6
Vapor Grown CF	0.1-10	10 – 500	250-500	3 - 7	7 x 10^{-5} - 1 x 10^{-3}	20 - 2000	40-50
Carbon Nanotube	0.007-0.1	1	1250 ~ 2000	50 ~ 180		3000	40,000
Single Crystal Graphite	0.4 - 2000	Thickness 0.005 - 100	1000	10 - 20	5 x 10^{-5}	3000	< 5

Theoretically the crystalline graphite has excellent mechanical, electrical, and thermal properties, and many crystalline graphite materials are available including natural and synthetic graphite. These materials are more abundant and more economical than graphite whiskers and VGCF, yet the properties are similar or better. Carbon nanotubes have better properties than those of crystalline graphite materials, yet the cost of crystalline graphite is much cheaper, which makes it a more realistic choice for commercial applications. If these particles were exfoliated and separated into single or few layers of graphene sheets and an appropriate surface treatment was applied, these materials could be excellent reinforcements in polymer composites in terms of mechanical, electrical, thermal and economical point of view.

1.4.2. Intercalated, Expanded, and Exfoliated Graphite as Reinforcements in Polymer Matrix

Graphite has been known as a host material of many chemicals, including metal halides, metal oxides, and mineral acids. Also, the exfoliation phenomena of some of the graphite intercalated compounds (GIC) have been investigated for a long time. In the 1910's, Aylsworth filed two patents related to expanded graphite and its usage in molding application [76, 77]. The claims include (1) the process of intercalating acids into graphite, (2) heat expansion of the intercalated graphite to make "fluffy graphite", and (3) compounding expanded graphite in resins, typically phenolic resins. He reported that the graphite have to be expanded, but not completely separated so the specific gravity was decreased significantly. As a result, his invention could offer lightweight, heat resistant, and chemically stable moldings suitable for gaskets and packing applications, but there was no claim about electrical conductivity. Since then, many researchers have been investigating the exfoliation phenomena of GICs [78, 79, 80, 81, 82, 83].

Based on the fact that the electrical conductivity of graphite particles can be enhanced by intercalating strong acid, halide salt, or metal halides, Lincoln and his coworkers proposed composites reinforced with intercalated graphite which had very high conductivity. [84] In their research, the intercalated graphite materials were not expanded. As a result, they needed to add 10 to 65 volume % of graphite in the system to achieve conductivity and the density of the final composites increased. Also, the mechanical properties of composites are not improved because of the lack of appropriate surface treatment on graphite materials.

After Lincoln's research, many people proposed using expanded or exfoliated graphite in polymer systems to fabricate lightweight and conductive polymer composites [85, 86, 87, 88, 89]. **Table 1.10.** shows the electrical properties of these composites.

Table 1.10. Electrical Properties of Intercalated or Expanded Graphite Reinforced Composites

Ref.	[77]	[85]	[86]	[87]	[88]	[89]
Graphite	Intercalated	Expanded	Expanded	Expanded	Expanded	Expanded
Aspect Ratio				2 or 20		100
Polymer		Vinyl ester	Polyimide	HDPE	Polyester	Epoxy
Vol % of Graphite	10 - 65	> 50	50	10 - 50	20 - 50	2 - 9
Density of Composite [g/cm^3]		< 0.7	~0.75	0.6 – 0.8	0.5 – 0.9	
Resistivity [Ω*cm]	1.6 x 10^{-3} (60 vol%)	< 5 x 10^{-1} (60 vol%)	1.4 (50 vol%)	1x 10^{-1} (40 vol%)	3 x 10^{-3} (50vlo%)	2 x 10^{-1} (9 vol%)
Percolation threshold				2.5 - 7.5 wt%	< 4.0 wt%	< 2.0 wt%

Typically these composites include 10 to 50 vol% of exfoliated graphite and show density of 0.5 to 0.9 g/cm^3. The resistivity reached as low as 10^{-1} to 10^{-3} Ω cm, which is low enough to be used in applications such as electromagnetic interference (EMI) shielding material, electrostatic discharge material, and electrical conductors. Percolation threshold was typically 4 wt% and it became less than 2 wt% in the case of exfoliated graphite with high aspect ratio (>100). However, the resulted composites often included many voids and the mechanical properties were expected to be poor, thus, these properties were ignored. Some authors reported improved mechanical properties of exfoliated graphite reinforced composites [90, 91]. Typically, these composites include

30 to 50 vol% of exfoliated graphite. The modulus was improved more than 200% in the case of above Tg condition and strength was improved by up to 20%.

Recent success of clay-polymer nanocomposite field provoked some researchers to apply the same concept to graphite-polymer nanocomposite systems. Several techniques have been reported to fabricate graphite nanocomposites. These techniques include the *in-situ* polymerization with expanded graphite (*In-situ* polymerization technique), the solution intercalation, the melt blending, and the *in-situ* polymerization with initiator–intercalated graphite (polymerization-filling technique).

- *In-situ* polymerization technique

Hu and his co-workers intercalated ε-caprolactam into exfoliated graphite galleries and applied *in-situ* polymerization technique to make nylon6/graphite nanocomposite [92]. They also achieved good conductivity and increased modulus with up to 3 vol % of graphite, which is much smaller loading than the previously reported results. At the same time, Chen and his group applied the same technique to polystyrene/graphite nanocomposite system [93, 94]. They achieved nanometer-size graphite platelets dispersed in polymer system and successfully improved tensile strength as well as conductivity. But impact strength was decreased in both cases. Gong et al. also made polystyrene/graphite composites and reported improved electrical conductivity and thermal resistance [95].

- Solution Intercalation

Shen et al. fabricated polypropylene/graphite nanocomposites by mixing expanded graphite with maleic anhydride grafted polypropylene in xylene solution. They call this process the solution intercalation technique and achieved composites with good

conductivity [96]. Wong et al. dissolved polymethylmethacrylate (PMMA) in chloroform and mixed this solution with expanded graphite to make composites with good electrical conductivity. The percolation threshold showed 0.6 vol% [97].

- Melt Blending

Wilkie et al. applied melt blending technique to nylon6/acid-intercalated graphite system [98]. The temperature setting for blending was 250°C and graphite flakes were exfoliated during the process. The resulted composites showed improved thermal stability, but reduced mechanical properties.

- Polymerization-filling technique

Organic molecules are known to be intercalated into graphite layers not by themselves alone but with alkali metals and make co-intercalated GICs. In this case, alkali metals, such as potassium, rubidium, and cesium, are first intercalated into highly oriented pyrolytic graphite galleries. Organic materials such as benzene, ethylene, propylene, acetylene, isoprene, styrene, 1,3-butadiene, acrylonitrile, 1-butane, and isobutene can then be intercalated and make co-intercalated compounds.

In 1976, Beguin and his group reported that benzene could form biphenyl inside Cs-GIC galleries [99]. Since then it has been confirmed that benzene can form oligomers in the layers of GICs [100, 101, 102, 103, 104]. Also ethylene and acetylene have been found to form oligomers in GICs galleries [105, 106, 107]. Based on these results, Shioyama and his group successfully polymerized unsaturated hydrocarbons inside GIC galleries [108, 109, 110, 111]. In their study, vaporized isoprene, styrene, and 1,3-butadiene were intercalated into GICs and polymerized, which caused exfoliation of graphite layers. The degree of polymerization of the resulted polyisoprene was estimated

about 3,800. The mechanism of polymerization reaction is considered to be similar to the anion living polymerization initiated by sodium-naphthalene [112, **Appendix A6**]. Wilkie and his group used the same technique to make polystyrene/graphite nanocomposites and found improved thermal stability, but decreased mechanical properties [113, 114]. Gong also fabricated polystyrene/graphite nanocomposite following the same reaction and reported improved thermal stability and good electrical conductivity with a percolation threshold of 8.2 wt% [115].

The properties of graphite nanocomposite based on *In-situ* polymerization and polymerization-filling technique are summarized in **Table 1.11**. Since graphite nanocomposite is a new field, not many papers have been published to date and the concept of nanoflake-reinforced composite has not been fully accomplished yet. Thus, more detailed research efforts are needed to understand this area, including design and evaluation of the interface and adhesion between graphite nanoplatelets and polymers. If the appropriate surface treatment can be found for graphite, its exfoliation and dispersion in a polymer matrix will result in a composite with excellent mechanical properties as well as electrical properties, opening up many new applications such as electromagnetic shielding and thermal conductors.

Table 1.11. Properties of Graphite-Polymer Nanocomposites (Ref. 92, 93, 94, 95, 96, 114, 115)

Ref.		92	93	94	95	96	114	115
Graphite		Natural Graphite	Natural Graphite	Natural Graphite	Natural Graphite	Natural Graphite	HOPG	Natural Graphite
Intercalate		H_2SO_4/HNO_3	H_2SO_4/HNO_3	H_2SO_4/HNO_3	H_2SO_4/HNO_3	H_2SO_4/HNO_3	K	K
Exfoliation		900 °C	1050 °C 15 sec.	1050 °C 15 sec.	800 °C 30 sec.	900-1000 °C		
Process		In-situ polym.	In-situ polym.	In-situ polym.	In-situ polym.	Solution Intercslation	Polym.-filling	Polym.-filling
Polymer		Nylon	Nylon	PS/PMMA	PS	PMA-PP	Styrene	Styrene
Aspect Ratio		150-300	15-40	10-40				
Graphite content	Wt%	0.0→5.0	0.0→5.0	0.0→5.0	0.0→7.0	0.0→6.5	0.0→5.0	0.0→8.0
Flexural Modulus	GPa	1.0 →1.18 (+18%)						
Flexural Strength	MPa	52→33 (-37%)						
Tensile Strength	MPa		30→38 (+26%)	25→29 (+16%)				
Impact Strength	J/m	59→32 (-46%)	12→6.4 (-47%)	29→15 (-48%)				
Resistivity	Ωcm	10^{15}→1 x 10^{3}	10^{15}→1 x 10^{2}	10^{15}→1 x 10^{1}	10^{15}→1 x 10^{1}	10^{15}→1 x 10^{3}		10^{16}→ 1
Percolation Threshold		1.5 wt% (0.75Vol%)	1.8 wt% (0.9Vol%)	1.8 wt% (0.9Vol%)	2.5 wt% (1.4 vol%)	1.0 wt% (0.67 vol%)		
Tg	°C				91→124 (+33°C)			(+5°C)
T10% Tmax	°C				(+28.66°C)		(~+50°C) (~+30°C)	

1.4.3. Advantages and Applications of Graphite-Polymer Nanocomposites

Since graphite flakes are discontinuous reinforcements, they cannot replace the applications which require superior mechanical properties and need continuous carbon fiber reinforced composites. Because of their small size, these flakes could be incorporated in various polymers and molded by widely used processing methods including injection molding, resin transfer molding, and sheet molding compounds. Accordingly, freedom of design can make it possible to consolidate parts and reduce the assembly steps, which could decrease the total cost. In addition to these advantages in processability point of view, graphite-polymer nanocomposites could have distinctive advantages including excellent mechanical, electrical, and thermal properties in addition to lightweight and lower coefficient of thermal expansion. Because of the overall excellent properties and easy processability, graphite-polymer nanocomposites could be used in many applications such as:

- Thermal conductors (Heat management component for notebook computers and PDAs)
- Electronic heat sink
- EMI shielding material (Disk drive housing. Bodies and parts for PDAs and cellular phones)
- Connectors and switches
- Electrostatic dissipative material (Interior parts and coatings for houses, automobiles, planes, ships, and spacecrafts. Wire and cable covers. Automobile fuel line components)
- Electrostatic painting (Automobile exterior trim)

1.5. Matrix System

1.5.1. Model Systems

Virtually all kinds of polymers could be incorporated with exfoliated graphite to make composite materials. The selection of polymers and process methods depends on the final application. It is required to design optimal surface and interface/interphase conditions to achieve maximum performance in each system. Since graphite-polymer nanocomposites is a new field, no systematic knowledge is available. Thus, it is reasonable to set up a model system and investigate the surface condition of graphite nanoreinforcement and overall properties of the resulted composites.

1.5.2. Epoxy

Epoxies are widely used thermoset polymers in many applications such as coatings, adhesives, sporting goods, and structural material for bridges, airplanes and spacecrafts. Also, they are some of the most widely used matrices for carbon fiber reinforced composite systems. Epoxies are available in relatively low-viscosity liquid forms that make them easy to process and penetrate into fiber bundles and leads low void formation. They also have low shrinkage and good chemical resistance. Chemical properties of monomers, curing agents, and cross-link density are the main factors for the properties of the resins.

Because of its availability and wide usage in carbon fiber-polymer composite systems, it is reasonable to choose an epoxy resin as a model system for this research. Diglycidyl ether of bisphenol A (DGEBA) is the most widely used epoxy resin and

suitable for the purpose. Epon 828 was purchased from Shell Chemicals and used in this research. The chemical structure of the resin is shown in **Figure 1.5.**.

The properties of epoxy can be controlled by choosing suitable curing agents. For example, Tg of epoxy systems can be controlled from -40°C to 182 °C by choosing different curing agents [45, 46, 116]. Also tensile moduli change from 3.5 to 3300 MPa and tensile strength from 0.6 to 75 MPa. **Table 1.12** summarizes some of the properties of epoxy systems. The chemical structures of these curing agents are shown in **Figure 1.6.** [45, 46, 117].

Table 1.12 Properties of Epoxy Systems

Epoxide		DGEBA (EPON 828)			
Curing Agent		Jeffamine D2000	Jeffamine D230	Jeffamine T403	mPDA
Curing Condition		75 °C, 2hr 125°C, 3hr	75°C, 3hr 125°C, 3hr	85°C, 2hr 150°C, 2hr	75°C, 2hr 125°C, 2hr
Tg	°C	-40	82	90	182
Tensile Strength	MPa	0.6	67	61	73
Tensile Modulus	MPa	3.5	2800	2500	3300
Elongation	%	25	9.6	9 ~ 10	4
Poisson's Ratio				0.35	0.35
CTE (below Tg)	um/m°C		80	89	
CTE (above Tg)	um/m°C		150	185	

Diglycidyl ether of bisphenol A (Epon 828, Shell Chemicals)

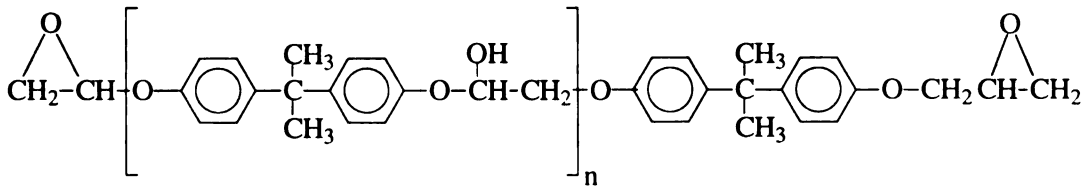

m = 0.14,
[m=0(88%) + m= 1(10%) + m=2(2%)]

Figure 1.5. Epoxy Resin

Jeffamine D2000
(Huntsman Petrochemical)

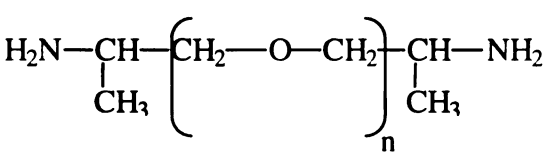

n = 33.1

Jeffamine D230
(Huntsman Petrochemical)

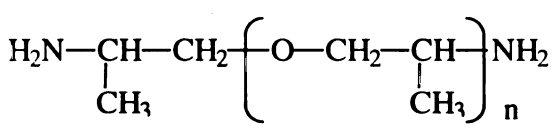

n = 2.6

Jeffamine T403
(Huntsman Petrochemical)

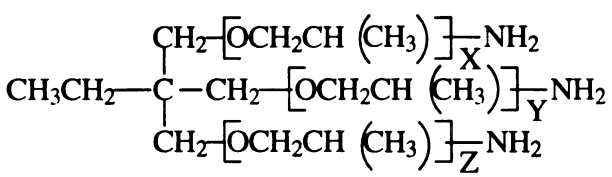

X+Y+Z=5.3

m-Phenylenediamine
(Aldrich Chemical)

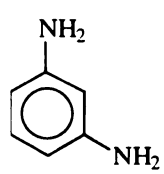

Figure 1.6. Curing Agents for Epoxy Systems

1.6. Adhesion of Nanoreinforcements to Polymer Matrix

Good interactions between reinforcements and a matrix are the key points to maximize performance of composite systems. Good adhesion effectively transfers stress from a matrix to reinforcements, making the system stronger, but it is not simple to define the optimal surface condition. For example very strong interaction between reinforcements and a matrix often leads to a stiff and brittle interphase, making the composite less useful. To design the optimal surface condition, it is necessary to understand basic concepts of interface and interphase, adhesion mechanisms, and the evaluation methods of adhesion.

1.6.1. Interface and Interphase

The interface between reinforcements and matrix used to be considered as a simple two-dimensional boundary, but actual interrelationships between them have complex structures including an interphase that has a three-dimensional region with thickness ranging from 5 to 5000Å [118]. **Figure 1.7.** shows a schematic model that includes various factors occurring in the interphase region [119]. This region includes surface treatment agents, surface chemical groups, absorbed gases on the reinforcement surface, and chemically and morphologically different polymers from bulk matrix. Topography and morphology of the reinforcements are also factors to be considered. The introduction of the strongly bound, concentric, and elastomeric interphase between reinforcements and a matrix is the key point of improving the overall mechanical properties of the composite systems.

Because of the structural and chemical complexity of the interphase, it is not easy to make models that can effectively predict the appropriate surface treatment required for a given reinforcement-matrix combination, but oversimplification often fails to estimate precise composite properties. Thus, precise characterization of the interphase region, such as chemical (functional groups) and physical (crystallinity, topography) structure of both reinforcements and matrix, as well as the elasticity of the interphase region are necessary for making effective composite models. XPS, FT-IR, and NMR measurements are often used to analyze the chemical structure while microscopes (SEM, TEM, AFM, and optical microscopes) as well as DSC measurement are used to analyze the physical properties. To investigate the modulus of the interphase region, precise nano-scale indentation experiments are required.

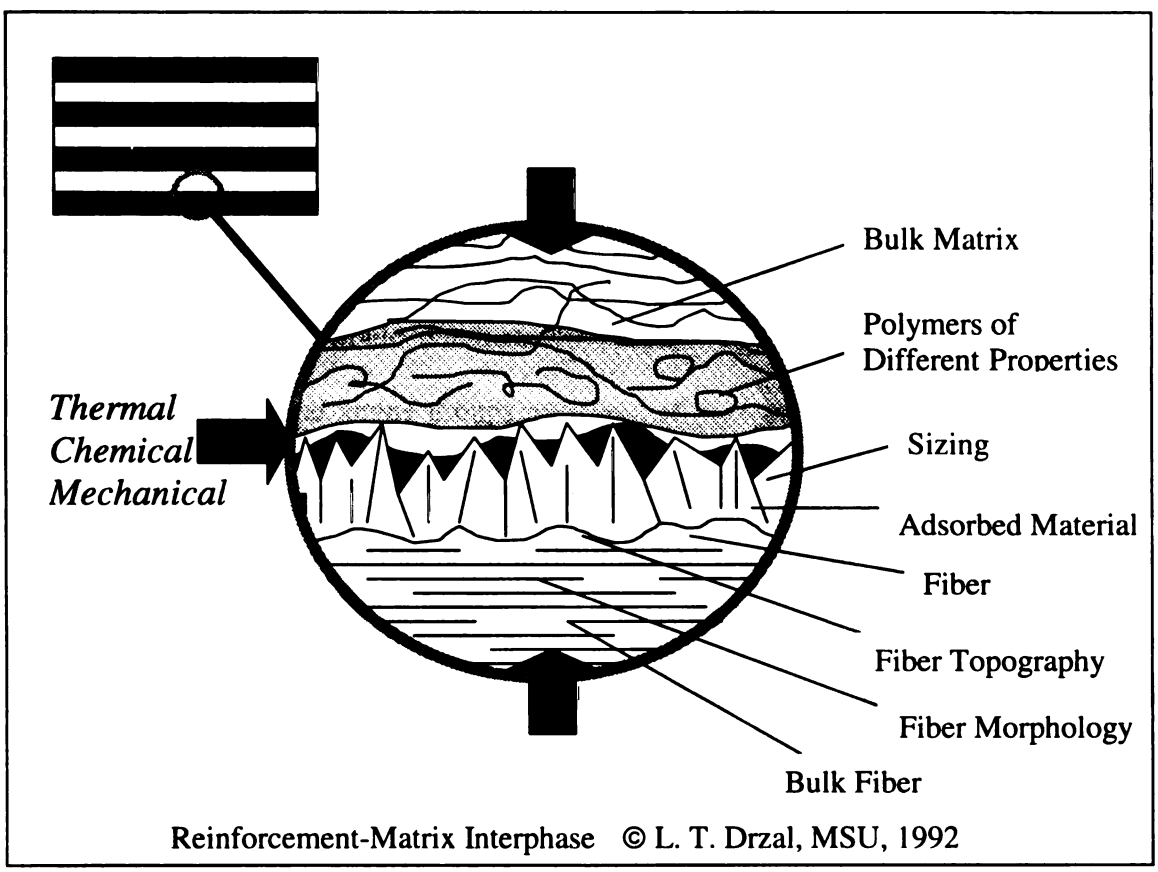

Figure 1.7. Schematic Diagram of the Interphase Region in Composite

1.6.2. The Mechanisms of Adhesion

Adhesion phenomena rely on many intermolecular interactions, which can be classified into three groups: physical, chemical, and mechanical interactions. The physical interactions are based on Van der Waals forces, hydrogen bonding, and other low energy interactions. Van der Waals forces include dipole-dipole interactions, induced dipole-dipole interactions, induced dipole-induced dipole interactions, and nondipole-nondipole interactions. Hydrogen bond is based on the interaction between a hydrogen atom and a nitrogen, oxygen or fluorine atom. The energy of these interactions is estimated to be up to 20 kcal/mole. Factors for these interactions are molecular conformation, atomic arrangement of the surface, and morphological properties of matrix and reinforcements. Although the individual bond is weak, it could show strong total bonding if the interaction occurs in a large area.

The chemical interactions contain covalent bonding, electrostatic attraction, and wetting. Chemical interactions make stronger bonding than physical or mechanical interactions and its energy are expected to be more than 20 kcal/mole. Thus, once these interactions occur, they would dominate the properties of the interphase and adhesion. Carboxyl, hydroxyl, and amine groups are some of the many functional groups, which play a main role in chemical interactions. Main factors are chemical constitution of the interface, chemical reactions that occur at the interface, and the strength of the bonding.

The mechanical interactions can be attributed mainly to the entanglement of the molecules at the interphase. Main factors are the length of the chains, molecular conformation, and ease of molecular motion at the interface.

1.6.3. Theory of Adhesion at Solid-Liquid Interface

The strength of adhesion at solid-liquid interface can be described by thermodynamics. In the early 19th century, Young found the fact that the contact angle of a droplet on a solid depends on the surface condition. He assumed thermodynamically-equilibrium condition and proposed an equation called Young's equation [120, **Appendix A7**].

In the 1860's, Dupre proposed that the energy required to separate a matrix and reinforcements can be expressed by using the surface energies of the matrix, reinforcements, and the interfacial free energy between them [121, **Appendix A8**]. The combination of these equations leads to the Young-Dupre equation,

$$W_a = \gamma_l(1+\cos\theta) \tag{1-8}$$

where *W*a is the work of adhesion, γ_l is the surface energy of the liquid, and the θ is the contact angle. When $\cos\theta=1$, or $\theta=0$, the work of adhesion reaches its maximum. In such conditions, the relations among surface energies becomes as follows:

$$\gamma_s - \gamma_{sl} = \gamma_l \tag{1-9}$$

where γ_s, γ_{sl}, and γ_l are the surface energies of solid, solid-liquid interface, and liquid. Here the surface energy must be equal or greater than zero. Thus, surface energy of the solid should be greater than that of the liquid for good adhesion.

In the 1950's, Girifalco and Good proposed that the work of adhesion could be expressed by the geometric mean rule (or the combination rule) [122, 123], which is:

$$\left[\begin{array}{c}\text{Work of adhesion between}\\ \text{solid and liquid}\end{array}\right] = \left\{\left[\begin{array}{c}\text{Work of cohesion}\\ \text{of liquid}\end{array}\right] \text{x} \left[\begin{array}{c}\text{Work of cohesion}\\ \text{of solid}\end{array}\right]\right\}^{1/2}$$

They considered a non-polar system where adhesions and cohesions are based only on dispersion interactions and derived the work of cohesion [**Appendix A9**]. Thus, the work of adhesion based on dispersion interactions can be written as:

$$W_a^D = 2\sqrt{\gamma_l^D \cdot \gamma_s^D} \tag{1-11}$$

In the 1950-60's, many people tried to incorporate interactions such as dipole-dipole interactions and hydrogen bond into the adhesion theory. Fowkes first proposed separating the surface energy into many components, but because of the complexity of the equation, later he suggested to summarize the equation into two dominant terms, which are dispersion and acid-base interactions [125]. Then, the work of adhesion is also expressed in two dominant terms. Based on the geometric mean rule and the fact that only positive and negative components attract each other, the acid-base component of the work of adhesion between solid and liquid can be written as: [126]

$$W_a^{AB} = 2\left(\sqrt{\gamma_s^+ \gamma_l^-} + \sqrt{\gamma_s^- \gamma_l^+}\right) \tag{1-12}$$

Now total work of adhesion can be expressed as:

$$W_a = \gamma_l(1+\cos\theta) = 2\left[\sqrt{\gamma_l^D \cdot \gamma_s^D} + \sqrt{\gamma_s^+ \gamma_l^-} + \sqrt{\gamma_s^- \gamma_l^+}\right] \tag{1-13}$$

This equation gives the basic theory of solid surface analysis. Suppose three liquids with known γ_l^D, γ_l^+, γ_l^- [**Appendix A10**] are available and the contact angles of these liquids on a solid can be determined experimentally [**Appendix A11**] and three equations based on (1-13) can be obtained. Then the surface energy components of the solid, γ_s^D, γ_s^+, and γ_s^- can be determined by solving these three equations. By using this technique, the work of adhesion between the matrix and reinforcements with different surface treatments can be evaluated. More detailed explanation of this theory is given in **Appendix A12**.

1.6.4. Surface Treatments of Carbon/Graphite Materials

To improve surface conditions and the wettability of carbon / graphite materials, many surface treatments methods have been developed and applied [128, 129]. Liquid phase chemical oxidation was one of the earliest methods applied for the materials. Nitric acid, hydrogen peroxide, and acidic potassium permanganese are some of the examples of oxidizing agents used to treat carbon materials. These oxidizing agents could successfully introduce acidic functionalities, especially at less crystalline regions, but also increased defects on the surface and thus decreased the tensile strength of the material. For example, high strength carbon fiber (less degree of graphitization) showed significant increase in both oxidized functionalities and surface area after nitric acid treatment compared to the high modulus carbon fiber (higher degree of graphitization), but the composites reinforced with the high strength fibers showed less improvement in properties because of the decreased fiber properties [130].

Electrochemical oxidation in an electrolyte bath generally offers a milder condition than liquid phase chemical treatment and doesn't cause many pittings or degradation of the material, but still loss in weight and tensile strength occurs in some degree. Because this method can treat large amount of continuous fibers in a short time, it is widely used in commercial manufacturing processes. Both acidic and basic functional groups have been introduced such as hydroxyl, carbonyl, carboxyl, and amine groups. The electrolytes used and treatment conditions are the main factors that determine how many functional groups are introduced [130].

Plasma treatment uses a cold plasma state. During the process, complex reactions including ionization, excitation, dissolution, and recombination can occur because of the

collision of electrons and other species existing in the reaction chamber. This reaction affects only the surface region of the sample up to 10 nm. The atmosphere could be O_2, air, N_2, NH_3, or Ar. The functional groups introduced on the material depend on the atmosphere. O_2 and air plasma treatments can add carboxyl and hydroxyl groups. They are relatively reactive and add more functional groups than Ar, N_2, or NH_3 Plasma. N_2 and NH_3 plasma treatment typically add primary and secondary amine groups. Some researchers reported that plasma treatment improved tensile strength of fibers themselves in addition to adhesion and flexural strength of composites [131].

Sizings are also used to improve adhesion. Epoxy sizing can significantly improve interfacial bonding, without affecting the properties of carbon fibers. As a result, tensile strength, compressive strength, and flexural strength are reported to increase while moduli remains almost the same. These results can be attributed to the change of failure mechanisms from the interface-initiated mode to matrix-initiated mode due to strong interfacial bonding [132, 133, 134, 135].

In each of the above cases, interfacial shear strength (IFSS) can be improved from 50 to 300% compared to untreated control sample. Also, improved tensile, flexural, and compressive properties are reported. However, loss of toughness is often accompanied with these improvements. Thus, the surface and interface structure should be designed carefully according to the final applications.

Grafting chemicals on carbon fibers has been also investigated to improve the surface condition of carbon fibers. Pittman et al., introduced amino groups on carbon fibers by grafting amines. First they applied nitric acid treatment to introduce carboxyl groups on carbon fibers, and then amines were introduced by forming amide bonds between the

fiber and amines used. The reactivity of these amine groups and epoxy resins were evaluated and it revealed that these amines can react more with smaller epoxy resins [136, 137]. Yamada et al introduced amine groups on carbon fibers by using graft polymerization of acryl amide. First, the fibers were treated by plasma to increase the active radicals on the fiber surface, and then vinyl monomers were applied to form polymers grafted on the fiber surfaces. The pull out force in the epoxy matrix was examined and showed increased value with increased degree of grafting [138].

1.7. Theories of Nanocomposites

1.7.1. Theory of Modulus

Many theories and models have been proposed to estimate the composite modulus theoretically [**Appendix A13**]. The basic concept of theoretical estimation of composite modulus began with the rule of mixtures. The model assumes fibers are uniaxially aligned and perfectly bonded to the matrix. Also it assumes both matrix and fibers are elastic and isotropic materials. According to this model, five basic elastic constants can be calculated [139, **Appendix A14**].

In the 1950's Eshelby introduced a totally new theory [140, 141]. His model has a single ellipsoidal inclusion embedded in an infinite medium which undergoes uniform deformation corresponding to imposed deformation in the media at large distances from the inclusion. The bonding between inclusion and the matrix is assumed to be perfect. Then he introduced an "equivalent homogeneous inclusion" (EHI), which is made of the same material of matrix, but has an appropriate misfit strain (equivalent transformation strain, ε^T) so that the stress field of the "equivalent homogeneous inclusion" in the composite has the same stress field as the actual inclusion. Eshelby defined ε^T as related to constraint strain, ε^C, and expressed it by introducing a new tensor called Eshelby's tensor, which is a function of the aspect ratio and Poisson's ratio of the inclusion. Thus, his model can predict elastic constants of composites with fillers of various shapes including flake-like shapes. The detailed explanation of his theory is shown in **Appendix A15**.

Shia and Hui pointed out that Eshelby's theory could have a large discrepancy from experimental data because of the perfect bonding assumption, especially when the

modulus of the reinforcement is much larger than that of the matrix. They insisted that slip should occur near the end of the reinforcement so that the "effective" length of it is shortened. As a result, the "effective" aspect ratio and the "effective" volume fraction of the reinforcement are also decreased from the real values. The definitions of these "effective" factors are described in **Appendix A16**. They incorporated these "effective" factors in to the Eshelby's theory and applied it to clay nanocomposite systems [142]. By substituting the experimentally obtained modulus into this equation, "effective" factors were calculated. The results are shown in **Table 1.13**. The "effective" values are decreased from real values by 30 to 43%. This theory gives a new method to investigate the adhesion of nanoreinforcements to the polymer matrix.

Table 1.13. The Effective Volume Fraction and Aspect Ratio in Clay Nanocomposite Systems

Volume Fraction (Vol%)	Effective Volume Fraction	Aspect Ratio	Effective Aspect Ratio
2.0	1.38 (-31%)	233	161 (-31%)
3.0	1.78 (-41%)	233	140 (-41%)
4.3	2.24 (-43%)	233	123 (-43%)

1.7.2. Theory of Failure

Failure mechanisms of materials can be classified into several categories **[Appendix A20]**, which include the yielding of ductile materials, the fracture of brittle materials, and fatigue. Many theories have been proposed to describe the mechanics of each failure mode. In the case of thermoplastic polymer materials, the yielding (plastic deformation) is the dominant failure mechanism except for very brittle polymers. On the other hand, either yielding or fracture can be the main failure mechanism for thermoset polymers since both brittle and ductile thermoset polymer materials can be fabricated by controlling the cross-link density and the molecular chain length between two adjacent cross-link points.

In the case of short-fiber reinforced polymer composites, the fracture process could be a combination of multiple mechanisms. If the bonding between matrix and fibers was perfect, the failure would occur by either plastic deformation of the matrix or breakage of the fibers. In practice, however, most of the composite failures are initiated by interfacial debonding around the reinforcements. SEM observations of the short-fiber reinforced composite failure process revealed that it included several steps [143, 144].

(1) The initiation of failure by interfacial debonding occurred at the fiber ends

(2) Plastic deformation of the matrix around the fibers

(3) Interfacial microcrack propagation along the fiber sides

(4) Catastrophic crack propagation throughout the matrix

Thus, it is important to investigate the adhesion condition and stress distribution at both the interface and the matrix regions to assess the failure condition.

The adhesion condition between fibers and a polymer matrix can be investigated experimentally by methods such as fiber pull-out test, microdrop technique, and single fiber fragmentation test [145]. It is difficult to assess the interfacial bond quality of flake-reinforced composites because of the variability in the dimension of the flakes. However, the stress distribution at the interface region of these composites can be simulated by using a finite element method.

To investigate the plastic deformation phenomena, many theories have been proposed and compared with experimental data. Among these, the von Mises yield criterion [146] is most widely used because it can provide the best agreement between theory and experimental results in many cases. This model assumes that the failure of ductile material occurs when the energy of distortion reaches the yield energy of the material. In the case of a material under principal stresses, the criterion is mathematically expressed as,

$$\sigma_{yield} \geq \sigma_{eff} = \frac{1}{\sqrt{2}}\left[(\sigma_1 - \sigma_2)^2 + (\sigma_2 - \sigma_3)^2 + (\sigma_3 - \sigma_1)^2\right]^{1/2} \qquad (1\text{-}14)$$

where σ_{eff} is the effective stress of the material and σ_1, σ_2, and σ_3 are the stresses in direction 1, 2, and 3. In the case of plane stress, only σ_1 and σ_2 exist. So the equation becomes,

$$\sigma_{yield} \geq \sigma_{eff} = \left(\sigma_1^2 - \sigma_1\sigma_2 + \sigma_2^2\right)^{1/2} \qquad (1\text{-}15)$$

This is expressed as a principal stress ellipse as illustrated in **Appendix A21**. The effective stress values can be affected by shape, size, and geometric arrangement of reinforcements. These effects can also be simulated by using a finite element method.

1.7.3. Toughness and Strength

The fracture toughness of composite materials could increase, remain constant, or decrease with increasing reinforcement content. This is a result of a complex combination of many mechanisms. Thus, it is important to consider all the possible effects to investigate the different tendencies. The positive effects on toughness include energy absorbing mechanisms such as more plastic deformation of the matrix around reinforcements, crack branching due to hindrance by reinforcements, shear deformation in the interphase region, creation of voids and crazes at the reinforcement edges, etc. The negative effects include the introduction of stress concentration sites. The toughness can be improved either by increasing strength, increasing energy absorption mechanisms, or both.

The strength of composites is related to adhesion condition and stress concentration at the interface. The better adhesion allows for a more efficient stress transfer from matrix to reinforcements, which leads to a higher ultimate strength. The stress concentration at the interface can be affected by the shape, aspect ratio, and geometric arrangement of reinforcements. If the stress concentration effect overcomes the improvement of adhesion, the composite material can fail at lower external stress, which leads to lower strength. The energy absorbing mechanisms described above don't have a positive effect on the strength of composite materials, thus, composite materials can show higher toughness with lower strength.

In the case of nanocomposite systems, the size of reinforcements is a lot smaller and the total surface area would increase. This is especially true for clay or graphite nanocomposite systems where exfoliation phenomena are involved. Theoretically the

stress should be transferred to the reinforcements more efficiently because of the increased surface area, if there are good interactions between matrix and reinforcements. Also, crack path length at the interface becomes longer, which leads to improved strength and toughness.

As shown in section 1.1.3, the average dispersion distance becomes shorter when the size of fillers decreases. The stress at the reinforcement edges could be reduced by the presence of other reinforcements located nearby. The factors to control this stress condition are the distance between reinforcements as well as the orientation of the adjacent reinforcements. If these reinforcements are positioned in parallel, the stress at the edges is transferred to each other and the stress concentration will be reduced. On the other hand, if two reinforcements are located in an edge-to-edge position, the stress at the edges could be increased and cause cracks at a lower stress. Thus, orientation of the reinforcements affects the strength and toughness of the composite.

As the number of the reinforcements increases, the edge area increases where high stress accumulates and initiates cracks. In the case of a short fiber reinforced system, the mechanical properties of the composite increased until the size of the fiber reached a certain point. Beyond the point, the strength and toughness decreased [145]. Also, the stress accumulated at the edges increases when the aspect ratio of the reinforcements increases. In the case of nanocomposites, both edge area and aspect ratio are very large. Thus, it is especially important to improve the adhesion at the edge area to improve the overall mechanical properties of the systems.

1.7.4. Electrical Conductivity

In the 1940's, Flory and Srockmayer investigated the theory of the gelation process of polymers through chemical bond formation between nearest neighbor molecules [148, 149, 150]. Once the system reached the gelation point, a network of chemical bonds would spread throughout the system. They developed a theory that now is called "Bethe lattice model" (or Cayley tree), which is one of the basic models used to explain critical phenomena. In the 1950s, Broadbent and Hammersley introduced the term "percolation theory" and tried to investigate it more mathematically, using geometrical and probabilistic concepts. Since then, many researchers reported many models and calculations to explain this critical phenomena. These theoretical approaches revealed that only a few models (1-dimensional model, 2-dimensional honeycomb model, 2-dimensional triangular model, and Bethe lattice model) have exact solutions, which are the general solutions for models with infinite size. But researchers could successfully simulate other models and found plausible solutions for theoretical investigation. **Table 1.14** summarized both site and bond percolation [**Appendix 23**] thresholds for various lattices [151].

Table 1.14 Theoretical Percolation Thresholds for Various Models

Dimensionality	Lattice	Site Percolation	Bond Percolation
1D		1.0	1.0
2D	Honeycomb	0.6962	0.6527
2D	Square	0.5927	0.5000
2D	Triangular	0.5000	0.3473
3D	Diamond	0.43	0.388
3D	Simple Cubic	0.3116	0.2488
3D	BCC	0.246	0.1803
3D	FCC	0.198	0.119
Infinite	Bethe (Z: # of bonds)	$\frac{1}{Z-1}$	$\frac{1}{Z-1}$

Through many theoretical calculations and simulations, researchers found that quantities of interest go to zero or infinity by simple power laws in various critical phenomena [151, 152]. In the case of composites with conductive and insulating phases, the effective conductivity or resistivity can be written as;

$$\sigma_{eff} = \sigma_0 (p - p_c)^t \qquad \text{for } p > p_c \qquad (1\text{-}16)$$

$$\rho_{eff} = \rho_0 (p - p_c)^{-t} \qquad \text{for } p > p_c \qquad (1\text{-}17)$$

where σ_{eff} and ρ_{eff} are the effective conductivity and resitivity of the composite, σ_0 and ρ_0 are the conductivity and resistivity of the conductive phase, p is the volume fraction of the conductive phase, p_c is the percolation threshold, and t is the conductivity exponent. Equation (1-16) and (1-17) can be rewritten as;

$$\log\left[\frac{\sigma_{eff}}{\sigma_0}\right] = t \bullet \log[p - p_c] \qquad \text{for } p > p_c \qquad (1\text{-}18)$$

$$\log\left[\frac{\rho_{eff}}{\rho_0}\right] = -t \bullet \log[p - p_c] \qquad \text{for } p > p_c \qquad (1\text{-}19)$$

Thus, t can be experimentally available by least-square linear fit of $\log[\sigma_{eff} / \sigma_0]$ vs $\log[p-p_c]$ or $\log[\rho_{eff} / \rho_0]$ vs $\log[p-p_c]$ data. The parameters are Pc, t, and σ_0.

All the simulation and calculation results reported so far strongly suggest that the critical exponent, t , depends only on dimensionality, not on the individual lattice model. Also it is reported that the critical exponent shows virtually the same value for both site and bond percolations. This is called the "universality" of percolation theory and also holds for thermal phase transition. **Table 1.15.** summarizes theoretical exponent values. It should be recognized that each simulation uses different lattice size and gives somewhat different values.

Table 1.15. Theoretical Critical Exponent Values

	[153]	[154]	[155]
Reference	153	154	155
2D model	t = 1.1-1.25	t = 1.1	t = 1.3
3D model	t = 1.70-1.75	t = 1.6	t = 2.0
Bethe Model		t = 3	t = 3.0

Several research groups have reported experimentally obtained conductivity critical exponents that showed good agreement with theoretical values for 3D models [156, 157, 158, 159, 160], while others have showed critical exponents greater than 2.0 [160, 161, 162, 163, 164]. **Table 1.16** and **1.17** summarize these results.

Table 1.16. Experimental Results of Universal Critical Exponents Values.

Reference	[156]	[157]	[158]	[159]	[160]
Filler	Carbon Black	Carbon Black	Carbon Black	Carbon Black	Silver coated glass spheres
Matrix	PP	Thermoset Polymer	Paraffin Wax	Teflon	Teflon
Process	Compression molding	Casting	Casting	Compression molding	Compression molding
Percolation threshold	Pc=6.2 Wt%		Pc=0.76 Vol%	Pc=29 Vol%	Pc=17 Vol%
Critical exponent	t=1.928 ±0.094	t=1.94 ±0.06	t=2.05 ±0.15	t=1.85 ±0.25	t=2.0 ±0.2

Table 1.17. Experimental Results of Nonuniversal Critical Exponents Values.

Reference	[161]	[160]	[162]	[163]	[164]
Filler	Carbon Black	Glass spheres	Short Carbon Fiber	Graphite Flakes	Carbon Black
Matrix	HDPE	Indium	Epoxy	Styrene	
Process	Compression molding	Compression molding	Casting	Casting	
Percolation threshold	Pc=17 Vol%	Pc=4.1-9.1 Vol%	Pc=1.6 Vol%	Pc=2 Vol%	Pc=17 Wtl%
Critical exponent	t=2.9 ±0.1	t=3.1 ±0.3	t=3.0 ±0.3	t=3.5 ±0.3	t=2.8 ±0.2

The discrepancy between experimental data and theoretical universal value for 3D models is explained by the fact that many conductive fillers form agglomerates, enabling them to interact with many neighbors with long-range interactions. If each particle (or agglomerate) interacts with many particles, one should consider an average value of the interactions to calculate a property of the system [161]. This is called mean-field environment. In the case of agglomerates, the "arms" of aggregates get entangled, making a distribution of the interparticle tunneling distances much narrower than that of the spherical 3D models [164]. Using mean-field theory, a critical dimensionality of a system which shows t=3 was determined as 6 [154].

1.7.5. Dielectric Properties

To investigate electrical behaviors of dielectric materials, various circuit models are used to represent those materials. In a gaseous phase under a low-pressure condition, molecules can rotate freely. Thus, resonance spectrums show sharp peaks at specific frequencies that correspond to quantized conditions. In this case a LRC circuit that represents the free resonator molecule [**Appendix A25**] is used to investigate the dielectric properties of the materials [166]. On the other hand, in the case of condensed phases, which include solids, liquids, and gases at high pressures, the molecules cannot rotate freely because of steric hindrance. Also thermal agitation disorders the quantized orientations of electrons. As a result, the resonance spectrums show broadened peaks and detailed information is lost. In this case, the peaks represent the average electronic and vibrational state of condensed molecules, not individual ones. An RC circuit is used to represent these materials [**Appendix A25**, 166]. Thus, the electrical behavior of a dielectric solid material can be represented by a model in which a capacitor and an RC circuit are connected in parallel. It is inevitably necessary to use sinusoidal signals when handling the calculations of AC circuit properties. Using trigonometric functions is straightforward, but it becomes very complex and often unmanageable when the AC circuit has multiple components. Instead, using complex exponential functions makes these calculations easier [**Appendix A24**].

The fundamental property of dielectric material is the permittivity in complex form. Usually complex relative permittivity is used to describe properties of dielectrics.

$$\varepsilon_r^* = \varepsilon_r' - i\varepsilon_r'' \qquad (1\text{-}20)$$

The real part of complex relative permittivity, ε_r', is called the dielectric constant. This factor is related to the polarizability of the material. A material with a high dielectric constant has lots of dipole moments including permanent dipoles due to polar functional groups. The imaginary part, ε_r'', is called the (dielectric) loss factor, which is related to the energy loss (heat dissipation) in the circuit. Also the loss tangent is defined as:

$$\tan\delta = \frac{\varepsilon_r''}{\varepsilon_r'} \qquad (1\text{-}21)$$

where δ is the phase difference between input voltage and output current and can be determined experimentally. Materials with large $\tan\delta$ can absorb energy and dissipate it as heat more efficiently.

The real part of the impedance, Z', and phase, δ, can be obtained experimentally. Then the imaginary part of the impedance is calculated. By using these data, the dielectric constant, ε_r', and the dielectric loss factor, ε_r'', can be determined by using the relations below. [**Appendix A26**]

$$\varepsilon_r'' = \frac{Z'}{\omega C_0 (Z'^2 + Z''^2)} \quad \text{and} \quad \varepsilon_r' = \frac{Z''}{\omega C_0 (Z'^2 + Z''^2)}$$

1.8. Summary of Introduction

As shown in this literature review, some of the clay-polymer nanocomposites achieved significant improvements in mechanical, thermal, and barrier properties. These results have not been seen in conventional short fiber reinforced polymer systems, but because of its inherent lack of good electrical and thermal properties set some limits in their applications.

Single crystal graphite has superior mechanical properties as well as other useful properties with very reasonable cost. Theoretical consideration implies the possibility of excellent composites in many aspects by incorporating this material in polymer matrices, which could be used a wide variety of applications. Yet there are problems to overcome to achieve the composites with such high performances.

First would be the lack of efficient exfoliation techniques to process graphite flakes into nano-scale layers. Thermal expansion produces graphite platelets with a thickness of 20 to 100nm and an aspect ratio of few hundreds to thousands. This material itself is considered as an excellent reinforcement, yet the fact that about 100 layers of graphene sheets are still stacking suggests room for further improvements. This could be achieved by chemical and/or physical methods by considering appropriate conditions such as the size of starting graphite material.

Second would be the lack of systematic knowledge about surface and interface design. It is important to notice that edge and/or surface areas of exfoliated nanoplatelets could be much larger than the other carbon/graphite materials including carbon fibers, whiskers, and nanotubes if the same amount of materials are compared. As depicted in theoretical considerations of composite mechanical properties, this fact could lead to

either good or bad results. Thus, surface and interface design should play a very important role in exfoliated graphite nanocomposite systems. Detailed investigations on surface treatments, characterizations, and their effect on the mechanical properties of resulted composites are required.

Third would be the total design of composite systems with well-balanced characteristics. Composites with good mechanical, electrical, and thermal properties with ease of processability, many freedoms of design, and adequate cost sound like ideal materials that engineers are looking for, yet the good balance is tough to achieve. The theoretical and previous experimental results suggest the graphite nanocomposites could have realistic possibility to achieve such high performance material within cost limitations. Total characteristics of the fabricated composites need to be examined and assessed.

The focus of this research is on the intercalation and exfoliation of graphite materials as well as fabrication and analysis of the properties of exfoliated graphite reinforced composites. The objectives of this research project are:

1. Investigate processes to achieve exfoliated nano-scale graphite platelets.
2. Investigate appropriate surface treatments and surface characteristics of graphite nanoreinforcement to achieve good dispersion and adhesion in polymer matrices.
3. Achieve nanocomposites with superior mechanical, thermal and electrical properties to expand the possibility of applications in which these materials may be used.

1.9. Reference

1.Griffith, A. A."The theory of rapture." Proceedings of the 1st International Congress on Applied Mechanics." 55, (1924).

2.Gordon, J. E. "The new science of strong materials." Penguin books, (1976).

3.Young, R. J. et al, "Tensile strength of poly(diacetylene) single crystals." Polymer, ***24***, 1023 (1983).

4.Griffith, A. A."The phenomena of rapture and flaw in solids." Phil. Trans. Roy. Soc., ***A221***, 163 (1920).

5.Weibull, W. J. "A statistical distribution function of wide applicability." J. Appl. Mech., Sep. 293 (1951).

6. Bunsell, A. R., "Fiber Reinforcements for Composite Materials." Elsevier, New York, p. 501 (1988).

7.Metcalfe, A. G., and Schmitz, G. K., Am. Soc. Test. Mater. Proc., ***64***, 1075 (1964).

8. Moreton R. "The Effect f Gauge Length on The Tensile Strength of R.A.E. Carbon Fibers." Fiber Sci. & Technol., ***1***, 273 (1969).

9.Watson A. S., and Smith, R. L., "An Examination of Statistical-Theories for Fibrous Materials in The Light of Experimental-Data.", J. Mater. Sci., ***20***, 3260 (1985).

10. Watt, W. and Perov, B. V., "Handbook of Composites, Vol. 1: Strong Fibers", North Holland, Amsterdam, pp.155-199 (1985).

11. Phoenix, S. L., Composite Reliability, ASTM-STP-580, 77 (1975).

12. Wagner, H. D., Phoenix, S. L., and Schwartz, P. "A Study of Statistical Valiability in The Strength of Single Aramid Filaments.", J. Composi. Mater., ***18***, 312 (1984).

13. Steenbakkers, L. W., and Wagner, H. D., "Elasticity and Mechanical Breakdown of Kevlar 149 Aramid Fibers by a Probabilistic Approach.", J. Mater. Sci. Lett., ***7***, 11, 1209 (1988).

14. Schwartz, P, Netravali, A, and Sembach, S., "Effects of Strain Rate and Gauge Length on The Failure of Ultrahigh Strength Polyethylene Fibers." Text, Res. J., ***56***, 8, 502, (1986).

15. Wagner, H. D., and Steenbakkers, L. W., "Stochastic Strength and Size Effect in Ultrahigh Strength Polyethylene Fibers", Philosophical Magazine Letters, ***59***, 2, 77 (1989).

16. Piggott, M. R., "Load Bearing Fibre Composites", Pergamon Press, p100 (1980).

17. Hoffman, U., Endell, K., and Wilm, D., Angew Chem., ***47***, 539 (1934).

18. Weiss A., "Organic Derivatives of Mica-Type Layer-Silicates." Angew. Chem. Internat., Edit., ***2***, 3, 134 (1963).

19. Okada, A., Kawasumi, M., Kurauchu, T., and Kamigaito, O. "Synthesis and Characterization of a Nylon 6-Clay hybrid." Polymer preprint, ***194***, 10 (1987).

20. Fukushima, Y. and Inagaki, S., "Synthesis of An Intercalated Compound of Montmorillonite and 6-Polyamide." J. Inclusion Phenom. ***5***, 473 (1987).

21. Giannelis, E. P. "Polymer Layered Silicate Nanocomposites." Adv. Mater., ***8***, 1, 29 (1996).

22. Giannelis, E. P., "Polymer-Layered Silicate Nanocomposites: Synthesis, Properties, and Applications." Appl. Organometalic Chem., ***12***, 675 (1998).

23. Lagaly, G., "Introduction: From Clay Mineral-Polymer Intercalations to Clay Mineral-Polymer Nanocomposites." Appl. Clay Sci., ***15***, 1 (1999).

24. LeBaron, P. C., Wang, Z., and Pinnavaia, T. J., "Polymer-layered silicate nanocomposites: an overview." Appl. Clay Sci., ***15***, 11 (1999).

25. Pinnavaia, T. J. and Beal, G. W., "Polymer Clay Nanocomposites." John Wiley & Sons, Chichester, England (2000).

26. Ishida, H., Campbell, S., and Blackwee, J., "General Approach to Nanocomposite Preparation." Chem. Mater., ***12***(5), 1260 (2000).

27. Lan, T., Kavirantna, D., and Pinnavaia, T. J., "Mechanism of Clay Tactoid Exfoliation in Epoxy-Clay Nanocomposites." Chem. Mater., ***7***, 214 (1995).

28. Lan, T. and Pinnavaia, T., J., "Nanolayer Ordering In An Epoxy-exfoliated Clay Hybrid Composite." Mat. Res,. Soc. Symp. Proc. ***435***, 79 (1996).

29. Porter D., Metcalfe, E., and Thomas, M. J. K., "Nanocomposite Fire Retardants – A Review.", Fire Mater., ***24***, 45 (2000).

30. Naqui, S. I., and Robinson, U. M. " Review, Tensile Dilatometric Studies of Deforation in Polymeric Materials and Their Composites." J. Mater. Sci., ***28***, 1421 (1993).

31. Maiti, S. N. and Sharma, K. K., "Studies on Polypropylene Composites Filled with Talc Particles." J. Mater. Sci., ***27***, 4605 (1992).

32. McGenity, P. M., Hooper, J. J., Paynter, C. D., Riley, A. M., Nutbeem, C., Elton, N. J., and Adams, J. M., "Nucleation and Crystallization of Polypropylene by Mineral Fillers: Relationship to Impact Strength." Polymer, ***33***, 5215 (1992).

33. Kojima, Y, Usuki, A.,. Kawasumi, M., Okada, A, Kurauchi, T, and Kamigaito, O., "Synthesis of Nylon 6-Clay Hybrid by Montmorillonite Intercalated with ε-Caprolactam." J. Polym. Sci.: A: Polym. Chem., ***31***, 983 (1993).

34. Kojima, Y., Usuki, A., Kawasumi, M., Okada, A., Kurauchi, T., and Kamigaito, O, "One-Pot Synthesis of Nylon 6-Clay Hybrid." J. Polym. Sci. A: Polym. Chem., ***31***, 1755 (1993).

35. Usuki, A., Kawasumi, M., Kojima, Y., Okada, A., Kurauchi, T., and Kamigaito, O., "Swelling Behavior of Montmorillonite Cation Exchanged for ω-Amino Acids by ε-caprolactam." J. Mater. Res., ***8***, 1174 (1993).

36. Usuki, A, Kojima, Y, Kawasumi, M., Okada, A., Fukushima, Y., Kurauchi, T. and Kamigaito, O.,"Synthesis of Nylon 6-Clay hybrid." J. Mater. Res., ***8***, 1179 (1993).

37. Kojima, Y., Usuki, A., Kawasumi, M., Okada, A., Fukushima, Y., Kurauchi, T., and Kamigaito, O., "Mechanical Properties of Nylon 6-Clay Hybrid." J. Mater. Res., ***8***, 1185 (1993).

38. Kojima, Y., Usuki, A., Kawasumi, M., Okada, A., Kurauchi, T, and, Kamigaito, O., "Sorption of Water in Nylon 6-Clay Hybrid." J. Appli. Polym. Sci., ***49***, 1259 (1993).

39. Usuki, A, Koiwai, A., Kojima, Y., Kawasumi, M., Okada, A. Kurauchi, T. and Kamigaito, O., "Interaction of Nylon 6-Clay Surface and Mechanical Properties of Nylon 6-Clay Hybrid.". J. Appl. Polym. Sci., **55**, 119 (1995).

40. Wang, M. S., and Pinnavaia, T. J., "Clay-Polymer Nanocomposites Formed from Acidic Derivatives of Montmorillonite and an Epoxy Resin.", Chem. Mater., ***6***, 468 (1994).

41. Messersmith, P. B. and Giannelis, E. P.," Synthesis and Characterization of Layered Silicate-Epoxy Nanocomposites." Chem. Mater., ***6***, 1719 (1994).

42. Lan, T. and Pinnavaia, T. J., "Clay-Reinforced Epoxy Nanocomposites." Chem. Mater., ***6***, 2216 (1994).

43. Lan, T., Padmananda, D., Kaviratna, D., and Pinnavaia, T. J., "Synthesis, Characterization and Mechanical Properties of Epoxy-Clay Nanocomposites." Polym. Mater. Sci. Eng., ***71***, 527 (1994).

44. Lan, T., Padmananda, D., Kaviratna, D., and Pinnavaia, T. J., "Epoxy Self-Polymerization in Smectite Clays."J Phys. Chem. Solids, ***57,*** 6-8, 1005 (1996).

45. Massam, J. and Pinnavaia, T. J.,"Clay Nanolayer Reinforcement of Glassy Epoxy Polymer." Mater. Res. Soc. Symp. Proc., ***520***, 223 (1998).

46. Wang, Z and Pinnavaia, T. J., "Hybrid Organic-Inorganic Nanocomposites: Exfoliation of Magadiite Nanolayer in an Elastomeric Epoxy Polymer." Chem. Mater., ***10***, 1820 (1998).

47. Messersmith, P. B. and Giannelis, E. p., "Polymer-Layered Silicate Nanocomposites: *In Situ* Intercalative Polymerization of ε-Caprolactone in Layered Silicates." Chem. Mater., ***5***, 1064 (1993).

48. Messersmith, P. B. and Giannelis, E. P. "Synthesis and Barrier Properties of Poly(ε-Caprolactone)-Layered Silicate Nanocomposites. J. Polym. Sci.: Part A: Polym. Chem., ***33***, 1047 (1995).

49. Mehrotra, V and Giannelis, E. P., "Metal-Insulator Molecular Multilayers of Electroactive polymers: Intercalation of Polyaniline in Mica-Type Layered Silicates." Solid State Communications, **77**, 2, 155 (1991).

50. Mehrotra, V. and Giannelis, E. P., "Nanometer Scale Multilayers of Electroactive polymers: Intercalation of Polypyrrole in Mica-Type Silicates." Solid State Ionics, ***51***, 115 (1992).

51. Yano, K., Usuki, A., Okada, A, Kurauchi, T., and Kamigaito, O., "Synthesis and Properties of Polyimide-Clay Hybrid." J. Polym. Sci.: Part A: Polym. Chem., ***31***, 2493 (1993).

52. Lan, T., Kavirantna, P. D., and Pinnavaia, T. J., "On the Nature of Polyimide-Clay Hybrid Composites." Chem. Mater., ***6***, 573 (1994).

53. Pinnavaia, T. J., Lan, T., Kaviratna P. D., and Wang, M. S., "Clay-Polymer Nanocomposites: Polyether and Polyimide Systems." Mat. Res. Soc. Symp. Proc., ***346***, 81 (1994).

54. Yano, K., Usuki, A., and Okada, A., "Synthesis and Properties of Polyimide-Clay Hybrid Films." J. Polym. Sci.: Part A: Polym. Chem., ***35***, 2289 (1997).

55. Vaia, R. A., Vasdevan, S., Krawiec, W., Scanlon, L. G., and Gizannelis, E. P., "New Polymer Electrolyte Nanocomposites – Melt Intercalation of Poly(Ethylene Oxide) in Mica-Type Silicates." Adv. Mater., ***7***, 2, 154 (1995).

56. Vaia, R. A., Jandt, K. D., Kramer, E. J., and Giannelis, E. P., "Kinetics of Polymer Melt Intercalation." Macromolecules, ***28***, 8080 (1995).

57. Vaia, R. A., and Giannelis, E. P., "Polymer Melt Intercalation in Organically-Modified Layered Silicates: Model Predictions and Experiment." Macromolecules, ***30***, 8000 (1997).

58. Kojima, Y., Fukumori, K., Usuki, A., Okada, A., and Kurauchi, T." Gas Permeabilities in Rubber-Clay Hybrid." J. Mater. Sci., Lett., ***12***, 889 (1993).

59. Kato, M., Usuki, A., and Okada, A., "Synthesis of Polypropylene Oligomer-Clay Intercalation Compounds." J. Appl. Polym. Sci., ***66***, 1781 (1997).

60. Hasegawa, N., Kawasumi, M., Kato, M., Usuki, A., and Okada, A., "Preparation and Mechanical properties of Polypropylene-Clay Hybrids Using a Maleic Anhydride-Modified Polypropylene Oligomer." J. Appl. Polym. Sci., ***67***, 87 (1998).

61. Theberge, J. E., "Recent Advances in Thermoplastic Composites." ANTEC SPE Journal, 177 (1979).

62. Milewski, J. V. and Katz, H. S., "Handbook of Reinforcements for Plastics." P.62, Van Nostrand Reinold Co., New York (1987).

63. Bajaj, P., Jha, N. K., and Kumar, R. A., "Effect of Coupling Agents on The Mechanical Properties of Mica/Epoxy and Glass Fiber/Mica/Epoxy Composites." J. Appl. Polym. Sci., ***44***, 1921 (1992).

64. Bajaj, P., Jha, N. K., and Kumar, R. A., "Effect of Coupling Agents on Thermal and Electrical Properties of Mica/Epoxy Composites." J. Appl. Polym. Sci., ***56***, 1339 (1995).

65. Sherman, L. M., "Nanocomposites: A Little Goes a Long Way." Plastic Technology, 52 (1999).

66. Garces, J. M., Moll, D. J., Bicerano, J., Fibiger, R., and McLeod, D. G., "Polymeric Nanocomposites for Automobile Applications." Adv. Mater., ***12***, 23, 1835 (2000).

67. Rice, B. P., Chen, C., and Cloos, L, "Carbon Fiber Composites: Organoclay-Aerospace Epoxy Nanocomposites, Part I." SAMPE Journal, ***37***, 5, 7 (2001).

68. Chen, C and Curliss, D., "Resin Matrix Composites: Organoclay-Aerospace Epoxy Nanocomposites, Part II." SAMPE Journal, ***37***, 5, 11 (2001).

69. Milewski, J. V. and Katz, H. S., "Handbook of Reinforcements for Plastics." P.42, Van Nostrand Reinold Co., New York (1987).

70. Ebbesen, T. W., "Carbon Nanotubes.", p.5, CRC Press, Boca Raton, (1997).

71. Milewski, K." Handbook of Fillers and Reinforcements for Plastics." Van Nostrand Reihold Co., New York, p277 (1978).

72. Bacon, R., "Growth, Structure, and Properties of Graphite Whiskers" J. Applied Physics, ***31***, 2, 283 (1960).

73. Peebles, L. H., "Carbon Fibers: Formation, Structure, and Properties." CRC Press Inc., Boca Raton (1995).

74. Kroto, H. W., Heath, J. R., O'Brien, S. C., Cul, R. F., and Smalley, R. E., "C-60-Buckminsterfullerene", Nature, ***318,*** 6042, 162 (1985).

75. Iijima, S., "Helical microtubules of graphitic carbon", Nature, ***354***, 6354, 56 (1991).

76. Aylsworth, J. W., "Expanded Graphite and Composition Thereof." US Patent 1,137,373 (1995).

77. Aylsworth, J. W., "Expanded Graphite." US Patent 1.191,383 (1916).

78. W. H. Martin, W. H. and Brocklehurst, J. E. , "The Thermal Expansion Behaviour of Pyrolytic Graphite-Bromine Residue Compounds." Carbon, 1, 133 (1964).

79. Chung, D. D. L. and Wong, L. W., "Electromechanical Behavior of Graphite Intercalated with Bromine.", Carbon, ***24***, (5), 639 (1986).

80. Chung, D. D. L., "Intercalate Vaporization During The Exfoliation of Graphite Intercalated with Bromine.", Carbon, ***25,*** (3); 361 (1987).

81. Yoshida, A., Hishiyama, Y., and Inagaki, M., "Exfoliation of Vapor-Grown Graphite Fiber as Studied by Scanning Electron Microscope.", Carbon, ***28***, (4), 539 (1990).

82. Yoshida, A., Hishiyama, Y., and Inagaki, M., "Exfoliation Graphite from Various Intercalation Compounds.", Carbon, ***29,*** (8): 1227 (1991).

83. Chung, D. D. L., "Review: Exfoliation of Graphite." J. Mater. Sci., ***22***, 4190 (1987).

84. Lincoln, V., F. and Claude, Z., "Organic Matrix Composites reinforced with Intercalated Graphite." US Patent 04,414,142 (1983).

85. Chung, D. D. L., "Low-density graphite-polymer electrical conductors." US Patent 04,704,231 (1984).

86. Chung, D. D. L., "Composites of *In-situ* Exfoliated Graphite." US Patent, 4,946,892 (1990).

87. Wang, Y. S., O'Gurkis, M. A., and Lindt, J. T., "Electrical Properties of Exfoliated-Graphite Filled Polyethylene Composites." Polym. Compos., *7*, 5, 349 (1986).

88. Foy, J. V. and Lindt, J. T., "Electrical Properties of Exfoliated-Graphite Filled Polyester Based Composites." Polym. Compos., *8*, 6, 419 (1987).

89. Celzerd, A., McRae, E., Mareche, J. F., Furdin, G., Dufort M., and Deleuze, C., "Composites Based on Micron-Sized Exfoliated Graphite Particle: Electrical Conduction, Critical Exponents, and Anisotropy." J. Phy. Chem. Solids, *57*, 6-8, 715 (1996).

90. Chung, D. D. L. and Wong, L. W., "Exfoliated Graphite-Polymer Composites." Proc. 4th Intern. Carbon Conf., 496 (1986).

91. Semko, L. S., Chernysh, I. G., Revo, S. L., and Dashevskii, N. N., "Mechanical Properties of Polyethylene-Exfoliated Graphite Composites.", Mech. Compos. Mater., *28*, 3, 208 (1992).

92. Pan, Y. X., Yu, Z. Z., Ou, Y. C., and Hu, G. H., "A New Process of Fabricating Electrically Conducting Nylon6/Graphite Nanocomposites via Intercalation Polymerization." J. Polym. Sci., Part B: Polym. Phy., *38*, 1626 (2000).

93. Chen, G. H., Wu, D. J., Weng, W. G., He, B., and Yan, W. L., "Preparation of Polystylene-Graphite Conducting Nanocomposites via Intercalation Polymerization." Polym. Int., *50*, 980 (2001).

94. Chen, G. H., Wu, D. J., Weng, W. G., He, B., and Yan, W. L., "Preparation of Polymer/Grphite Conducting Nanocomposites by a Intercalation Polymerization." Appl. Polym. Sci., *82*, 2506 (2001).

95. Xiao, P, Xiao, M., and Gong, K., "Preparation of Exfoliated Graphite/Polystyrene Composite by Polymerization-filling technique." Polymer, *42*, 4813 (2001).

96. Chen, X. M., Shen, J. W., and Huang, W., Y., "Novel Electrically Conductive Polypropyrene/Graphite Nanocomposites." J. Mater. Sci. Lett., *21*, 213 (2002).

97. Zeng, W., Wong, SC., and Sue, HJ., "Transport Behavior of PMMA/Expanded Graphite Nanocomposites.", Polymer, *73*, 6767 (2002).

98. Uhl, F. M. and Wilkie, C. A., "Nylon/Graphite Nanocomposites", Polymer preprints, 42, 2, 176 (2001).

99. Beguin, F. and Setton, R., "Dehydrogenation of Benzene to Biphenyl by a Potassium-Graphite Lamellar Compounds." J. Chem. Soc., Chem. Commun, 611 (1976).

100. Merle, G. and Beguin, F., "Insertion of Benzene in The Lamellar Graphite Compound, KC24." Carbon, , (5), 371 (1980).

101. Setton, R., "Metals Intercalated in Graphite-Reagents or Catalysts" J. Mol. Catal., ***27***, (1-2), 263 (1984).

102. Matsuzaki, S and Sano, M., "Benzene in Graphite Potassium Intercalation Compounds Studied by Resonance Raman-Spectroscopy." Chem. Phys. Lett., ***115***, (4-5), 424 (1985).

103. Matsuzaki, S, Taniguchi, M, and Sano, M., "Polymerization of Benzene Occluded in Graphite-Alkali Metal Intercalation Compounds", Synth. Met., ***16***, 343 (1986).

104. Shioyama, H, Wakukawa, Y., and Sawada, Y., Mol. Cryst. And Liq., Cryst., ***310***, 69 (1998).

105. Takahashi, Y., Oi, K., Terai, T., and Akuzawa, N., "A New Ternary Compounds CsC24(C2H4)x." Carbon, ***29***, (2), 283 (1991).

106. Pilliere, Takahashi, Y., Yonekawa, T., and Otosaka, T., "Oligomerization Process during The Intercalation of Ethylene in CsC24", Synth. Met., ***59***, 191 (1993).

107. Akuzawa, N., Kondou, S., Kaburagi, Y., Hishiyama, Y., and Takahashi, Y., "Electrical Conductivity, Hall Coefficient, and Magnetresistance in Binary CsCx and Ternary CsC24(C2H2)1.1 and CsC24(C2H4)1.1." Carbon, ***31***, (6), 963 (1993).

108. Shioyama, H, "Polymerization of Isoprene and Styrene in The Interlayer Spacing of Graphite." Carbon, ***35***, (10-11), 1664 (1997).

109. Shioyama, H., Tatsumi, K., Iwashita, N., Fujita, K., and Sawada, Y., "On The Interaction between The Potassium-GIC and Unsaturated Hydrocarbons." Synth. Met., 96, 229 (1998).

110. Shioyama, H., "Review: The Interactions of Two Chemical Species in The Interlayer Spacing of Graphite." Synth. Met., ***114***, 1 (2000).

111. Shioyama, H., "On The Interaction between Alkali Metal-GIC and Unsaturated Hydrocarbons." Mol. Cryst. And Liq. Cryst., ***340***, 101 (2000).

112. Szwarc, M., Levy, M., and Milkovich, R., "Polymerization Initiated by Electron Transfer to Monomer. A New Method of Formation of Block Polymers", J. Am. Chem. Soc., ***78***, 2656 (1956).

113. Uhl, F. M., Lamelas, F. J., and Wilkie, C. A., "Flame Retardancy of Graphite Nanocomposites", Proc. ACS: Division of Polym. Mater. Sci., and Eng., ***83***, 56 (2000).

114. Uhl, F. M., and Wilkie, C. A., "Polystyrene/Graphite Nanocomposites: Effect on Thermal Stability", Polym. Degradation and Stability, ***76***, 111 (2002).

115. Xiao, M, Sun, L. Y., Liu, J. J., Li, Y., and Gong, K. C., "Synthesis and Properties of Polystyrene/Graphite Nanocomposite", Polymer, ***43***, 8, 2245 (2002).

116. B. Z. Jang, 'Advanced Polymer Composites: Principles and Applications' ASM International, Materials Park (1994).

117. Gupta, V. B., Drzal, L. T., and Rich, M. J., "The Temperature Dependence of Some Mechanical Properties of a Cured Epoxy Resin System." Polym. Eng. And Sci., ***25***, 3761 (1986).

118. Drzal, L. T., 'Advances in Polymer Science II', **75**, (K. Dusek ed.), Spring-Verlag, (1985).

119. Drzal, L. T., "Fiber-Matrix Interphase', Copy right, Michigan State University (1992).

120. Young, T. Trans. R. Soc. London, ***95***, 65 (1805).

121. Dupre, A. "Theorie Mechanique de la Chaleur." P.369. Gauthier-Villars, Paris (1869).

122. Girifalco, L. A. and Good, R. J., "A Theory for The Estimation of Surface and Interface Interfacial Energies. I. Derivation and Application to Interfacial Tension." J. Phys. Chem., ***61***, 904 (1957).

123. Good, R. J., "Contact Angle, Wetting, and Adhesion: A Critical review." J. Adhesion Sci., Technol., ***6***, 12, 1269 (1992).

124. Fowkes, F. M., "contact Angle, Wettability, and Adhesion. Advanced Chemical Series No. 43, American Chemical Society.", p.99, Washington D.C. (1964).

125. Fowkes, F. M., McCarthy, M. K., and Mostafa, M. A., J. Colloid Interface Sci., ***78***, 200 (1980).

126. Lee, L. H. "Fundamentals in Adhesion." P.153, Plenum Press, New York (1991).

127. Washburn, E. W., " The Dynamics of Capillary Flow." Phys. Rev., ***17***, 273 (1921).

128. Tang, L. G., and Kardos, J. L. "A review of Method for Improving the Interfacial Adhesion Between Carbon Fiber and Polymer Matrix.", Polym. Compos., ***18***, 1, 100 (1997).

129. Kim, J. K and Mai, Y. W., "Engineered Interfaces in Fiber Reinforced Composites." P.186, Elsevior, Amsterdam (1998).

130. Donnet, J-B., Wang, T. K., Rebbouillat, S., and Peng, J. C. M., "Carbon Fibers, Third Edition", Mercel Decker, New York, (1998).

131. Dilsiz, N., Erinc, N. K., Bayramli, E., and Akovali, G., "Surface Energy and Mechanical Properties of Plasma-Modified Carbon Fibers." Carbon, ***33***, 6, 853 (1995).

132. Madhukar, M. S.and Drzal, L. T., "Fiber-Matrix Adhesion and Its Effect on Composite Machanical Properties.I. Inplane and Interlaminar Shear Behavior of Graphite Epoxy Composites." J. Composite Mater., **25**, 932 (1991).

133. Madhukar, M. S.and Drzal, L. T., "Fiber-Matrix Adhesion and Its Effect on Composite Machanical Properties.II. Longitudinal and Transverse Tensile and Flexure Behavior of Graphite Epoxy Composites." J. Composite. Mater., **25**, 958 (1991).

134. Madhukar, M. S.and Drzal, L. T., "Fiber-Matrix Adhesion and Its Effect on Composite Machanical Properties.III. Longitudinal Compressive Properties of Graphite Epoxy Composites." J. Composite Mater., ***26***, 310 (1992).

135. Madhukar, M. S.and Drzal, L. T., "Fiber-Matrix Adhesion and Its Effect on Composite Machanical Properties.IV. Mode I and Mode II fracture Toughness of Graphite/Epoxy Composites." J. Composite. Mater., **26,** 936 (1992).

136. Pittman, Jr., C. U., He, G-R., Wu, B., and Gardner, S. D., "Chemical Modification of Carbon Fiber Surfaces by Nitric Acid Oxidation followed by Reaction with Tetraethylenepentamine." Carbon, ***35***, (3), 317 (1997).

137. Pittman, Jr., C. U., Wu, Z., Jiang, W., He, G-R., Wu, B., Li, W., and Gardner, S. D., "Reactions of Amine Functions Grafted to Carbon Fiber Surfaces by Tetraethylenepentamine. Designing Interfacial Bonding.", Carbon, ***35***, (7), 929 (1997).

138. Yamada, K, Haraguchi, T., and Kajiyama, T., "Plasma-Graft Polymerization of Vinyl Monomer with an Acid Amide Group onto a Surface of Carbon Fiber and Its Adhesion to Epoxy Resin.", J. Appl. Polym. Sci., ***75***, 284 (2000).

139. Piggott, M. R., "Load Bearing Fiber Composites", Pergamon Press, p69-71 (1980).

140. Eshelby, J. D. "The continuum Theory of Lattice Defects, Progress in Solid State Physics 3.", Academic Press, New York, P79 (1956).

141. Eshelby, J. D., Proc. Ro. Soc. London, ***A241***, 376 (1957).

142. Shia, D. Hui, C. Y., Burnside, S. D., and Giannelis, E. P., "An Interface Model for The Prediction of Young's Modulus of Layered Silicate-Elastomer Nanocomposites." Polym. Compos., ***19***, 5, 608 (1998).

143. Sato, N, Kurauchi, T, Sato, S., and Kamigaito, O, "SEM Observations of The Initiation and Propagation of Cracks in a Short Fiber Reinforced Thermoplastic Composite under Stress", J. Mater. Sci. Lett., ***2***, 188 (1983).

144. Sato, N., Kurauchi, T, Sato, S., and Kamigaito, O., "Reinforcing Mechanism by Small Diameter Fiber in Short Fiber Composite." J. Compos. Mater., ***22***, 850 (1988).

145. Nardin, M and Schultz, J., "Interactions and Properties of Composites: a) Fiber-Matrix Adhesion Measurements." in "The Interfacial Interactions in Polymeric Composites.", Kliwer Academic Publishers, p81-93 (1993).

146. Mendelson, A., "Plasticity: Theory and Application", Robert E. Krieger Publishing Company, Malabar, Florida (1983).

147. Flory, P. J., "Molecular Size Distribution in Three Dimensional Polymers. I. Gelation." J. Am. Chem. Soc., ***63***, 3083 (1941).

148. Flory, P. J., "Molecular Size Distribution in Three Dimensional Polymers. II. Trifunctional Branching Units." J. Am. Chem. Soc., ***63***, 3091, (1941).

149. Flory, P. J., "Molecular Size Distribution in Three Dimensional Polymers. III. Tetrafunctional Branching Units." J. Am. Chem. Soc., ***63***, 3096, (1941).

150. Stockmeyer, W. H., "Theory of Molecular Size Distribution and Gel Formation in Branched-Chain Polymers." J. Chem. Phys., ***11***, 45 (1943).

151. Stauffer, D., and Aharony, A., "Introduction to Percolation Theory", Taylor and Francis Inc., Washington DC., (1992).

152. Zallen, R., "The Physics of Amorphous Solids.", John Wiley and Sons, New York (1983).

153. Straley, J. P., "Critical Exponent for The Conductivity of Random Resistor Lattice.", Phys. Rev. B; ***15***, 12, 5733 (1977).

154. Harris, A. B., and Kirkpatrick, S., "Low-frequency Response Functions of Random Magnetic Systems." Phys. Rev. B; ***16***, 1, 542 (1977).

155. Stauffer, D., "Introduction to Percolation Theory", Taylor and Francis Inc., Washington DC., (1979).

156. Zois, H, Apekis, L., and Omastova, M., "Electrical Properties of Carbon Black-filled Polymer Composites.", Macromol. Symp., ***170***, 249 (2001).

157. Putten, D. V. D., Moonen, J. T., Brom, H. B., Brokken-Zijp, J. C. M., and Michels, M. A. J., "Evidence for Superlocalization on a Fractal Network in Conductive Carbon-Black-Polymer Composites.", Phys. Rev. Lett., ***69***, 3, 494(1992).

158. Chakrabarty, R. K., Bardhan, K. K., and Basu, A., "Nonlinear I-V Characteristics Near The Percolation Threshold.", Phys. Rev. B; ***44***, 13, 6773 (1991).

159. Son, Y., Noh, T. W., Lee, S. I., and Gaines, J. R., "Experimental Study of The Three-dimensional AC Conductivity and Dielectric Constant of a Conductor-Insulator Composite near the Percolation Threshold.", Phy. Rev. B; ***33***, 2, (1986).

160. Lee, S. I., Song, Y., Noh, T. W., Chen, X. D., and Gaines, J. R., "Experimental Observations of Nonuniversal Behavior of The Conductivity Exponent for Three-dimensional continuum percolation systems.", Phys. Rev. B; ***34***, 10, 6719 (1986).

161. Heaney, M. B., "Measurement and Interpretation of Nonuniversal Critical Exponents in Disordered Conductor-Insulator Composites.", Phys. Rev. B; ***52***, 17, 12477 (1995).

162. Carmora, F., and Amarti, A. E., "Anisotropic Electrical Conductivity in Heterogeneous Solids with Cylindrical Conducting Inclusions." Phys. Rev. B; ***35***, 7, (1987).

163. Quivy, A., Deltour, R., Jansen, A. G. M., and Wyder, P., "Transport Phenomena in Polymer-graphite Composite Materials.", Phys. Rev. B; ***39***, 2, 1026 (1989).

164. Balberg, I., "Tunneling and Nonuniversal Conductivity in Composite Materials.", Phys. Rev. Lett., ***59***, 12, (1987).

165. Evane, A. G. and Jones, R. L., "Evaluation of a Fundamental Approach for The Statistical Analysis of Fracture." J. Amer. Ceram. Soc., ***61***, 3-4, 156 (1978).

166. Von Hippel, Arther R. "Dielectric Materials and Applications.", Artech House Publishers, Boston, p.36., (1995).

CHAPTER 2.

EXFOLIATION PROCESS

FOR

GRAPHITE INTERCALATION COMPOUNDS

2.1. Introduction

Graphite is one of the strongest and stiffest materials found in nature. Recent discovery of new nano-size graphite materials, such as fullerene and carbon nanotubes, are attracting attention because of their superior mechanical, electrical, thermal and other properties. [1, 2] These materials are expected to be used in many applications such as advanced composites for high strength structural materials, high conductive materials for EMI shielding and fuel cell parts, anode materials for batteries, and hydrogen fuel storage. One main drawback of these nano-size graphite materials is their high cost. The cost of nanotubes is in the $50-500/g ($22,700-227,000/lb) range, depending on the structure and purity of the material. It is obvious that this material is still too expensive for many commercial applications.

Crystalline graphite has excellent mechanical, electrical, and thermal properties. Many crystalline graphite materials are available including natural and synthetic forms. These materials are more abundant and more economical than graphite whiskers and VGCF. Pure crystalline graphite has similar or better properties than these materials [3]. Carbon nanotubes have better properties than these crystalline graphite materials, yet the costs of nanotubes are far beyond the level for commercial applications. [4] If nanosize crystalline graphite flakes can be produced at a reasonable cost, the material can be used in many commercial applications because of its excellent mechanical, thermal, and electrical properties.

Graphite has been known as a host material for many chemicals, including metal halides, metal oxides, and mineral acids. The exfoliation phenomena of the graphite intercalated compounds (GIC) have been investigated for a long time. Aylsworth filed

two patents related to expanded graphite and its usage in molding application in the 1910's. [5, 6] The claims include (1) the process of intercalating acids into graphite, (2) heat expansion of the intercalated graphite to make "fluffy graphite", and (3) compounding expanded graphite in resins, typically phenolic resins. Since then, many researches have been investigating the exfoliation of GICs [7, 8, 9, 10, 11]. Chung wrote a review about the exfoliation phenomena of GICs [12].

There are several methods to expand GICs. The most commonly used technique is the rapid heating in a furnace. This is widely used in the commercial stage. Other methods can include infrared, laser, microwave, and electric current. Among these, microwave systems are available in many sizes and power levels, yet very little has been investigated about microwave exfoliation of GICs. In this research, natural crystalline graphite-based acid intercalated graphite compounds were exfoliated by heating or a microwave processes. The effects of temperature, microwave power, and the size of graphite flakes on degree of expansion were examined by XRD. Also the surface chemistry of the exfoliated graphite samples was investigated by XPS. It revealed that the microwave process could give a better degree of expansion and a cleaner surface at lower cost. These expanded graphite samples were pulverized and milled into sub-micron graphite flakes. SEM and TEM images showed that the average size of graphite became 0.86um and the thickness of around 10 nm. The cost of this new nano-size graphite material was estimated to be around $5/lb. With its superior mechanical, electrical, thermal properties and cost effectiveness, this material could be used in variety of applications such as nanocomposites, secondary batteries, and fuel cells.

2.2. Experiment

2.2.1. Graphite Materials

The graphite samples used in this research were Graphite Intercalate Compounds (GICs), which were acid intercalated natural crystalline graphite flakes offered from UCAR Inc. The acid components consist of sulfuric and nitric acid. Nitric acid acts as an oxidizer while sulfuric acid acts as an intercalant. The acid intercalated graphite exhibits multiple stages, ranging from stage 1 to 5. The stage number indicates the number of graphene sheets between adjacent intercalated galleries. Upon heating, the intercalated acids become vapor and force layers apart, causing exfoliation of graphite layers. The sample grades used in this research are Grafguard^{TM} 160-50A, 160-50B, and 160-50N. Here "160" refers to the onset temperature at which intercalated acid begins to be released and exfoliation of the graphite occurs. "50" indicates the average size of the flakes is 50 mesh, which is 300 um. A, B, and N show the conditions of the sample surface, which are acidic, basic, and neutral.

2.2.2. Measurements

- Thermogravimetric Analysis (TGA)

A Cahn TG System 121 analyzer was used for thermogravimetric analysis. 10 to 20mg of GICs were heated up to 800°C at the rate of 10°C/min. The weight loss was monitored and the acid intercalate content was determined.

- X-Ray Diffraction (XRD)

A Rigaku rotaflex 200B diffractometer was used for XRD analysis. The X-ray source was Cu-Kα with a curved graphite monochromator. The operational setting was

45kV and 100mA. The diffraction patterns were collected from 1° to 60° (2θ) at a scanning rate of 3°/min.

Since graphite materials have a layered structure, they show characteristic peaks in their XRD patterns. Among these, the peak from d002 is the highest and most distinctive one, appearing at $2\theta = 26.5°$ or 0.335 nm. The height of the d002 peak is a measure of how many layers are stacking together to form graphite flakes. Thus, the degree of exfoliation was investigated by measuring the d002 peak height after the exfoliation process.

- X-Ray Photoelectroscopy (XPS) or Electron Spectroscopy for Chemical Analysis (ESCA)

X-ray photoelectron spectra were obtained from a Physical Electronics PHI 5400 ESCA system. A non-monochromatic Mg source (with a $K_{\alpha 1,2}$ wavelength at 1253.6 eV) was used with a take-off angle of 45 degrees. Data was collected by a multi-channel detector with an Omni VI lens assembly. The instrument was operated with a pass energy of 93.90 eV for survey scans and 29.35 eV for regional scans. All peaks were referenced to adventitious carbon at 284.6 eV. Semi quantitative atomic concentrations were calculated using pre-determined sensitivity factors. XPS samples were prepared by applying the graphite directly to double sided copper tape on a stainless steel stub.

XPS analysis was used to investigate the acid remaining on the surface of exfoliated graphite. The sulfur and nitrogen content of graphite suggest the existence of sulfuric and nitric acid, since pure natural crystalline graphite has no or very little amount of these atoms on its surface.

- Environmental Scanning Electron Microscopy (ESEM)

ElectroScan 2020 environmental SEM (ESEM™) outfitted with a LaB_6 filament was used for SEM analysis. GSED detector with a 1.0 mm bore was used. Working condition of electron-beam energy was 20 kV, a working distance was 10 mm, and a chamber pressure was 3 Torr. SEM images of expanded and exfoliated graphite were taken to investigate the physical structure, morphology, and size of the graphite flakes. The diameter of a few hundred flakes was measured and a size distribution curve was established.

- Transmission Electron Microscope (TEM)

Hitachi H-8100 TEM or JEOL 2010F with 200 kV electron-beam energy microscope was used to investigate the nanoscale structure of the exfoliated graphite samples.

- BET Surface Area Measurement

Micromeritics TRISTAR 3000 was used to analyze the surface areas of reinforcement materials. Each sample was outgassed at 250°C under 0.1 torr for 12 hours prior to the measurement, except the as-received graphite sample. Since this sample has acid intercalates which can evaporate at 160°C, it was dried at 150°C. BET surface areas were determined from the region between P/P_0 of 0 to 0.2. Eight data points were collected for each sample and an average value was calculated. Error margins for the measurements were determined by using standard samples with similar surface areas.

2.3. Results and Discussion

2.3.1. Expansion of Graphite Flakes by Heating

Figure 2.1 is a TGA data that shows the expansion condition of 160-50A. It revealed that initial expansion occurs around 160°C, but most of it occurs in the range of 250 to 350 °C. The amount of acid intercalated in 160-50A was determined at around 21 wt%. 160-50N showed almost the same tendency in TGA curves but has less acid intercalates, around 16wt%. 160-50B showed a slightly different degradation curve, showing two steps in the weight loss curve. This sample has base on its surface that could affect this result. The acid content of 160-50B is around 12wt%. During the expansion process, a graphite flake expands 100 to 1000 times in c-axis direction and makes a worm-like shape with flakes attached together [**Figure 2.2**]. This sample was defined as expanded graphite. Since 160-50A has the largest amount of acid and shows the highest degree of expansion, this research mainly used 160-50A as the starting material.

Two factors affect the degree of expansion: temperature and the size of the graphite flakes. To investigate the effect of temperature, 4g of 160-50A was exfoliated at 300, 400, 500, 600, 700, 800, 900, and 1000°C for 3 min. **Figure 2.3** shows the image of the expanded graphite samples after the treatment. This image reveals that the degree of expansion increased as temperature increased up to 600°C, then it reached a plateau beyond that temperature. Thus, it is concluded that the temperature of 600°C or higher is required to achieve maximum degree of expansion. This also agrees with literature citations indicate that temperatures above 800°C were used to expand acid intercalated graphite flakes in their research [13, 14, 15, 16, 17].

To investigate the effect of size, 160-50A flakes were sieved into different sizes, less than 25um, 25 to 75um, 75 to 106um, 106 to 180um, 180 to 300um, 300 to 500 um, and over 500 um. 0.1 g of each sample was dispersed in a crucible and expanded at 900 °C for 5 min at the same time in the same furnace. **Figure 2.4** shows the image of expanded graphite after the heat treatment. The larger the sample size is, the larger the degree of expansion is. This is because the vaporized intercalate escapes from the edge region, rather than pushes the layers apart, when the size of the flake is small. Also TGA data revealed that the smaller graphite has less acid intercalates, which should lead less expansion (**Figure 2.5**). Judging from these experiments, it is concluded that graphite flakes of 75 um or larger size show good expansion, and those of 180 um or larger show the maximum expansion.

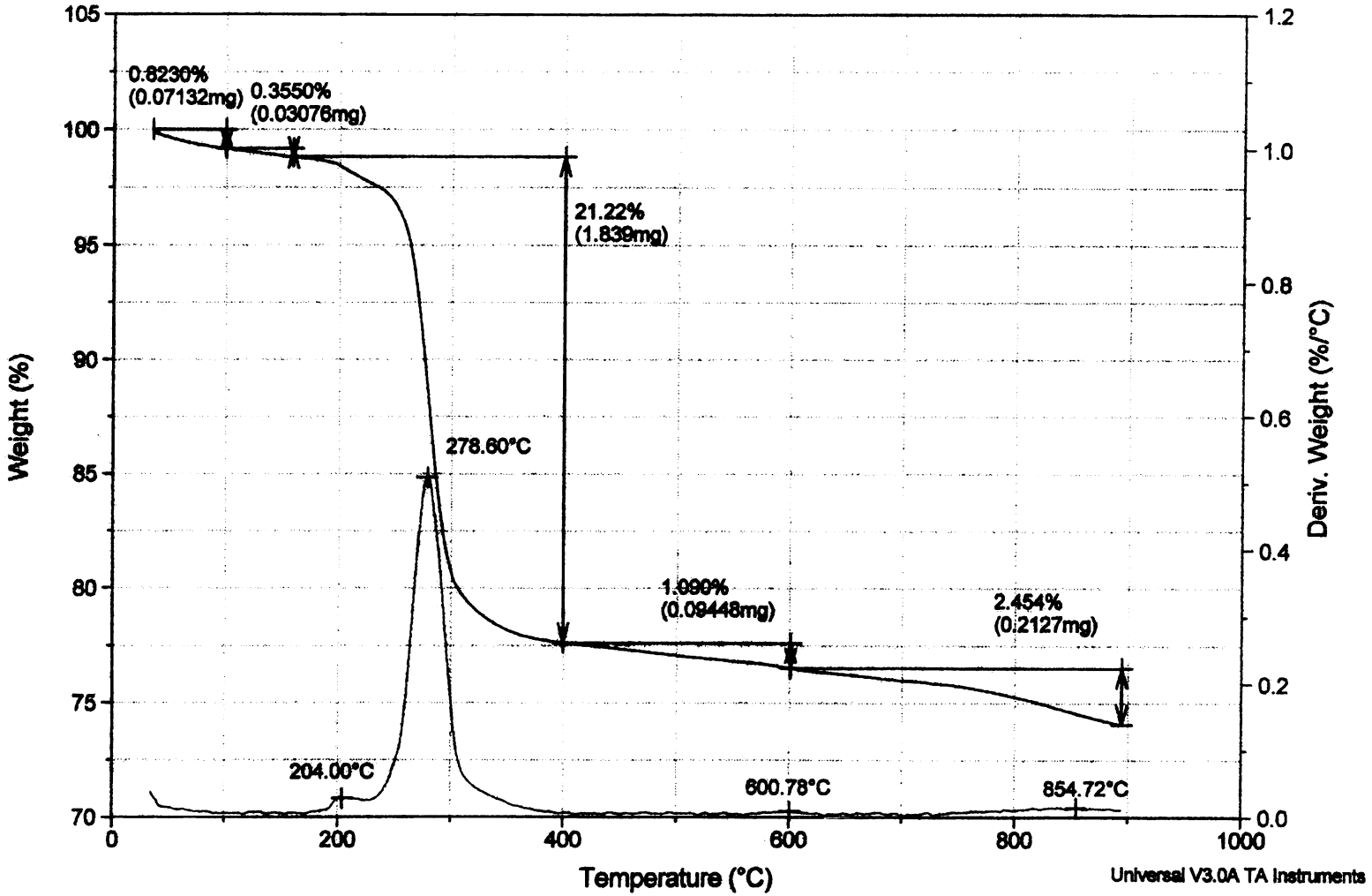

Figure 2.1. TGA Data of Acid Intercalated Graphite Sample (160-50A)

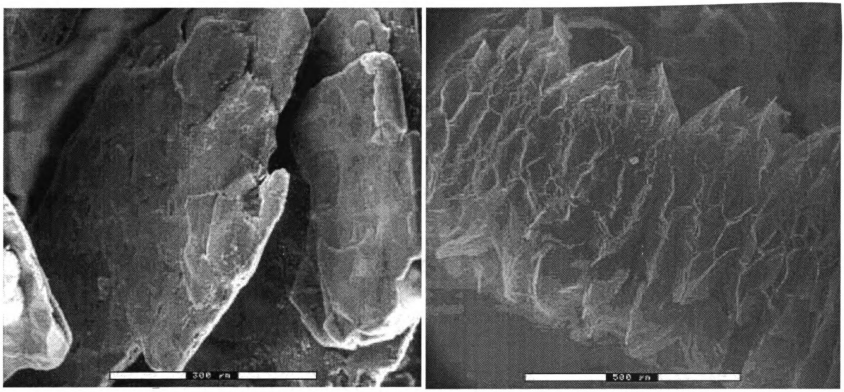

Figure 2.2. ESEM images of as-received 160-50A (left) and expanded graphite at 900°C (right). (Scale Bar = 500 um)

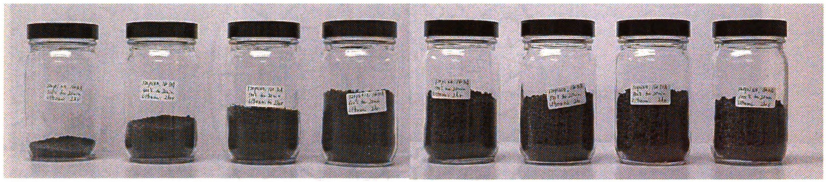

300°C 400°C 500°C 600°C 700°C 800°C 900°C 1000°C

Figure 2.3. The Effect of Temperature on Degree of Expansion (160-50A)

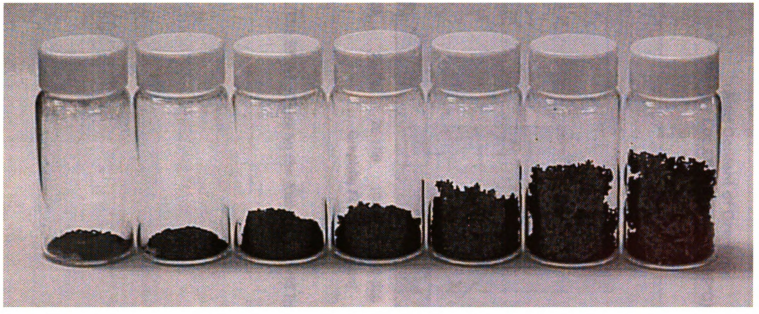

0-25um 25-75um 75-106um 106-180um 180-300um 300-500um +500um

Figure 2.4. The Effect of Size on Degree of Expansion (Heating Process at 900°C.)

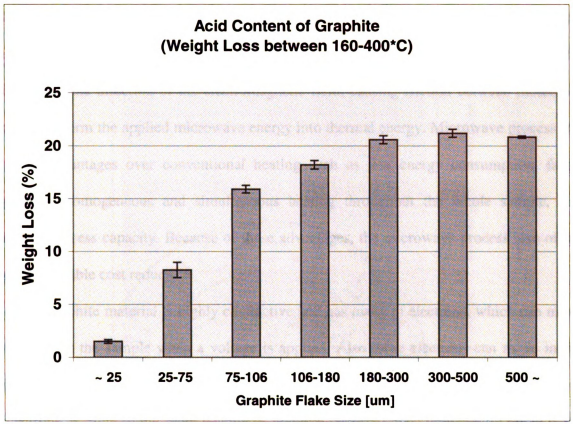

Figure 2.5. The Effect of Size on the Amount of Acid Intercalate Content

2.3.2. Expansion of Graphite Flakes by Microwave

The physical principle of dielectric heating, which includes microwave and radio frequency heating, is based on the transformation of electromagnetic field energy into thermal energy in polar materials. Dipoles of polar materials change their direction by following the direction of the electromagnetic field, causing friction between molecules and transform the applied microwave energy into thermal energy. Microwave process has many advantages over conventional heating such as less energy consumption, faster process, homogeneous and simultaneous heating throughout the whole sample, and higher process capacity. Because of these advantages, the microwave process also offers a considerable cost reduction.

Graphite material is highly conductive and has many pi electrons, which can move throughout the sample when a voltage is applied. Also these electrons can move in the direction of the electromagnetic field when it is applied. This causes vigorous vibration of electrons, leading to the rapid heating of graphite materials. The temperature could reach few hundred degrees Celsius within a few seconds. Thus, the microwave process can provide an alternative method to expand graphite-intercalated compounds.

Figure 2.6 shows the effect of size of graphite flakes on the expansion by microwave processing. 0.1 g of sieved graphite samples were put in sample vials and microwaved at 900 W for 5 seconds. The frequency of the microwave was 2.45 GHz. It showed that the larger the size, the better the expansion. By comparing the heating process, **Figure 2.4**, and the microwave process, **Figure 2.6**, it was shown that microwave process could give the same or better degree of expansion for graphite flakes.

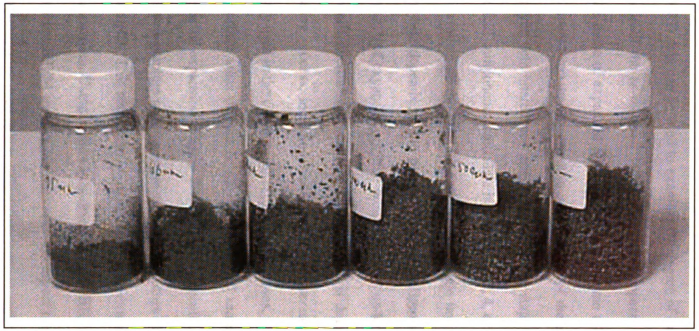

25-75um 75-106um 106-180um 180-300um 300-500um +500um

Figure 2.6. The Effect of Size on Degree of Expansion (Microwave Process at 1300W)

2.3.3. Comparisons of Conventional Heating and Microwave Process

2.3.3.1. Degree of Expansion

Since graphite flakes have layered structures, they show distinctive peaks in XRD patterns. These XRD data can be used to examine the degree of expansion of GICs. The peak of d002 plane of the as-received 160-50A samples appears as a large sharp peak (**Figure 2.7**) while those of expanded graphite samples became a lot smaller, suggesting that most of the layered structures were destroyed because of the expansion. (**Figure2.8, Figure 2.9**) However, acid intercalated graphite has multiple stage structures from 1 to 5, which means the acid components intercalate in every 1, 2, 3, 4, or 5 layers of graphite. It is impossible to exfoliate all the graphite material into single layers. The peak height of the expanded graphite depends on the process condition. **Figure 2.10** shows the peak height of d002 planes of expanded graphite samples treated under various conditions. It revealed that overall microwave treatment showed a better degree of expansion than conventional heating process, including heating at the temperature of 600°C to 800°C, which is commonly used in the commercial expansion processes.

Also BET surface areas of heat or microwave treated samples were measured to estimate the degree of expansion. **Figure 2.11** shows the results. The surface areas of microwave exfoliated graphite samples were more than 4 times larger than those of the heat exfoliated samples. This result also supports that the microwave process can give a better degree of expansion. Using surface area determined by BET measurements and the average diameter from ESEM images, the thickness and aspect ratio of each sample was calculated. The assumptions used in this calculation were 1) each flake has an octagonal shape, 2) the thickness is constant, and 3) the density of graphite is 2.0 g/cm^3. The results

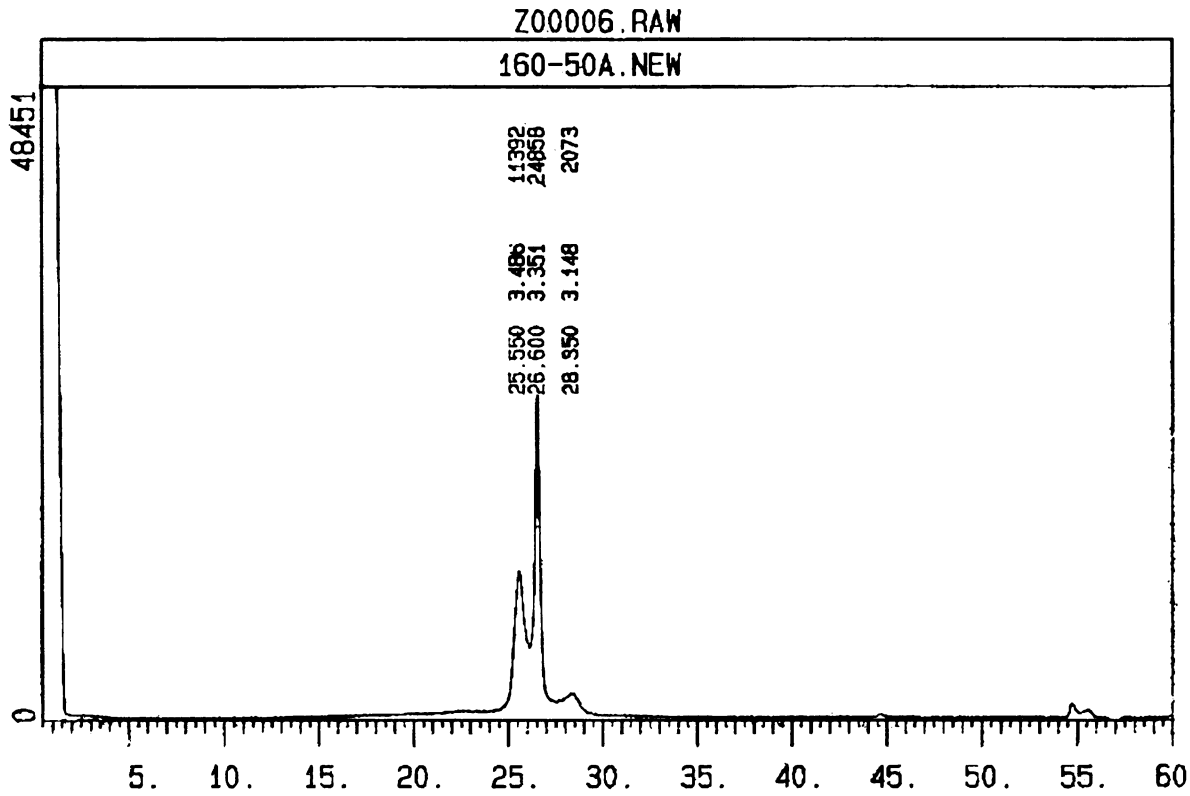

Figure 2.7. XRD curves of Graphite Samples. As-received Graphite Sample (160-50A, d002=24858 cps)

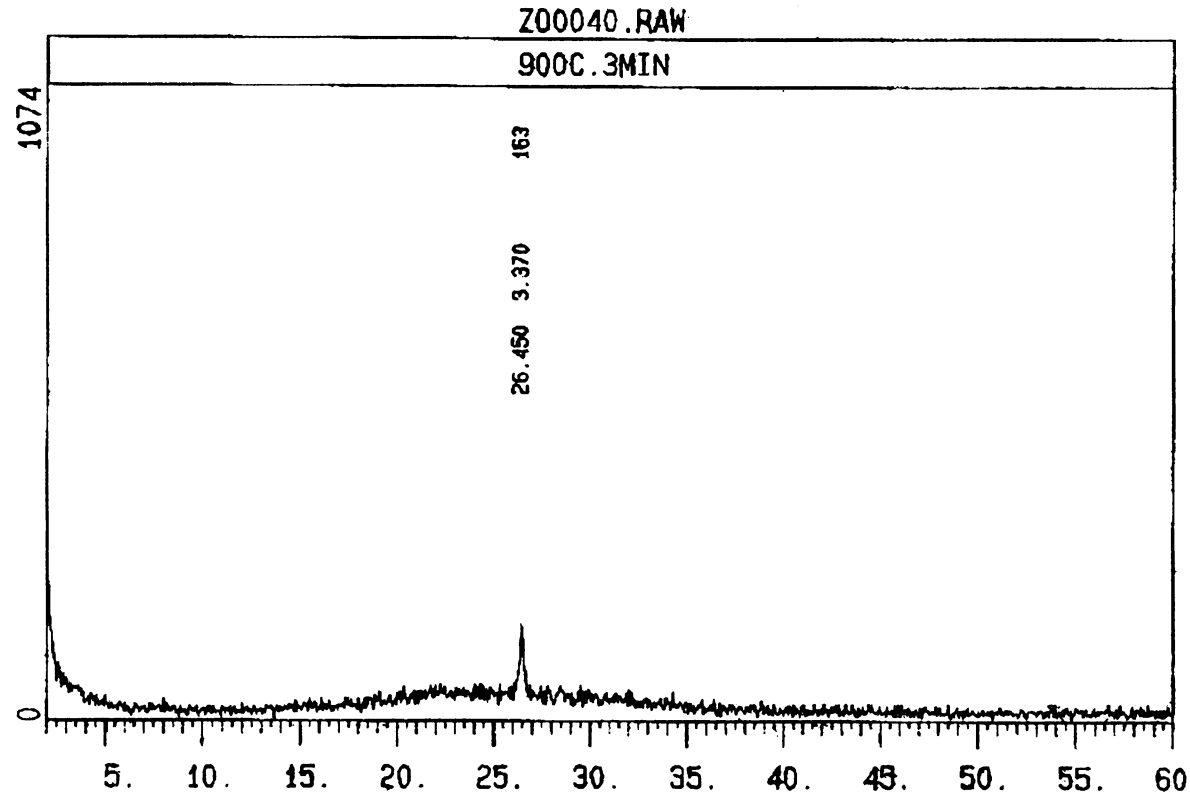

Figure 2.8. XRD curves of Graphite Samples after Expansion by Heating, (900°C for 3min, d002=163 cps)

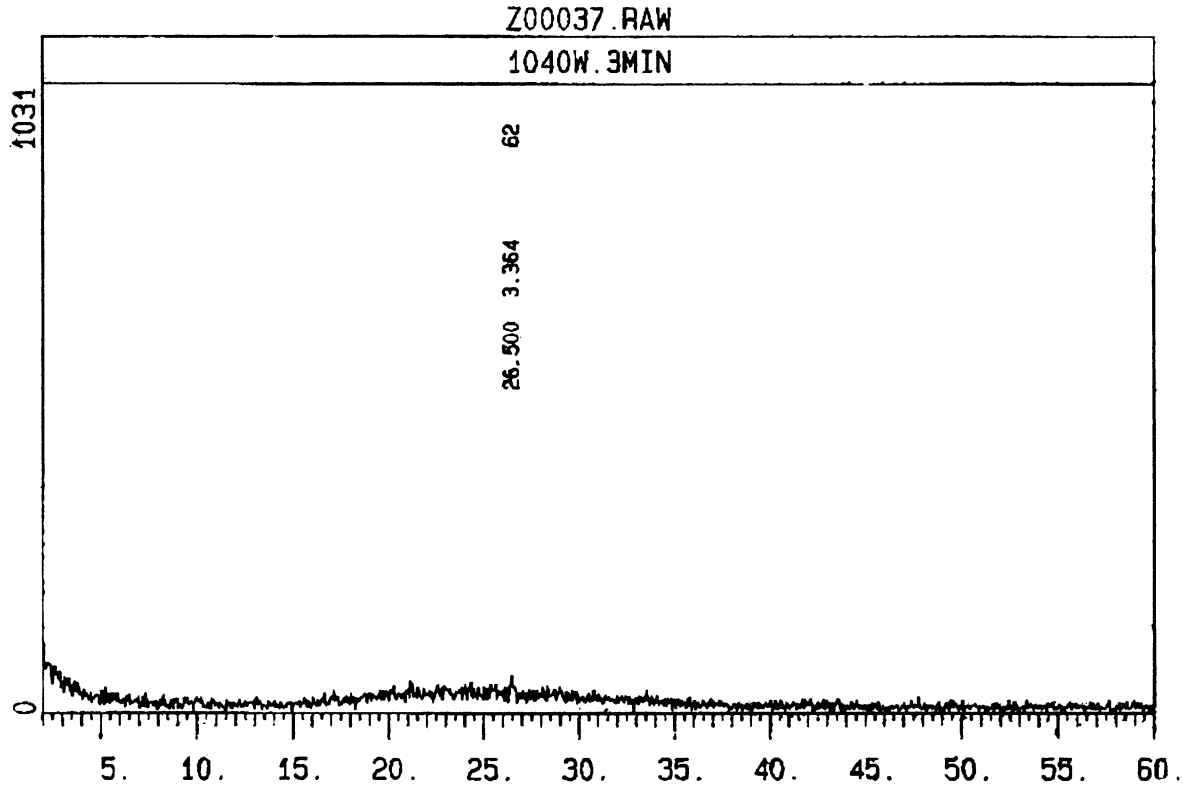

Figure 2.9. XRD curves of Graphite Samples after Expansion by Microwave (1040W for 3min, d002=62 cps)

(A) XRD of Expanded Graphite by Heating

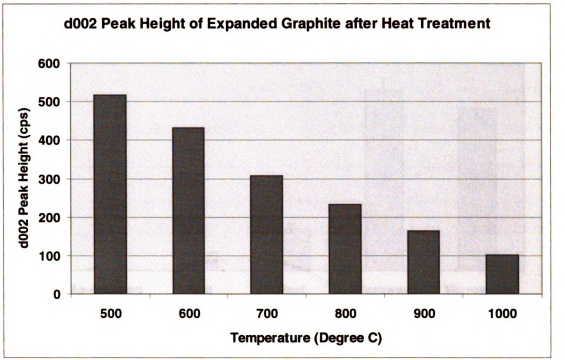

(B) XRD of Expanded Graphite by Heating

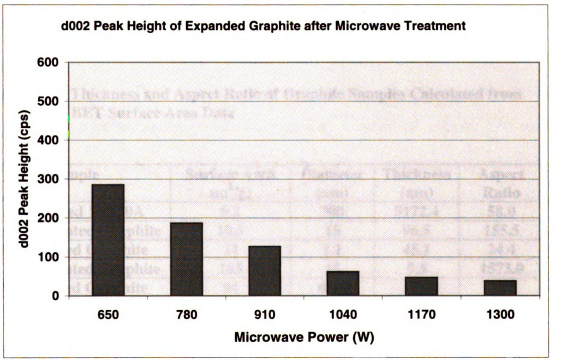

Figure 2.10. d002 Peak Height for Expanded Graphite Treated by Heating (A) or Microwave (B) under various conditions.

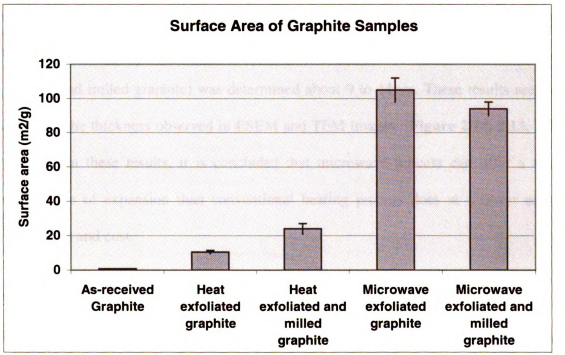

Figure 2.11. Surface Area of Graphite Samples determined by BET measurement

Table 2.1. Thickness and Aspect Ratio of Graphite Samples Calculated from BET Surface Area Data

Sample	Surface Area (m^2/g)	Diameter (um)	Thickness (nm)	Aspect Ratio
As-received 160-50A	0.2	300	5172.4	58.0
Heat Exfoliated Graphite	10.5	15	96.5	155.5
Heat Milled Graphite	24	1.1	45.1	24.4
MW Exfoliated Graphite	105	15	9.5	1573.0
MW Milled Graphite	94	0.86	10.9	78.8

are shown in **Table 2.1**. The thickness of the as-received graphite was estimated around 5 um. The thickness of the Heat Milled Graphite (heat-exfoliated and milled graphite) was estimated around 50 to 100 nm while that of the MW Milled Graphite (microwave-exfoliated and milled graphite) was determined about 9 to 11nm. These results are well matched to the thickness observed in ESEM and TEM images. (**Figure 2.12, 2.13, 2.14**) Judging from these results, it is concluded that microwave process can offer a much better degree of expansion than conventional heating process does at a lower energy consumption and cost.

2.3.3.2. Cleanness of Surface

Although the expansion occurs within a second, there could be some acid components left on graphite surfaces even after treatments, which could cause problems when the expanded graphite materials are used in further applications. To investigate the surface condition of expanded graphite, XPS (X-Ray Photoelectron Microscopy) data were collected and analyzed. **Figure 2.15** shows the sulfur/carbon and nitrogen/carbon ratio of the expanded graphite. Sulfur content suggests the existence of sulfuric acid while nitrogen implies nitric acid. At 600°C treatment, the sulfur and nitrogen components were detected even after 10 minutes of treatment. At 800°C, these components were almost removed from the sample after 5 minutes of treatment. At 1000°C, it required about 2 minutes to remove these components. **Figure 2.16** shows the XPS results of expanded graphite by microwave treatment. In this case, the sulfur and nitrogen component were removed after 2 minutes treatment at 910W and 1300W. This implies that the microwave treatment also has advantage over conventional heating process in terms of removal of the residual intercalates.

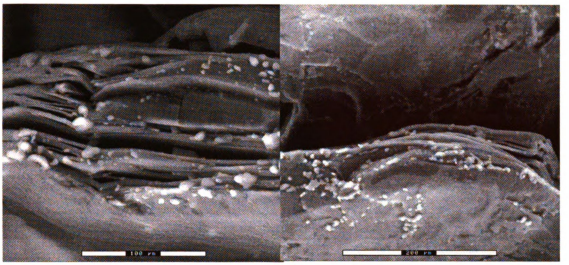

Figure 2.12. ESEM Images of As-received Graphite Sample
Scale Bar = 100 um (Left), 200 um (Right)

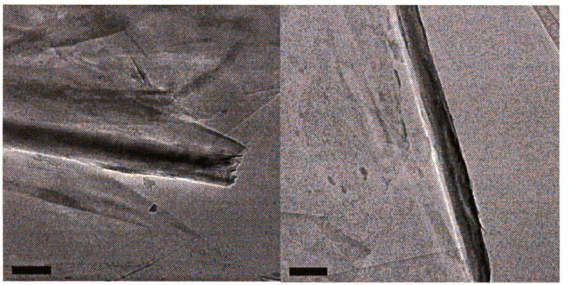

Figure 2.13. TEM Image of Heat-exfoliated Graphite Sample
Scale Bar = 100 nm (Left, Right)

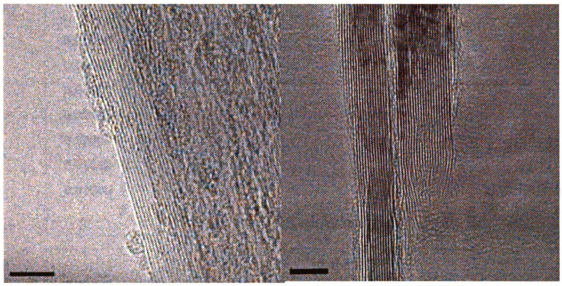

Figure 2.14. TEM Images of Microwave-exfoliated Graphite Sample Scale Bar = 5 nm (Left, Right)

(A)

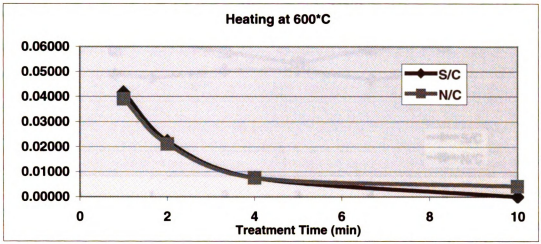

(B)

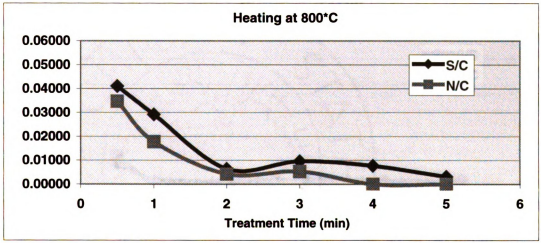

(C)

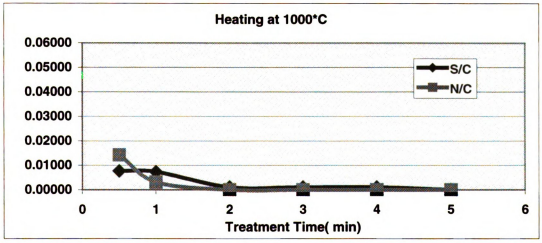

Figure 2.15. Acid Components on The Surface of Expanded Graphite under Various Conditions. Heating Process at 600°C (A), 800°C (B), and 1000 °C (C).

(A)

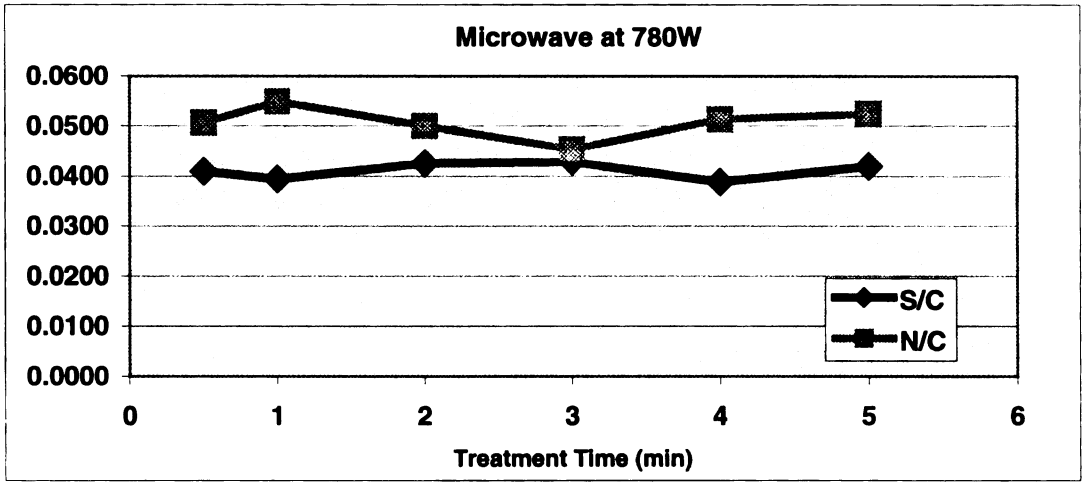

(B)

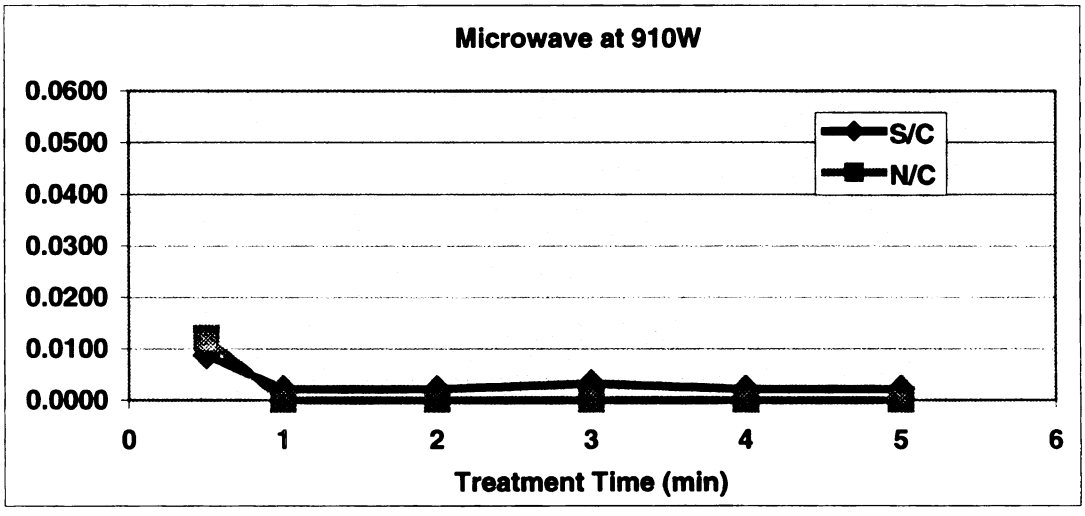

(C)

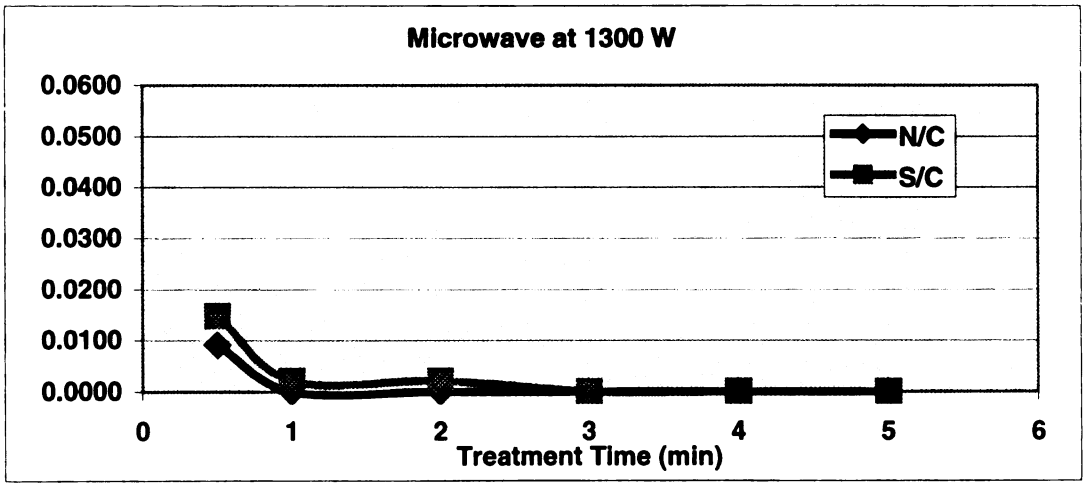

Figure 2.16. Acid Components on the Surface of Expanded Graphite under Various Conditions. Microwave Process at 780W (A), 910W (B), and 1300W(C).

2.3.4. Grinding Process for Expanded Graphite

The worm-like graphite samples can be pulverized into small flakes by ultrasonic waves, mechanical grinding, or other methods. **Figure 2.17** shows an ESEM image and **Figure 2.18** shows the size distribution of the graphite particles after pulverization by sonication. 20 g of the expanded graphite sample was dispersed in 2 liters of acetone and pulverized by the 20 kHz ultrasonic wave at 100W for 2 hours. The average size of this sample was 14.25 um.

These samples can be ground into smaller flakes by ball milling, planetary milling, or vibratory milling. **Figure 2.19** shows the ESEM images of graphite flakes after 72 hours of vibratory ball milling. The slurry was made around 12 to 15 wt% of graphite in 2-propanol. **Figure 2.20** shows the size distribution of the sample. The average size became 0.86 um.

2.4. Conclusions

The microwave and heat exfoliation processes of GICs were investigated and compared. It revealed that the microwave process could give a better degree of expansion and a cleaner surface at a lower cost. These expanded graphite samples were pulverized and milled into sub-micron size graphite flakes. SEM, TEM and AFM images showed that the average size of graphite became 0.86um and the thickness became10 nm. The cost of this new nano-size graphite material was estimated around $5/lb. [CHAPTER 6] Because of its superior mechanical, electrical, thermal properties and cost effectiveness, this material is expected to be used in a variety of applications such as nanocomposites, secondary batteries, and fuel cells.

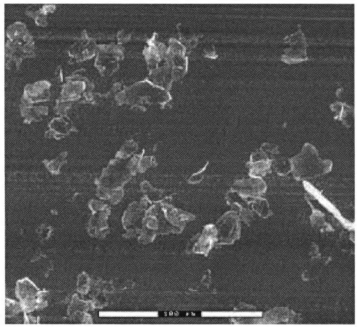

Figure 2.17. ESEM image of Graphite Fakes after Exfoliation and Pulverization (Scale Bar = 100um)

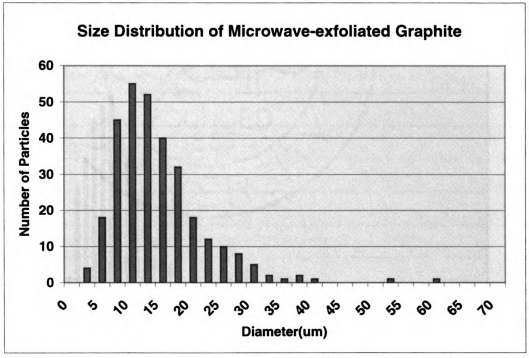

Figure 2.18. Size Distribution of Graphite Particle after Exfoliation and Pulverization by Sonication, Average Size = 14.25 um (Standard Deviation = 7.53 um)

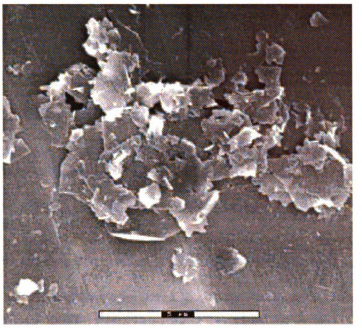

Figure 2.19. ESEM image of Graphite Fakes after Ball Milling (Scale Bar = 5um)

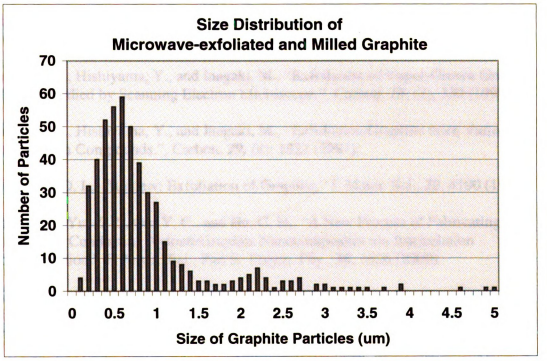

Figure 2.20. Size Distribution of Graphite Particle after Ball Milling (72 hr) Average Size = 0.86 um (Standard Deviation = 0.73 um)

2.5. Reference

1. Kroto, H. W., Heath, J. R., O'Brien, S. C., Cul, R. F., and Smalley, R. E., "C-60-Buckminsterfullerene", Nature, ***318,*** 6042, 162 (1985).

2. Iijima, S., "Helical microtubules of graphitic carbon", Nature, ***354***, 6354, 56 (1991).

3. Ebbesen, T. W., "Carbon Nanotubes" CRC Press, Boca Raton, Florida (1997).

4. Saito, R, Dresselhaus, G. & Dresselhaus, M. S., "Physical Properties of carbon Nanotubes." Imperial College Press, London (1999).

5. Aylsworth, J. W., "Expanded Graphite and Composition Thereof." US Patent 1,137,373 : (1915).

6. Aylsworth, J. W., "Expanded Graphite." US Patent 1.191,383 : (1916).

7. W. H. Martin, W. H. and Brocklehurst, J. E. , "The Thermal Expansion Behaviour of Pyrolytic Graphite-Bromine Residue Compounds." Carbon, ***1***, 133 (1964).

8. Chung, D. D. L. and Wong, L. W., "Electromechanical Behavior of Graphite Intercalated with Bromine.", Carbon, ***24***, (5), 639 (1986).

9. Chung, D. D. L., "Intercalate Vaporization During The Exfoliation of Graphite Intercalated with Bromine.", Carbon, ***25,*** (3); 361 (1987).

10. Yoshida, A., Hishiyama, Y., and Inagaki, M., "Exfoliation of Vapor-Grown Graphite Fiber as Studied by Scanning Electron Microscope.", Carbon, ***28***, (4), 539 (1990).

11. Yoshida, A., Hishiyama, Y., and Inagaki, M., "Exfoliation Graphite from Various Intercalation Compounds.", Carbon, ***29,*** (8): 1227 (1991).

12. Chung, D. D. L., "Review: Exfoliation of Graphite." J. Mater. Sci., ***22***, 4190 (1987).

13. Pan, Y. X., Yu, Z. Z., Ou, Y. C., and Hu, G. H., "A New Process of Fabricating Electrically Conducting Nylon6/Graphite Nanocomposites via Intercalation Polymerization." J. Polym. Sci., Part B: Polym. Phy., ***38***, 1626 (2000).

14. Chen, G. H., Wu, D. J., Weng, W. G., He, B., and Yan, W. L., "Preparation of Polystylene-Graphite Conducting Nanocomposites via Intercalation Polymerization." Polym. Int., ***50***, 980 (2001).

15. Chen, G. H., Wu, D. J., Weng, W. G., He, B., and Yan, W. L., "Preparation of Polymer/Grphite Conducting Nanocomposites by a Intercalation Polymerization." Appl. Polym. Sci., ***82***, 2506 (2001).

16. Xiao, P, Xiao, M., and Gong, K., "Preparation of Exfoliated Graphite/Polystyrene Composite by Polymerization-filling technique." Polymer, ***42***, 4813 (2001).

17. Chen, X. M., Shen, J. W., and Huang, W., Y., "Novel Electrically Conductive Polypropyrene/Graphite Nanocomposites." J. Mater. Sci. Lett., ***21***, 213 (2002).

CHAPTER 3.

SURFACE TREATMENT OF EXFOLIATED GRAPHITE

3.1. Introduction

To understand the bonding between reinforcements and matrix, it is necessary to know the type, the quantity, and the reactivity of the functional groups on the reinforcements. The type of the functional groups required on the reinforcements depends on the chemical structure of the interphase. Epoxies can undergo both acid-catalyzed and base-catalyzed reactions. Thus, acidic groups such as carboxyl group and basic group such as amine groups can react and make covalent bonds. Therefore, it is necessary to introduce these functional groups on the surface of reinforcement to enhance the chemical bonding between reinforcements and epoxy matrix.

3.2. Experiment

3.2.1. Graphite Samples

Four different exfoliated graphite samples were investigated. The details of these samples are listed in **Table 3.1**.

Table 3.1. The Exfoliated Graphite Samples

	Exfoliation Process	Pulverization Process	Average Diameter (um)	Average Thickness (nm)	Surface Area (m^2/g)
Heat-exfoliated Graphite	Heat (900°C)	Sonication	15	97	10.5
Heat-exfoliated and milled graphite	Heat (900°C)	Sonication + vibratory mill	1.1	48	24
Microwave-exfoliated Graphite	Microwave (1300 W)	Sonication	15	10	105
Microwave-exfoliated and milled Graphite	Microwave (1300 W)	Sonication + vibratory mill	0.86	11	94

3.2.2. Surface Treatments

According to the XPS data of exfoliated graphite samples, these materials have very few functional groups on their surface, implying poor interaction with polymer matrices. To improve the surface condition of exfoliated graphite samples, various surface treatments were applied and the surface condition was investigated by XPS. The treatments used were liquid oxidization by sulfuric acid, plasma treatment under oxygen, heating under ozone atmosphere, UV treatment under ozone atmosphere, and grafting amine grafting, and acrylamide polymerization.

- O_2 Plasma Treatment

Graphite nanoplatelets were dispersed on an aluminum foil and covered by a stainless steel mesh. Then the sample was treated by O2 plasma at RF level of 50% (275W). After the first treatment, the sample was re-dispersed on the foil and applied another plasma treatment. This process was repeated more than 3 times. The total treatment time was 1 minute.

- Nitric Acid Treatment

Graphite nanoplatelet sample was dispersed in 69 % (weight) of nitric acid and heated at 115 °C for 5 hours. The sample was then washed by distilled water and dried in a vacuum oven.

- Ozone/Heat Treatment

Graphite nanoplatelets were dispersed in a petri dish then placed in an oven which was filled with ozone . (Concentration: 2000 ppm) Then the samples were heated at 80°C for 20 min. During the time the sample was re-dispersed several times so that the all the graphite flakes were exposed to the ozone environment.

- UV/Ozone Treatment

Graphite nanoplatelets were packed in a quartz tube (ID: 22 mm, OD: 25 mm, Transparent to UV light down to a wave length of 150 nm). The tube was filled with ozone (Concentration: 2000 ppm, Flow rate: 4.7 L/min) and rotated at 3 rpm. Then the samples were exposed to UV light for 5min.

- Amine Grafting

Graphite nanoplatelets were treated by O_2 plasma to introduce the carboxyl groups. Then the sample was dispersed in tetraethylenepentamine (TEPA) and heated at 190°C for 5 hours to graft TEPA by forming the amide linkages. The sample was washed with distilled water and methanol, then dried in a vacuum oven. [1, 2]

- Acrylamide Grafting

Graphite nanoplatelets were treated by O_2 plasma to introduce peroxide groups, which can initiate radical polymerization. Then the sample was dispersed in 1M acrylamide/benzene solution and heated at 80°C for 5 hours to graft and polymerize acrylamide. The sample was washed with acetone and dried in a vacuum oven. [3]

3.2.3. X-Ray Photoelectroscopy (XPS)

X-ray photoelectron spectra were obtained from a Physical Electronics PHI 5400 ESCA system. A non-monochromatic Mg source (with a $K_{\alpha 1,2}$ wavelength at 1253.6 eV) was used with a take-off angle of 45 degrees. Data was collected by a multi-channel detector with an Omni VI lens assembly. The instrument was operated with a pass energy of 93.90 eV for survey scans and 29.35 eV for regional scans. All peaks were referenced to adventitious carbon at 284.6 eV. Semi quantitative atomic concentrations were calculated using pre-determined sensitivity factors. XPS samples were prepared by applying the graphite directly to double side copper tape on a stainless steel stub.

A non-linear least square curve fitting routine was used to interpret the carbon, nitrogen, and oxygen peaks into functional groups, which exist on graphite samples. First, preliminary fitting for O1s curves was made and the ratio of two types of oxygen was determined. Then the carbon C1s and N1s curve fittings were made to separate these curves into several functional group categories [**Table 3.2**]. An asymmetric Gaussian-Lorentzian mixed band shape proposed by Sherwood *et al.* [4, 5] was used to fit the curves. Because of the graphitic nature of the graphite materials, an exponential tail feature was found necessary for C1s 284.4ev curve. These curve-fitting routines have been developed based on extensive XPS work in our laboratory and the model proposed by Sherwood *et al.* [5, 6, 7]. The combination of O1s, N1s, and C1s curve fittings were used to determine the types and amount of functional groups, which existed on the reinforcements.

Table 3.2. Asymmetric Gaussian Lorentzian curve fit model

O1s		C1s		N1s	
Binding Energy	Functional Group	Binding Energy	Functional Group	Binding Energy	Functional Groups
~532 ev	-C-O-C- -C=O -CO-NH2 -CO-NH- -CO-OH	284.4 ev	Graphitic	< 400ev	-NH2 -NH-
		284.6 ev	-C-NH2 -C-NH-	402 ev	-CO-NH2 -CO-NH-
		286 ev	-C-O-C- -C-O-H		
		287.8 ev	-C=O		
~533ev	-C-O-H -CO-OH -NO2	288.4 ev	-CO-NH- -CONH2	>405ev	Oxidized amine
		289 ev	-COOH -COOR		
		290.5 ev	$-CO3^{+}$ $\pi-\pi^{*}$		

3.3. Results and Discussion

3.3.1. Surface Chemistry of Graphite Samples with No Surface Treatments

Surface chemistry of exfoliated graphite samples was investigated with XPS. Five to seven data points were collected and the average values were calculated. When a sample contained contaminates such as Zr, Si,, and Al, the oxygen content of the sample was recalculated assuming these contaminates were ZrO_2, SiO_2, and $AlO_{1.5}$. Based on these data, the ratio of oxygen/carbon (O/C), nitrogen/carbon (N/C), and sulfur/carbon (S/C) were calculated. The first two indicate the presence of functional groups which contain oxygen or nitrogen. The S/C ratio indicates the existence of sulfuric acid, which was intercalated into the as-received graphite flakes.

Table 3.3 shows the XPS data while **Figure 3.1** shows the O/C, N/C, and S/C ratios. These data revealed that the diameter affects the functionality of graphite flakes while thickness does not. Calculations show that the edge area of flake materials increases significantly when the diameter becomes small, while it is affected very little by thickness of the flakes, (**Figure 3.2**) which supports these XPS results. Thus, it is concluded that the graphite flakes with smaller diameter could have more functional groups than those with larger diameters. Also the results revealed that these materials have no nitrogen or sulfur.

Curve fitting analysis of XPS data showed the functional groups, which exist on the surface of these samples. **Figure 3.3** shows the results. It revealed that the graphite flakes with smaller diameters have more hydroxyl and ether groups than those with larger diameters do, but the amount of carboxyl group was almost the same for all of these graphite flakes.

Table 3.3. XPS Data of Exfoliated Graphite Samples with no Surface Treatment

	C	O	N	S	Zr	Na	Si	Al	O*	O/C	N/C	S/C
Heat-exfoliated Gr.	96.87	3.13	0.00	0.00	0.00	0.00	0.00	0.00	3.13	0.0324	0.0000	0.0000
Heat and Milled Gr.	93.50	6.14	0.00	0.00	0.22	0.00	0.17	0.00	5.37	0.0575	0.0000	0.0000
MW-exfoliated Gr.	96.79	3.21	0.00	0.00	0.00	0.00	0.00	0.00	3.21	0.0332	0.0000	0.0000
MW and Milled Gr.	91.17	8.02	0.00	0.00	0.81	0.00	0.00	0.00	6.41	0.0703	0.0000	0.0000

O* is the adjusted oxygen value

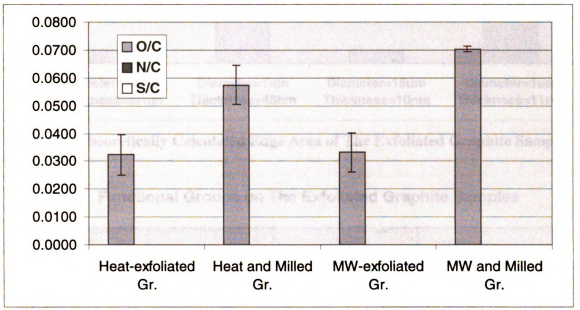

Figure 3.1. Surface Chemistry of The Exfoliated Graphite Samples

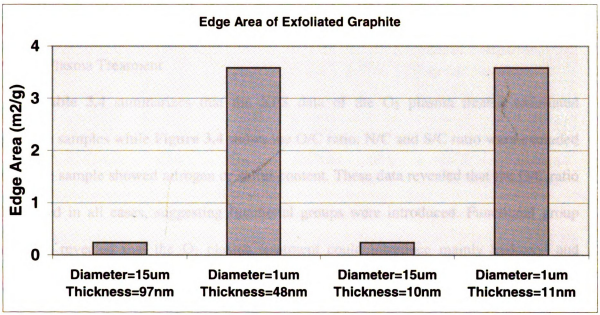

Figure 3.2. Theoretically Calculated Edge Area of The Exfoliated Graphite Samples

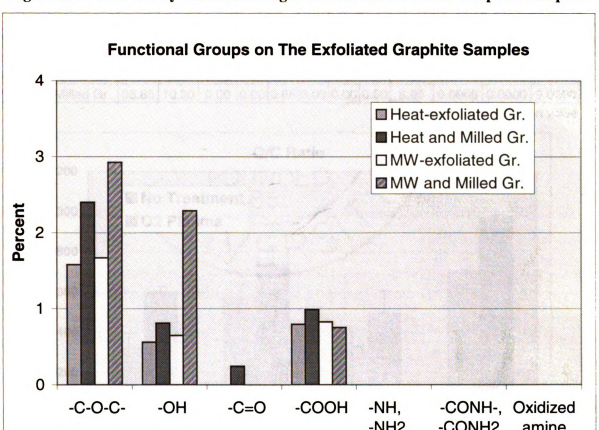

Figure 3.3. Functional Groups of the Exfoliated Graphite Flakes

3.3.2. The Effect of Various Surface Treatments on Surface Chemistry of Exfoliated Graphite Flakes

- O_2 Plasma Treatment

Table 3.4 summarizes that the XPS data of the O_2 plasma treated exfoliated graphite samples while **Figure 3.4** shows the O/C ratio. N/C and S/C ratio were excluded since no sample showed nitrogen or sulfur content. These data revealed that the O/C ratio increased in all cases, suggesting functional groups were introduced. Functional group analysis revealed that the O_2 plasma treatment could introduce mainly hydroxyl and carbonyl groups (**Figure 3.5**). The hydroxyl groups could improve surface condition.

Table 3.4. XPS Data of Exfoliated Graphite Samples after O_2 Plasma Treatment

	C	O	N	S	Zr	Na	Si	Al	O*	O/C	N/C	S/C
Heat-exfoliated Gr.	94.07	5.83	0.00	0.00	0.00	0.00	0.09	0.00	5.65	0.0601	0.0000	0.0000
Heat and Milled Gr.	91.36	8.05	0.00	0.00	0.25	0.00	0.40	0.00	6.75	0.0739	0.0000	0.0000
MW-exfoliated Gr.	94.73	5.07	0.00	0.00	0.00	0.00	0.20	0.00	4.67	0.0493	0.0000	0.0000
MW and Milled Gr.	88.85	10.30	0.00	0.00	0.85	0.00	0.00	0.00	8.60	0.0968	0.0000	0.0000

O* is the adjusted oxygen value

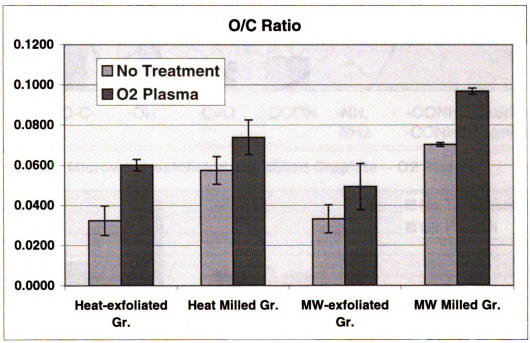

Figure 3.4. Surface Chemistry (O/C Ratio) of The Exfoliated Graphite Samples after O_2 Plasma Treatment

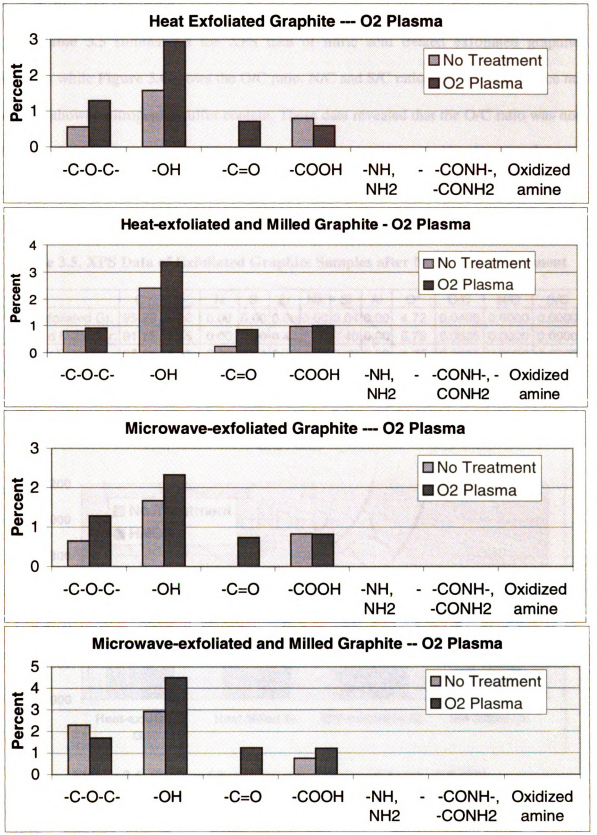

Figure 3.5. Functionality Analysis after O2 Plasma treatment

- Nitric Acid Treatment

Table 3.5 summarizes the XPS data of nitric acid treated exfoliated graphite samples while **Figure 3.6** shows the O/C ratio. N/C and S/C ratio were excluded since no sample showed nitrogen or sulfur content. These data revealed that the O/C ratio was not increased as much as it was in the case of the O_2 Plasma treatment. Also functional group analysis showed little increase in functionality (**Figure 3.7**). Thus, it is concluded that the nitric acid treatment was not as effective as O_2 plasma treatment.

Table 3.5. XPS Data of Exfoliated Graphite Samples after Nitric Acid Treatment

	C	O	N	S	Zr	Na	Si	Al	O*	O/C	N/C	S/C
Heat-exfoliated Gr.	95.22	4.80	0.00	0.00	0.00	0.00	0.04	0.00	4.72	0.0496	0.0000	0.0000
Heat and Milled Gr.	91.73	7.45	0.00	0.00	0.43	0.00	0.40	0.00	5.79	0.0635	0.0000	0.0000
MW-exfoliated Gr.	95.65	4.35	0.00	0.00	0.00	0.00	0.00	0.00	4.35	0.0455	0.0000	0.0000
MW and Milled Gr.	92.38	6.78	0.00	0.00	0.25	0.00	0.00	0.00	6.28	0.0680	0.0000	0.0000

O* is the adjusted oxygen value

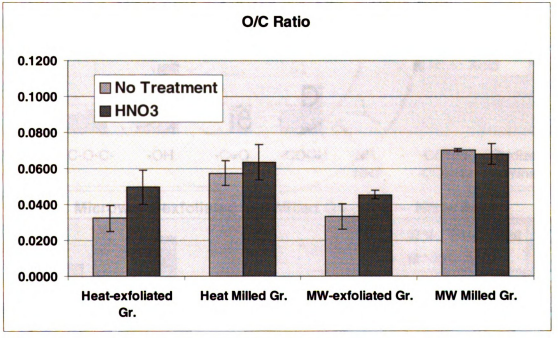

Figure 3.6. Surface Chemistry (O/C Ratio) of The Exfoliated Graphite Samples after Nitric Acid Treatment

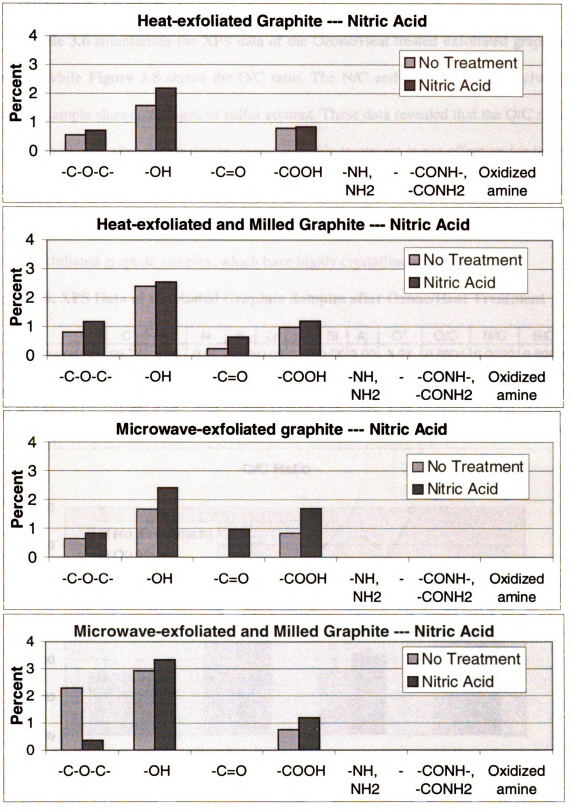

Figure 3.7. Functionality Analysis after Nitric Acid Treatment

- Ozone/Heat Treatment

Table 3.6 summarizes the XPS data of the Ozone/Heat treated exfoliated graphite samples while **Figure 3.8** shows the O/C ratio. The N/C and S/C ratio were excluded since no sample showed nitrogen or sulfur content. These data revealed that the O/C ratio was not increased after the treatment, suggesting this treatment is not effective for these graphite materials. Functionality analysis supported this conclusion (**Figure 3.9**). It is considered that this treatment is effective for amorphous regions of graphite samples, but not for exfoliated graphite samples, which have highly crystalline structures.

Table 3.6. XPS Data of Exfoliated Graphite Samples after Ozone/Heat Treatment

	C	O	N	S	Zr	Na	Si	Al	O*	O/C	N/C	S/C
Heat-exfoliated Gr.	96.77	3.24	0.00	0.00	0.00	0.00	0.00	0.00	3.24	0.0334	0.0000	0.0000
Heat and Milled Gr.	94.48	5.38	0.00	0.00	0.15	0.00	0.00	0.00	5.08	0.0538	0.0000	0.0000
MW-exfoliated Gr.	95.30	4.50	0.00	0.00	0.00	0.00	0.20	0.00	4.10	0.0430	0.0000	0.0000
MW and Milled Gr.	94.92	4.96	0.00	0.00	0.11	0.00	0.00	0.00	4.74	0.0499	0.0000	0.0000

O* is the adjusted oxygen value

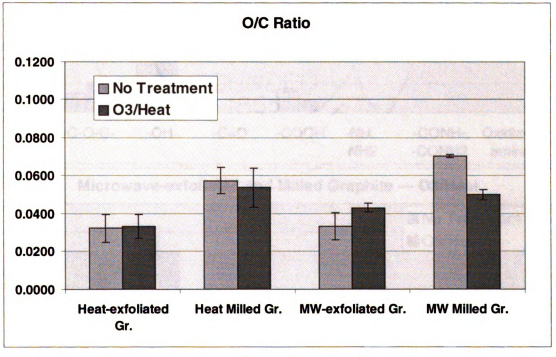

Figure 3.8. Surface Chemistry (O/C Ratio) of The Exfoliated Graphite Samples after Ozone/Heat Treatment

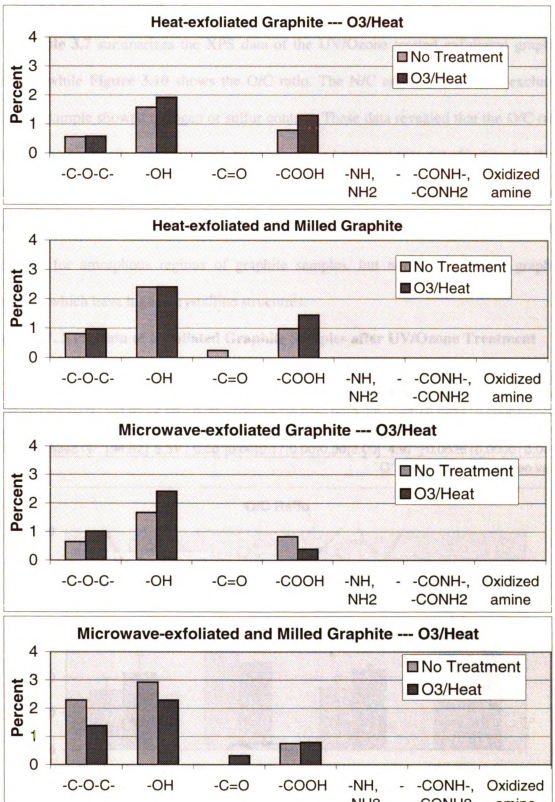

Figure 3.9. Functionality Analysis after Ozone/Heat Treatment

- UV/Ozone Treatment

Table 3.7 summarizes the XPS data of the UV/Ozone treated exfoliated graphite samples while **Figure 3.10** shows the O/C ratio. The N/C and S/C ratio was excluded since no sample showed nitrogen or sulfur content. These data revealed that the O/C ratio was not increased after the treatment, suggesting this treatment was not effective for these graphite materials. Functionality analysis showed this process could introduce carboxyl groups, but not significantly (**Figure 3.11**). It is considered that this treatment is also effective for amorphous regions of graphite samples, but not for exfoliated graphite samples, which have highly crystalline structures.

Table 3.7. XPS Data of Exfoliated Graphite Samples after UV/Ozone Treatment

	C	O	N	S	Zr	Na	Si	Al	O*	O/C	N/C	S/C
Heat-exfoliated Gr.	95.94	4.06	0.00	0.00	0.00	0.00	0.00	0.00	4.06	0.0423	0.0000	0.0000
Heat and Milled Gr.	94.93	4.90	0.00	0.00	0.17	0.00	0.00	0.00	4.56	0.0481	0.0000	0.0000
MW-exfoliated Gr.	95.79	4.21	0.00	0.00	0.00	0.00	0.00	0.00	4.21	0.0440	0.0000	0.0000
MW and Milled Gr.	94.52	5.31	0.00	0.00	0.17	0.00	0.00	0.00	4.97	0.0526	0.0000	0.0000

O* is the adjusted oxygen value

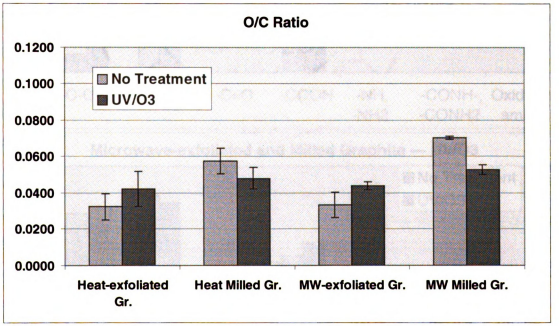

Figure 3.10. Surface Chemistry (O/C Ratio) of The Exfoliated Graphite Samples after UV/Ozone Treatment

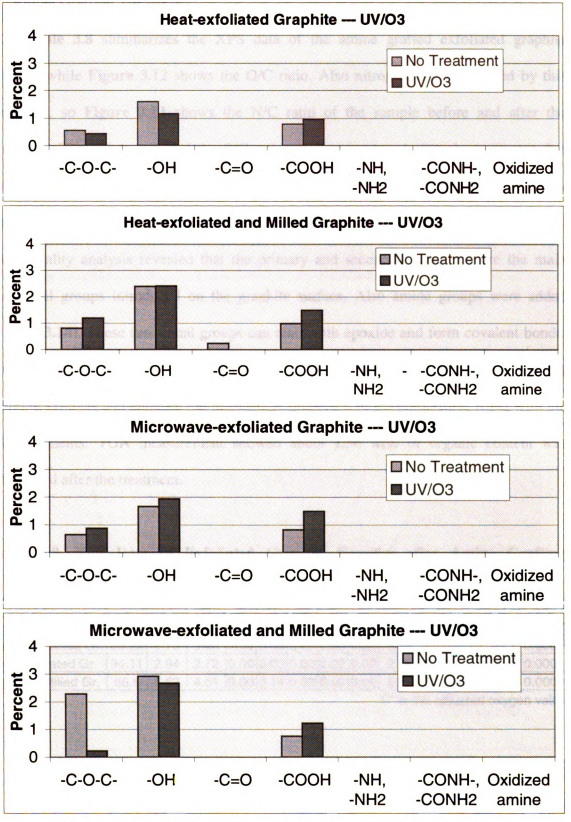

Figure 3.11. Functionality Analysis after UV/Ozone Treatment

- Amine Grafting Treatment

Table 3.8 summarizes the XPS data of the amine grafted exfoliated graphite samples while **Figure 3.12** shows the O/C ratio. Also nitrogen was introduced by this treatment, so **Figure 3.13** shows the N/C ratio of the sample before and after the treatment. These data revealed the O/C ratio was not increased after the treatment, but nitrogen were introduced and N/C ratio was increased significantly, suggesting many functional groups that include nitrogen were attached to the surface of the sample. Functionality analysis revealed that the primary and secondary amines were the main functional groups introduced on the graphite surface. Also amide groups were added (**Figure 3.14**). These functional groups can react with epoxide and form covalent bonds. Thus, amine grafting treatment could improve the surface condition of the exfoliated graphite samples and enhance the mechanical properties of the composites filled with the reinforcements. TGA measurement showed about 1.56 wt% of organic content was introduced after the treatment.

Table 3.8. XPS Data of Exfoliated Graphite Samples after Amine Grafting Treatment

	C	O	N	S	Zr	Na	Si	Al	O*	O/C	N/C	S/C
Heat-exfoliated Gr.	94.65	2.89	2.05	0.00	0.00	0.00	0.42	0.00	2.05	0.0217	0.0217	0.0000
Heat and Milled Gr.	89.23	6.79	3.33	0.00	0.66	0.00	0.00	0.00	5.48	0.0615	0.0373	0.0000
MW-exfoliated Gr.	94.11	2.94	2.72	0.00	0.00	0.00	0.22	0.00	2.50	0.0266	0.0289	0.0000
MW and Milled Gr.	86.6	5.62	4.61	0.00	0.14	0.00	0.00	0.00	5.34	0.0616	0.0532	0.0000

O* is the adjusted oxygen value

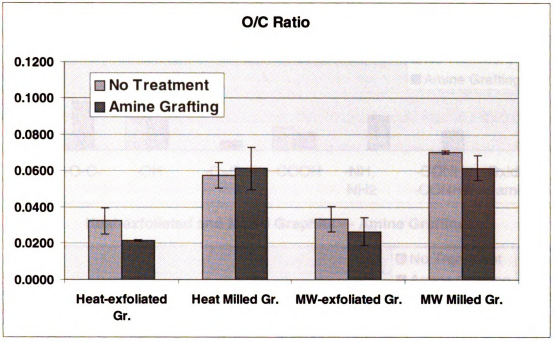

Figure 3.12. Surface Chemistry (O/C Ratio) of The Exfoliated Graphite Samples after Amine Grafting Treatment

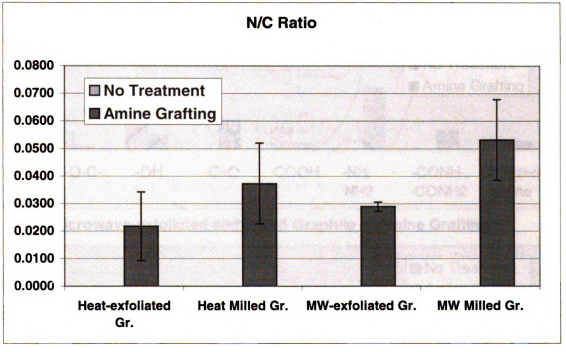

Figure 3.13. Surface Chemistry (N/C Ratio) of The Exfoliated Graphite Samples after Amine Grafting Treatment

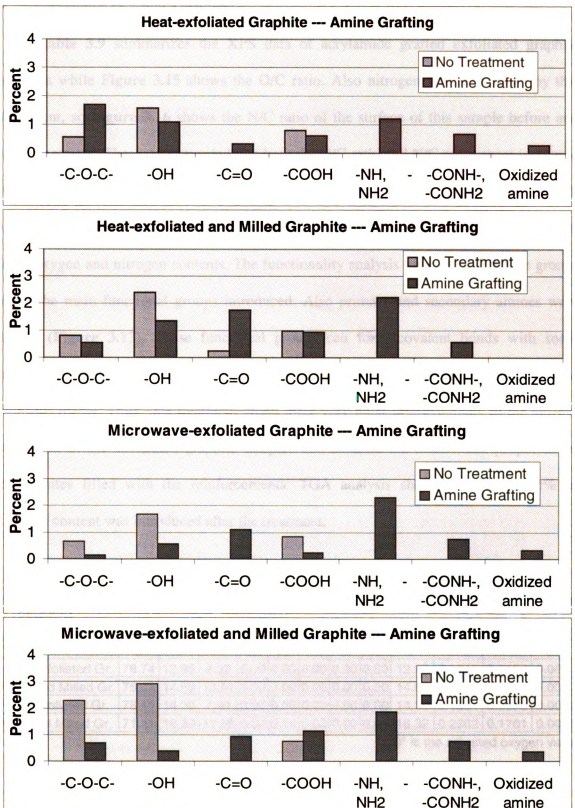

Figure 3.14. Functionality Analysis after Amine Grafting Treatment

- Acrylamide Grafting Treatment

Table 3.9 summarizes the XPS data of acrylamide grafted exfoliated graphite samples while **Figure 3.15** shows the O/C ratio. Also nitrogen was introduced by this treatment, so **Figure 3.16** shows the N/C ratio of the surface of this sample before and after treatment. These data revealed that both the O/C ratio and N/C ratios were increased significantly, suggesting many functional groups that include oxygen, nitrogen, or both were introduced. In fact, acrylamide grafting treatment showed the biggest increase in both oxygen and nitrogen contents. The functionality analysis revealed that amide groups were the main functional groups introduced. Also primary and secondary amines were added (**Figure 3.17**). These functional groups can form covalent bonds with some polymers, including epoxies, and improve adhesion between the matrix and reinforcements. Thus, this treatment could offer very good improvements to the surface condition of the exfoliated graphite samples and enhance the mechanical properties of composites filled with the reinforcements. TGA analysis showed about 34 wt% of organic content was introduced after the treatment.

Table 3.9. XPS Data of Exfoliated Graphite Samples after Acrylamide Grafting Treatment

	C	O	N	S	Zr	Na	Si	Al	O*	O/C	N/C	S/C
Heat-exfoliated Gr.	78.74	12.95	8.32	0.00	0.00	0.00	0.00	0.00	12.95	0.1645	0.1057	0.0000
Heat and Milled Gr.	75.31	14.69	10.01	0.00	0.00	0.00	0.00	0.00	14.69	0.1950	0.1329	0.0000
MW-exfoliated Gr.	78.11	14.30	7.60	0.00	0.00	0.00	0.00	0.00	14.30	0.1831	0.0972	0.0000
MW and Milled Gr.	71.41	16.59	11.86	0.00	0.14	0.00	0.00	0.00	16.32	0.2302	0.1701	0.0000

O* is the adjusted oxygen value

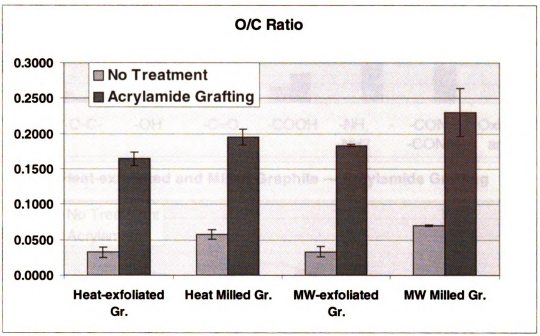

Figure 3.15. Surface Chemistry (O/C Ratio) of The Exfoliated Graphite Samples after Acrylamide Grafting Treatment

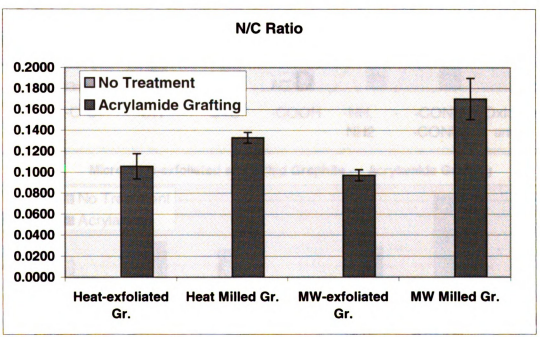

Figure 3.16. Surface Chemistry (N/C Ratio) of The Exfoliated Graphite Samples after Acrylamide Grafting Treatment

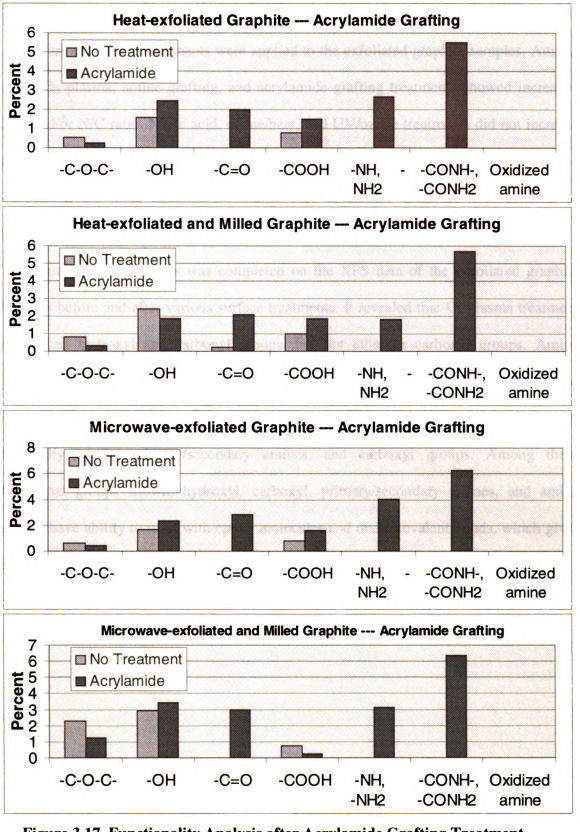

Figure 3.17. Functionality Analysis after Acrylamide Grafting Treatment

3.4. Conclusions

Various surface treatments were applied to the exfoliated graphite samples. Among these, O_2 plasma, amine grafting, and acrylamide grafting treatments showed increased O/C and/or N/C ratio. Nitric acid, ozone/heat, and UV/ozone treatments did not increase these atomic contents and were considered to be less effective methods to treat these samples. Since these samples are highly pure crystalline graphite, it is difficult to improve functionality by some surface treatments used for conventional carbon fibers.

Curve fitting analysis was completed on the XPS data of the exfoliated graphite samples before and after various surface treatments. It revealed that O_2 plasma treatment introduced hydroxyl and carbonyl groups, but not ether or carboxyl groups. Amine grafting treatment introduced primary amine, secondary amine, amide bond, and oxidized amine groups. Acrylamide grafting introduced a large number of functional groups, especially amide, primary/secondary amines, and carboxyl groups. Among these functional groups shown, hydroxyl, carboxyl, primary/secondary amines, and amide groups have ability to react with epoxy molecules and make covalent bonds, which gives good interaction between graphite flakes and epoxy matrix.

3.5. Reference

1. Pittman, Jr., C. U., He, G-R., Wu, B., and Gardner, S. D., "Chemical Modification of Carbon Fiber Surfaces by Nitric Acid Oxidation followed by Reaction with Tetraethylenepentamine." Carbon, ***35***, (3), 317 (1997).

2. Pittman, Jr., C. U., Wu, Z., Jiang, W., He, G-R., Wu, B., Li, W., and Gardner, S. D., "Reactions of Amine Functions Grafted to Carbon Fiber Surfaces by Tetraethylenepentamine. Designing Interfacial Bonding.", Carbon, ***35***, (7), 929 (1997).

3. Yamada, K, Haraguchi, T., and Kajiyama, T., "Plasma-Graft Polymerization of Vinyl Monomer with an Acid Amide Group onto a Surface of Carbon Fiber and Its Adhesion to Epoxy Resin.", J. Appl. Polym. Sci., ***75***, 284 (2000).

4. Proctor, A., and Sherwood, P. M. A., "X-Ray Photoelectron Spectroscopic Studies f Carbon Fiber Surfaces.1. Carbon Fiber Spectra and The Effects of Heat Treatment." J. Electron Spectrosc. Relate. Phenom.,, ***27***, 39 (1982).

5. Xie, Y., and Sherwood, P. M. A., "X-ray Photoelectron Spectroscopic Studies of Carbon Fiber Surfaces.9. The Effect of Microwave Plasma Treatment on Carbon Fiber Surfaces." Appl. Spectrosc., 43, 7, 1153 (1989).

6. Sherwood, P. M. A., "In Practical Surface Analysis by Auger an X-Ray Photoelectron Spectroscopy, 2nd Edition.", Briggs and M. P. Seah editors, Wiley & Sons., (1990).

7. Xie, Y., and Sherwood, P. M. A., "X-Ray Photoelectron Spectroscopic Studies of Carbon Fiber Surfaces.12. The Effect of Microwave Plasma Treatment on Pitch-Based Carbon Fiber Surfaces." Appl. Spectrosc., 44, 797 (1990).

CHAPTER 4

FABRICATION AND PROPERTIES

OF

GRAPHITE NANOCOMPOSITES

4.1. Introduction

Nanocomposites composed of polymer matrices with reinforcements less than 100 nm in size, are being considered for applications such as interior and exterior accessories for automobiles, structural components for portable electronic devices, and films for food packaging. [1, 2] While most nanocomposite research has focused on exfoliated clay platelets, the same nanoreinforcement concept can be applied to another layered material, graphite, to produce nanoplatelets and nanocomposites [3, 4, 5, 6, 7, 8, 9]. Graphite is the stiffest material found in nature (Young's Modulus = 1060 GPa), having a modulus several times that of clay, but also with excellent electrical and thermal conductivities. The key to utilizing graphite as a platelet nanoreinforcement is in the ability to exfoliate this material. Also, if the appropriate surface treatment can be found for the graphite, its exfoliation and dispersion in a polymer matrix will result in a composite with not only excellent mechanical properties but electrical properties as well. This will open up many new structural applications as well as non-structural ones where electromagnetic shielding and high thermal conductivity are requirements. In addition, the graphite nanoplatelets are ~500 times less expensive than carbon nanotubes.

In this research, a special thermal treatment was applied to the graphite flakes to produce exfoliated graphite reinforcements. The composite material was fabricated by combining the exfoliated graphite flakes with an amine-epoxy resin. X-ray Diffraction (XRD) and Transmission Electron Microscopy (TEM) were used to assess the degree of exfoliation of the graphite platelets. The mechanical properties of these composites were investigated by flexural testing. The glass transition temperature (Tg) of composite samples was determined by Differential Mechanical Analysis (DMA). The coefficient of

thermal expansion was examined by Thermal Mechanical Analysis (TMA). The electrical conductivity was investigated by impedance measurements using the 2-probe method. Thermal conductivity was measured by using the DSC method. [10, 11]. The dielectric properties of nanocomposites were also investigated.

4.2. Experiment

4.2.1. Materials

Four exfoliated graphite samples and three commercially available carbon materials were used as reinforcements. The detailed characterization of the four exfoliated graphite materials are listed in **Table 4.1**.

Table 4.1. The Exfoliated Graphite Samples

	Average Diameter, d (um)	Average Thickness, t (nm)	Aspect Ratio	Surface Area (m^2/g)	Density (g/cm^2)
Heat-exfoliated Graphite	15	97	d/t=153 t/d=0.00654	10.5	2.0
Heat-exfoliated and milled graphite	1.1	48	d/t=22.8 t/d=0.0439	24	2.0
Microwave-exfoliated Graphite	15	10	d/t=1571 t/d=0.000637	105	2.0
Microwave-exfoliated and milled Graphite	0.86	11	d/t=77.26 t/d=0.0129	94	2.0

The control carbon materials were 1) PAN based carbon fiber (PANEX 33 MC Milled Carbon Fibers, Zoltek Co.), 2) Vapor Grown Carbon Fiber or VGCF (Pyrograf™ III, PR-19 PS grade, Pyrograf Products, Inc.), and 3) nanosize carbon black (KETJENBLACK EC-600 JD, Akzo Novel Polymer Chemicals LLC). **Table 4.2** summarizes the characterization of these materials and **Figure 4.1** shows the ESEM images of these materials.

Table 4.2. The Commercially Available Carbon Materials

	Average Length (um)	Average Diameter (nm)	Aspect Ratio	Surface Area (m^2/g)	Density (g/cm^2)
CF	175	7200	24.3	16	1.81
VGCF	50-100	150	333-666	25	2.0
Carbon Black		10-30	1	1400	1.8

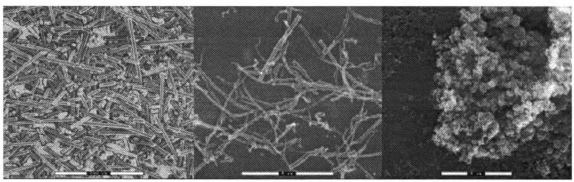

A: PAN based Carbon Fiber (Scale bar = 200 um)

B: VGCF (Scale bar = 200 um)

C: Carbon Black (Scale bar = 5 um)

Figure 4.1. SEM images of PAN based carbon fiber (A), VGCF (B), and carbon black (C).

4.2.2. Composite Fabrication

Epoxy was used as the matrix material. Diglycidyl ether of bisphenol A (Epon 828) was purchased from the Shell Chemical Co. Jeffamine T403 from Huntsman Petrochemical was used as the curing agent for this matrix system. The chemical structures of these materials are shown in **Figure 4.2**. The stoichimetry of these chemicals is 100 (DGEBA) to 45 (T403) by weight. The calculated amount of reinforcements were added to DGEBA and mixed with the aid of an ultrasonic homogenizer for 5 to 10 minutes. Then stoichiometric amount of Jeffamine T403 were

added and mixed at room temperature. To avoid voids, thorough outgassing process was applied before curing. The system was cured at 85°C for 2 hours, followed by post curing at 150°C for 2 hours. The density of graphite flakes was assumed as 2.0 g/cm^3. The densities of other carbon materials were obtained from manufactures. The density of the epoxy matrix was measured as 1.159 g/cm^3. Using these values, the volume fraction of carbon materials in composite samples was calculated.

A. Epon 828

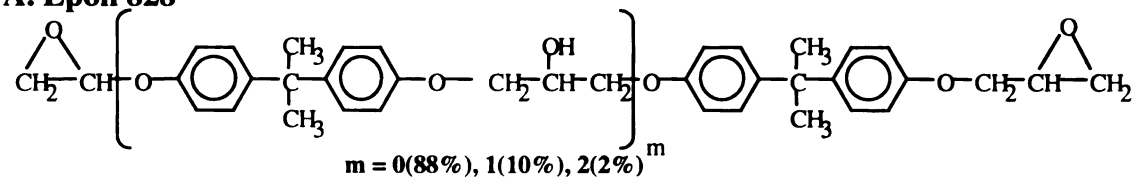

Epoxide Equivalent Weight 185-192

B. Jeffermine T403

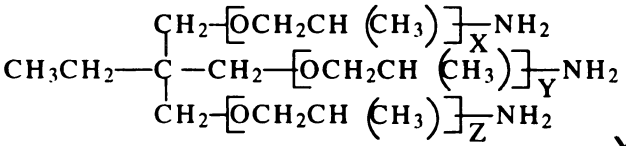

X+Y+Z=5.3

Figure 4.2 Chemical structure of Diglycidyl ether of bisphenol A (A, Epon 828, Shell Chemical Co.) and Jeffamine T403 (B, Huntsman Petrochemical Co.)

4.2.3. Analysis

- Flexural Test

The flexural test was performed on a UTS testing machine [United Calibration Corp.] at room temperature by following ASTM D790 standard test method. The samples were made in a standard bar shape and polished carefully so that the thickness of the samples was constant through out the samples. The final dimension of the bar samples was 60 x 12.5 x 3 mm. The test was performed at flexural rate of 0.05 inches per minute.

- Tensile Test

The tensile test was performed on a UTS machine [United Calibration Corp.] at room temperature by following ASTM D638 standard test method. The samples were made in a standard dog-bone shape and polished carefully so that the dimension was constant through out the samples. The test was performed at an elongation rate of 0.05 inches per minute.

- Dynamic Mechanical Analysis [DMA]

DMA data for each sample was measured by DMA 2980 [TA Instrumrnt] using a single cantilever mode. The size of each sample was about 30 x 12.5 x 1.5 mm. The temperature range was from 30 to 150°C and the ramp rate was 2°C per minute. The frequency and amplitude were set to 1Hz and 100um respectively so that the force applied to the sample was more than 1N, which assures a stable measurement. Since 1 % error in dimension causes about 3 % error in storage modulus data, each sample was carefully polished and confirmed that the error margin in dimension was less than 1%.

- Thermomechanical Analysis (TMA)

The coefficient of thermal expansion (CTE) was measured by TMA 2940 (TA Instrument). The samples were cut into small pieces, approximately 10 x 5 x 5 mm, and the dimension change was measured during the heating process. The temperature range was from 30 to 200 °C and ramp rate was 2°C per minute.

- Resistivity Measurement

The resistivity of composite samples was measured in Impedance Spectroscopy by applying two-probe method at room temperature. The size of each sample was about 30 x 12.5 x 8.0 mm. Since sample dimension and surface condition greatly affect the data,

polishing process was applied with extreme care. After polishing, O_2 plasma was applied on the sample to etch polymers on the surface region. After the process, gold coating with about 20nm thickness was applied. During the process, sidewalls of each sample were masked so that no conductive connections between the top and bottom planes occured through gold coatings. Then, copper tape was attached to the top and bottom surfaces of the sample and connected to the instrument. The resistance of sample was measured in frequency range of 0.1 to 100,000Hz. Then the data was recalculated to resistivity by incorporating dimension factors. The resistivity at 0.1Hz was considered as the AC resistivity since the difference should be very small.

4.3. Results and Discussion

4.3.1. The Effect of Size of Exfoliated Graphite flakes on Flexural Properties

Composite samples with four different exfoliated graphite flakes were fabricated and the flexural properties of these composites were investigated. **Figure 4.3** shows the XPS data of these exfoliated graphite flakes. The flexural and tensile properties of each sample were measured and summarized in **Figure 4.4** and **4.5**. It revealed that flexural and tensile results showed the same tendency, which is that the composites filled with smaller graphite flakes showed better strength, implying those have better interactions with the matrix. These results agree with the fact that smaller graphite flakes have larger edge area and higher functionalities than larger graphite flakes. The modulus data was not affected by the size of graphite flakes. In theories, composites filled with fillers with larger aspect ratio should show higher modulus. But also adhesion condition between

fillers and matrix affect the efficiency of stress transfer in the matrix system. These factors may compensate and resulted almost the same modulus values in this case.

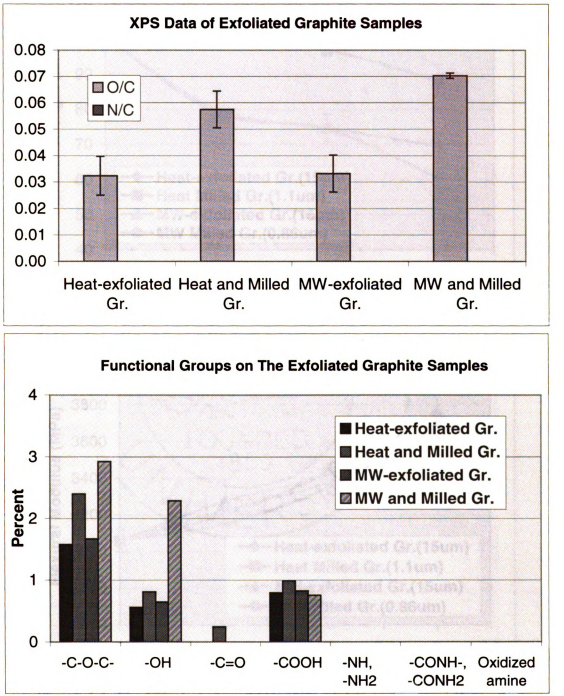

Figure 4.3. Surface Chemistry of The Exfoliated Graphite Samples

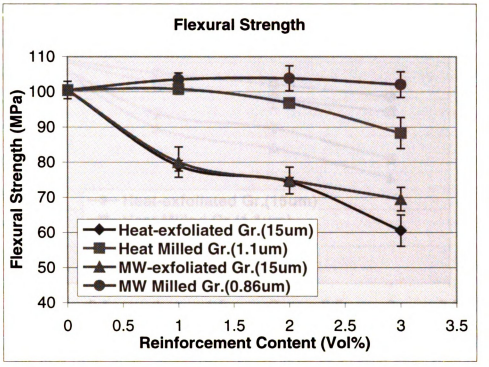

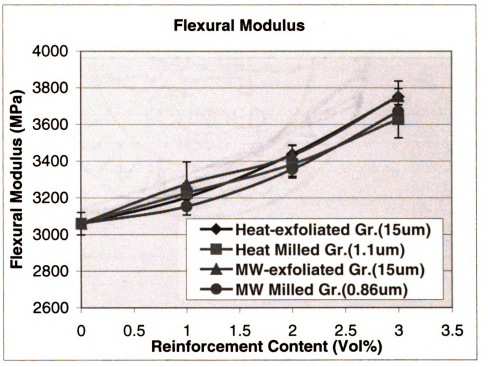

Figure 4.4. The Effect of Size of Graphite Flakes on Flexural Properties (MW: microwave-exfoliated)

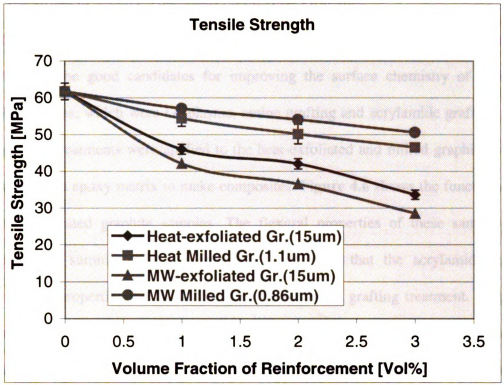

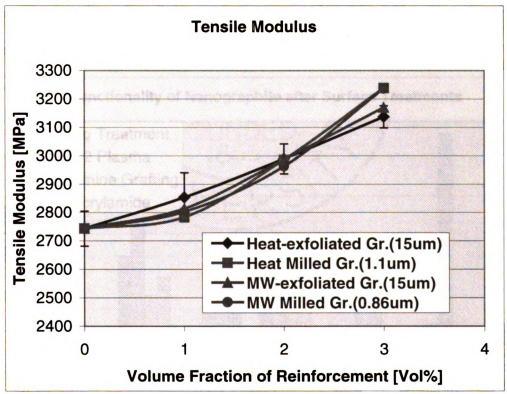

Figure 4.5. The Effect of Size of Graphite Flakes on Tensile properties

4.3.2. The Effect of Surface Treatments on Flexural Properties

In Chapter 3, various surface treatments were examined and three of them were considered to be good candidates for improving the surface chemistry of exfoliated graphite samples, which were O_2 plasma, amine grafting and acrylamide grafting. These three surface treatments were applied to the heat-exfoliated and milled graphite samples and mixed with epoxy matrix to make composites. **Figure 4.6** shows the functionality of the surface treated graphite samples. The flexural properties of these samples were measured and summarized in **Figure 4.7**. It revealed that the acrylamide grafting improved the properties the most, followed by the amine grafting treatment. O_2 plasma treatment did not improve the mechanical properties. These results suggest chemical interactions between amine functional groups on graphite and epoxy matrix, physical, and mechanical interactions between grafted polymers/oligomers and matrix polymer play roles to enhance the flexural properties of the resulted composite samples.

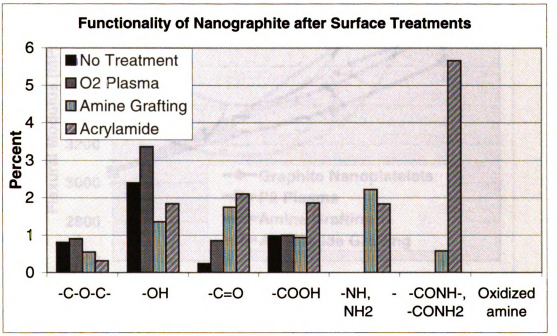

Figure 4.6. Surface Chemistry of Exfoliated Graphite after Various Surface Treatments

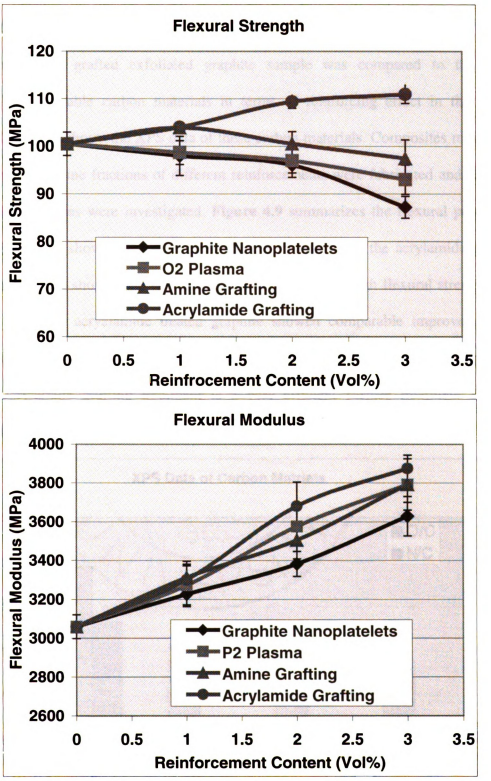

Figure 4.7. The Effect of Surface Treatments on Flexural Properties

4.3.3. The Comparison of Exfoliated Graphite Flakes and Commercially Available Carbon Materials

Acrylamide grafted exfoliated graphite sample was compared to the three commercially available carbon materials in terms of reinforcing effect in the epoxy matrix. **Figure 4.8** shows the XPS data of these carbon materials. Composites reinforced with the same volume fractions of different reinforcements were fabricated and flexural and tensile properties were investigated. **Figure 4.9** summarizes the flexural properties while **Figure 4.10** shows the tensile properties. It revealed that the acrylamide grafted graphite nanoflakes showed the best improvement in terms of both flexural strength and modulus. Also the acryalamide treated graphite showed comparable improvement in tensile properties over commercially available carbon fiber samples. These results proved that the acrylamide grafting treatment is a very efficient surface treatment for the exfoliated graphite samples.

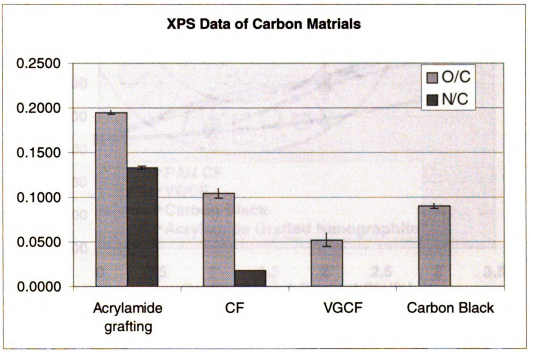

Figure 4.8. Surface Chemistry of Various Carbon Materials

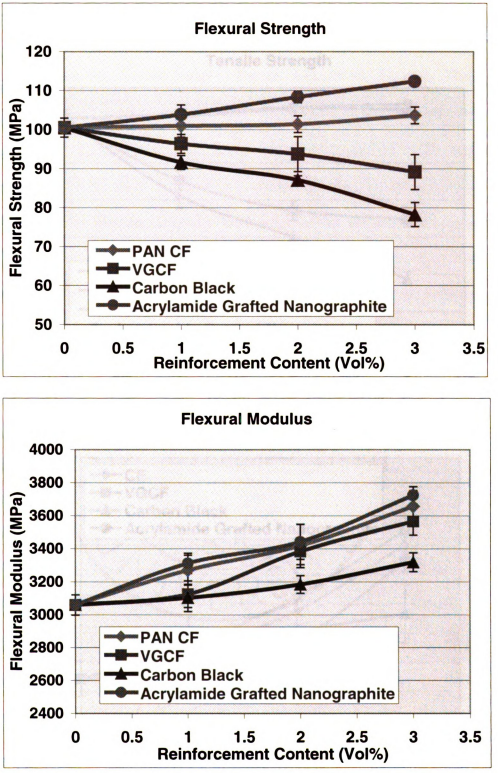

Figure 4.9. Comparison of Exfoliated Graphite Flakes to Commercially Available Carbon Materials (1) Flexural Properties

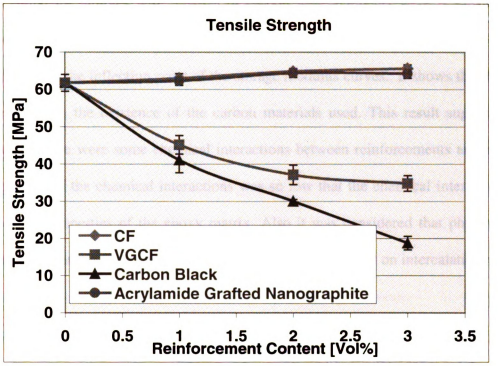

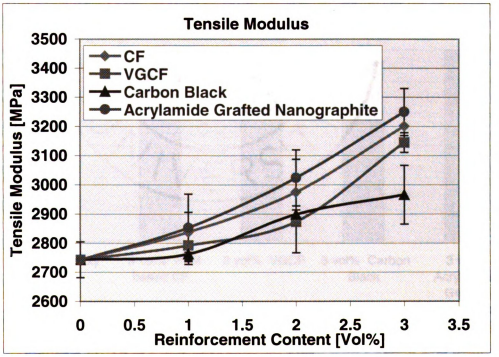

Figure 4.10. Comparison of Exfoliated Graphite Flakes to Commercially Available Carbon Materials (2) Tensile properties

4.3.4. Dynamic Mechanical Analysis (DMA)

Composite samples with 3 vol% of carbon reinforcements were fabricated and used to determine Tg of each sample. **Figure 4.11** shows Tg data. The Tg was determined from the inflection point of the storage modulus curves. It shows that Tg was not affected with the existence of the carbon materials used. This result suggests that even though there were some chemical interactions between reinforcements and matrix, the proportion of the chemical interactions was so low that the chemical interaction did not affect the properties of the epoxy matrix. Also it was considered that physical and mechanical interactions between matrix and reinforcements based on intercalation did not occur.

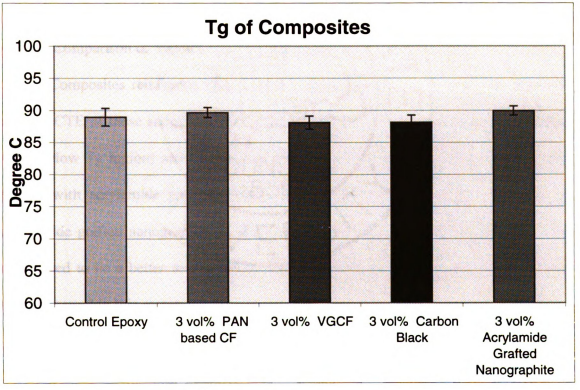

Figure 4.11. Tg of Composite Samples Filled with Carbon Materials

4.3.5. Thermomechanical Analysis (TMA)

4.3.5.1. The Effect of Surface Treatments on CTE

Composites reinforced with 3 vol% of nanographite flakes with O_2 plasma, amine grafting, or acrylamide grafting treatments were fabricated. Control epoxy samples were also made. CTE of these samples were measured and the data are summarized in **Figure 4.12** (below Tg region) and **Figure 4.13** (above Tg region). In the case of CTE below Tg region, nanographite with better surface treatments showed lower CTE, implying better dimension stability. Nanographite treated with acrylamide grafting showed about 23% lower value than the control epoxy. Surface treatments did not affect on the CTE above Tg region, but each composite sample showed about 7% improvement.

4.3.5.2. Comparison of Various Carbon Materials

Composites reinforced with 3 vol% of various carbon materials were fabricated and the CTE of these samples were measured. The CTE data are summarized in **Figure 4.14** (below Tg region) and **Figure 4.15** (above Tg region). In both cases nanographite treated with acrylamide grafting showed the lowest CTE. Thus, it is concluded that acrylamide grafted nanographite sample had better interactions with the matrix and was considered to be a better reinforcement compared to the commercially available carbon materials used in this research.

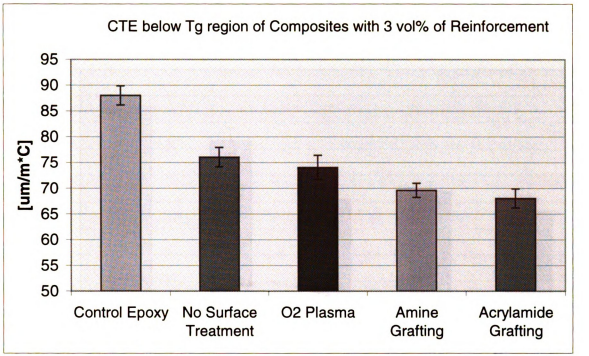

Figure 4.12. CTE (below Tg) of Composite Samples Filled with Nanographite with different Surface Treatments

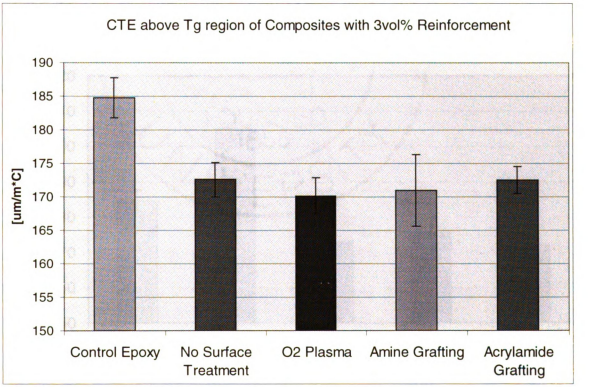

Figure 4.13. CTE of (above Tg) Composite Samples Filled with Nanographite with different Surface Treatments

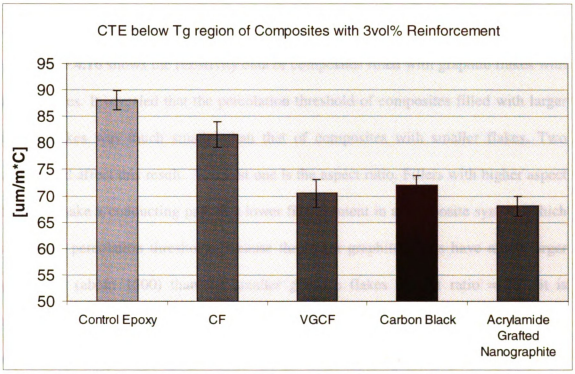

Figure 4.14. CTE (below Tg) of Composite Samples Filled with Various Carbon Materials

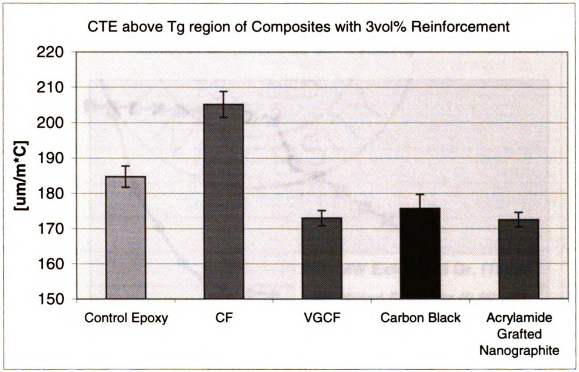

Figure 4.15. CTE (above Tg) of Composite Samples Filled with Various Carbon Materials

4.3.6. Electrical Properties

4.3.6.1. Effect of Graphite Flake Size

Figure 4.16 shows the resistivity data of composites filled with graphite flakes with different sizes. It revealed that the percolation threshold of composites filled with larger graphite flakes was much smaller than that of composites with smaller flakes. Two factors could affect this result. The first one is the aspect ratio. Fillers with higher aspect ratios can make a conducting path at a lower filler content in a composite system, which leads lower percolation threshold. Because the larger graphite flakes have much larger aspect ratio (about 1500) than the smaller graphite flakes (aspect ratio = 78), it is reasonable that the larger graphite flakes showed a lower percolation threshold. Also dispersion condition of fillers in the matrix affects the percolation data. Judging from the surface analysis and mechanical properties data, smaller graphite flakes have better surface condition and thus, a better dispersion condition in the epoxy matrix.

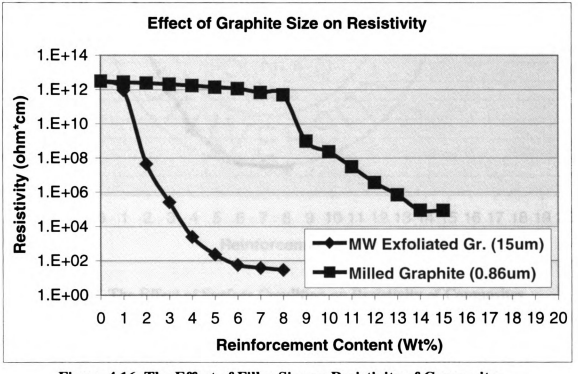

Figure 4.16. The Effect of Filler Size on Resistivity of Composites

4.3.6.2. Effect of Surface Condition of Graphite Flakes

Figure 4.17 shows the resistivity data of composites filled with graphite flakes with or without acrylamide grafting treatment. It revealed that the percolation threshold of composites filled with graphite flakes with no surface treatment was much smaller than that of composites with acrylamide grafted flakes. It is known that the dispersion condition of fillers in the matrix affect the percolation data significantly. The acrylamide grafting treatment has proved to be a very good surface treatment. Thus, these flakes are more likely to be separated into individual fakes rather than being aggregated and make up agglomerates. In such a condition, it is difficult to make a conductive path through out the composite system.

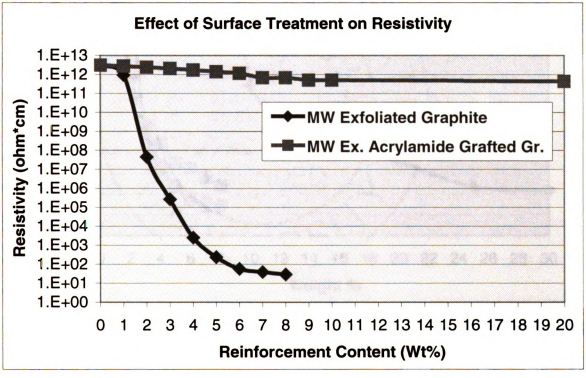

Figure 4.17. The Effect of Surface Condition on Resistivity of Composites

4.3.6.3 Comparison of Various Carbon Materials

Figure 4.18 shows the resistivity data of composites filled with various carbon materials. It revealed that the composites filled with exfoliated graphite flakes showed the same level of the percolation threshold and resistivity of the composites filled with carbon black or VGCF. These results showed that the exfoliated graphite flakes were as effective as other commercially available carbon materials as conductive fillers. The cost of these exfoliated graphite flakes were estimated about $5/lb or less, which was cheaper than $12/lb carbon black or $40-50/lb VGCF.

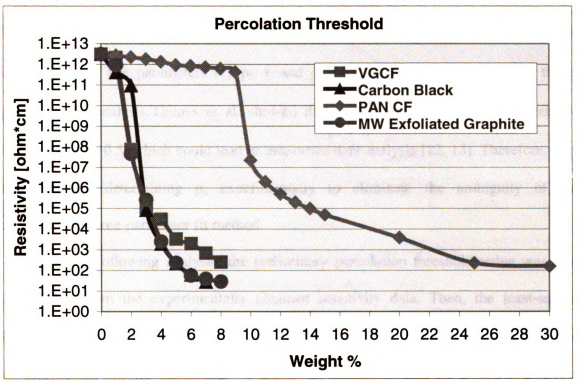

Figure 4.18. Resistivity of Composite Samples Filled with Various Carbon Materials

4.3.6.4 Percolation Theories

According to the percolation theory, the effective resistivity can be written as;

$$\rho_{eff} = \rho_0 (p - p_c)^{-t} \qquad \text{for } p > p_c \tag{4-1}$$

where ρ_{eff} is the effective resitivity of composite, ρ_0 is the resistivity of conductive phase, p is the volume fraction of conductive phase, p_c is the percolation threshold, and t is the conductivity exponent. Equation (4-1) can be rewritten as;

$$\log\left[\frac{\rho_{eff}}{\rho_0}\right] = -t \bullet \log[p - p_c] \qquad \text{for } p > p_c \tag{4-2}$$

Thus, t can be experimentally available by the least-square linear fit of $\log[\rho_{eff} / \rho_0]$ vs $\log[p-p_c]$ data. The parameters are p_c, t, and ρ_0 and this analysis is called the three-parameter fit analysis. Gaines et al. showed that the change of p_c by 0.5% produced changes in t by 0.5, which could lead to inaccurate data analysis [12, 13]. Therefore, they recommended determining p_c experimentally to eliminate the ambiguity of the conventional three-parameter fit method.

In the following analysis, the preliminary percolation threshold value was first determined from the experimentally obtained resistivity data. Then, the least-square linear fit of $\log[\rho_{eff} / \rho_0]$ vs $\log[p-p_c]$ data was performed to obtain t by changing ρ_0 and p_c. During the fitting, the change in the p_c value was limited up to 0.2% to avoid inaccurate analysis. Once t, ρ_0 and p_c were determined, these values were substituted into equation (4-1) and a theoretical resistivity curve was made and acompared to the experimental data.

- Microwave-exfoliated Graphite Flake

Table 4.3 shows the values of the percolation threshold, p_c, the resistivity of conductive phase, ρ_0, and the conductivity exponent, t. **Figure 4.19** shows the least-square linear fit of $\log[\rho_{eff} / \rho_0]$ vs $\log[p-p_c]$, and **Figure 4.20** shows the theoretically and experimentally obtained resistivity curves.

Table 4.3. Results of Three-parameter Fit Analysis for Microwave Exfoliated Graphite System

Reinforcement	pc (Vol%)	pc (Wt%)	ρ_0 (ohm*cm)	t
MW Exfoliated Gr.	1.13	1.93	0.001	3.12

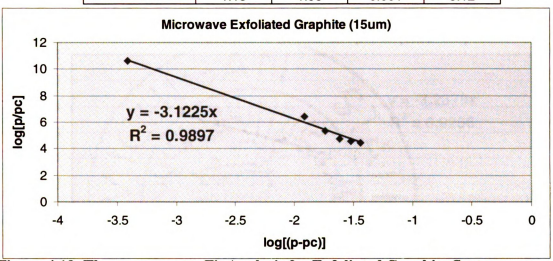

Figure 4.19. Three-parameter Fit Analysis for Exfoliated Graphite System

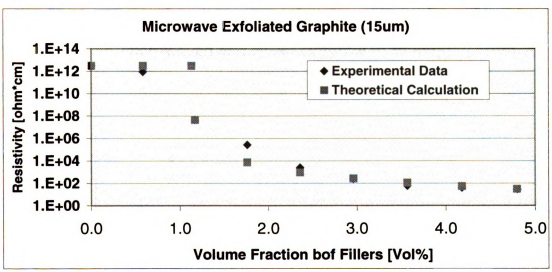

Figure 4.20. Theoretical and Experimentally Obtained Resistivity for Microwave Exfoliated Graphite Composites

- Microwave-exfoliated and Milled Graphite Flake

Table 4.4 shows the values of the percolation threshold, p_c, the resistivity of conductive phase, ρ_0, and the conductivity exponent, t. **Figure 4.21** shows the least-square linear fit of $\log[\rho_{eff} / \rho_0]$ vs $\log[p-p_c]$, and **Figure 4.22** shows the theoretically and experimentally obtained resistivity curves.

Table 4.4. Results of Three-parameter Fit Analysis for Microwave Exfoliated and Milled Graphite System

Reinforcement	pc (Vol%)	pc (Wt%)	ρ_0 (ohm*cm)	t
MW and Milled Gr.	4.9	8.17	15	3.24

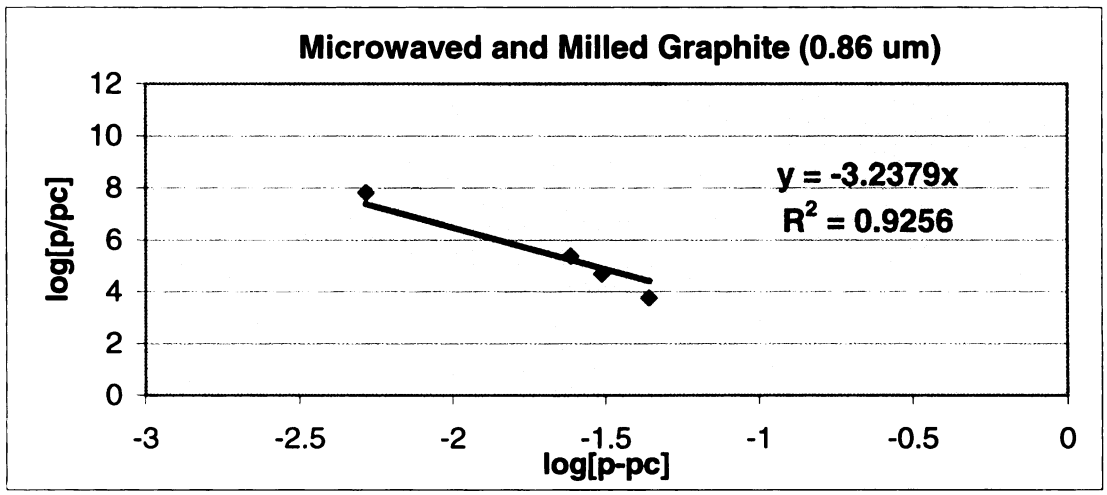

Figure 4.21. Three-parameter Fit Analysis for Milled Graphite System

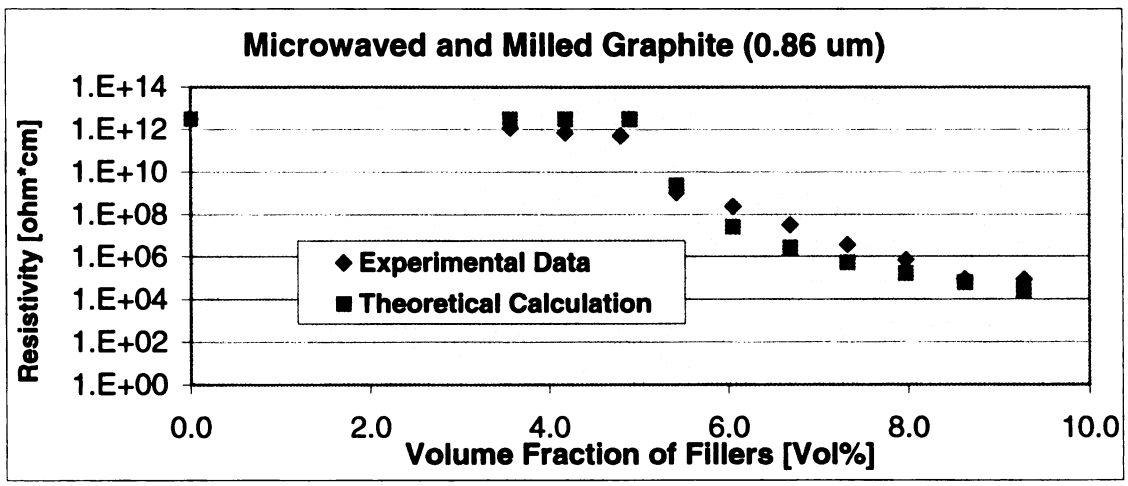

Figure 4.22. Theoretically and Experimentally Obtained Resistivity for Microwave Exfoliated and Milled Graphite Composites

- Milled Carbon Fiber

Table 4.5 shows the values of the percolation threshold, p_c, the resistivity of conductive phase, ρ_0, and the conductivity exponent, t. **Figure 4.23** shows the least-square linear fit of $\log[\rho_{eff} / \rho_0]$ vs $\log[p-p_c]$, and **Figure 4.24** shows the theoretically and experimentally obtained resistivity curves.

Table 4.5. Results of Three-parameter Fit Analysis for Milled Carbon Fiber System

Reinforcement	pc (Vol%)	pc (Wt%)	ρ_0 (ohm*cm)	t
CF	5.9	9.76	0.4	3.26

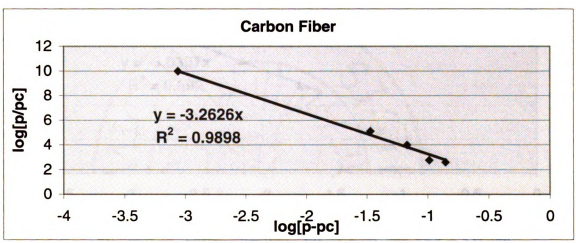

Figure 4.23. Three-parameter Fit Analysis for Milled Carbon Fiber System

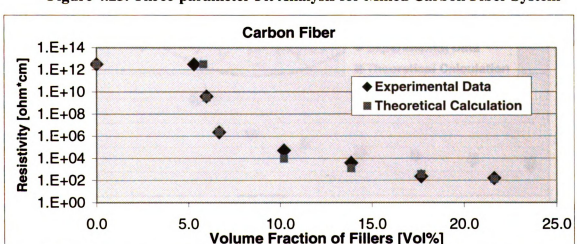

Figure 4.24. Theoretically and Experimentally Obtained Resistivity for Milled Carbon Fiber Composites

- VGCF

Table 4.6 shows the values of the percolation threshold, p_c, the resistivity of conductive phase, ρ_0, and the conductivity exponent, t. **Figure 4.25** shows the least-square linear fit of $\log[\rho_{eff} / \rho_0]$ vs $\log[p-p_c]$, and **Figure 4.26** shows the theoretically and experimentally obtained resistivity curves.

Table 4.6. Results of Three-parameter Fit Analysis for VGCF System

Reinforcement	pc (Vol%)	pc (Wt%)	ρ_0 (ohm*cm)	t
VGCF	1.09	1.87	0.03	3.03

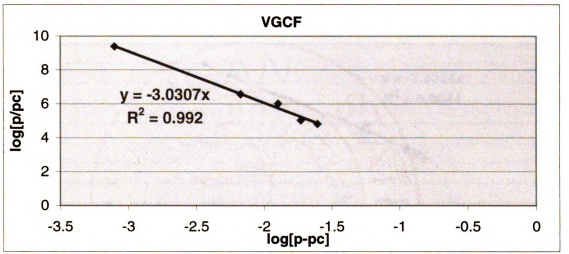

Figure 4.25. Three-parameter Fit Analysis for VGCF System

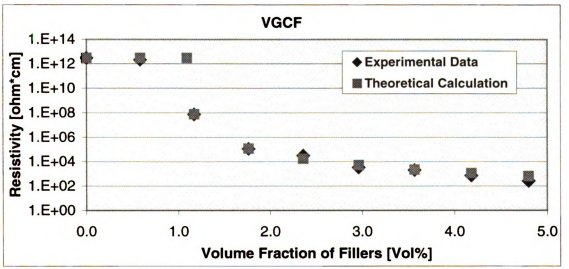

Figure 4.26. Theoretically and Experimentally Obtained Resistivity for VGCF Composites

- Carbon Black

Table 4.7 shows the values of the percolation threshold, p_c, the resistivity of conductive phase, ρ_0, and the conductivity exponent, t. **Figure 4.27** shows the least-square linear fit of $\log[\rho_{eff} / \rho_0]$ vs $\log[p-p_c]$, and **Figure 4.28** shows the theoretically and experimentally obtained resistivity curves.

Table 4.7. Results of Three-parameter Fit Analysis for Carbon Black System

Reinforcement	pc (Vol%)	pc (Wt%)	ρ_0 (ohm*cm)	t
Carbon Black	1.29	2	0.01	3.03

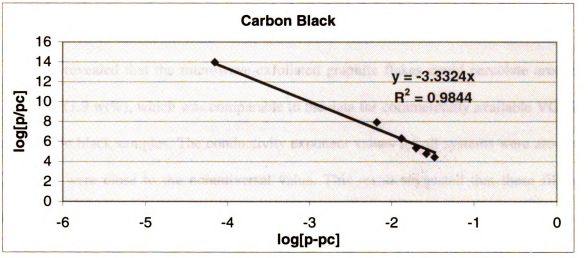

Figure 4.27. Three-parameter Fit Analysis for Carbon Black System

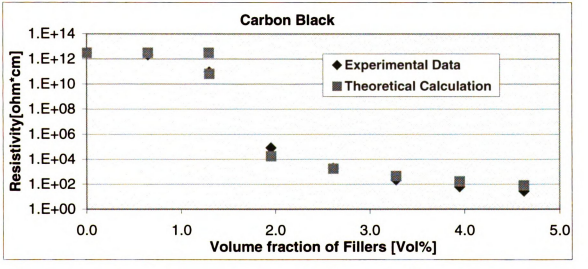

Figure 4.28. Theoretically and Experimentally Obtained Resistivity for Carbon Black Composites

Table 4.8 summarizes the values of the percolation threshold, p_c, the resistivity of conductive phase, ρ_0, and the conductivity exponent, t for all carbon materials investigated.

Table 4.8. Results of Three-parameter Fit Analysis for Various Carbon Material based Composites

Reinforcement	pc (Vol%)	pc (Wt%)	ρ_0 (ohm*cm)	t
MW Exfoliated Gr.	1.13	1.93	0.001	3.12
MW and Milled Gr.	4.90	8.17	15	3.24
CF	5.90	9.76	0.4	3.26
VGCF	1.09	1.87	0.03	3.03
Carbon Black	1.29	2.00	0.01	3.03

It revealed that the microwave-exfoliated graphite flakes could percolate around 1.1 vol% (1.9 wt%), which was comparable to the data for commercially available VGCF and carbon black samples. The conductivity exponent values for all systems were around 3, which were close to the nonuniversal value. This result suggested that these fillers form agglomerate in epoxy matrix.

4.3.7. Thermal Conductivity

Thermal conductivity of composites filled with microwave-exfoliated graphite flakes was measured by using the DSC method. **Figure 4.29** shows the results. Also electrical conductivity data was included as a comparison. Both data are shown in logarithmic scale. **Figure 4.30** shows the relation between thermal and electrical conductivity. This result suggested that these data had a linear relation, which was reasonable for solid samples.

Figure 4.31 shows the thermal conductivity of composites filled with various carbon materials. It revealed that composites filled with exfoliated graphite showed the highest thermal conductivity.

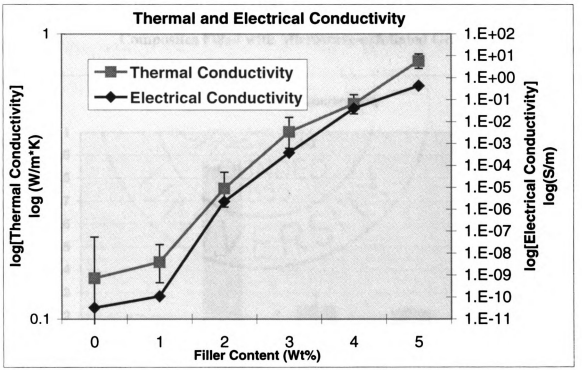

Figure 4.29. Thermal and Electrical Conductivity of Composites Filled with Microwave-exfoliated Graphite Flakes

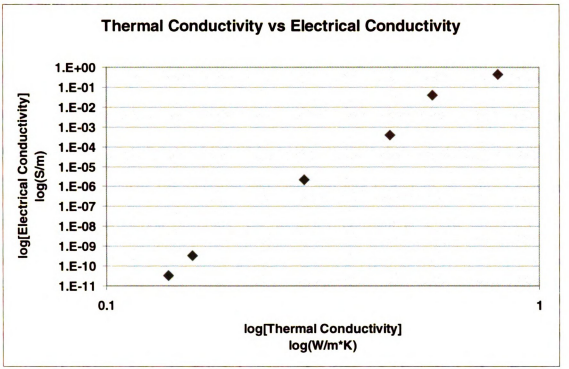

Figure 4.30. Relation between Thermal and Electrical Conductivity of Composites Filled with Microwave-exfoliated Graphite Flakes

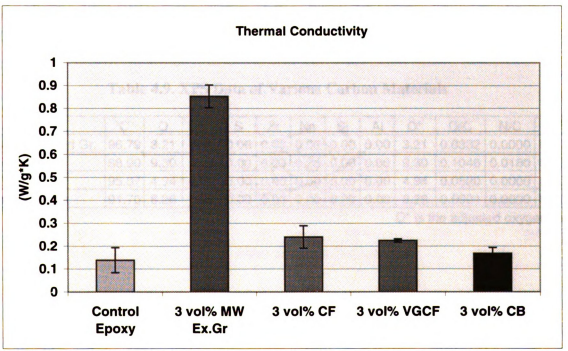

Figure 4.31. Thermal Conductivity of Composites Filled with Various Carbon Materials

4.3.8. Dielectric Properties

Dielectric properties of composite samples were calculated from the Impedance Spectroscopy data. The measurement gives the real and imaginary parts of impedance, Z' and Z", over a frequency range of 0.1 to 100,000Hz. The relation between the real and imaginary parts of impedance and the relative permittivity is shown in **Appendix A20**.

Figure 4.32 shows the dielectric constants and loss factors of composite samples filled with various carbon materials. The dielectric constant at a low frequency is a measure of the amount of permanent polar functional groups. These results implied that the microwave-exfoliated graphite and carbon black had the highest density of polar groups. The XPS data (**Table 4.9**) showed that the carbon fiber sample had the highest oxygen and nitrogen contents. This is because other factors such as the total surface area of fillers and the dispersion condition of the fillers in the matrix affected the dielectric properties of composite systems.

Table 4.9. XPS Data of Various Carbon Materials

	C	O	N	S	Zr	Na	Si	Al	O*	O/C	N/C	S/C
MW-exfoliated Gr.	96.79	3.21	0.00	0.00	0.00	0.00	0.00	0.00	3.21	0.0332	0.0000	0.0000
CF	88.90	9.30	1.60	0.00	0.00	0.25	0.00	0.00	9.30	0.1046	0.0180	0.0000
VGCF	95.07	4.94	0.00	0.00	0.00	0.00	0.00	0.00	4.94	0.0520	0.0000	0.0000
Carbon Black	91.70	8.26	0.00	0.00	0.00	0.00	0.00	0.00	8.26	0.0901	0.0000	0.0000

O* is the adjusted oxygen value

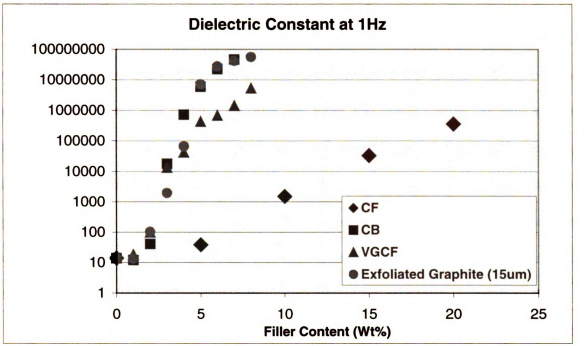

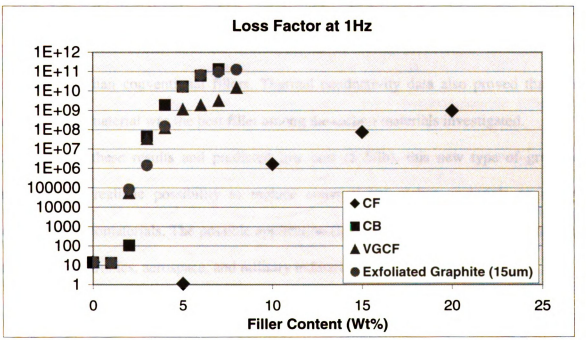

Figure 4.32. Dielectric Properties of Composites Filled with Various Carbon Materials

4.4. Conclusions

Newly developed graphite nanoflakes were used as reinforcements in epoxy matrix. It was revealed that the size of the flakes affected the properties of composites, since smaller flakes had larger edge area and more functional groups. Several surface treatments were investigated to improve the surface condition of the graphite and the acrylamide grafting was found to be very effective to enhance the interaction between the graphite sample and the epoxy matrix. The acrylamide treated graphite nanoflakes reinforced composites showed better mechanical properties than those reinforced with commercially available carbon materials.

The electrical conductivity of composites was also investigated. The results revealed that the exfoliated graphite sample with a high aspect ratio was an excellent conductive filler, which showed a comparable or better percolation threshold and conductivity than conventional fillers. Thermal conductivity data also proved that this new graphite material was the best filler among the carbon materials investigated.

From these results and predicted low cost ($ 5/lb), this new type of graphite material has realistic possibility to replace conventional carbon materials or newly developed nanomaterials. The possible application fields are broad, including automobile, electrical/electronics, aerospace, and military industries.

4.5 Reference

1. Giannelis, E. P., "Polymer-Layered Silicate Nanocomposites: Synthesis, Properties, and Applications." Appl. Organometalic Chem., ***12***, 675 (1998).

2. Pinnavaia, T. J. and Beal, G. W., "Polymer Clay Nanocomposites." John Wiley & Sons, Chichester, England, (2000).

3. Pan, Y. X., Yu, Z. Z., Ou, Y. C., and Hu, G. H., "A New Process of Fabricationg Electrically Conducting Nylon6/Graphite Nanocomposites via Intercalation Polymerization." J. Polym. Sci., Part B: Polym. Phy., ***38***, 1626 (2000).

4. Chen, G. H., Wu, D. J., Weng, W. G., He, B., and Yan, W. L., "Preparation of Polymer/Graphite Conducting Nanocomposites by Intercalation Polymerization." J. Appl. Polym. Sci., ***82***, 2506 (2001).

5. Chen, G. H., Wu, D. J., Weng, W. G., He, B., and Yan, W. L., "Preparation of Polystylene-Graphite Conducting Nanocomposites via Intercalation Polymerization." Polym. Int., ***50***, 980 (2001).

6. Xiao, P, Xiao, M., and Gong, K., "Preparation of Exfoliated Graphite/Polystyrene Composite by Polymerization-filling technique." Polymer, ***42***, 4813 (2001).

7. Chen, X. M., Shen, J. W., and Huang, W., Y., "Novel Electrically Conductive Polypropyrene/Graphite Nanocomposites." J. Mater. Sci. Lett., ***21***, 213 (2002).

8. Uhl, F. M., and Wilkie, C. A., "Polystyrene/Graphite Nanocomposites: Effect on Thermal Stability", Polym. Degradation and Stability, ***76***, 111 (2002).

9. Xiao, M, Sun, L. Y., Liu, J. J., Li, Y., and Gong, K. C., "Synthesis and Properties of Polystyrene/Graphite Nanocomposite", Polymer, ***43***, 8, 2245 (2002).

10. Khanna, Y. P., Taylor, T. J., and Chomyn, G., "A New Differential Calorimetry Based Approach for the Estimation of Thermal Conductivity of Polymer Solids and Melts.", Polym. Eng. And Sci., ***28***, 16, (1988).

11. Flynn, J. H., and Levin, D. M., "A Method for The Determination of Thermal Conductivity of Sheet Materials by Differential Scanning Calorimetry (DSC).", Thermochimica Acta, ***126***, 93 (1988).

12. Son, Y., Noh, T. W., Lee, S. I., and Gaines, J. R., "Experimental Study of The Three-dimensional AC Conductivity and Dielectric Constant of a Conductor-Insulator Composite near the Percolation Threshold.", Phy. Rev. B; ***33***, 2, (1986).

13. Lee, S. I., Song, Y., Noh, T. W., Chen, X. D., and Gaines, J. R., "Experimental Observations of Nonuniversal Behavior of The Conductivity Exponent for Three-dimensional continuum percolation systems.", Phys. Rev. B; ***34***, 10, 6719 (1986).

CHAPTER 5

STRESS ANALYSIS OF NANOCOMPOSITES

BY

FINITE ELEMENT METHOD

5.1 Introduction

Failure mechanisms of materials can be classified into several categories such as the yielding of ductile materials, the fracture of brittle materials, fatigue, and buckling. In the case of short-fiber reinforced polymer composites, the fracture process could be a combination of multiple mechanisms. If the bonding between matrix and fibers was perfect, the failure would occur by either the plastic deformation of the matrix or the breakage of a fiber. In practice, however, most of the composite failures are initiated by interfacial debonding around reinforcements. SEM observations of the failure process of a short-fiber reinforced composite revealed that the process included several steps [1, 2].

(1) The initiation of failure by interfacial debonding occurred at the fiber ends

(2) Plastic deformation of matrix around the fibers

(3) Interfacial microcrack propagation along fiber sides

(4) Catastrophic crack propagation throughout the matrix

Thus, it is important to investigate the adhesion condition between fibers and matrix and stress concentration at the interface and the matrix regions to assess the failure condition.

The adhesion condition between fibers and a polymer matrix can be investigated experimentally by testing methods such as the fiber pullout test, the microdrop technique, and the single fiber fragmentation test [3]. But it is difficult to assess the interfacial bond quality of flake-reinforced composites because of the inconsistency of the dimension of the flakes. However, the stress distribution at the interface region of these composites can be simulated by using the finite element method.

To investigate the plastic deformation phenomena, many theories have been proposed and compared with experimental data. Among these, the von Mises yield

criterion [4] is most widely used because it can provide the best agreement between theory and experimental results in many cases. This model assumes that the failure of ductile material occurs when the energy of distortion reaches the yield energy of the material. In the case of a material under principal stresses, the criterion is mathematically expressed as,

$$\sigma_{yield} \geq \sigma_{eff} = \frac{1}{\sqrt{2}}\left[(\sigma_1 - \sigma_2)^2 + (\sigma_2 - \sigma_3)^2 + (\sigma_3 - \sigma_1)^2\right]^{1/2} \qquad (5\text{-}1)$$

where σ_{eff} is the effective stress of the material and $\sigma 1$, $\sigma 2$, and $\sigma 3$ are the stresses in directions 1, 2, and 3. In the case of plane stress, only $\sigma 1$ and $\sigma 2$ exist. So the equation becomes,

$$\sigma_{yield} \geq \sigma_{eff} = \left(\sigma_1{}^2 - \sigma_1\sigma_2 + \sigma_2{}^2\right)^{1/2} \qquad (5\text{-}2)$$

The von Mises stress distribution condition of composite systems can also be simulated theoretically by using the finite element method.

The presence of an inclusion in a polymer matrix often increases the stress concentration, which could initiate the cracking and/or plastic failure. The stress field can be affected by many factors such as the shape of inclusions, the morphology of the system, a large mismatch in expansion/shrinkage condition, and the adhesion between matrix and inclusions. To design good composite systems for a specific application, it is important to understand the effect of these factors on the properties of composite systems.

To evaluate the local stress fields of composite systems, single inclusion models were investigated first [5, 6]. These models represent the dilute inclusion condition. When inclusions are closely packed, the stress fields from each inclusion interact each other, forming very complex stress fields. To solve this problem, a new concept called

the effective medium approach has been introduced [6, 7, 8]. In this case, theoretical calculations usually assume that the inclusions are arranged in periodic ways [9, 10, 11, 12, 13]. This approach is useful to predict the effective elastic and thermal constants, but it cannot handle the local stress fields in composite systems with randomly oriented inclusions.

In the real composite systems, the dispersion of inclusions is generally disordered. It is required to investigate the local stress conditions in composite systems to understand the damage initiation and propagation, since damage mechanisms such as plasticity and fracture are affected by these local conditions. To investigate the effect of the arrangement of inclusions on the local stress fields and effective properties, models with two neighboring inclusions have been used in this basic approach [14, 15, 16].

The objective of this research is to investigate the effect of the shape and geometric arrangement of inclusions on the local stress condition of nanocomposite systems by using the finite element analysis method. The factors investigated were (1) the shape of inclusion, (2) the aspect ratio of inclusion, and (3) the geometric arrangement of inclusions. Single-inclusion models were used to investigate the first two factors while two-inclusion models were used to investigate the last one. In the case of two-inclusion models, the inclusions were not allowed to overlap each other. To focus on these factors, the perfect bonding condition between inclusions and matrix was assumed and no residual stress due to the difference in CTE of matrix and inclusions was considered.

5.2 Finite Element Method

The software used was ANSYS 57. In the simulation, the quadrilateral plane elements system was used so that each element was defined by eight nodes and each node has two degrees of freedom in the x- and y- directions. All the simulations were done under the plane stress condition. By assigning symmetric boundary conditions on the x- and y- axis, only a quarter of the whole model system was required to be input as a simulation model. The engineering constants of the matrix and graphite material are summarized in **Table 5.1.** [17]

Table 5.1. Engineering Constants of Matrix and Graphite Sample

	Matrix	Inclusion
	Epoxy	Graphite
	Isotropic	Transversely Isotropic
Young's Modulus ($E_{11} = E_{22}$)	2,500 MPa	1060,000 MPa
Young's Modulus (E_{33})		36,500 MPa
Poisson's ratio ($\nu_{12}=\nu_{21}$)	0.35	0.165
Poisson's Ratio ($\nu_{13}=\nu_{23}$)		0.343
Shear Modulus ($G_{12} = G_{21}$)		440,000 MPa
Shear Modulus ($G_{13} = G_{23}$)		4,500 MPa

5.3 Results and Discussion

5.3.1 The Effect of Edge Angle against Input Stress

5.3.1.1 Model

Four models were used to investigate the effect of the inclusion's edge angle against the input stress. Each model had a rhombus shape inclusion with different edge angles against the input stress. In each case, the engineering constants of reinforcement in directions 1 and 2 were assigned as those in the X- and Y- directions, and both axes were assumed as symmetric boundaries. The length of each edge line was fixed at 5. The input

stress was fixed at 1, and applied in Y-direction on a line which is located the same distance from the top corner of each rhombus inclusion. **Figure 5.1** shows these models.

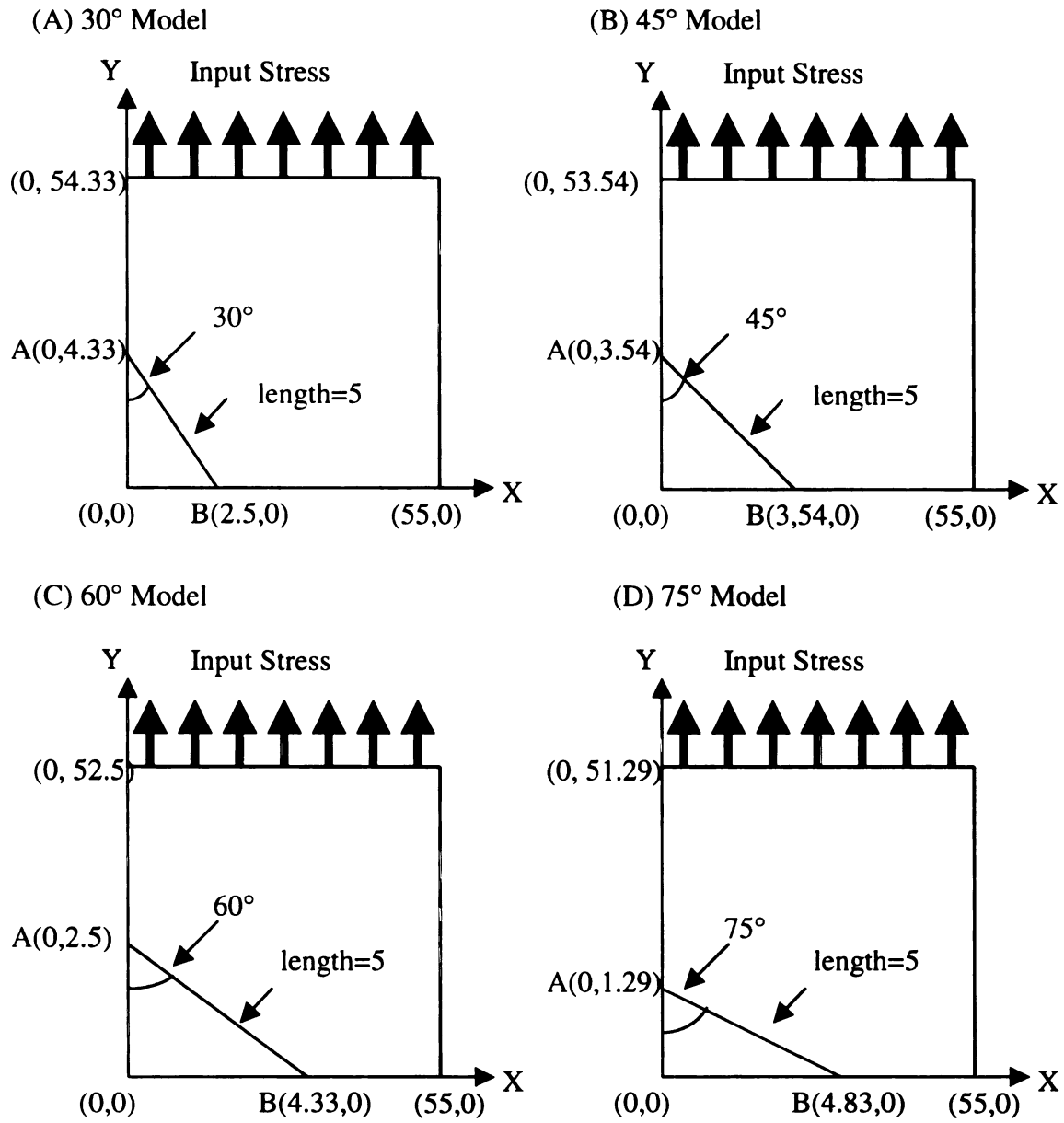

Figure 5.1. The Models Used to Investigate The Effect of Edge Angle against Input Stress on The Stress Distribution of Composite Systems

5.3.1.2. The Effect of The Edge Angle on The Interface Stress Condition

The absolute values of the maximum stresses at the interface (line 1) are summarized in **Figure 5.2**. The simulation revealed that the maximum stress in the Y-direction appeared at corner A (top corner) and showed the highest value when the angle was the smallest, while that of the X-direction appeared at corner B (side corner) and showed the highest value when the angle was the largest. The maximum shear stress appeared at either corner A or B, depending on the other two values, and showed optimal angle condition. In all models, the stress in the Y-direction showed the highest value among these three stresses, suggesting the debonding would occur at corner A. If the adhesion condition was the same for all models, the 30° model would fail at the lowest input stress. In other words, this geometry produced the lowest strength.

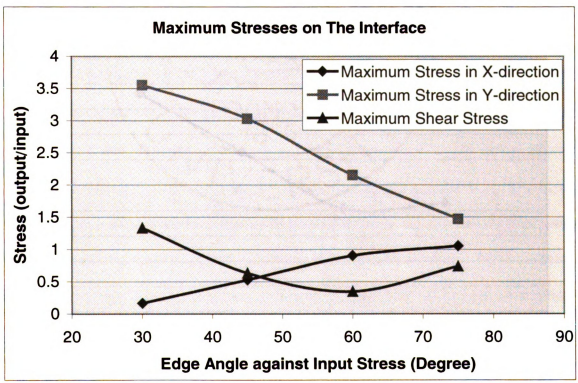

Figure 5.2. The Effect of Edge Angle on The Maximum Stress at The Interface (line 1)

5.3.1.3 The Effect of The Edge Angle on The Effective Stress in The Matrix Region

The maximum effective stress in the matrix region in each model was calculated based on the von Mises model and the values are summarized in **Figure 5.3**. The simulation revealed that the maximum effective stress decreased with the increasing edge angles up to 60°, then increased a little. The maximum effective stress appeared near corner A (top corner) in 30°-, 45°-, and 60°-models, while that appeared near corner B in 75 ° model. Thus, if the adhesion between filler and matrix was strong enough, yielding would occur near the corners which initiate the failure of the system. Since the 30° model shows the highest value under the same input stress condition, this model would yield at the lowest input stress. This result also suggests that the model with a lower edge angle would show lower strength as a composite.

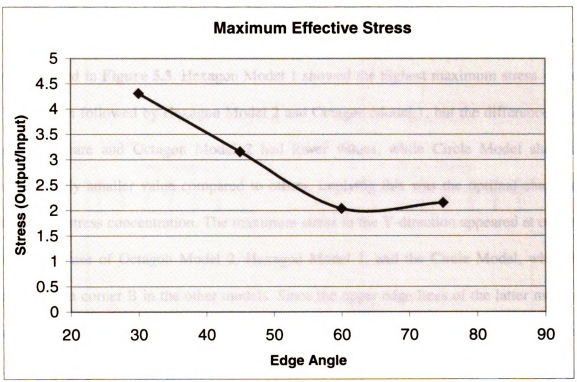

Figure 5.3. The Effect of Edge Angle on The Maximum Effective Stress in The Matrix Region

5.3.2 The Effect of Filler Shape

5.3.2.1 Model

Square, circular, hexagonal, and octagonal shaped reinforcements were used as models. Two different geometric arrangements were investigated in both hexagonal and octagonal reinforcement models. **Figure 5.4** shows the details of these. In each model, the engineering constants of reinforcement in directions 1 and 2 were also assigned as those in X- and Y- directions and both the X- and Y- axes were assumed as symmetric boundaries. The input stress value was fixed at 1 and applied in the Y-direction on a line, which is located the same distance from the inclusion. All the simulations were done under the plane stress condition.

5.3.2.2. The Effect of Filler Shape on The Interface Stress Condition

The absolute values of maximum stresses at the interface in each model are summarized in **Figure 5.5**. Hexagon Model 1 showed the highest maximum stress in the Y-direction followed by Hexagon Model 2 and Octagon Model 1, but the difference was small. Square and Octagon Model 2 had lower values, while Circle Model showed distinctively smaller value compared to others, implying this was the optimal shape to minimize stress concentration. The maximum stress in the Y-direction appeared at corner A in the case of Octagon Model 2, Hexagon Model 1, and the Circle Model, while it appeared at corner B in the other models. Since the upper edge lines of the latter models are perpendicular to the input stress, it is reasonable that the maximum stress appeared at corner B.

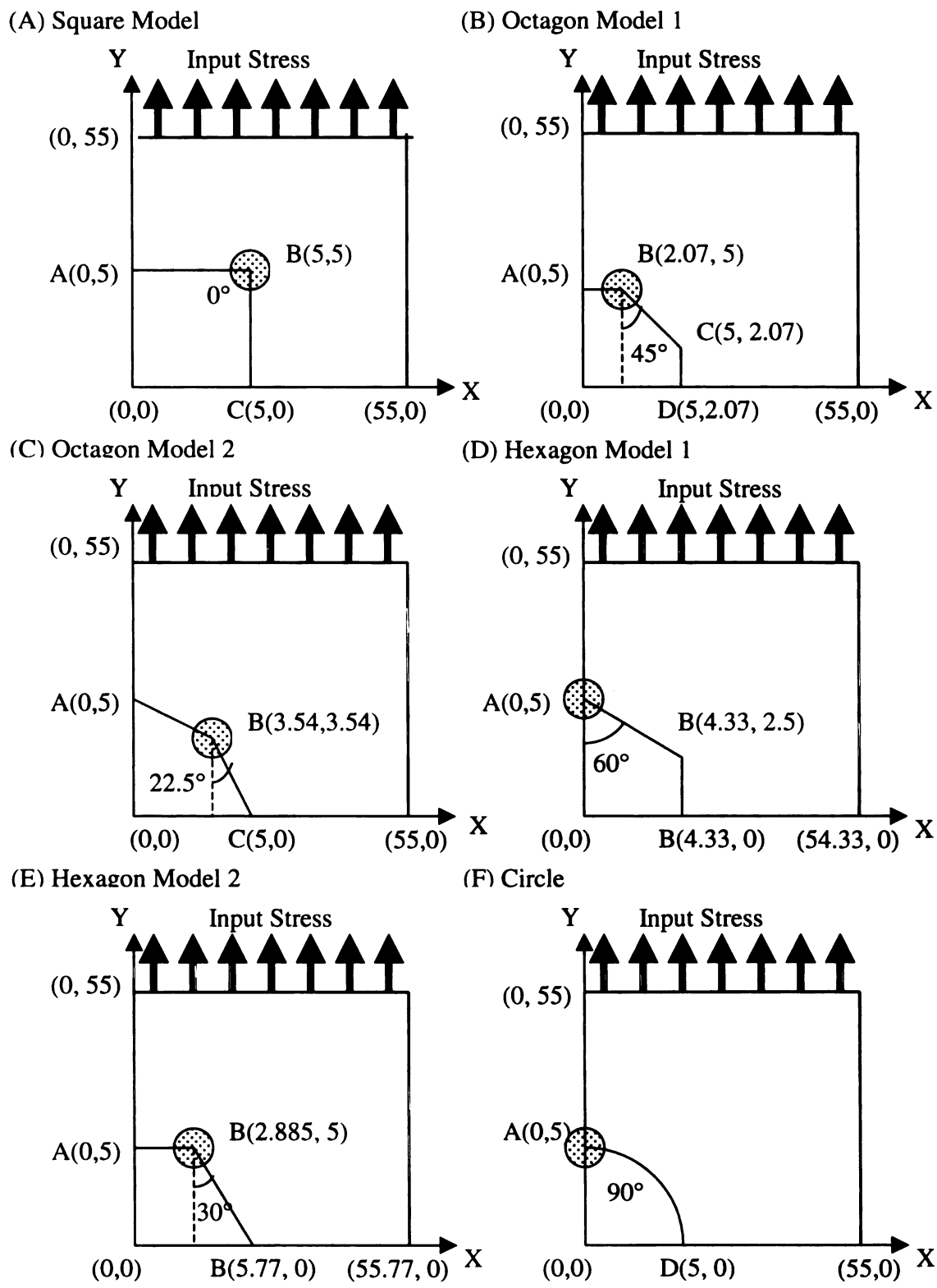

Figure 5.4. The Models Used to Investigate The Effect of Shape Difference on The Stress Distribution of Composite Systems

In the case of the stress in the X-direction, all models showed almost the same maximum stress and there was no tendency related to the filler shape. The Square model showed a higher maximum shear stress, while the Circle Model had a lower value. This results also suggested that the Circle Model was the best in terms of introducing minimum stress concentration. Thus, the composite with circular shape reinforcements would stand higher input stress before it reaches the point where debonding of the interface begins, which means the material has the highest strength.

5.3.2.3 The Effect of Filler Shape on The Effective Stress in The Matrix Region

The maximum effective stress values in the matrix region in each model were calculated based on the von Mises criteria and are summarized in **Figure 5.6**. The maximum stress appeared at corner A in Hexagon Model 1 and the Circle Model, while it showed up at corner B in other models. The angles of edge lines connected to these corners are shown in **Figure 5.4**. The results showed that the maximum effective stress decreased with decreasing edge angles against the input stress, which showed the same tendency as in the previous simulation. Also, the Circle Model showed a considerably smaller maximum effective stress compared to the other models, suggesting that the Circle Model would be the best in terms of creating the minimum stress concentration in the matrix region, which implies that this model can stand the highest input stress before it reaches its yielding point. If the adhesion condition between reinforcements and matrix was perfect in all models, the Circle Model would show the highest strength.

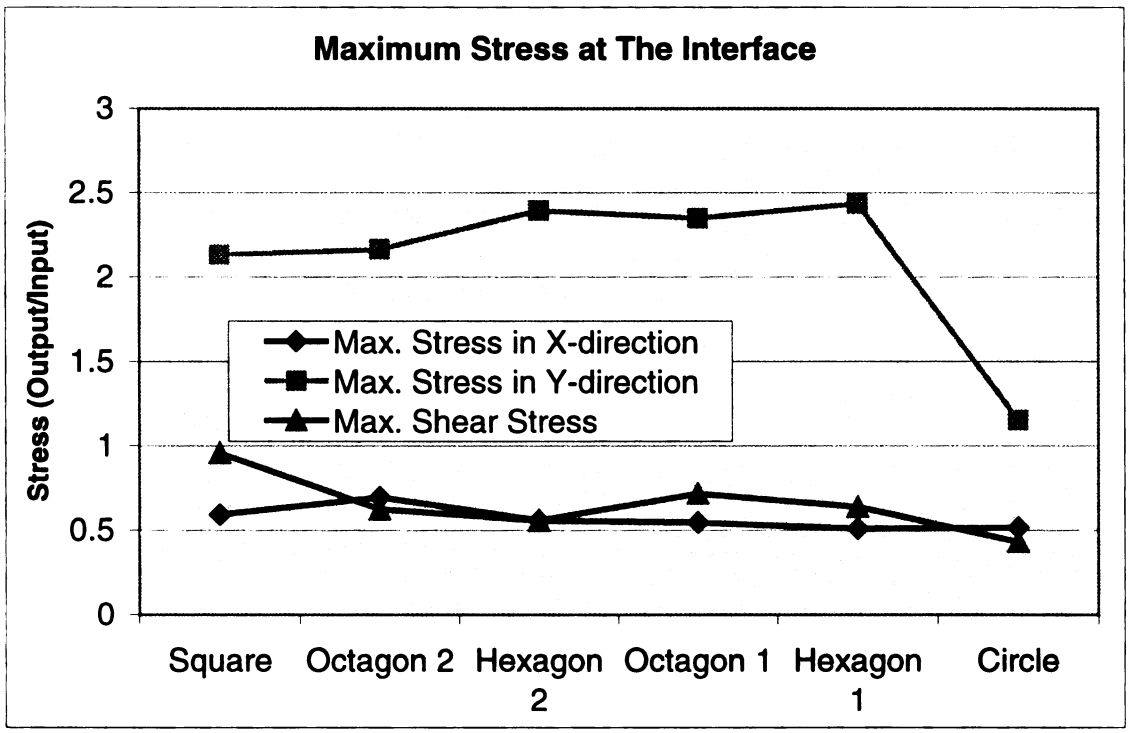

Figure 5.5. The Effect of Filler Shape on The Maximum Stress at The Interface

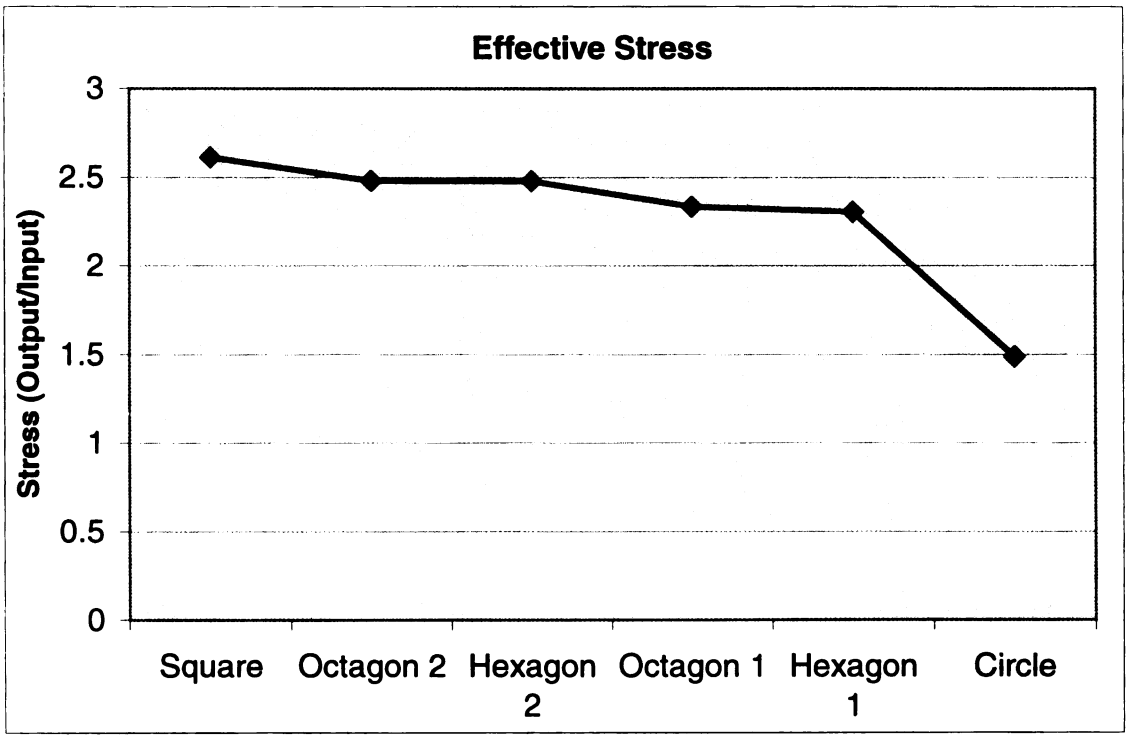

Figure 5.6. The Effect of Filler Shape on The Maximum Effective Stress in The Matrix Region

5.3.3 The Effect of Aspect Ratio

5.3.3.1 Model

Composites with plate reinforcements with different aspect ratios were used as models. The length of the reinforcements was fixed, but the thickness was changed to adjust the aspect ratio. The aspect ratios investigated were 200, 100, 50, 20, 10, 5, and 1. The stress distribution was analyzed under two different input stress conditions, one in the X- and the other in the Y-direction. In both cases, the stresses were applied on the lines, which were the same distance from the reinforcement. The input stress value was fixed at 1 in each case. **Figure 5.7** shows the details of these models. In each model, the engineering constants of reinforcement in direction 3 were assigned as those in the X-direction and the engineering constants in direction 1 were assigned as those in the Y-direction. Both the X- and Y-axes were assumed as symmetric boundaries. All the simulations were done under the plane stress condition.

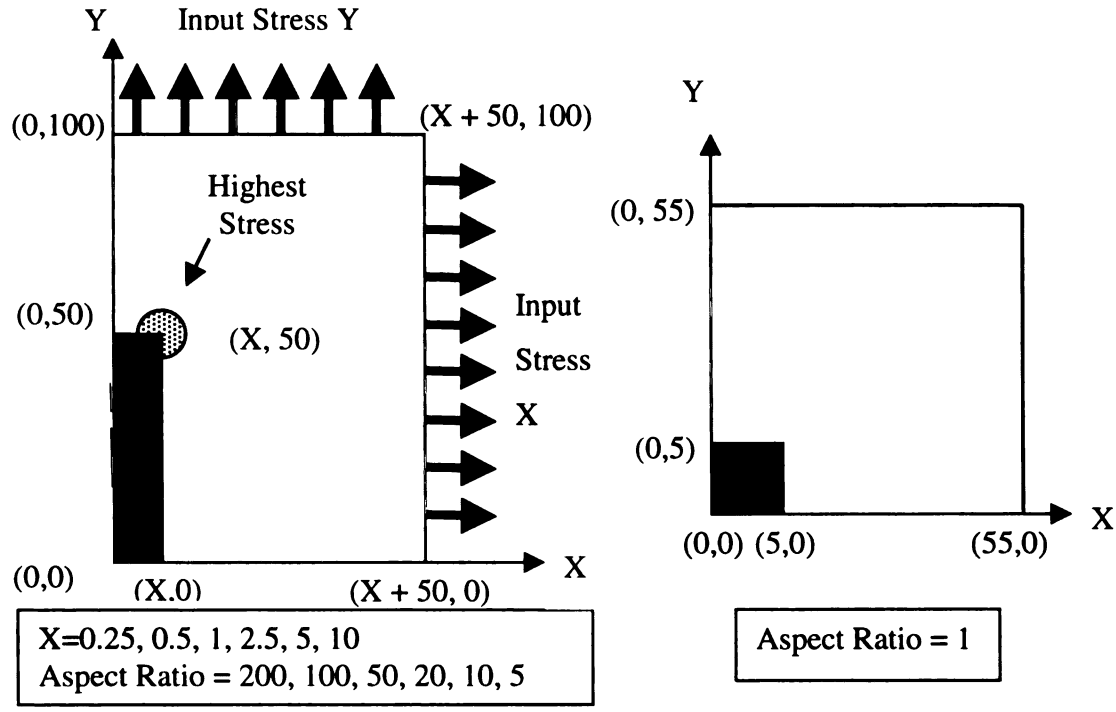

Figure 5.7. The Models Used to Investigate The Effect of Filler Aspect Ratio on The Stress Distribution of Composite Systems

5.3.3.2. The Effect of Aspect Ratio on The Interface Stress Condition

The absolute values of maximum stresses at the interface under input stresses in the X- and Y-directions are shown in **Figure 5.8**. In the case of input stress was applied in the Y direction, the maximum stress at the interface was increased with increasing aspect ratios. This result revealed that composites with higher aspect ratio would have lower strength under such a condition. In the case of input stress was applied in the X-direction, the maximum stress in the X-direction was decreased with increasing aspect ratios while that in the Y-direction was increased. These values reversed at the point where the aspect ratio was around 25. The shear stress on the interface showed the lowest value when the aspect ratio was around 50. These results suggest that there is an optimal aspect ratio to minimize stress concentration under this condition. If the fillers are randomly oriented in a composite, the former mechanism will be the dominant factor since there should always be some fillers that are aligned parallel to the input stress.

5.3.3.3 The Effect of Filler Shape on The Effective Stress in The Matrix Region

The maximum effective stress values in the matrix region are summarized in **Figure 5.9**. The results showed the same tendency that the maximum stress at the interface did. In the case of input stress was applied in the Y-direction, the effective stress increased with increasing aspect ratios, while it showed the lowest value when the aspect ratio was around 20, suggesting there was an optimal aspect ratio to minimize stress concentration. If the fillers are randomly oriented in a composite, the former mechanism will be the dominant factor for the same reason discussed above.

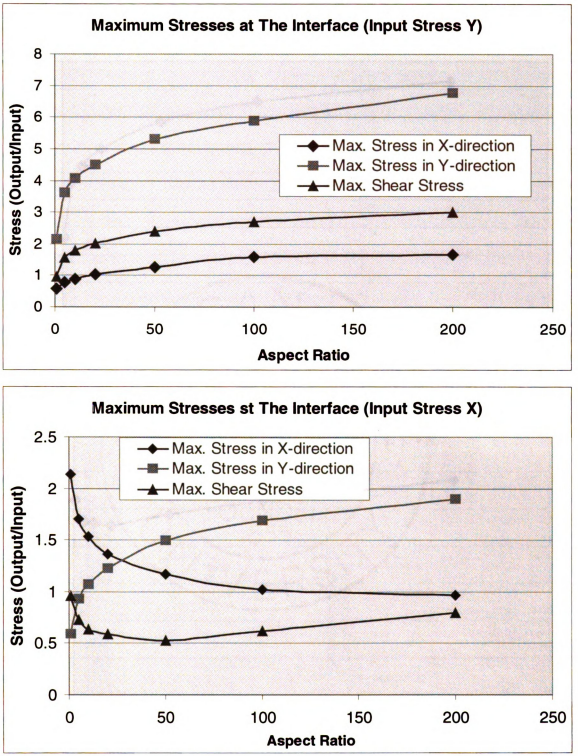

Figure 5.8. The Effect of Aspect Ratio on The Maximum Stress at The Interface

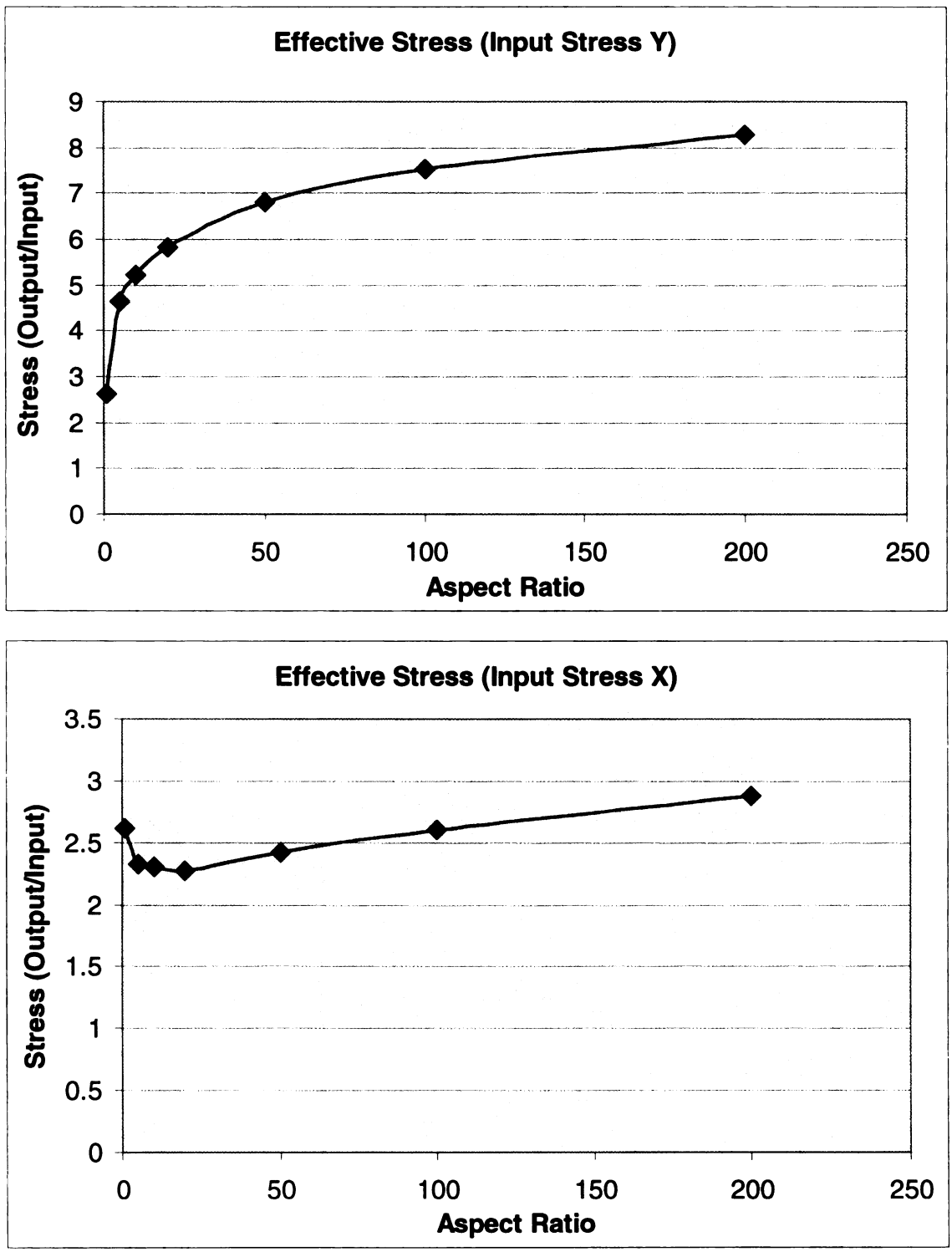

Figure 5.9. The Effect of Aspect Ratio on The Maximum Effective Stress in The Matrix Region

5.3.4 The Effect of Distance between Aligned Fillers

5.3.4.1 Model

Composites with two aligned plate fillers with a fixed aspect ratio of 20 were used as the models. The distance between two fillers was defined as the multiple of filler thickness. The stress distribution was analyzed under two different input stress conditions, one in the X- and the other in the Y-direction. In both cases, the stresses were applied on the lines, which were the same distance from the reinforcement. The input stress value was fixed at 1 in each case. **Figure 5.10** shows the details of these models. In each model, the engineering constants of reinforcement in direction 3 were assigned as those in the X-direction and the constants in direction 1 were assigned as those in the Y-direction. Both the X- and Y-axes were assumed as symmetric boundaries. All the simulations were done under the plane stress condition.

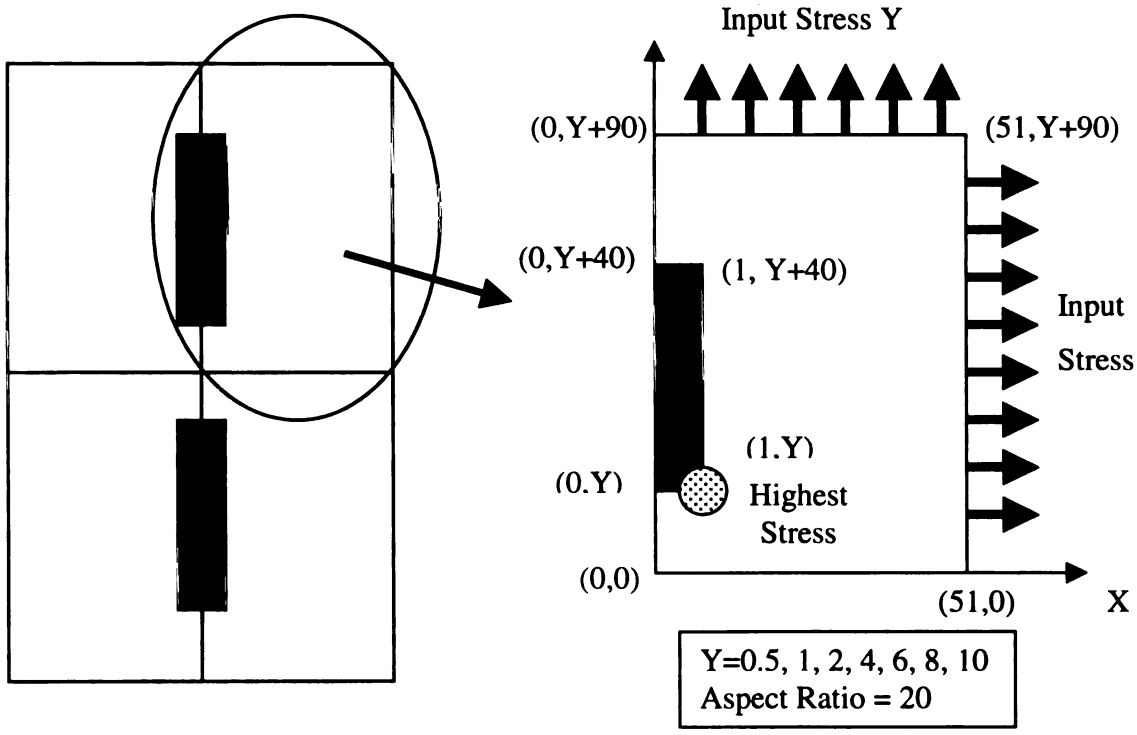

Figure 5.10. The Models Used to Investigate the Effect of Distance between Aligned Fillers on The Stress Distribution of Composite Systems

5.3.4.2. The Effect of Distance between Aligned Fillers on The Interface Stress Condition

The maximum stresses at the interface are shown in **Figure 5.11**. The theoretical calculations showed that all output stresses increased with decreasing distance between fillers. Especially in the case of input stress in the Y-direction, the maximum stresses at interface increased significantly when the distance became smaller. This implied that stress concentration would be very high if the two fillers were aligned and closely located. In the case of the input stress was applied in the X-direction, the maximum stresses showed the same tendency, but the output stress values were not as high as the former case. These results suggest that the composites would fail at a lower input stress when the fillers are aligned and closely packed.

5.3.4.3 The Effect of Distance between Aligned Fillers on the Effective Stress in The Matrix Region

The maximum effective stress values in the matrix region are summarized in **Figure 5.12**. The results showed the same tendency that maximum stresses at the interface did. When the input stress was applied in the Y-direction, the effective stress increased significantly with decreasing distance. In the case of the input stress was applied in the X-direction, the effective stress values were not as high as the former condition. These results showed that even if a composite system had perfect bonding condition between fillers and matrix, the matrix region would reach a yielding point at a lower input stress when the fillers are aligned and closely packed, showing overall lower strength. Thus, this type of geometric arrangement is not good in terms of composite mechanical properties.

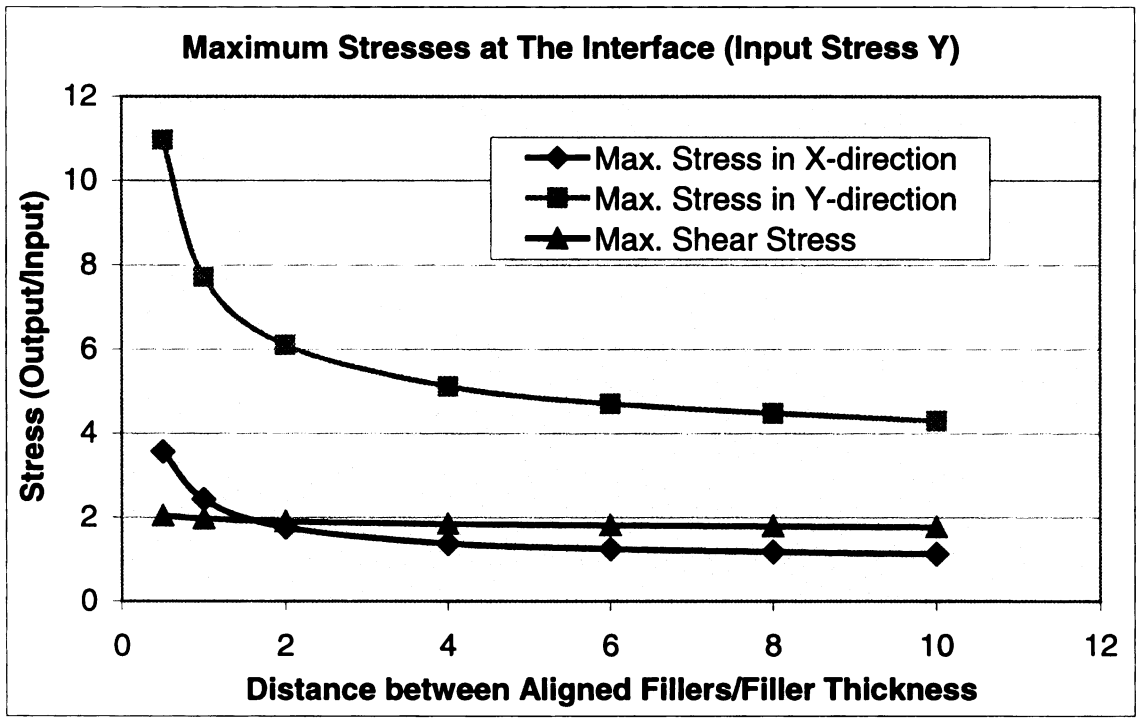

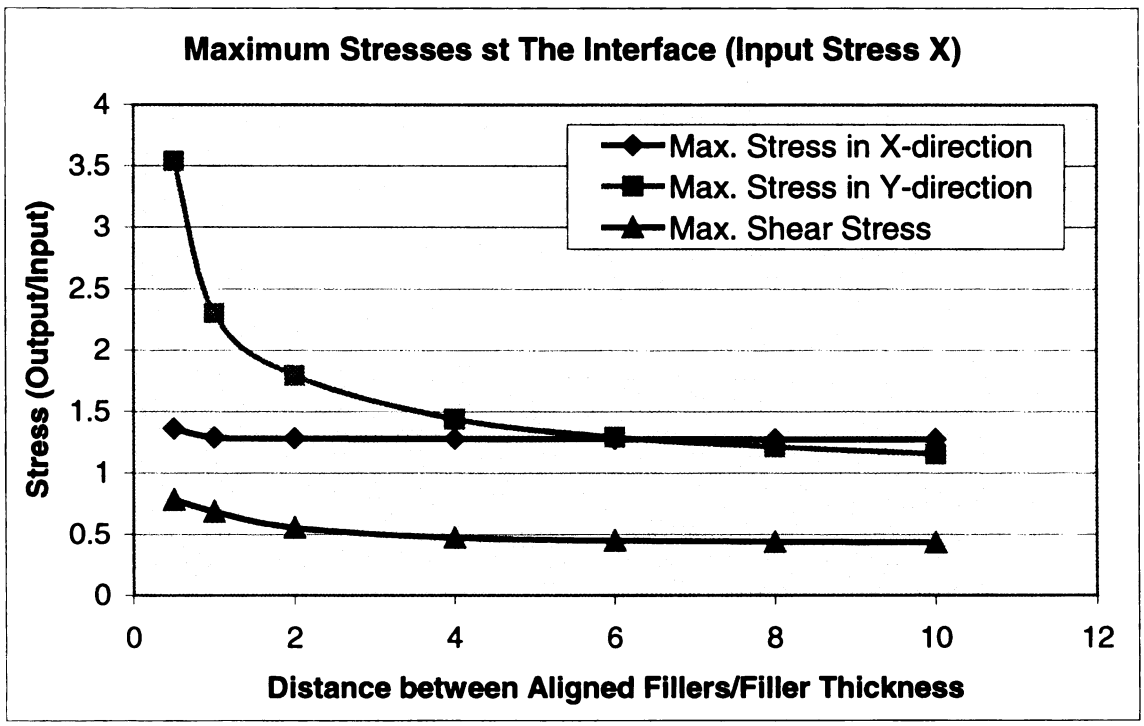

Figure 5.11. The Effect of Distance between Aligned Fillers on The Maximum Stress at The Interface

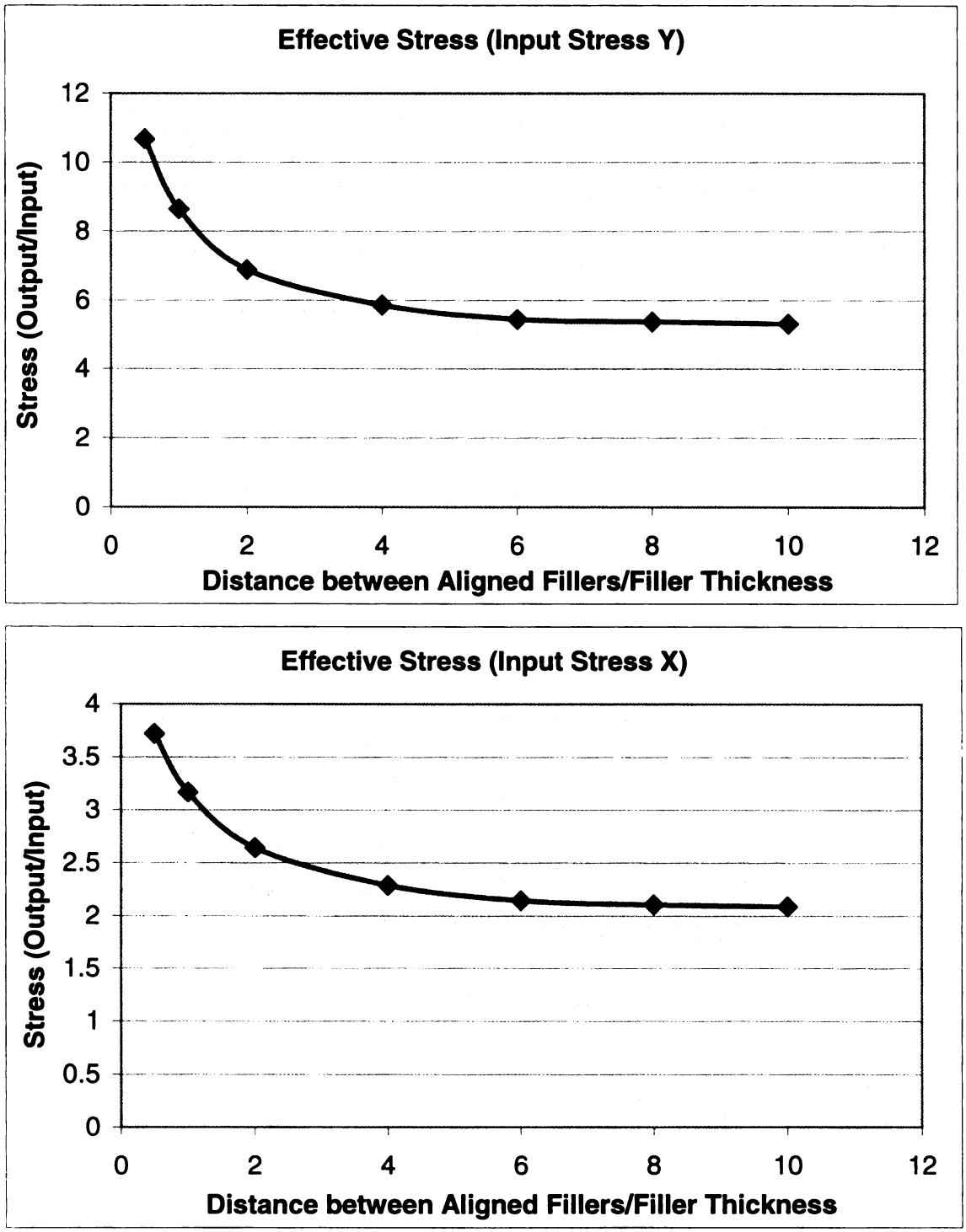

Figure 5.12. The Effect of Distance between Aligned Fillers on The Maximum Effective Stress in The Matrix Region

5.3.5 The Effect of Distance between Parallel Fillers

5.3.5.1 Model

Composites with two parallel plate fillers with fixed aspect ratio of 20 were used as the models. The distance between two fillers was changed. The stress distribution was analyzed under two different input stress conditions, one in the X- and the other in the Y-direction. In both cases, the stresses were applied on the lines, which were the same distance from the reinforcement. The input stress value was fixed at 1 in each case. **Figure 5.13** shows the details of these models. In each model, the engineering constants of reinforcement in direction 3 were assigned as those in the X-direction and the constants in direction 1 were assigned as those in the Y-direction. Both the X- and Y-axes were assumed as symmetric boundaries. All the simulations were done under the plane stress condition.

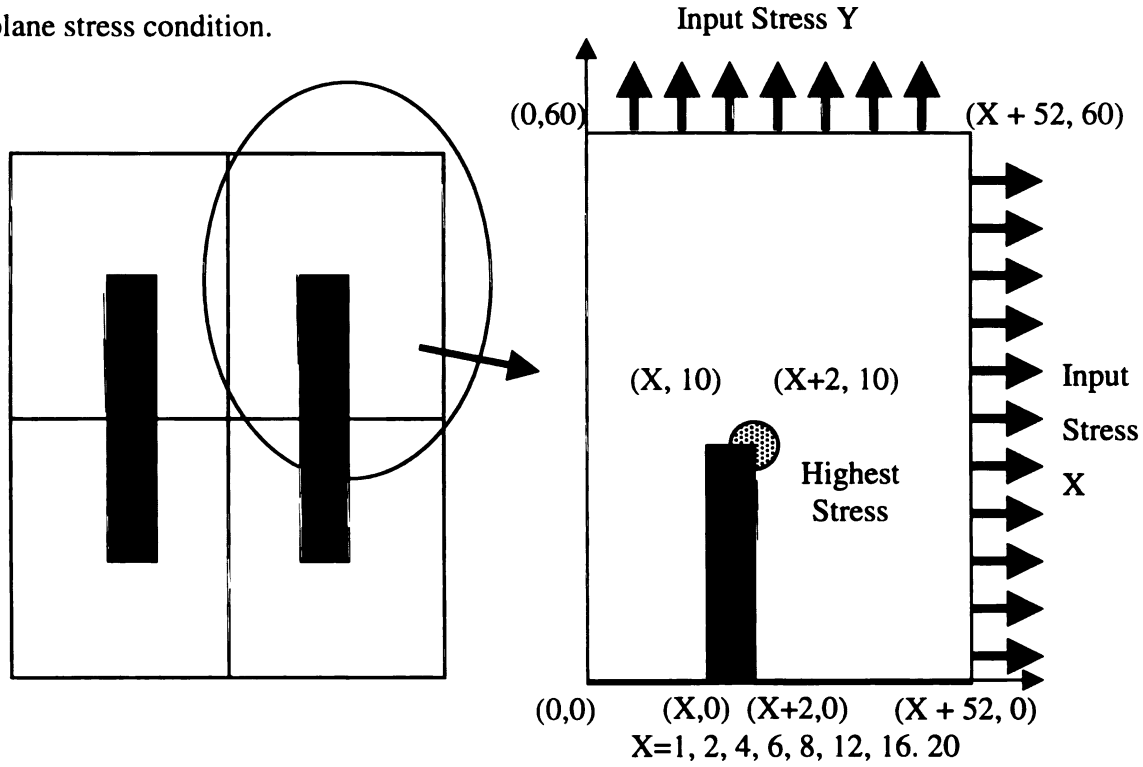

Figure 5.13. The Models Used to Investigate The Effect of Distance between Parallel Fillers on The Stress Distribution of Composite Systems

5.3.5.2. The Effect of Distance between Parallel Fillers on The Interface Stress Condition

The maximum stresses at the interface are shown in **Figure 5.14**. Compared to the other models, the calculated values showed little change but clear tendency throughout the condition investigated. Each stress showed the minimum value at some point, suggesting there was an optimal distance condition for each stress. Although the optimal point was somewhat different in each case, it appeared at the distance around 5. These results suggest that the stress can transfer to neighbor fillers when they are located in parallel position, but stress concentration effect overcome this effect beyond one point. These factors control the optimal point for stress concentration in a composite with the filler aligned in parallel.

5.3.5.3 The Effect of Distance between Parallel Fillers on the Effective Stress in The Matrix Region

The maximum effective stress values in the matrix region are summarized in **Figure 5.15**. These data showed the effect of distance more clearly. Both data showed the minimum stress at a distance around 6 to 8, showing the optimal condition for stress concentration in the matrix region. This result also supports the discussion that the stress can transfer from one filler to another, decreasing stress concentration. Thus, the strength of a composite can be improved if the geometrical arrangement of fillers is controlled such that the system shows the optimal stress transfer condition.

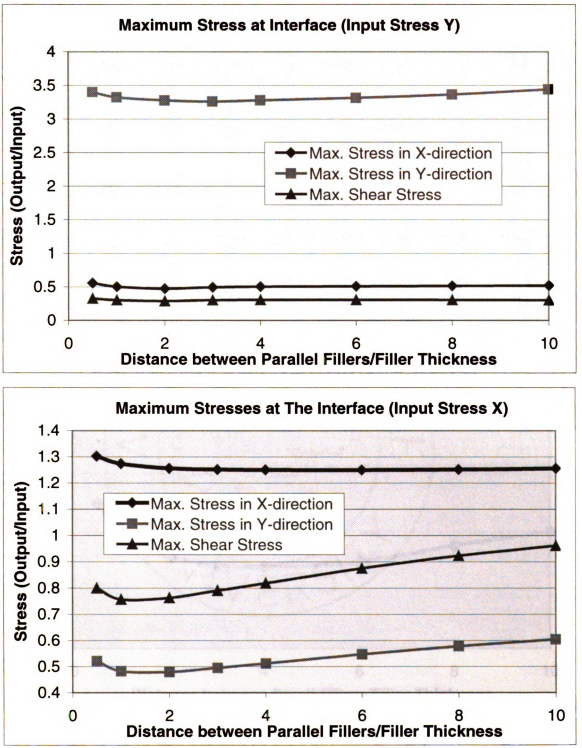

Figure 5.14. The Effect of Distance between Parallel Fillers on The Maximum Stress at The Interface

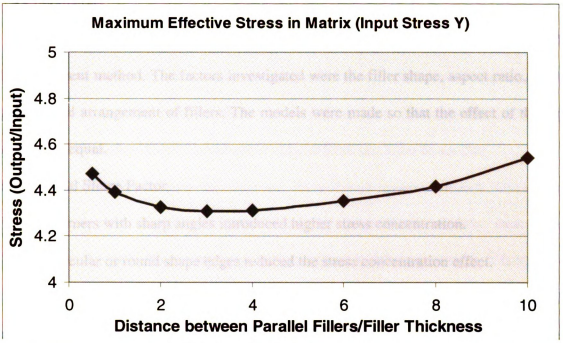

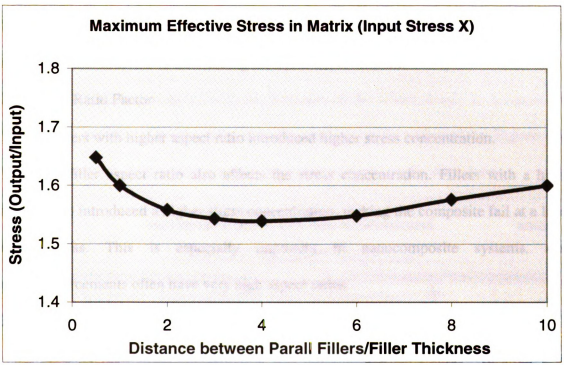

Figure 5.15. The Effect of Distance between Parallel Fillers on The Maximum Effective Stresses in The Matrix Region

5.4 Conclusions

The stress concentration condition of the composite systems was investigated by the finite element method. The factors investigated were the filler shape, aspect ratio, and the geometrical arrangement of fillers. The models were made so that the effect of the input stress was equal.

1. Material Shape Factor

- Corners with sharp angles introduced higher stress concentration.
- Circular or round shape edges reduced the stress concentration effect.

The fillers with sharp corners showed higher stress concentration at/around a corner, while fillers with a round shape showed much less stress concentration effect. Thus, the fillers with circular, elipsoidal, or other round shapes considered to be better reinforcements in terms of minimizing the stress concentration.

2. Aspect Ratio Factor

- Fillers with higher aspect ratio introduced higher stress concentration.

The filler aspect ratio also affects the stress concentration. Fillers with a higher aspect ratio introduced a higher stress concentration, making the composite fail at a lower input stress. This is especially important in nanocomposite systems, since nanoreinforcements often have very high aspect ratios.

3. Filler Arrangement Factor

- A very high stress concentration was introduced when fillers were aligned and located close to each other.
- Stress concentration could be reduced when fillers were located in parallel at an optimal distance.

If fillers were aligned, the stress concentration could be very high when fillers were located close to each other at high volume fraction, while the stress concentration effect plateau out when fillers were separated with enough distance. However, if fillers were located in parallel position, there was an optimal separation condition to minimize the stress concentration since stress could transfer from one filler to another.

If the fillers were randomly oriented, these should maintain enough distance from each other to avoid high stress concentration. In this case, the material cannot show percolation. To make the material conductive without sacrificing strength, it is necessary to arrange fillers in close distance in parallel positions so that they do not introduce a high stress concentration. The simulations revealed that there was an optimal distance for parallel-filler systems, which appeared to be around 2 to 4 times of the thickness of the fillers. Thus, to maintain the distance below the limit that tunneling phenomena occurs (about 10 nm at room temperature), the thickness of the fillers should be 5 nm or less. From these results, optimal nanocomposite morphology is proposed in **Figure 5.16**, which could show good mechanical and electrical properties at the same time.

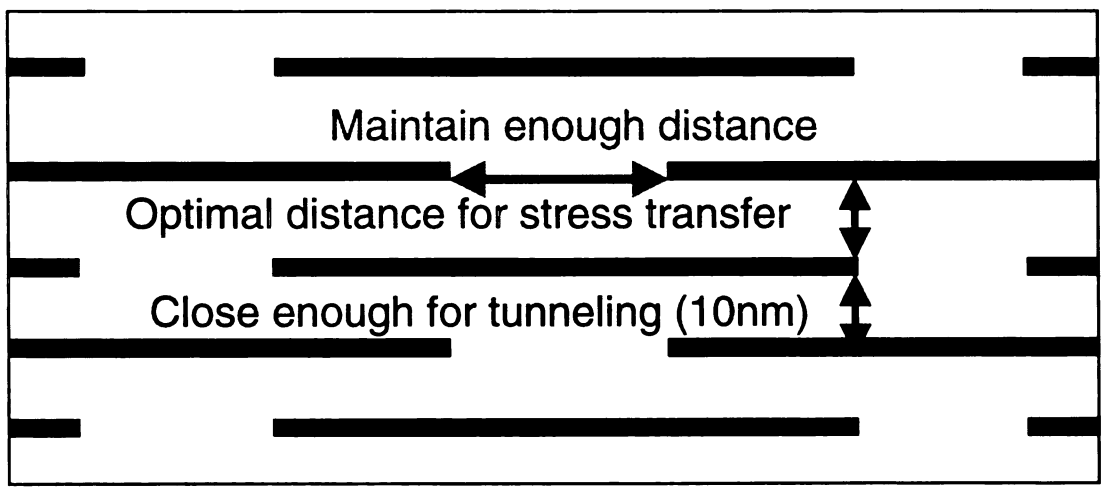

Figure 5.16. The Optimal Morphology for Graphite Nanocomposite Systems

5.5. Reference

1. Sato, N, Kurauchi, T, Sato, S., and Kamigaito, O, "SEM Observations of The Initiation and Propagation of Cracks in a Short Fiber Reinforced Thermoplastic Composite under Stress", J. Mater. Sci. Lett., ***2***, 188 (1983).

2. Sato, N., Kurauchi, T, Sato, S., and Kamigaito, O., "Reinforcing Mechanism by Small Diameter Fiber in Short Fiber Composite." J. Compos. Mater., ***22***, 850 (1988).

3. Nardin, M and Schultz, J., "Interactions and Properties of Composites: a) Fiber-Matrix Adhesion Measurements." in "The Interfacial Interactions in Polymeric Composites.", Kliwer Academic Publishers, p81-93 (1993).

4. Mendelson, A., "Plasticity: Theory and Application", Robert E. Krieger Publishing Company, Malabar, Florida (1983).

5. Eshelby, J. D., "The continuum Theory of Lattice Defects, Progress in Solid State Physics, 3" Academic Press, New York (1956).

6. Mori, T. and Tanaka, K., "Average Stress in Matrix and Average Elastic Energy of Materials with Misfitting Inclusions." ACTA METALLURGICA, ***21***, 571 (1973).

7. Benveniste Y., "A New Approach to The Application of Mori-Tanaka Theory in Composite-Materials.' Mech. Mater., ***7***, 2, 305, (1987).

8. Benveniste Y. Dvorak, G. J., and Chen, T., "Stress-fields in Composites with Coated Inclusions." Mech. Mater., ***7***, 4, 305 (1989).

9. Zhu, H. and Achenbach J. D., "Radial Matrix Cracking and Interphase Failure in Transversely Loaded Fiber Composites." Mech. Mater., ***11***, 4, 347 (1991).

10. Bigelow C. A., "The Effects of Uneven Fiber Spacing on Thermal Residual-stresses in a Unidirectional SCS-6/Ti-15-3 Laminate." J. Compos. Technol. Res., ***14***, 4, 211 (1992).

11. Li, D. S., and Wisnom, M. R., "Finite-Element Micromechanical Modeling of Unidirectional Fiber-reinforced Metal-Matrix Composites." Compos. Sci. & Technol., ***51***, 4, 545 (1994).

12. Sorense, B. F., and Talreja, R., "Effects of Nonuniformity of Fiber Distribution on Thermally-induced Residual Stresses and Cracking in Ceramic-matrix Composites." Mech. Mater., ***16***, 4, 351 (1993).

13. Bohm, H. J., Rammerstorfer, F. G., Fischer, F. D., and Siegmund, T., "Microscale Arrangement Effects on The Thermomechanical Behavior of Advanced 2-phase Materials." J. Eng. Mater. & Technol., ***116***, 3, 268 (1994).

14. Kouris, D. and Tsuchida, E., "On The Elastic Interaction between 2 Fibers in a Continuous Fiber Composite under Thermal Loading." Mech. Mater., ***12***, 2, 131 (1991).

15. Kouris D., "Stress-concentration due to The Interaction between 2 Imperfectly Bonded Fibers in a Continuous Fiber Composite." J. Appl. Mech., ***60***, 1, 203 (1993).

16. Kouris D. and Marshall, D., "Damage Mechanisms in Ti3Al Matrix Composites." J. Eng. Mater. & Technol., ***116***, 3, 319 (1994).

17. Ebbessen, T. W., "Carbon Nanotubes: Preparation and Properties.", CRC Press, Boca Raton, Florida, pp.5 (1997).

CHAPTER 6

MARKET RESEARCH

AND

VENTURE BUSINESS FEASIBILITY PLAN

6.1. Executive Summary

A new nano-size graphite flakes and its fabrication process has been established and a provisional patent has been applied by Michigan State University. This material can be commercially produced and sold at competitive price and there is a realistic possibility to make a successful venture business based on this technology.

The product of this technology is conductive nano-size graphite flakes, which can be molded into various resins to form parts and/or enclosures for Electrical and Electronics Industry (E/E Industry) and Automobile Industry.

The applications include:

A. Electrical & Electronics

- Enclosures for Cellular Phones, PDAs, and other Portable Electronics Products
- Disk Drive Housings
- Connectors
- Power Cable Shield

B. Automobile

- Mirror Housings, Door Panels
- Front Grilles, Spoilers, Air Dams
- Radiator Parts, Fans, Air Conditioner Parts,
- Air Inlet Parts
- Fuel Filters

The innovative carbon nanocomposite technology developed at MSU promises to add value to the electrical/electronics enclosure and automobile parts by providing cost

effective alternatives to conventional and/or emerging conductive resins with maintaining good mechanical properties, heat dissipation, and surface quality.

The lead users of this technology are polymer producers and compounders. Polymer producers are seeking to expand the markets for their specific polymers or at least improve the performance and/or cost profile within their specific polymer type. Compounders view nanocomposite technology as another differentiated product that is not easily produced by all compounders, and are looking to carve out an early market lead. Throughout a survey, many resin producers and compounders have shown their interest in this new technology.

In the electrical/electronics enclosure market, the market potential for conductive resins is estimated to be 65 million pounds in 2003 and 78 million pounds by 2009. Since the versatility and cost advantage of the new technology, it has the potential to displace many of the materials currently being used. Electrically conductive plastics are used in the automobile industry, where electrostatic painting methods have been adopted in response to regulations limiting emissions of volatile organic compounds (VOCs). The conductive resin market in automobile industry is predicted to be 38 million pounds in 2004, rising to 140 million pounds in 2009.

The most important attributes for customers have been determined through a marketing survey. The results showed the ranking as:

(1) Cost

(2) Processability

(3) Better EMI Shielding

(4) Light Weight

(5) Toughness

In EMI shielding applications, the proposed technology has the best cost performance compared to other technologies while also maintaining top level properties in processability, EMI shielding ability, and light weight categories. Thus the technology is highly competitive in terms of customer benefits.

The current plan outlines the strategy to set up a plant and provide nanoflakes for resin producers/compounder and/or provide special grade conductive resins to final product manufacturers by toll manufacturing. The team estimates that it would need $1.6 million dollars as the initial investment to cover the machine cost and 4 months of operating cost.

6.2 Product

6.2.1. Purpose of The Product

The product of this technology is conductive **nano-size graphite flakes**, which can be molded into various resins to form parts and/or enclosures for;

- **Electrical and Electronics Industry (E/E Industry)**
- **Automobile Industry**

The graphite nanoflakes can give resins electrical and thermal conductivity that can provide advanced properties/applications such as;

- Electrostatic Dissipation
- Electrostatic Painting
- Electromagnetic Interference (EMI) Shielding
- Heat Management System

Due to the small size of the graphite flakes, they can be incorporated into various commercially available polymers and molded by widely used processing methods including injection molding, resin transfer molding, and sheet molding.

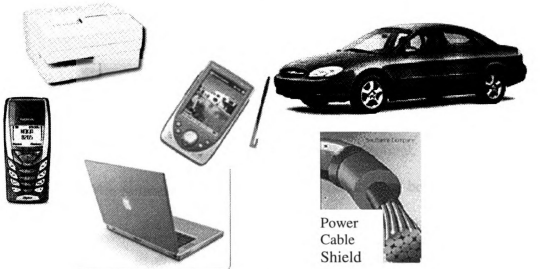

Figure 6.1. Applications for The Proposed Technology

6.2.2. Stage of Development and Proprietary Rights

Process parameters and product specifications have been determined. Michigan State University has filed a provisional patent regarding this technology. The primary inventor is Professor Lawrence T. Drzal (Director, Composite Materials and Structures Center, Michigan State University. drzal@egr.msu.edu) and a co-inventor is Hiroyuki Fukushima (Research Assistant, Composite Materials and Structures Center, Michigan State University. fukushi3@msu.edu).

6.3.3. Product Limitations

Since metals have inherently superior conductivity to graphite, the proposed technology is not suitable for applications, which need very high attenuation of EMI such as military TEMPEST requirement and special aerospace applications. Since cost is not the fist priority in these applications, more complex, expensive, and/or labor-intensive methods are used.

No governmental approvals are required to use this product in commercial applications.

6.2.4. Product Liability

Graphite is basically not toxic to human body. But small flakes may cause inhalation of dust generated during processing and handling. Dermal, ocular, and oral contact must be avoided. High concentrations of graphite dusts may be irritating to the eyes, mucous membranes, and respiratory tract. Since graphite dusts are electrically conductive, accumulations of dust may cause shorting of electrical circuit. The dust

should not be emitted to the atmosphere where they may settle on and cause shorting of outside electrical equipment. To avoid these problems, local exhaust ventilation should be provided in the places where these graphite nanoflakes are processed/handled.

Once these nanoflakes are compounded into resins, there is no further problem. Thus, final users should not have any problem regarding with this technology. And there are no governmental regulations, which limit the use of this material. Also graphite nanoflakes have no environmental concern, since these materials exist in nature. But the resins, in which the graphite nanoflakes are compounded, may have. It totally depends on the property of the resin.

6.2.5. Related Products and Spin-offs

- Power Cable Shield
- Fuel Cell Parts & Hydrogen Storage
- ESD interior and Heat Dissipation Parts for Aircraft
- ESD interior and Heat Dissipation Parts for Military Equipment

6.3. Market Analysis

6.3.1. Market Size

Figure 6.2 shows the predicted market potential for three categories, which are:

- Electronics enclosures
- Electronics Inside Parts
- Automobile Exteriors

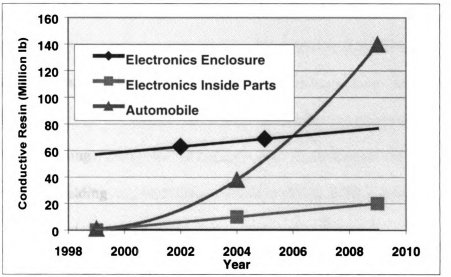

Figure 6.2. Predicted Conductive Resin Market Size

6.3.2. Growth Potential

In the automobile exterior market, only minor quantity of conductive resins was used in 1999. However, considerable growth is expected in the next 5 to 10-year period, averaging **30%** a year. The main driving force of this growth is strict federal and/or local governmental regulations that limit the VOCs emissions. These regulations force automobile manufactures adopt environmentally friendly electrostatic painting process, which requires conductive plastic parts.

On the other hand, the growth rates for electronics enclosure and inside parts markets are expected to be relatively constant. Two forces are at play, the growth in demand for electronic equipment and the ever-shrinking size of the equipment itself. Shrinking dimensions and/or weight dampen the growth in resin consumption. Overall, the growth rate of conductive resin consumption in computer/business market is predicted as **4%.**

6.3.3. Market Trend

A. Electrical/Electronics Market

(1) Final Products

- Thinwalling
- EMI Shielding
- Flame Retardance Property
- Short Product Life Cycle

Since smaller and lighter products with better performance are introduced every year, three major technological attributes are becoming more and more important in this market, which are thinwalling, EMI shielding, and flame retardance property. Other trends include short product life cycles and dropping retail prices. Because of these trends, resin producers and compounders have to change/adjust their products' specifications frequently. Thus, many combinations of resins and fillers are used and many competitors exist in this market.

The purpose of the proposed technology is to offer EMI shielding property for computer/business equipment enclosures while catching up the thinwalling requirement

by providing good processability and surface quality by using conductive nano-size fillers.

(2) EMI Shielding Technology

- Shift from Sheet Metals to Plastics (Light weight, Design Flexibility)
- Popularity of Direct Thermal Evaporation and Conductive Resin is increasing mainly because of environmental concern.

Numerous EMI shielding techniques have been developed to date. These techniques are categorized into three, sheet metal, plastics with coating/plating, and conductive plastics. Among these, most widely used techniques are conductive paints and electroless painting. Table 6.1 summarizes the advantages and disadvantages of widely used Technologies as well as and newly emerging conductive plastic technologies.

Table 6.1. Comparison of Commonly Used EMI Shielding Technologies

Technology	Advantages	Disadvantages	Trends
Sheet Metal	• >65 db • Good for Large Parts	• Heavy • Poor Design Flexibility • Labor Intensive for complex parts	• Being replaced by plastics
Conductive Paints (Ni, Ag, Cu)	• 30-60 db (Ni) • >65db (Ag) • Versatile	• Environmental Concern • (Voss)	• Environmental Concern Limits the Expansion
Electroless Plating (Cu/Ni)	• 65-100db • Typical for Injection Molding Process	• Requires Large Amount of Poisonous Chemicals	• Environmental Concern Limits the Expansion
Direct Thermal Evaporation (Al, Ag, Cu, Ni)	• 60-120 db • New Process Can Offer Good Enough Adhesion • Minimal Environmental Concern	• Complex Process -Level of Expertise Required • Limited Suppliers Exist	• Gaining Popularity
Conductive Resin (CF, Ni-CF, Stainless steel fiber, Al fakes, VGCF, MSU Technology)	• 30-60 db • Lower Total Cost for Small, Complex Parts • No Environmental Concern	• Surface Quality Concern (Can be overcome by nanotechnology) • Needs Painting Process	• Gaining Popularity (Nanotechnology)

B. Automobile market

- Electrostatic Painting (Environmentally friendly process)
- Body-matched Colors for Exterior Plastic Parts
- More and More Electrically Controlled Devices are used in Under the Hood Applications (Demand for More EMI shielding without adding heavy weight)

Every year, plastic resins are replacing metals in automobile parts applications and this trend is expected to be maintained for the future. The main advantages of plastic usage in automobile parts include lightweight and design flexibility.

Because of increasing environmental concerns, both federal and local governments are setting more and more strict regulations, which limit the maximum total VOCs that can be emitted from a factory. To increase productivity, automobile manufacturers have to adopt painting processes with low VOCs emission. To overcome this problem, people have been using conductive primer (coating) on plastic parts prior to the painting process. But overall cost was increased because of the additional step. Recently some companies reported that conductive nanocomposites, could offer enough conductivity for electrostatic painting while maintaining enough mechanical properties and surface quality. At this point, the prices of those fillers are too expensive to be used in many applications. But once affordable nano-size fillers are available, they should be widely accepted in these applications. Electrostatic painting is eco-compliant and conductive resins can carry Eco-labels.

Also automobile buyers' preference for body-matched color for exterior plastic parts promotes the shift from conventional spraying to electrostatic painting.

Manufactures can assemble the conductive plastic parts on metal bodies and apply one-step painting using the same paints for metal bodies and plastic parts.

6.3.4. Competition Profile – Conductive Plastics

Table 6.2 directly compares MSU's conductive filler technology with the other technologies. It shows the MSU technology has apparent cost advantage in EMI shielding applications while maintaining good processability, lightweight, strength, and surface quality. Thus, this technology is considered to be very competitive in EMI shielding applications and can replace some of the existing conductive plastics in the market today.

In electrical/electronics market, shorter product life cycle forced resin producers to adjust or change the specifications of their products frequently. Thus, many competitors exist and variety of resin/filler combinations are used. On the other hand, the automobile application is dominated by GE plastics' Noryl GTX (PPE/PA//VGCF). The advantages of this material include low percolation threshold, good mechanical properties, good surface quality, and good processability. The main disadvantage is cost, since the price of VGCF is still high ($30-$40/lb). This technology is categorized as nanotechnology VGCF in **Table 6.2** (second column from right). The proposed technology has the same level of percolation threshold, mechanical properties, surface quality and processability, while total cost would be lower. Thus this technology has realistic possibility to replace VGCF in this market and in fact GE plastics showed strong interest in our technology during the research.

Table 6.2. Comparison of Conductive Fillers

	Conventional Fillers					Naotechnology		
Fillers	Stainless Steel Fiber	Al Flake	Ni coated CF	PAN based CF	Carbon Black	Nanosize Carbon Black	VGCF (GE)	MSU
Cost of Fillers ($/lb)	25	3.27	30	15	0.29	12.8	30	5 *
Dimension	D=8 um L=5 mm	T=25um D=1mm	D=7um L=5mm	D=7um L=5mm	D=30um	D=500 nm	D=150 nm L=50um	T=20nm D=1um
Wt% Filler for ESD **	4	15	5	10	20	3	3	3
Cost for *** ESD ($/lb)	1.48	0.916	1.975	1.95	0.458	0.869	1.385	0.635
Wt% filler for EMI****	7	30	10	25	---	6	6	6
Cost for *** EMI ($/lb)	2.215	1.331	3.45	4.125	---	1.238	2.27	0.77
Process-ability	Good	Poor	Good	Fair	Poor	Poor	Good	Good
Weight	Heavy	Heavy	Heavy	Heavy	Heavy	Light	Light	Light
Toughness	Fair	Poor	Fair	Fair	Fair	Fair	Fair	Fair
Strength	Fair	Fair	Good	Good	Fair	Fair	Fair	Fair
Surface Quality	Fair	Poor	Fair	Fair	Poor	Poor	Good	Good

* Estimated from pricing analysis. ** To achieve resistivity of 10^6 ohm*cm

*** Material cost. The cost of resin is assumed as $0.5/lb. The processing cost was not incorporated in this analysis.

**** To achieve resistivity of 10^1 ohm*cm

6.3.5. Customer Profile

The supply-chain in this business includes filler producers, resin producers, compounders/molders, and final product manufactures. Since resin producers and molders are the real conductive resin manufactures, the report is focused on these two categolies.

A. Resin Producers

The major players in this market are the resin producers themselves. They posses the expertise and carry the responsibility of providing resin to molders that meet strict shrinkage, warping, surface quality, and processability requirements. The resins must also meet the impact strength, stiffness, flexural strength, and cost requirements of the enclosure manufacturers. Some resin producers are selling their own grades of conductive resins. These resin producers are buyers of conductive fillers, decision makers of the specifications of the products, and influencers in the market.

Table 6.3. Resin Producers for E/E Industry in North America

Company	Contact
BASF Plastics	www.basf.com/static/989496184326.html
Bayer Corporation	www.bayer.com/kontact/kontact_en.html
Chevron Corporation	www.chevron.com/about/about.shtml
Dow Chemicals	http://www.dow.com/wire/region_na/power/semi.htm
GE Plastics	www.geplastics.com/resins/contact/staticindex.html
Georgia-Gulf, Inc.	www.ggc.com/f_contacts.asp
NOVA Chemicals	www.novachem.com/02_this/02_contacts_f.htm
Oxyvinyls	www.oxyvinyls.com/tech-licensing/edc-vcmcontacts.html

Among these, BASF plastics, Bayer Inc., Dow Chemicals and GE Plastics are the main resin producers for both automobile and electrical/electronics industries. Especially, Dow and GE Plastics are investing huge money on conductive resin research and these companies are most likely interested in our new technology.

B. Compounders

Some of the compounders are selling conductive plastics with various combinations of resins and fillers. They have their own R & D divisions and seeking new technologies in the area. **Table 6.4** shows the compounders who make conductive resins in North America. These companies often provide custom grade products according to their customer needs. They are buyers of conductive fillers and decision makers who decide which fillers to use.

Table 6.4. Compounders for E/E Industry in North America

Company	Contact
Albis Corporation	www.albisna.com
A. Schulman Inc.	http://www.aschulman.com/markets.asp?market_id=2
DSM Engineering Plastic Products	http://www.dsmep.com/america/products/product_porfolio/electra_grades.asp
Ferro Corporation	http://www.ferro.com/our+products/
LNP Engineering Plastics	http://www.lnp.com/LNPSite.nsf
RTP Corporation	http://www.rtpcompany.com/products/conductive/index.htm
Ticona	http://www.ticona-us.com/MktApps/ITOver.cfm
Thermofil	

Among these, DSM Engineering Plastic Products and Ticona showed interests in our new conductive fillers.

6.3.6. Customer Benefits

A. Survey

To investigate the most important attributes for customers, a marketing survey has been conducted. A questionnaire has been sent to resin producers and compounders listed in **Table 6.3** and **6.4**. The objectives of this survey were:

- Identify Current Technologies and their problems.
- Investigate the interest level in our technology and possibility of introducing our fillers into their products.
- Quantify benefits/attributes.

B. Survey Results

GE Plastics, NOVA Chemicals, and DSM Engineering have replied the survey. Also DOW Chemicals and Ticona responded. Among these GE Plastics, DOW Chemicals and DSM Engineering showed strong interest in MSU technology. NOVA Chemicals and Ticona showed moderate interest at this point.

Basically these companies are using many filler/resin combinations. Some said they choose carbon blacks for economy and carbon fibers for mechanical properties. But none of the conventional conductive plastics shows well-balanced combination of cost, toughness, EMI shielding ability, and surface quality. A plastic that is cost effective as metal, but with good processability, toughness, and low percolation threshold (better EMI shielding) would be what these people want to see. Nanocomposite technology could provide a valid answer for this demand.

Figure 6.4 shows the quantitative data of attributes by accumulating the survey results.

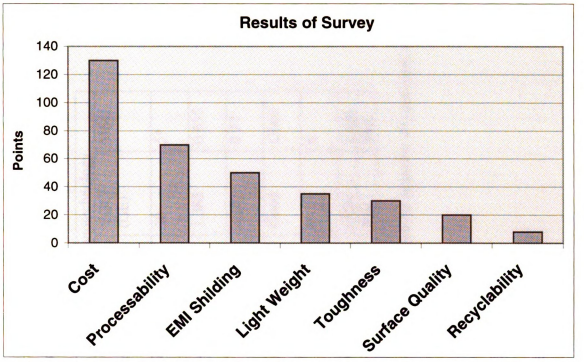

Figure 6.3. Quantification of Attributes for Conductive Resins

Thus, the important attributes for conductive resins are ranked as:

(1) Cost

(2) Processability

(3) Better EMI Shielding

(4) Light Weight

(5) Toughness

C. Value Proposition

Table 6.5 summarized the competition profile of MSU technology against other conductive plastics in these five attributes. The MSU technology has the best-cost performance as EMI shielding material while maintaining good processability, lower percolation threshold (wt% filler for EMI) and lightweight.

Table 6.5. Conductive Fillers Comparison

	Conventional Fillers					Nanotechnology		
Fillers	Stainless Steel Fiber	Al Flake	Ni coated CF	PAN based CF	Carbon Black	Nanosize Carbon Black	VGCF (GE)	MSU
Cost of Fillers ($/lb)	25	3.27	30	15	0.29	12.8	30	5*
Cost for** ESD ($/lb)	1.48	0.916	1.975	1.95	0.458	0.869	1.385	0.635
Cost for** EMI ($/lb)	2.215	1.331	3.45	4.125	---	1.238	2.27	0.77
Process-ability	Good	Poor	Good	Fair	Poor	Poor	Good	Good
Wt% filler for EMI	7	30	10	25	---	6	6	6
Weight	Heavy	Heavy	Heavy	Heavy	Heavy	Light	Light	Light
Toughness	Fair	Poor	Fair	Fair	Fair	Fair	Fair	Fair

* Estimated from pricing analysis.

** The cost of resin is assumed as $0.5/lb. The processing cost was assumed the same for all cases and, thus, was not incorporated in this cost analysis.

6.3.7. Target markets

A. Electrical & Electronics

- Enclosures for Cellular Phones, PDAs, and other Portable Electronics Products
- Disk Drive Housings
- Connectors
- Power Cable Shield

B. Automobile

- Mirror Housings, Door panels
- Front Grilles, Spoilers, Air Dams
- Radiator parts, fans, Air conditioner parts,
- Air inlet parts
- Fuel Filters

6.3.8. Market Penetration

Since target customers are well identified, the products will be sold directly to these customers.

6.4. Price and Profitability

6.4.1. Predicted Production Volume

Table 6.6 shows the predicted nanoflakes production based on the market size shown in Figure 1 and target market share. Since competition in electronics enclosure market is considered tough, the market share in this category is estimated at relatively low. On the other hand, the market shares in the automobile market and E/E inside parts categories are predicted high, since there are less competitions exist. Actually GE plastics' Noryl GTX now dominates these markets, but the proposed technology has apparent cost advantages over this and GE is strongly interested in our technology because of this cost advantage. Thus, it is possible to replace some or all of the fillers now used in Noryl GTX with the proposed graphite nanoflakes.

6.4.2. Pricing, Sales, and Net Operating Income (Gross Margin)

Price of product is determined by mathematical pricing strategy, which is based on the cost of production. **Table 6.7**. shows the predicted variable costs, which include materials, labor and other variable costs. Table 8 shows the fixed costs.

Based on the costs and predicted production volume, the pricing and the sales are estimated as follows. The net operating income (gross margin) is calculated from these estimates. These values are summarized in **Table 6.9**.

6.4.3. Breakeven Point Analysis

The breakeven point in terms of both sales and production volume was calculated based on contribution margin ratio in **Table 6.7.** The results are shown in **Table 6.10**.

6.4.4. Start-up Costs and Additional Investment

The start-up cost is estimated from required machine cost for the first two years and the operating cost for the first four months, which includes variable costs and rent. The additional investment is based on the machine cost, which is required to expand the production in each of the following years. These are summarized in **Table 6.11**.

6.4.5. Horizon Analysis

The horizon value for this business (technology) in the year 2010 is estimated in 6 different cases. The assumptions for the calculations include:

- The NPV (Net Present Value) of investment is calculated by assuming people can get 6%/year interest when they invest the money on bonds and/or other methods.
- The growth rate after year 2010 is assumed to be perpetual. The rate is fixed at 10, 8, 6, 4, 2, and 0 % in each case.
- Discount rate is fixed at 12%.

Table 6-12 summarized the pro forma financial projection until 2009 and **Table 2-13** shows the horizon analysis in each case.

Table 6.6. Predicted Graphite Nanoflakes Production

Calendar Year	2003	2004	2005	2006	2007	2008	2009
E/E Enclosure (lb)	65,327,750	67,286,550	69,030,000	71,095,000	73,233,750	75,431,500	77,703,000
Market Share of MSU Technology	2%	4%	6%	8%	10%	10%	10%
E/E Inside Parts (lb)	2,000,000	10,000,000	11,500,000	13,225,000	15,209,000	17,500,000	20,000,000
Market Share of MSU Technology	10%	15%	20%	25%	30%	35%	35%
Automobile (lb)	29,230,000	38,000,000	49,400,000	64,220,000	83,486,000	108,532,000	140,000,000
Market Share of MSU Technology	10%	15%	20%	25%	30%	35%	35%
Power Cable Shield	-	-	-	-	-	-	-
Fuel Cell	-	-	-	-	-	-	-
Total Resin Consumption (lb)	96,557,750	115,286,550	129,930,000	148,540,000	171,928,750	201,463,500	237,703,000
Resins based of MSU technology (lb)	4,429,555	9,891,462	16,321,800	25,048,850	36,931,875	51,654,350	63,770,300
Predicted Nanoflakes Production (lb)	221,478	494,573	816,090	1,252,443	1,846,594	2,582,718	3,188,515

Table 6.7. Variable Costs

Variable Cost	2003	2004	2005	2006	2007	2008	2009
Raw Material ($1.6/lb)	538,674	1,028,712	1,697,467	2,605,080	3,840,915	5,372,052	6,632,111
Water (400L/hr, $0.05/L)	38,400	76,800	115,200	120,960	322,560	322,560	322,560
Chemicals (100L/hr, $0.5/L)	96,000	192,000	288,000	302,400	806,400	806,400	806,400
Chemicals Disposal Fee ($0.5/lb)	38,847	74,186	122,414	140,900	276,989	387,408	478,277
Electricity ($0.065/kW)	74,880	149,760	224,640	235,872	314,496	314,496	314,496
Cost of Sales [Packaging] ($0.2/lb)	51,796	98,915	163,218	250,489	369,319	516,544	637,703
Delivery Charges ($0.5/lb)	129,489	247,287	408,045	626,221	923,297	1,291,359	1,594,258
Wages ($40,000/person, 6% increase/yr)	120,000	212,000	314,608	428,766	656,488	695,877	737,630
Payroll Tax ($8400/person, 6% Increase /yr)	25,200	44,520	47,191	70,032	74,234	75,045	83,409
Benefits ($6000/person. 6% Increase/yr)	18,000	31,800	47,191	64,315	98,473	104,382	110,644
<Total Valuable Cost>	1,131,285	2,155,979	3,427,974	4,845,034	7,683,171	9,886,123	11,717,488
Contribution Margin	293,093	415,801	652,476	1,417,178	1,549,798	2,769,193	3,587,384
Contribution Margin Ratio	0.206	0.162	0.160	0.226	0.168	0.219	0.234
Variable cost per lb	4.368	4.359	4.200	3.868	4.161	3.828	3.675

Table 6.8. Fixed Costs

Fixed Cost	2003	2004	2005	2006	2007	2008	2009
Rent (6% Increase/year)	120,000	127,200	134,832	142,922	151,497	160,587	170,222
Depreciation (10years for each machine)	122,000	122,000	122,000	162,000	202,000	268,500	328,500
Machine Maintenance Cost (6% Increase/yr)	24,000	25,440	26,966	28,584	60,599	64,235	68,089
Insurance (Machines, Rent, 6% Increase/yr)	15,000	15,900	16,854	17,865	18,937	20,073	21,278
Fees for Consultants (6% Increase/yr)	12,000	12,720	13,483	14,292	15,150	16,059	17,022
Fees for Attorneys (6% Increase/yr)	30,000	31,800	33,708	35,730	37,874	40,147	42,556
Fees for Accountants (6% Increase/yr)	12,000	12,720	13,483	14,292	15,150	16,059	17,022
R & D Cost ($30,000/RA, 6% Increase/yr)	30,000	31,800	33,708	71,461	75,749	80,294	85,111
Electricity (Office, $2,000/month)	24,000	24,000	24,000	24,000	24,000	24,000	24,000
Office Supply, Internet (6% Increase/yr)	12,000	12,720	13,483	14,292	15,150	16,059	17,022
Advertising (6% Increase/year)	12,000	12,720	13,483	14,292	15,150	16,059	17,022
<Total Fixed Cost>	413,000	429,020	446,001	539,732	631,255	722,070	807,845
Fixed Cost per lb	1.595	0.867	0.547	0.431	0.342	0.280	0.253

Table 6.9. Pricing, Sales, and Net Operating Income

Calendar Year	2003	2004	2005	2006	2007	2008	2009
Price ($/lb)	5.50	5.20	5.00	5.00	5.00	4.90	4.80
<Sales>	1,218,128	2,571,780	4,080,450	6,262,213	9,232,969	12,655,316	15,304,872
Total Valuable Cost	1,131,285	2,155,979	3,427,974	4,845,034	7,683,171	9,886,123	11,717,488
Total Fixed Cost	413,000	429,020	446,001	539,732	631,255	722,070	807,845
Net Operating Income	(119,907)	(13,219)	206,475	877,446	918,543	2,047,123	2,779,539
Income/Sales	(8.42)	(0.51)	5.06	14.01	9.95	16.18	18.16

Table 6.10. Breakeven point

Calendar Year	2003	2004	2005	2006	2007	2008	2009
Break Even point (Sales $)	2,007,105	2,653,542	2,789,200	2,384,961	3,760,721	3,299,889	3,446,511
Predicted sales (4)	1,424,378	2,571,780	4,080,450	6,262,213	9,232,969	12,655,316	15,304,872
Break Even Point (Production lb)	364,928	510,296	557,840	476,992	752,144	673,447	718,023
Predicted production (lb)	258,978	494,573	816,090	1,252,443	1,846,594	2,582,718	3,188,515

Table 6.11. Start-up Costs and Additional Investment

Calendar Year	2003	2004	2005	2006	2007	2008	2009
Machine Cost	1,220,000	-	400,000	400,000	665,000	600,000	600,000
Monthly Operating Cost	104,874	-	-	-	-	-	-
Total Investment	1,639,495	-	400,000	400,000	665,000	600,000	600,000
Cumulative Investment	1,639,495		2,039,495	2,439,495	3,104,495	3,704,495	4,304,495

Table 6.12. Pro Forma Financial Projection

Calendar Year	2003	2004	2005	2006	2007	2008	2009
Growth Rate %	-	80.55	58.66	53.47	47.44	37.07	20.94
Revenue (Sales)	1,424,378	2,571,780	4,080,450	6,262,213	9,232,969	12,655,316	15,304,872
Variable Costs	1,131,285	2,155,979	3,427,974	4,845,034	7,683,171	9,886,123	11,717,488
Capital (Cumulative Investment)	1,639,495	1,639,495	2,039,495	2,439,495	3,104,495	3,704,495	4,304,495
Depreciation	163,949	163,949	203,949	243,949	310,449	370,449	430,449
Pretax Profit	(119,907)	(13,219)	206,475	877,446	918,543	2,047,123	2,779,539
After-tax Profit (Tax = 38%)	(119,907)	(13,219)	128,014	544,017	569,497	1,269,216	1,723,314
Increase in Capital (Investment)	-	-	400,000	400,000	665,000	600,000	600,000
Free Cash Flow	44,042	150,730	(68,036)	387,966	214,946	1,039,666	1,553,764
Cumulative Cash Flow	44,042	194,773	126,737	514,703	729,649	1,769,315	3,323,078

Table 6.13. Horizon Analysis

	Free Cash Flow @2010	Assumed Growth Rate	Discount Rate	Horizon Value at 2010	NPV	IRR
Case A (Assume 10% annual growth after 2010)	1,686,346	10.00%	12.00%	92,749,042	35,754,144	24.587%
Case B (Assume 8% annual growth after 2010)	1,637,379	8.00%	12.00%	44,209,231	16,149,728	23.376%
Case C (Assume 6% annual growth after 2010)	1,588,412	6.00%	12.00%	28,061,939	9,628,107	22.194%
Case D (Assume 4% annual growth after 2010)	1,539,444	4.00%	12.00%	20,012,776	6,377,186	21.040%
Case E (Assume 2% annual growth after 2010)	1,490,477	2.00%	12.00%	15,202,866	4,434,544	19.916%
Case F (Assume 0% annual growth after 2010)	1,441,510	0.00%	12.00%	12,012,581	3,146,041	18.821%

6.5. Business Model

6.5.1. Commercial Validation

This research revealed a realistic commercialization possibility of the "Electrically and Thermally Conductive Carbon Nanocomposites" developed at Michigan State University. The potential customers and markets are identified. These companies are very important for this technology to be accepted in real business world. Noe the next step for this business should be commercial validation. The graphite nanoflake samples would be sent to the potential customers (resin producers and compounders) and evaluated.

6.5.2. Commercialization Strategy

Once commercial validation goes well and some of the potential customers are interested in the technology, next step will be applying utility patents to protect all the proprietary rights. More detailed IP strategy is written in the next section.

After proprietary rights are protected, the initial investment capital will be raised and the business will start as a filler producer. The products will be sold to resin producers and compounders.

6.5.3. IP Strategy

Although a provisional patent has been filed, it DOES NOT provide any legal protection and "Patent Pending" is only a warning to competitors implying an utility patent may be files at any time with claims covered by the provisional patent. A utility patent, which covers all the necessary claims, must be filed within 1 year from the provisional patent filing date to protect this technology.

Additional patents may be required to expand the possibility of this technology, especially in terms of product patents including fuel cell and other battery applications. Also filing foreign patents may also be required in the future since this technology is versatile and could be used various industries worldwide. In this case the foreign patents must be filed within 1 year from the date when the utility patent is filed.

6.5.4. Mid Term Business Strategy

To expand the business opportunity of this technology, further research effort should be focused on investigating various polymer systems and establish our own conductive plastic grade, which can be sold to the final product manufactures. This requires more marketing and R & D efforts, but certainly helps to expand the market share of the technology.

The key polymer systems for this technology are:

1. E/E Industry - GE Plastics, Dow Chemical, BASF, Bayer
    - ABS (Acrylonitrile-Butadiene-Styrene rubber)
    - ABS/PC (Polycarbonate)
    - HIPS, SAN (Styrene-Acrylonirile copolymer)
    - PVC (Polyvinyl chloride)
2. Automobile Industry – GE Plastics, DuPont, Dow Chemical, BASF
    - PPE/Nylon (Polyphenylether/Nylon)
    - TPEs (Thermoplastic Elastomers), Polyurethane
    - Nylons

- PET, PBT (Polyethylene terephthalate, Polybutylene terephthalate)

3. Power Cable - DOW Chemical
   - PE (Polyethylene)
4. Aerospace
   - Polyimide

Once the specification of these composites are determined, these samples can be provided to the final product manufactures in electrical/electronics, automobile, medical, and aerospace, industries to expand the business.

6.5.5. Long Term Business Strategy

Investigating other markets such as fuel cell, lithium battery, and space/defense markets could provide attractive opportunities. Among these, fuel cell technology seems to be most attractive. It takes further research effort to confirm the validation of this technology in fuel cell application. This should be considered as a long-term business plan.

6.6.6. Exit Strategy

Once the business is established and achieves sustainable growth, it will be sold to other company. Filler producers and/or resin producers will most likely acquire this business to enhance their market share and presence in the conductive resin market.

6.6. Award

The venture business plan based on this new technology won "The Most Innovative Design" award at 2002 Michigan Collegiate Entrepreneur's Conference.

CHAPTER 7.

CONCLUSIONS

AND

RECOMMENDATIONS FOR FUTURE RESEARCH

Natural crystalline graphite has excellent mechanical, electrical, and thermal properties while the cost is very low. This material could be used in many applications if an appropriate process was established. Recent development of clay nanocomposite systems gave motivations to developed graphite nanocomposites to design new advanced nanocomposite systems, which can be used in a variety of applications, yet this field has not been investigated in depth. The objectives of this research were:

- Investigate processes to achieve exfoliated nano-scale graphite platelets.
- Investigate appropriate surface treatments and surface characteristics of graphite nanoreinforcement to achieve good dispersion and adhesion in polymer matrices.
- Achieve nanocomposites with superior mechanical, thermal and electrical properties to expand the possibility of applications in which these materials may be used.

CONCLUSIONS

(1) New process to fabricate nanosize graphite flakes

A new process to fabricate new nanosize graphite material has been developed. This research revealed the size of the graphite flakes was about 10nm in thickness. The diameter of the nanoflakes can be controlled, down to less than 1um. The surface area of the material was around 100 m^2/g. These materials can be used as reinforcements in polymer matrices as well as other advanced applications. A provisional patent has been filed about this new process and material.

(2) Appropriate Surface Treatment

An appropriate surface treatment for the materials was investigated and acrylamide grafting treatment was proved to be effective to enhance the adhesion between graphite nanoreinforcement and epoxy matrix.

(3) Properties of Graphite Nanocomposites

The surface treated graphite reinforced composites showed better mechanical properties than those reinforced with commercially available carbon materials. The new graphite nanoflakes was also proved as excellent conductive filler. The composite systems with this new material showed comparable or better conductivity properties than those with conventional CF, VGCF, or carbon black. Overall, this new material has been proved to be an excellent reinforcement for epoxy composite systems.

(4) Optimal Nanocomposite Design

Theoretical simulations showed various factors affect the stress condition of the nanocomposite systems. The results suggested that a composite with fillers in parallel arrangement at an optimal distance could give the best performance in terms of mechanical properties. If the adjacent fillers are packed close enough, the tunneling phenomena occur and the total system would be conductive. Thus, a nanocomposite with good mechanical and electrical properties could be designed based on this knowledge.

(5) Market Research and Possibility of Commercialization

Market research and cost estimation showed the material could be sold at $5/lb or less, which is very economical as a carbon/graphite based material and gives realistic possibility for it to be used in many applications. Possible applications include automobile, electrical/electronics, aerospace, and military industries. A provisional patent has been filed, which includes both the material and the process. A venture business plan has been proposed based on this new technology and the plan won "The Most Innovative Design" Award at 2002 Michigan Collegiate Entrepreneurship Conference.

RECOMMENDATIONS FOR FUTURE WORK

(1) Single Layer Crystalline Graphite

The newly developed graphite nanoflakes have thickness of around 10nm. This indicates that 20 to 30 layers of graphene sheets are still stacking together. Because of this layered structure, the graphite flakes show significantly lower properties in c-direction. If these layers are completely exfoliated to form single layer graphite nano flakes, the resulted material could show excellent properties in any directions. To fabricate this material, a totally new process is required.

(2) New Graphite Nanocomposites

The new graphite nanoflakes can be used in many polymer composite systems and the optimal surface and process conditions should depend on matrix and application. Thus, it is necessary to investigate these conditions for applicable thermoplastic and thermoset polymers. The key polymer systems for this technology are:

1. E/E Industry

   ABS (Acrylonitrile-Butadiene-Styrene rubber), ABS/PC (Polycarbonate), HIPS, SAN (Styrene-Acrylonirile copolymer), PVC (Polyvinyl chloride)

2. Automobile Industry

   PPE/Nylon (Polyphenylether/Nylon), TPEs (Thermoplastic Elastomers), Polyurethane, Nylons, PET, PBT (Polyethylene terephthalate, Polybutylene terephthalate), Biodegradable Plymers

3. Power Cable

   PE (Polyethylene)

4. Aerospace

   Polyimide

(3) Fuel Cell

Also this material could be used in other advanced applications. One is the parts for fuel cell systems. Separators for fuel cell systems have been made of thin metal plates, but they are heavy and corrosive. Strong, light weight, and non-corrosive graphite sheets and/or graphite based conductive composites could replace the existing metal based separators. Also this new graphite nanoflakes could be used in fuel storage systems. Carbon nanotubes and VGCF are known to store hydrogen well and considered to be used as fuel storage media, but the cost of these materials are high. The new graphite material developed in this research has high surface area with reasonable cost and considered to be used in this application, too. The absorption/desorption condition of hydrogen gas need to be investigated.

(4) Lithium Batteries

Lithium batteries are another possible applications. Many carbon-based materials are used as anode and/or cathode materials in this application. The lithium capacity, charge retention, and thermal stability are key factors.

CHAPTER 8

APPENDIX

Appendix A1

Griffith Crack Theory

Consider a crack of length a is introduced in a material which is subjected to an applied uniform tensile stress. The energy to create new surface that has surface tension γ_s can be written as:

$$S = 2a\gamma_s \tag{A1-1}$$

for a small change in length *d*a, it becomes:

$$dS = 2\lambda_s \cdot da \tag{A1-2}$$

Assume the volume of the crack is πa^2. The change in elastic energy due to crack propagation is written as:

$$U = \frac{\sigma^2}{2E}\pi a^2 \tag{A1-3}$$

where E is Young's modulus of the material. For a small change in length *d*a,

$$dU = \frac{\sigma^2}{E}\pi a \cdot da \tag{A1-4}$$

Griffith assumed (A1-2) and (A1-4) are equal, thus:

$$\sigma = \sqrt{\frac{2E\gamma_s}{\pi a}} \tag{A1-5}$$

Appendix A2

Weibull Equation

Assume a piece of pure solid material is made of many small portions, which are linked together by chains, and the probability of failure of a single link under a fixed stress is P_0. Now the probability of survival of the link is expressed as $1-P_0$. If the material has total of n chains inside, the probability of survival of all the chains, thus the material, will be $(1-P_0)^n$ and the probability of failure of the material, P_n, is written as:

$$P_n = 1-(1-P_0)^n \qquad \text{or} \qquad 1-P_n = (1-P_0)^n \tag{A2-1}$$

Here,

$$\ln(1-P_n) = n \cdot \ln(1-P_0)$$

$$(1-P_n) = \exp\{n \cdot \ln(1-P_0)\}$$

$$P_n = 1-\exp\{n \cdot \ln(1-P_0)\} \tag{A2-2}$$

Weibull defined the risk of failure, R, as:

$$R = -n \cdot \ln(1-P_0) \tag{A2-3}$$

Now assume the total volume of the solid material is V and this can be divided into small volumes, V_0. Then the number of links, n, should be a function of V/V_0, thus:

$$R \propto -\frac{V}{V_0} \cdot \ln(1-P_0) \tag{A2-4}$$

Now think V is infinitesimally small volume, dV:

$$dR \propto -\frac{dV}{V_0} \cdot \ln(1-P_0) \tag{A2-5}$$

which shows that the risk of failure of a material with infinitesimally small volume is a

function of volume, V_0. Also it should be a function of stress, too. Thus dR can be expressed as:

$$dR = f\left(\sigma, \frac{1}{V_0}\right)dV \tag{A2-6}$$

If V_0 is a constant value, we can integrate (2A-6) and get:

$$R = \int f\left(\sigma, \frac{1}{V_0}\right)dV \tag{A2-7}$$

Combine (2A-2), (2A-3), and (2A-7) and summarize it.

$$P_n = P_v = 1 - \exp\left\{-\int f\left(\sigma, \frac{1}{V_0}\right)dV\right\} \tag{A2-8}$$

To get an appropriate function for this equation, Weibull conducted a large scale of experiments and plotted the fraction of broken fibers against failure stress. The result showed a smooth curve (Fig. 2A-1). To represent the curve, Weibull proposed a function shown below.

$$f\left(\sigma, \frac{1}{V_0}\right) = \left(\frac{\sigma - \sigma_u}{\sigma_0}\right)^m \tag{A2-9}$$

where σ is the applied stress, σ_u is the stress below which no failure occurs, σ_0 is a material constant which is related to the density of the material, and m is the Weibull modulus or Weibull shape factor which is related to the variability of flaw size in the material. The values of material constants σ_u, σ_0, and m are based on empirical data. Now substitute (2A-9) into (2A-8) and we can get:

$$P_v = 1 - \exp\left\{-\int\left(\frac{\sigma - \sigma_u}{\sigma_0}\right)^m dV\right\} \tag{A2-10}$$

If the stress is distributed evenly throughout the material, (2A-10) should be written as:

$$P_v = 1 - \exp\left\{-\left(\frac{\sigma - \sigma_u}{\sigma_0}\right)^m V\right\} \qquad \text{(A2-11)}$$

This equation represents empirical data curve very well. (165)

Now consider a material with σ_u is 0. Suppose there are two specimens which are made of the same material but have different volumes, V_1 and V_2. Here assume the median failure stresses, at which P_v=0.5, for both specimens are σ_1 and σ_2. Put these into (2A-11) and we get:

$$0.5 = 1 - \exp\left\{-\left(\frac{\sigma_1}{\sigma_0}\right)^m V_1\right\} \quad \text{and} \quad 0.5 = 1 - \exp\left\{-\left(\frac{\sigma_2}{\sigma_0}\right)^m V_2\right\}$$

Compare these and summarize it.

$$\frac{V_2}{V_1} = \left(\frac{\sigma_1}{\sigma_2}\right)^m \qquad \text{(A2-12)}$$

This equation shows that if V_2 is larger than V_1, σ_1 is larger than σ_2 and vise versa, which means smaller specimen has higher strength.

Appendix A3

Critical Reinforcement Volume

The assumptions for this theory includes:

1. Perfect bonding between matrix and reinforcements.
2. Reinforcements have high aspect ratio.
3. Fibers are not necessarily aligned.

If very small amount of reinforcements are added to a matrix, the material will be weakened rather than strengthened. But if we add enough amount of reinforcements, the composite will be stronger than the matrix itself. Thus, there should be a critical filler volume fraction necessary to achieve reinforcement by fillers. At critical reinforcement volume, the strength of composite should be the same as that of matrix. Thus,

$$\sigma_{cu} = \sigma_{mu} \tag{A3-1}$$

where σ_{cu}: Ultimate strength or breaking stress of composite

σ_{mu}: Ultimate strength or breaking stress of matrix

Here introduce rule of mixtures.

$$E_c = V_f \cdot E_f + V_m \cdot E_m \tag{A3-2}$$

where E_c, E_f, E_m: Tensile modulus of composite, reinforcement, and matrix.

V_f, V_m: Volume fraction of reinforcements and matrix.

Now we assumed that the reinforcements are not necessarily aligned in stress direction, thus (A3-2) should be rewritten as:

$$E_c = x_1 \cdot V_f \cdot E_f + V_m \cdot E_m \tag{A3-3}$$

where x_1: A factor which relates the reinforcements alignment, $0<x_1<1$.

From the definition, E_c is written as:

$$E_c = \frac{\sigma_{cu}}{\varepsilon_{cu}} \tag{A3-4}$$

where ε_{cu}: Ultimate strain of composite.

Now consider the ultimate strain of reinforcement is smaller than that of matrix. (Most polymer composites are included in this category.) In this case, the composite begins to fail when the strain of composite reaches the ultimate strain of reinforcement. Thus,

$$\varepsilon_{cu} = \varepsilon_{fu} = \frac{\sigma_{fu}}{E_f} \tag{A3-5}$$

Substitute (A3-5) into (A3-4), and then substitute it into (A3-3) gives:

$$E_c = \frac{\sigma_{cu}}{\sigma_{fu}/E_f} = x_1 \cdot V_f \cdot E_f + V_m \cdot E_m \tag{A3-6}$$

Denote the critical reinforcement volume as $V_{f\,min}$, thus:

$$V_f = V_{f\,\min} \quad \text{and} \quad V_m = (1 - V_{f\,\min}) \tag{A3-7}$$

Now substitute (A3-1) and (A3-7) into (A3-6) and summarize it.

$$V_{f.\min} = \frac{E_f \sigma_{mu} - E_m \sigma_{fu}}{(x_1 E_f - E_m)\sigma_{fu}} \tag{A3-8}$$

This shows that stronger (higher σ_{fu}) gives smaller $V_{f\,min}$.

Appendix A4

Average Dispersion Distance --- Spherical filers

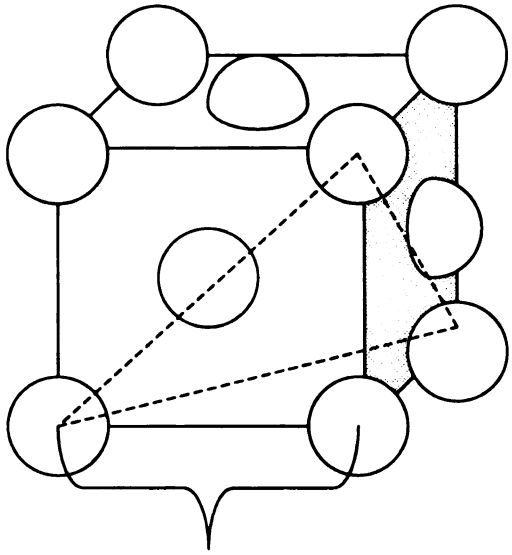

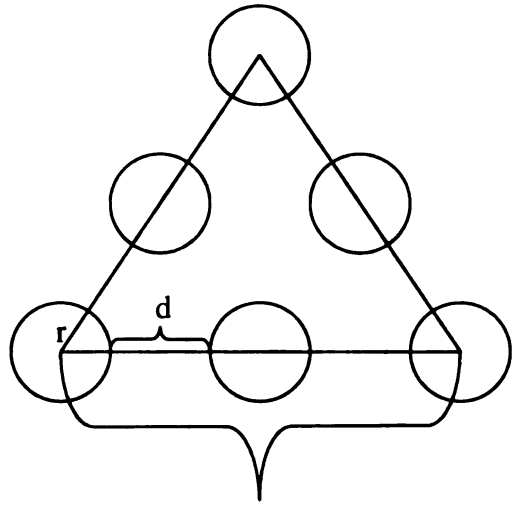

$$\sqrt{2}L = 4r + 2d$$

Now the volume fraction of fillers can be written as:

$$V_f = \frac{4 \cdot \frac{4}{3}\pi r^3}{L^3} = \frac{\frac{16}{3}\pi r^3}{\left(\frac{4r+2d}{\sqrt{2}}\right)^3} \qquad \text{(A4-1)}$$

Summarize this equation and we can get:

$$d = \left\{\left(\frac{4\sqrt{2}\pi}{V_f}\right)^{1/3} - 2\right\} r \qquad \text{(A4-2)}$$

Appendix A5

Percolation Threshold with Platelet Fillers

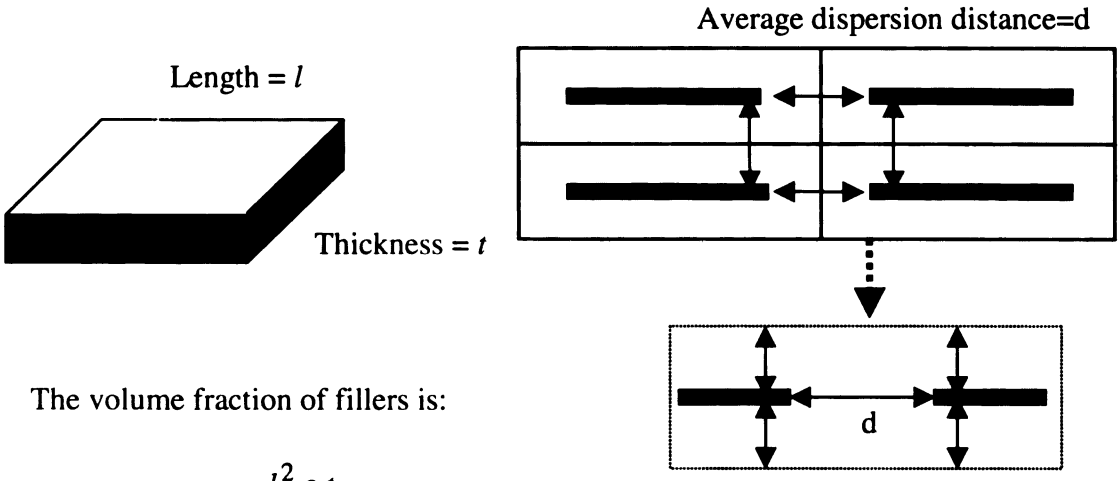

The volume fraction of fillers is:

$$V_f = \frac{l^2 \bullet t}{(l+d)^2(t+d)} \tag{A5-1}$$

Now assume d is fixed at a distance where tunneling occurs, say 100nm at room temperature. Also assume l is fixed, then (A5-1) can be rewritten as:

$$V_f = \frac{1}{\left(1+\frac{d}{l}\right)^2\left(1+\frac{d}{t}\right)} \tag{A5-2}$$

This equation shows the fact that the thinner or shorter the fillers are, the smaller the percolation threshold is. Now define aspect ratio as:

$$a = \frac{l}{t} \tag{A5-3}$$

Substitute (A5-3) into (A5-2).

$$V_f = \frac{1}{\left(1+\frac{d}{l}\right)^2\left(1+\frac{d}{l}a\right)} \tag{A5-4}$$

This reveals that we need fillers with shorter length but higher aspect ratio for smaller percolation threshold.

Appendix A6

Anion Living Polymerization of Stylene initiated by Sodium Naphthalene System

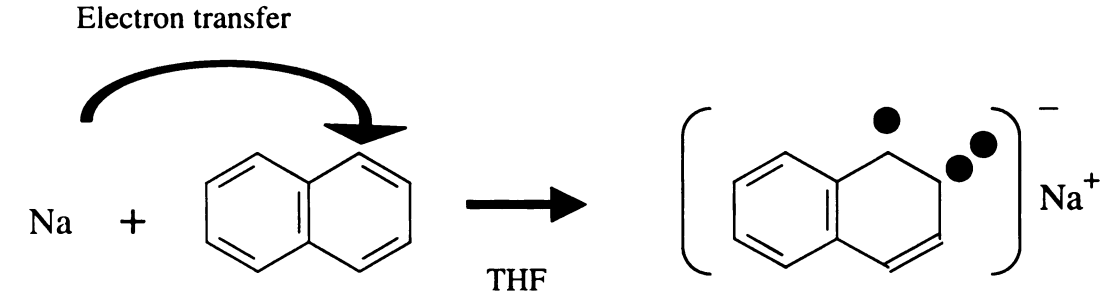

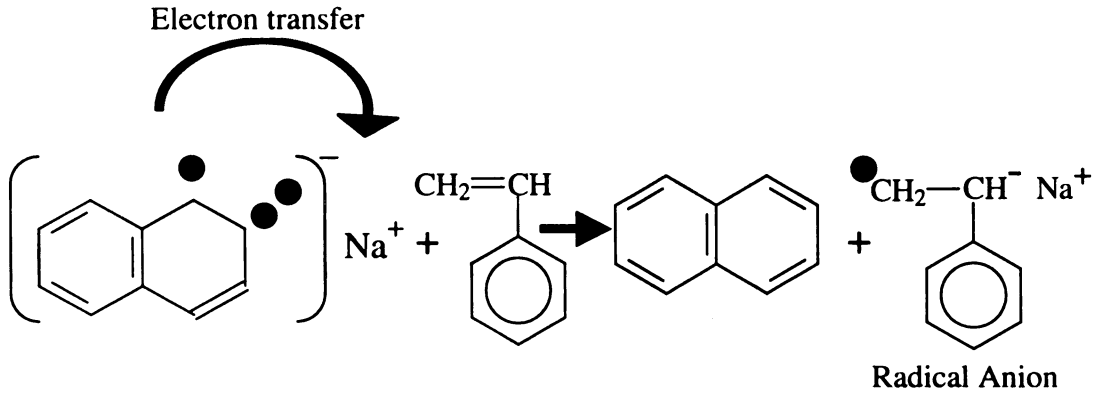

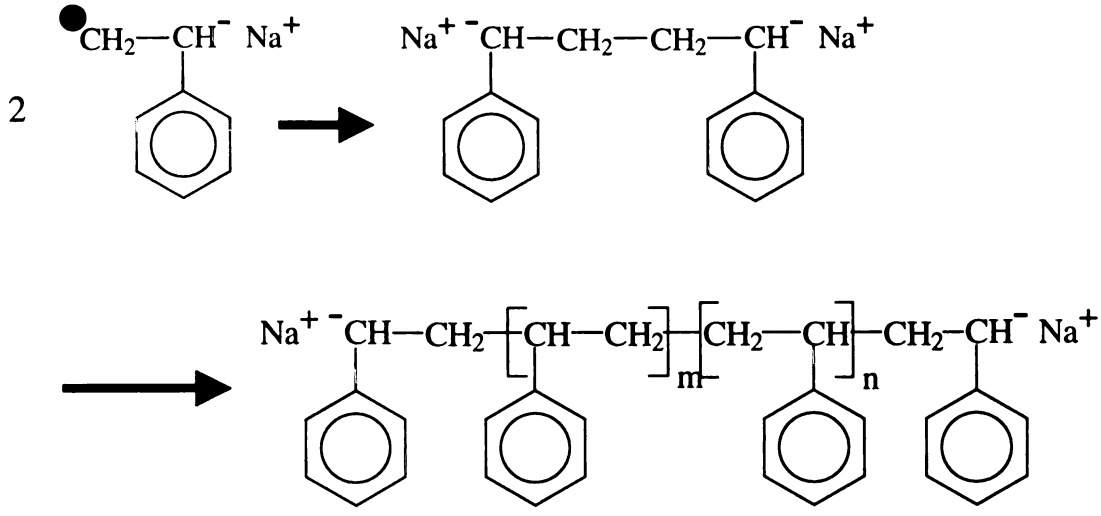

Appendix A7

Young's Equation --- Work of Adhesion

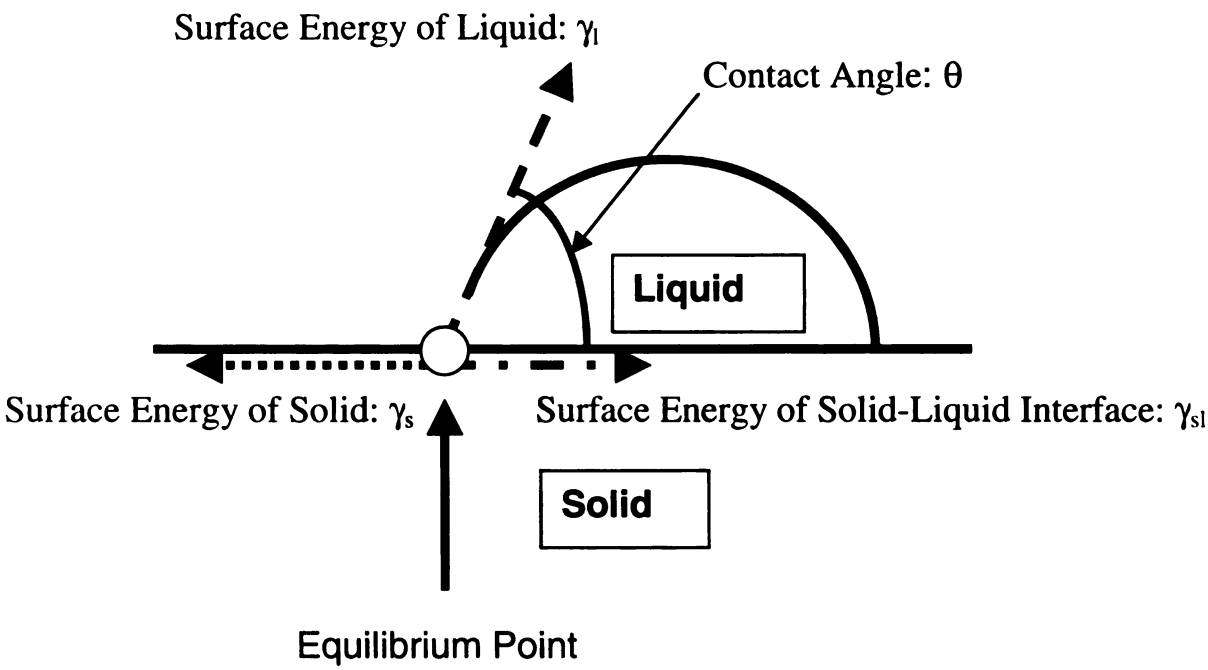

Here, the equilibrium cindition can be written as:

$$\gamma_s = \gamma_{sl} + \gamma_l \cdot \cos\theta \qquad \text{(A7-1)}$$

where γ_s: Surface Energy of solid

γ_l: Surface Energy of Liquid

γ_{sl}: Surface Energy of Solid-Liquid Interface

θ: Contact Angle

Appendix A8

Dupre's Equation --- Work of Adhesion

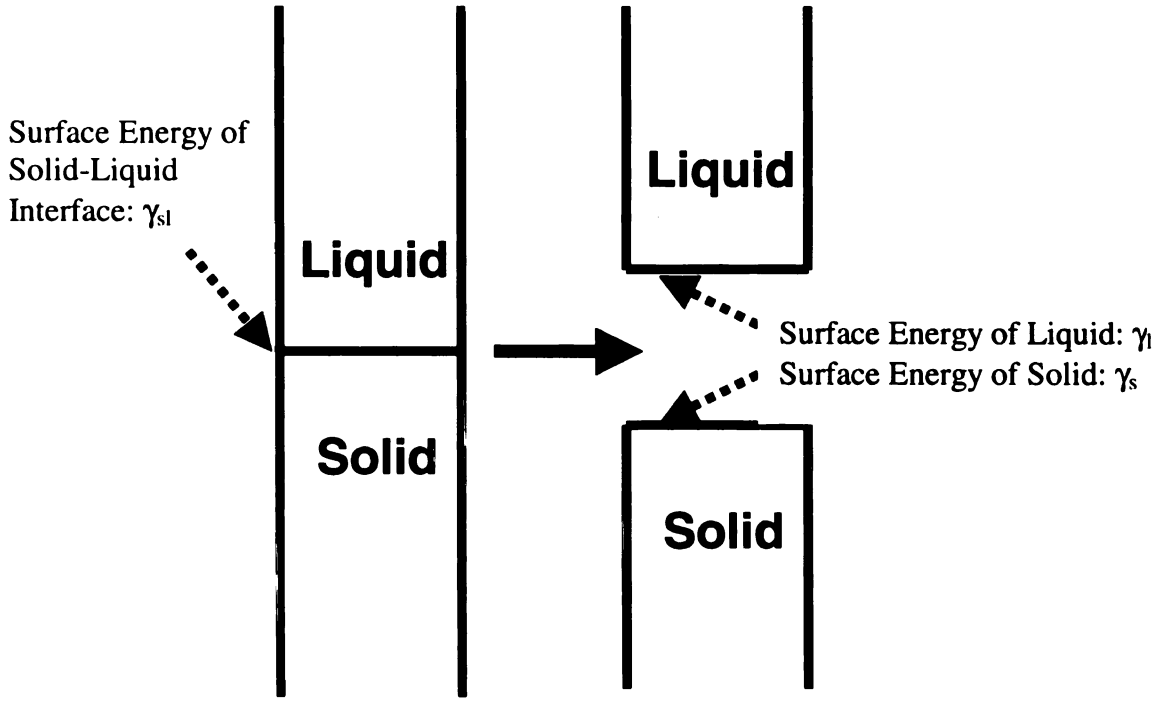

Here, the work of adhesion can be expressed as:

$$W_a = \gamma_s + \gamma_l - \gamma_{sl} \qquad \text{(A8-1)}$$

where *Wa*: Work of adhesion. (Energy required to separate matrix and reinforcements), γ_s, γ_l, γ_{sl} : Surface energies of solid, liquid and interfacial energy between them.

Or the free energy of adhesion can be expressed as:

$$\Delta G_a = -W_a = \gamma_{sl} - \gamma_s - \gamma_l \qquad \text{(A8-2)}$$

Appendix A9

Work of Cohesion for Non-Polar System

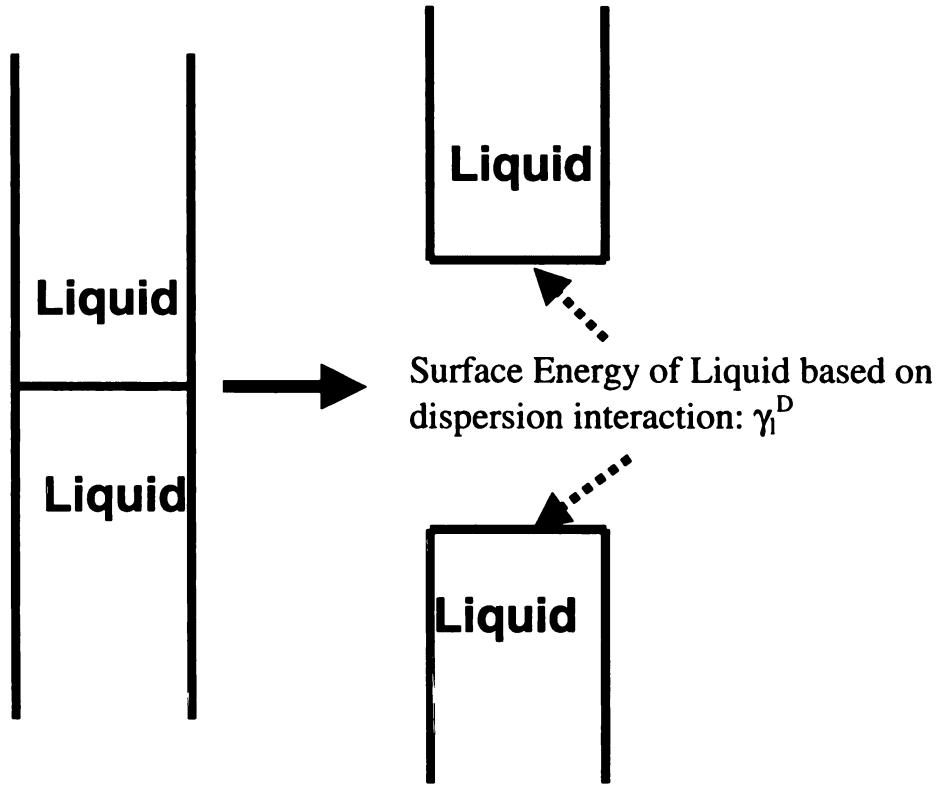

Here, the work of cohesion of liquid can be expressed as:

$$W_{c,l} = \gamma_l^D + \gamma_l^D - 0 = 2\gamma_l^D \qquad \text{(A9-1)}$$

where $W_{c,l}$: Work of cohesion of liquid

γ_l^D: Surface energy of liquid based on dispersion interaction

In the same way, the work of cohesion of slid can be written as:

$$W_{c,s} = \gamma_s^D + \gamma_s^D - 0 = 2\gamma_s^D \qquad \text{(A9-2)}$$

where $W_{c,s}$: Work of cohesion of solid

γ_s^D : Surface energy of solid based on dispersion interaction

Appendix A10

Surface Energy Components of Liquids for Surface Energy Measurement

	γ	γ^D	γ^{AB}	γ^+	γ^-
Water	72.8	21.8	51.0	25.5	25.5
Glycerol	64	34	30	3.92	57.4
Ethylene Glycol	48.0	29	19.0	1.92	47.0
Formamide	58	39	19	2.28	39.6
Dimethyl Sulfoxide	44	36	8	0.5	32
Chloroform	27.15	27.15	0	3.8	0
α–Bromonaphthalene	44.4	43.5	≈ 0		
Diiodomethane	50.8	50.8	0		

Appendix A11

Contact Angle Measurement

A. Bulk solid --- Optical Goniometer

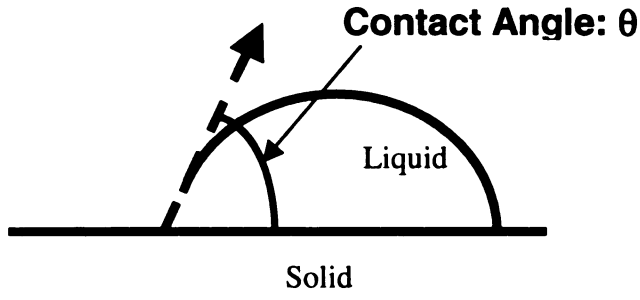

In the case of bulk solid with clean, flat surface, a droplet of a liquid can directly put on the surface and the contact angle ca be measured by optical goniometer.

B. Fiber or small plate --- Wilhelmy Method

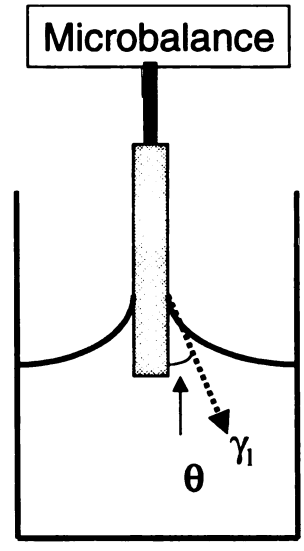

One end of a sample is connected to a microbalance and the other end is attached to a liquid. The liquid goes up along the sample and eventually reaches an equilibrium state.

$$W_{total} = W_{plate} + p \cdot \gamma_l \cos\theta \qquad \text{(A11-1)}$$

where W_{total}: Total weight at equilibrium

W_{plate}: Weight of plate or fiber

P: Perimeter of plate or fiber

γ_l: Surface free energy of liquid

C. Short fibers or particles --- Washburn Theory

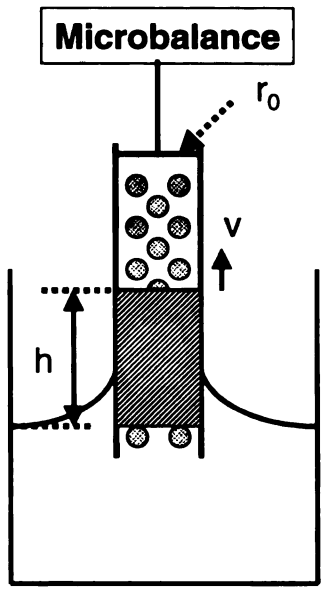

Particles are packed in a small tefron tube and connected to a microbalance. When the other end of tube is attached to a liquid, it begins to swell up. Washburn proposed a theory which describes the relation between contact angle and the mass of liquid sucked at time t as:

$$C \cdot \gamma_l \cos\theta = \frac{W_l^2 \cdot \eta}{t \cdot \rho^2} \qquad \text{(A11-2)}$$

where C: Capillary constant

γ_l: Surface free energy of liquid

W_l: Weifgt of liquid sucked into the pours at time t

ρ: density of liquid

η: Viscosity of liquid

He defined the capillary constant for a porous material as:

$$C = \frac{1}{2}\pi^2 r^5 (1-f)^2 \qquad \text{(A11-3)}$$

where r: Radius of capillary

f: Volume fraction of solid

(1-f): Volume fraction of capillary space

Substitute (A9-3) into (A9-2) and summarizing the equation gives:

$$\cos\theta = \frac{2 \cdot W_l^2 \cdot \eta}{t \cdot \rho^2 \cdot \gamma_l \pi^2 r^5 (1-f)^2} \qquad \text{(A11-4)}$$

W_1 /t can be measured experimentally. f can be determined by measuring total weight of sample packed and density of the sample. Others should be given.

In a real measurement, W_1^2/t changes in termes of time because of the buoyancy effect. Thus, this term should be determined in the early stage of experiment where the effect is minimun and the relation between W_1^2 and t is almost linear.

Appendix A12

Theory of Adhesion at Solid-Liquid Interface

The strength of adhesion at solid-liquid interface can be described by thermodynamics. In early 19th century, Young found the fact that the contact angle of a droplet on a solid depends on the surface condition of the solid. He assumed thermodynamically equilibrium condition and proposed an equation called Young's equation. [120] [**Appendix A7**].

$$\gamma_s = \gamma_{sl} + \gamma_l \cdot \cos\theta \qquad \text{(A12-1)}$$

where γ_s: surface free energy of solid, γ_l: surface free energy of liquid, γ_{sl}: surface free energy of solid-liquid interface, and θ: contact angle

In 1860's, Dupre proposed that the energy required to separate matrix and reinforcements can be expressed by using surface energies of matrix, reinforcements, and interfacial free energy between them. [121] [**Appendix A8**]

$$W_a = \gamma_s + \gamma_l - \gamma_{sl} \qquad \text{(A12-2)}$$

where *Wa*: Work of adhesion. (Energy required to separate matrix and reinforcements), Combination of equations (A12-1) and (A12-2) leads Young-Dupre equation,

$$W_a = \gamma_l(1 + \cos\theta) \qquad \text{(A12-3)}$$

When cosθ=1, or θ=0, the work of adhesion reaches its maximum. In such condition, the relations among surface energies becomes as follows:

$$\gamma_s - \gamma_{sl} = \gamma_l \qquad \text{(A12-4)}$$

Here the surface energy must equal or greater than zero. Thus, surface energy of the solid should be greater than that of liquid for good adhesion.

In 1950's, Girifalco and Good proposed that the work of adhesion could be expressed by geometric mean rule (or combination rule), [122, 123] which is:

$$\left[\begin{array}{c}\text{Work of adhesion between}\\ \text{solid and liquid}\end{array}\right] = \left\{\left[\begin{array}{c}\text{Work of cohesion}\\ \text{of liquid}\end{array}\right] \text{x} \left[\begin{array}{c}\text{Work of cohesion}\\ \text{of solid}\end{array}\right]\right\}^{1/2}$$

They considered a non-polar system where adhesions and cohesions are based only on dispersion interactions and derived the work of cohesion as: [**Appendix A9**]

$$W_{c,l} = \gamma_l^D + \gamma_l^D - 0 = 2\gamma_l^D \qquad \text{(A12-5)}$$

where $W_{c,l}$: Work of cohesion of liquid, γ_l^D: Surface free energy of liquid based on dispersion interaction

$$W_{c,s} = \gamma_s^D + \gamma_s^D - 0 = 2\gamma_s^D \qquad \text{(A12-6)}$$

where $W_{c,s}$: work of cohesion of solid, γ_s^D : surface free energy of solid based on dispersion interaction. Thus, the work of adhesion based on dispersion interactions can be written as:

$$W_a^D = 2\sqrt{\gamma_l^D \cdot \gamma_s^D} \qquad \text{(A12-7)}$$

In 1950-60's, many people tried to incorporate interactions such as dipole-dipole interactions and hydrogen bond into the adhesion theory. Fowkes first proposed separating the surface energy into many components such as: [124]

$$\gamma = \gamma^D + \gamma^{ind} + \gamma^H + --- \qquad \text{(A12-8)}$$

where γ^D, γ^{ind}, γ^H: Surface free energy based on dispersion, induced dipole, and hydrogen interaction. But because of the complexity of the equation, later he suggested to summarize the equation into two dominant terms. [125]

$$\gamma = \gamma^D + \gamma^{AB} \qquad \text{(A12-9)}$$

where γ^{AB}: Surface free energy based on acid-base interactions. Then, the work of adhesion is also expressed in two dominant terms.

$$W_a = W_a^D + W_a^{AB} \tag{A12-10}$$

Based on geometric mean rule considering only positive and negative components attract each other, the acid-base component of the surface energy of a pure substance is written as: [126]

$$\gamma^{AB} = 2\sqrt{\gamma^+ \gamma^-} \tag{A12-11}$$

where γ^+, γ^- : Lewis acid or base component of surface free energy.

In the same way, the acid-base component of the work of adhesion between solid and liquid can be written as:

$$W_a^{AB} = 2\left(\sqrt{\gamma_s{}^+ \gamma_l{}^-} + \sqrt{\gamma_s{}^- \gamma_l{}^+}\right) \tag{A12-12}$$

Now substitute equation (A12-7) and (A12-12) into (A12-10), then:

$$W_a = W_a^D + W_a^{AB} = 2\left[\sqrt{\gamma_l^D \cdot \gamma_s^D} + \sqrt{\gamma_s{}^+ \gamma_l{}^-} + \sqrt{\gamma_s{}^- \gamma_l{}^+}\right] \tag{A12-13}$$

Here compare equations (A12-3) and (A12-13);

$$W_a = \gamma_l(1+\cos\theta) = 2\left[\sqrt{\gamma_l^D \cdot \gamma_s^D} + \sqrt{\gamma_s{}^+ \gamma_l{}^-} + \sqrt{\gamma_s{}^- \gamma_l{}^+}\right] \tag{A12-14}$$

This equation gives the basic theory of solid surface analysis. Since contact angles of liquids with known γ_l^D, γ_l^+, γ_l^- **[Appendix A10]** can be determined experimentally **[Appendix A11]**, then more than three equations based on (A12-14) can be obtained. The surface energy components of the solid, γ_s^D, γ_s^+, and γ_s^- can be determined by solving these equations. By using this technique, the work of adhesion between matrix and reinforcements with different surface treatments can be evaluated.

Appendix A13

Theories of Composite Mechanics 1

Theory	Inclusion	Assumptions	Model	Elastic Constants	Comments
Rule of Mixtures	Long fibers (No end effect)	• Perfect bonding • Fibers are uniaxially aligned • Both fibers and matrix are elastic	• Constant strain • Constant stress	E11, E22, ν12, G12	Upper/Lower Bound (Voigt /Rauss Model)
Modified Rule of Mixtures Halpin-Tsai	Short Fiber	• Introduced semi-empirical shape factor and geometric factor in rule of mixtures • Fibers are uniaxially aligned		E11	
Eshelby's Method	Spheres Discs Short/long fibers (Ellipsoid)	• Uniform deformation in ellipsoidal inclusion • Stress of actual inclusion is expressed by using "equivalent homogenous inclusion" (EHI) • Dilute, external loading condition • Fibers are uniaxially aligned • Perfect bonding	• EHI model	E11 E22 ν12 G12 G23	• Eshelby's tensor • Effect of aspect ratio • Various shape fillers
Mori-Tanaka	Ellipsoid	• Mean Field Theory		E	
Tandon-Weng	Spheres Discs Fibers	• Based on Eshelby's and Mori-Tanaka Method • 3D averaging	• EHI model	K G	
Hui-Shia		• Based on Eshelby's and Mori-Tanaka Method • Introduce imperfect bonding.	• Effective aspect ratio/volume fraction	E11, E22, ν12, G12, G23	

Theories of Composite Mechanics 2

Theory	Inclusion	Assumptions	Model	Elastic Constants	Comments
Shear Slip Theory	Short fibers		• Constant IFSS on edge parts of the fiber	E11	Critical fiber length
Shear Lag Theory	Short fibers	• Fibers & matrix are elastic • Stress transfers without slip or yielding • Fibers are packed in orderly fashion • The tensile strain of matrix is constant • At distance R from a fiber, the stress of matrix is same as that of composite	• IFSS is changed gradually	E11	Packing factor (Hexagonal, Square)
Christensen's method Mura's method	Spherical	• Dilute condition • Averaging technique	• Energy method • Spherical coordinate	K μ	
Composite Spheres Method	Spherical	• Non-dilute condition (radius of inclusion)/(radius of Matrix) =const.	• Christensen's method	K μ	
Self-Consistent Generalized S-C	Spherical	• Non-dilute condition	• 3-D model	K ν μ	
Composite Cylinders Method	Long fibers	• Non-dilute condition	• 2-D model	E K ν	Does not give μ $\rightarrow$ Need another model

E: Elastic Modulus, G: Shear Modulus, ν: Poisson's Ratio, μ: Shear Modulus, K: Bulk Modulus

Appendix A14

Rule of Mixtures

This model is based on assumptions that include

- Both fibers and matrix are elastic
- Fibers in the composite is uniaxially aligned,
- Adhesion between fibers and matrix are complete

A. Elastic Modulus in Longitudinal Direction

The modulus of the composite in longitudinal direction is derived by constant strain approach, in which the longitudinal strain in fibers is considered to be the same as that in the matrix. Suppose the stress in longitudinal direction (1 direction) is σ_1.

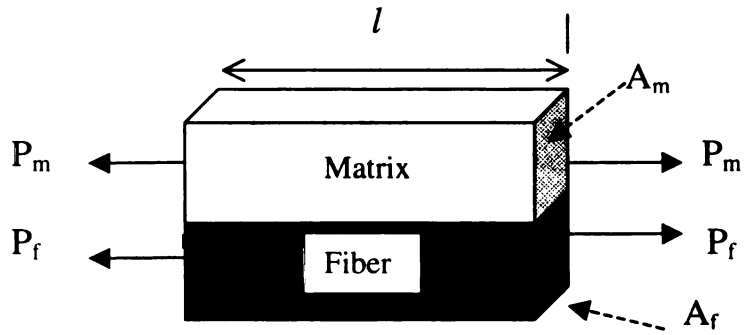

Now the elongation (ε) of matrix and fibers is the same, and so is the deformation (δ).

$$\varepsilon_{fiber} = \varepsilon_{matrix} = \varepsilon_{composite} \quad \text{(A14-1)}$$

$$\delta_{fiber} = \delta_{matrix} = \delta_{composite} \quad \text{(Compatibility Equation)} \quad \text{(A14-2)}$$

$$\text{Now} \qquad \varepsilon = \frac{\delta}{l} = \frac{\sigma}{E} = \frac{P}{AE} \quad \text{and} \quad P = \frac{AE\delta}{l} \quad \text{(A14-3)}$$

where δ:deformation, l: Length, σ:stress, E:Young's Modulus, A:Area, P: Force

Now the force applied on the composite can be considered as the sum of the force on matrix and that of fibers.

$$P_C = P_m + P_f \qquad \text{(Equilibrium Equation)} \qquad \text{(A14-4)}$$

where c, m, and f denote composite, matrix, and fiber, respectively.

Equation (A13-4) can be rewritten as

$$\frac{E_c A_c \delta_c}{l} = \frac{E_m A_m \delta_m}{l} + \frac{E_f A_f \delta_f}{l} \qquad \text{(A14-5)}$$

From equation (A13-1) and (A13-3), we can say

$$\frac{\delta_c}{l} = \varepsilon_c = \frac{\delta_m}{l} = \varepsilon_m = \frac{\delta_f}{l} = \varepsilon_f$$

Thus equation (A13-5) becomes

$$E_c = \frac{A_m}{A_c} E_m + \frac{A_f}{A_c} E_f$$

Which can be expressed as

$$E_{1,c} = E_f \cdot V_f + E_m \cdot (1 - V_f) \qquad \text{(A14-6)}$$

where Ef and Em represent moduli of fiber and matrix

Vf and Vm represent volume fraction of fibers and matrix in composite

B. Elastic Modulus in Transverse Direction

The modulus of transverse direction is derived by constant stress approach, in which the transverse stress of fibers is same as that of matrix.

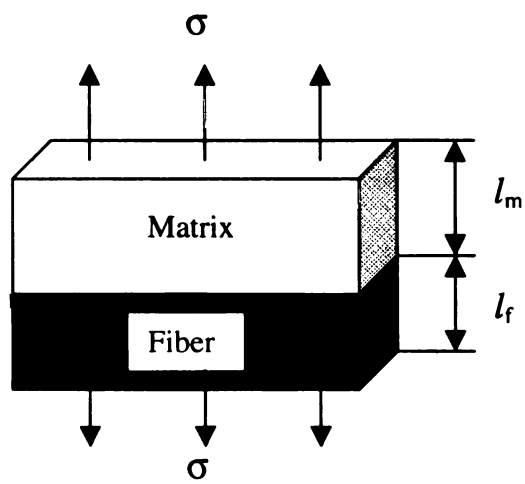

Now the force applied on the upper plane of matrix is equal to that of lower plane of fiber, and also this is equal to the force acts on the composite.

$$P_c = P_m = P_f \tag{A14-7}$$

Now we realize $A_c=A_m=A_f$, thus

$$\sigma_c = \sigma_m = \sigma_f = \sigma \qquad \text{(Compatibility Equation)} \tag{A14-8}$$

Here consider deformation of composite in transverse direction is the sum of that of matrix and fibers.

$$\delta_c = \delta_m + \delta_f \qquad \text{(Equilibrium Equation)} \tag{A14-9}$$

Now apply equation (A14-3) to (A14-9) and we get,

$$\frac{P_c l_c}{A_c E_c} = \frac{P_m l_m}{A_m E_m} + \frac{P_f l_f}{A_f E_f} \tag{A14-10}$$

And consider $\frac{P_c}{A_c} = \sigma_c = \frac{P_m}{A_m} = \sigma_m = \frac{P_f}{A_f} = \sigma_f$, we get

$$\frac{1}{E_c} = \frac{l_m}{l_c E_m} + \frac{l_f}{l_c E_f}$$

This can be rewritten as

$$\frac{1}{E_{2,c}} = \frac{V_f}{E_f} + \frac{1-V_f}{E_m} \quad \text{or} \quad E_{2.c} = \frac{E_f \cdot E_m}{V_f \cdot E_m + (1-V_f) \cdot E_f} \tag{A14-11}$$

C. Poisson's ratio, ν_{12}

Apply a stress in longitudinal direction (1 direction), then the matrix and fibers elongate in longitudinal direction and contract in transverse direction.

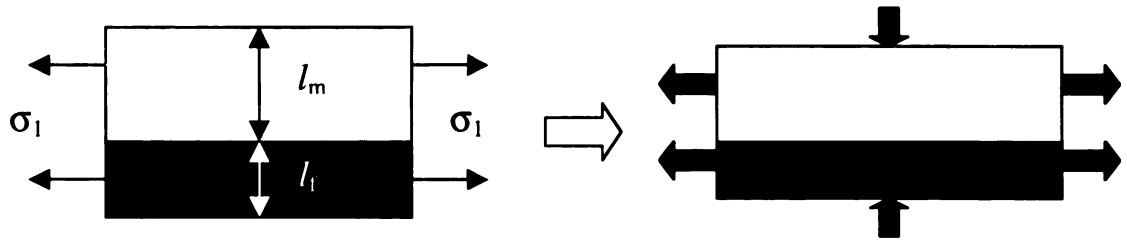

Since fibers and matrix are perfectly bonded, the elongation in longitudinal direction should be the same and that is the elongation of composite.

$$\varepsilon_{1,c} = \varepsilon_{1,m} = \varepsilon_{1,f} = \varepsilon_1 \quad \text{(Compatibility Equation)} \tag{A14-12}$$

Now consider the contract in transverse direction.

The contract of matrix can be written by using Poisson's ration of the matrix.

$$\nu_m = -\frac{\varepsilon_{2,m}}{\varepsilon_{1,m}} \quad \text{or} \quad \varepsilon_{2,m} = -\nu_m \varepsilon_{1,m} \tag{A14-13}$$

In the same way, the contract of fibers is

$$\nu_f = -\frac{\varepsilon_{2,f}}{\varepsilon_{1,f}} \quad \text{or} \quad \varepsilon_{2,f} = -\nu_f \varepsilon_{1,f} \tag{A14-14}$$

The deformation of composite in transverse direction is the sum ofdeformation of matrix and fibers..

$$\varepsilon_{2,c} l_c = \varepsilon_{2,m} l_m + \varepsilon_{2,f} l_f \quad \text{(Equilibrium Equation)} \tag{A14-15}$$

Substitute equations (A14-13) and (A14-14) into (A14-15), we get,

$$\varepsilon_{2,c} = -\left(\varepsilon_{2,m} \frac{l_m}{l_c} + \varepsilon_{2,f} \frac{l_f}{l_c} \right) = -\left(\varepsilon_{2,m} V_m + \varepsilon_{2,f} V_f \right) \tag{A14-16}$$

Now the Poisson's ratio of composite is written as

$$\nu_{12,c} = -\frac{\varepsilon_{2,c}}{\varepsilon_{1,c}} = \frac{\varepsilon_{2,m} V_m + \varepsilon_{2,f} V_f}{\varepsilon_1} \tag{A14-17}$$

Using equations (A14-12), (A14-13), and (A14-14), we can rewrite (A14-17) as

$$\nu_{12,c} = \nu_m(1-V_f) + \nu_f V_f \qquad \text{(A14-18)}$$

D. Poisson's ratio, ν_{21}

Here we know the relation $\frac{\nu_{12}}{E_1} = \frac{\nu_{21}}{E_2}$. Then

$$\nu_{21,c} = \frac{E_{2,c}}{E_{1,c}}\nu_{12,c} = \left(\frac{E_f \cdot E_m}{V_f \cdot E_m + (1-V_f)\cdot E_f}\right)\cdot\left(\frac{1}{E_f \cdot V_f + E_m \cdot (1-V_f)}\right)\cdot\left\{\nu_m(1-V_f) + \nu_f V_f\right\}$$

(A14-19)

E. Shear Modulus, G_{12}

Apply shear stress on a composite.

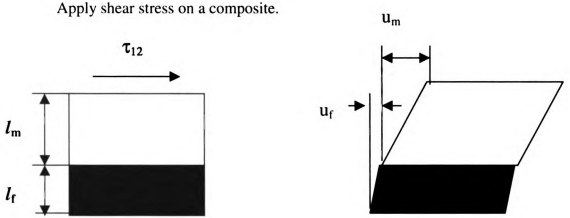

The shear stress on the composite is equal to that of matrix and fiber.

$$\tau_{12,c} = \tau_{12,m} = \tau_{12,f} \qquad \text{(A14-20)}$$

The displacement of matrix is different from that of fiber, and the displacement of composite is the sum of these.

$$u_c = u_m + u_f \quad \text{(Equilibrium Equation)} \qquad \text{(A14-21)}$$

where u_c, u_m, and u_f denote desplacement of composite, matrix, and fiber, respectively.

Now consider shear strain of matrix

$$\gamma_m = \frac{u_m}{l_m} = \frac{\tau_{12}}{G_m} \qquad \text{and} \qquad u_m = \frac{\tau_{12} l_m}{G_m} \tag{A14-22}$$

In the same way, for fibers

$$\gamma_f = \frac{u_f}{l_f} = \frac{\tau_{12}}{G_f} \qquad \text{and} \qquad u_m = \frac{\tau_{12} l_m}{G_m} \tag{A14-23}$$

Substitute equations (A14-22) and (A14-23) into (A14-21),

$$u_m = \frac{\tau_{12} l_c}{G_c} = \frac{\tau_{12} l_m}{G_m} + \frac{\tau_{12} l_m}{G_m} \tag{A14-24}$$

Thus we can conclude,

$$\frac{1}{G_c} = \frac{(1-V_f)}{G_m} + \frac{V_f}{G_f} \quad \text{or} \quad G_{.c} = \frac{G_f \cdot G_m}{V_f \cdot G_m + (1-V_f) \cdot G_f} \tag{A14-25}$$

F. Summary of Five Elastic Constants Derived from Rule of Mixtures

(1) Elastic Modulus in Longitudinal Direction

$$E_{1,c} = E_f \cdot V_f + E_m \cdot (1 - V_f)$$

(2) Elastic modulus in Transverse Direction

$$E_{2.c} = \frac{E_f \cdot E_m}{V_f \cdot E_m + (1 - V_f) \cdot E_f}$$

(3) Poisson's Ration, ν_{12}

$$\nu_{12,c} = \nu_m (1 - V_f) + \nu_f V_f$$

(4) Poisson's Ration, ν_{21}

$$\nu_{21,c} = \frac{E_{2,c}}{E_{1,c}} \nu_{12,c} = \left(\frac{E_f \cdot E_m}{V_f \cdot E_m + (1 - V_f) \cdot E_f} \right) \cdot \left(\frac{1}{E_f \cdot V_f + E_m \cdot (1 - V_f)} \right) \cdot \{ \nu_m V_m + \nu_f V_f \}$$

(5) Shear Modulus

$$G_{.c} = \frac{G_f \cdot G_m}{V_f \cdot G_m + (1 - V_f) \cdot G_f}$$

Here consider matrix and fibers are isotropic. Thus,

$$G_m = \frac{E_m}{2(1 - \nu_m)} \quad \text{and} \quad G_f = \frac{E_f}{2(1 - \nu_f)}$$

Since the rule of mixtures doesn't take aspect ratio into account, each elastic constant is the function of volume fraction of fibers only. Thus it gives only one line for each constant.

Appendix A15

Eshlby's Method

[1] Manifestation

Eshelby showed theoretical approach to predict mechanical properties of materials which are consist of inhomogeneous phases. To accomplish this, he made some manifestations.

1. A single ellipsoidal inclusion embedded in an infinite medium undergoes uniform deformation corresponding to imposed deformation in the media at large distance from the inclusion.
2. Introduce "equivalent homogeneous inclusion" (EHI). The inclusion is made of the same material of matrix, but has an appropriate misfit strain (equivalent transformation strain, ε^T) so that the stress field of "equivalent homogeneous inclusion" in composite has the same stress field for the actual inclusion. And ε^T and constraint strain, ε^C is related as follows.

$$\varepsilon^C = S_E \cdot \varepsilon^T \qquad \text{(A15-1)}$$

where S_E is Eshelby's tensor, a function of aspect ratio and Poisson's ratio of inclusion.

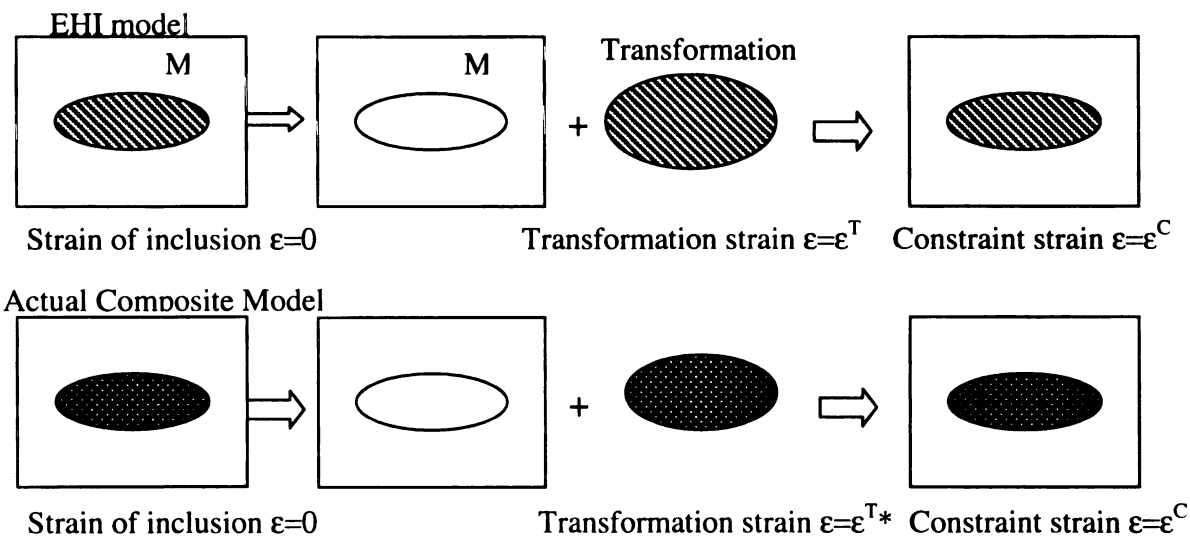

3. The stress of actual inclusion, which has transformed strain ε^{T*} and final constrained strain ε^{C} can be expressed using EHI which has transformation strain, ε^{T} and same final constrained strain.

$$\sigma_f = C_f(\varepsilon^C - \varepsilon^{T*}) = C_m(\varepsilon^C - \varepsilon^T) \quad \text{(A15-2)}$$

where C_f and C_m represent modulus of fiber and matrix, respectively.

From equation (A15-1) and (A15-2), we can get

$$\sigma_f = C_m(S_E - I)\varepsilon^T \quad \text{(A15-3)}$$

where I is identity tensor.

[2] Theory

Consider non-dilute, inhomogeneous composite model. In this model, we consider one fiber and homogeneous composite media. The stress in the fiber is expressed by the stress of fiber in the dilute model and background stress, or the mean field stress of "homogeneous" composite media surrounding the fiber. Thus, fibers are assumed to be distributed randomly and no individual fiber-fiber interaction are exists.

$$\sigma_f + \overline{\sigma_m} = C_f(\varepsilon^C + \overline{\varepsilon_m} + \varepsilon^{T*}) = C_m(\varepsilon^C + \overline{\varepsilon_m} + \varepsilon^T) \quad \text{(A15-4)}$$

where σ_m and ε_m is the mean field stress and strain, respectively.

Now assume no external force is applied so that the average stress of the composite is zero.

$$\overline{\sigma_c} = 0 = V_f \cdot \overline{\sigma_f} + (1 - V_f) \cdot \overline{\sigma_m} \quad \text{and} \quad \overline{\sigma_m} = \frac{V_f}{V_f - 1}\overline{\sigma_f} \quad \text{(A15-5)}$$

Also we can get $\overline{\sigma_m} = C_m \cdot \overline{\sigma_f}$ (A15-6)

Substitute equation (A15-4) and (A15-6) into (A15-5) and summarize it.

$$\overline{\varepsilon_m} = V_f(\varepsilon^T - \varepsilon^C) \quad \text{and} \quad \overline{\sigma_m} = V_f \cdot C_m(\varepsilon^T - \varepsilon^C) \tag{A15-7}$$

Substitute equations (A15-7) into (A15-4) and summarize it.

$$\varepsilon^T = \frac{C_f \cdot \varepsilon^{T*}}{(C_f - C_m)\{(1-\nu_f)S_E + C_f \cdot V_f + C_m\}} \tag{A15-8}$$

Now consider external loading, σ^A, and repeat the process.

$$\varepsilon^T = \frac{(C_m - C_f)\cdot \varepsilon^A}{(C_f - C_m)\{S_E - V_f(S_E - I)\} + C_m} \tag{A15-9}$$

Here consider average strain of the composite under external loading.

$$\sigma^A = C_C \cdot \overline{\varepsilon_C{}^A} = C_C(\varepsilon^A + \overline{\varepsilon_C}) \tag{A15-10}$$

where ε_C is the internal strain due to shape mismatch and can be expressed as

$$\overline{\varepsilon_C} = \overline{\varepsilon_m} + V_f \cdot \varepsilon^C \tag{A15-11}$$

Substitute equation (A15-7) into (A15-11) and summarize it.

$$\overline{\varepsilon_C} = V_f \cdot \varepsilon^T \tag{A15-12}$$

Substitute equation (A15-12) into (A15-10) and summarize it.

$$\sigma^A = C_C(\varepsilon^A + V_f \cdot \varepsilon^T) \tag{A15-13}$$

Now substitute equation (A15-9) into (A15-13) and compare it to

$$\sigma^A = C_m \cdot \varepsilon^A \tag{A15-14}$$

Then we get

$$C_c = C_m \frac{(C_f - C_m)\{S_E - V_f(S_E - I)\} + C_m}{(C_f - C_m)\{S_E - V_f S_E\} + C_m} \tag{A15-15}$$

[3] Model

Assume both fibers and matrix are isotropic. The stiffness of these materials are written as

$$C_f = \begin{bmatrix} C_{f11} & C_{f12} & C_{f12} & 0 & 0 & 0 \\ C_{f12} & C_{f11} & C_{f12} & 0 & 0 & 0 \\ C_{f12} & C_{f12} & C_{f11} & 0 & 0 & 0 \\ 0 & 0 & 0 & \frac{C_{f11}-C_{f12}}{2} & 0 & 0 \\ 0 & 0 & 0 & 0 & \frac{C_{f11}-C_{f12}}{2} & 0 \\ 0 & 0 & 0 & 0 & 0 & \frac{C_{f11}-C_{f12}}{2} \end{bmatrix} \quad \text{(A15-16)}$$

$$\text{where } C_{f11} = \frac{(2-3\nu_f)E}{(1+\nu_f)(1-2\nu_f)} \text{ and } C_{f12} = \frac{\nu_f E}{(1+\nu_f)(1-2\nu_f)}.$$

$$C_m = \begin{bmatrix} C_{m11} & C_{m12} & C_{m12} & 0 & 0 & 0 \\ C_{m12} & C_{m11} & C_{m12} & 0 & 0 & 0 \\ C_{m12} & C_{m12} & C_{m11} & 0 & 0 & 0 \\ 0 & 0 & 0 & \frac{C_{m11}-C_{m12}}{2} & 0 & 0 \\ 0 & 0 & 0 & 0 & \frac{C_{m11}-C_{m12}}{2} & 0 \\ 0 & 0 & 0 & 0 & 0 & \frac{C_{m11}-C_{m12}}{2} \end{bmatrix} \quad \text{(A15-17)}$$

$$\text{where } C_{m11} = \frac{(2-3\nu_m)E}{(1+\nu_m)(1-2\nu_m)} \text{ and } C_{m12} = \frac{\nu_m E}{(1+\nu_m)(1-2\nu_m)}.$$

Now consider a model that has an ellipsoidal inclusion embedded and aligned in 3-direction. This model is transversely isotropic.

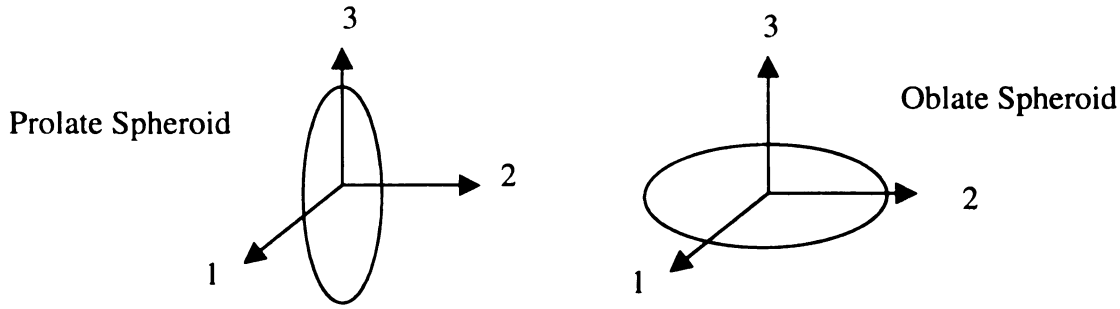

The Eshelby's tensor for this model is expressed as

$$S_E = \begin{bmatrix} S_{1111} & S_{1122} & S_{1133} & 0 & 0 & 0 \\ S_{2211} & S_{2222} & S_{2233} & 0 & 0 & 0 \\ S_{3311} & S_{3322} & S_{3333} & 0 & 0 & 0 \\ 0 & 0 & 0 & S_{2323} & 0 & 0 \\ 0 & 0 & 0 & 0 & S_{1313} & 0 \\ 0 & 0 & 0 & 0 & 0 & S_{1212} \end{bmatrix} \quad \text{(A15-18)}$$

where

$$S_{1111} = S_{2222} = Q + RI_i + \frac{3T}{4} \quad \text{(A15-19)}$$

$$S_{3333} = \frac{4Q}{3} + RI_3 + 2s^2T \quad \text{(A15-20)}$$

$$S_{1122} = S_{2211} = \frac{Q}{3} - RI_1 + \frac{4T}{3} \quad \text{(A15-21)}$$

$$S_{1133} = S_{2233} = -RI_1 - s^2T \quad \text{(A15-22)}$$

$$S_{3311} = S_{3322} = -RI_3 - T \quad \text{(A15-23)}$$

$$S_{2323} = S_{1313} = 2R - \frac{I_1R}{2} - \frac{1+s^2}{2}T \quad \text{(A15-24)}$$

where s is aspect ratio.

$$Q = \frac{3}{8(1-\nu_m)} \tag{A15-25}$$

$$R = \frac{1-2\nu_m}{8(1-\nu_m)} \tag{A15-26}$$

$$T = Q\frac{(4-3I_1)}{3(s^2-1)} \tag{A15-27}$$

$$I_1 = \frac{2s}{(s^2-1)^{3/2}}\left\{s(s^2-1)^{1/2} - \cosh^{-1} s\right\} \text{ for prolate spheroid} \tag{A15-28}$$

$$I_1 = \frac{2s}{(s^2-1)^{3/2}}\left\{\cosh^{-1} s - s(s^2-1)^{1/2}\right\} \text{for oblate spheroid} \tag{A15-29}$$

where $\cosh^{-1} x = \dfrac{2}{e^x + e^{-x}}$

$$I_3 = 4 - 2I_1 \tag{A15-30}$$

Appendix A16

Effective Width, Aspect Ratio, and Volume fraction

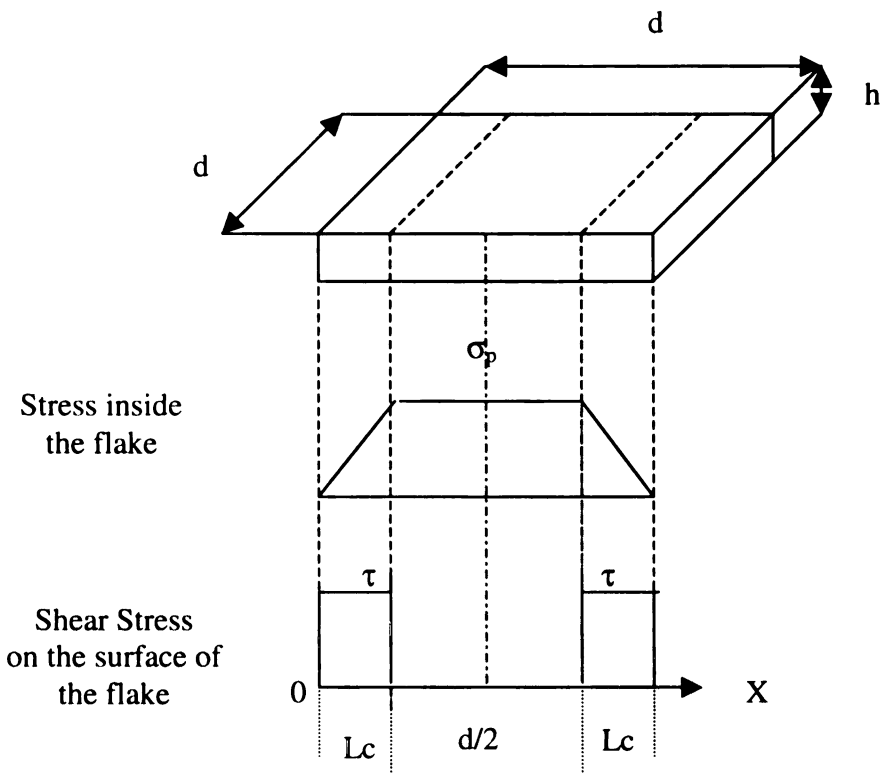

(1) 0 < X < Lc

$$2(h+d)dx \cdot \tau = h \cdot d \cdot d\sigma$$

$$\frac{d\sigma}{dX} = \frac{2(h+d)}{h \cdot d}\tau = \frac{2(h/d+1)}{h}\tau \cong \frac{2}{h}\tau \quad \text{Thus, } \sigma = \frac{2\tau}{h}X \qquad \text{(A16-1)}$$

(2) Lc < X < d/2

$$\sigma = \sigma_p \qquad \text{(A16-2)}$$

When X = d/2, σ = σp. thus, $\sigma_p = \frac{2\tau}{h}L_c$ or $L_c = \frac{\sigma_p h}{2\tau}$ (A16-3)

Now, the average stress in side the flake for 0 < X < d/2 is:

$$\bar{\sigma} = \frac{1}{d/2}\int_0^{d/2} \sigma \cdot dX = \sigma_p\left(1 - \frac{L_c}{d}\right) \qquad \text{(A16-4)}$$

Here define effective width, d_{eff} as follows:

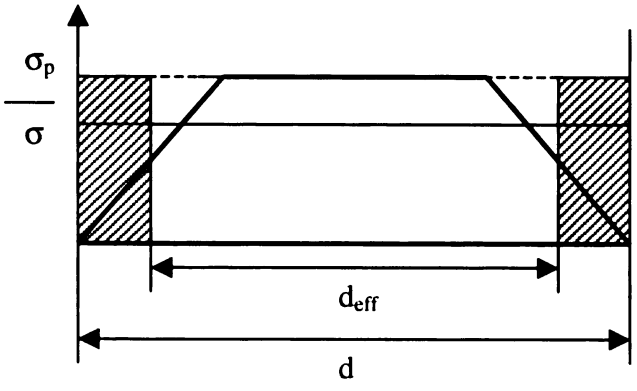

$$\sigma_p \cdot d_{eff} = \bar{\sigma} \cdot d \qquad \text{(A16-5)}$$

then

$$d_{eff} = \frac{\bar{\sigma}}{\sigma_p} d \qquad \text{(A16-6)}$$

Substitute (A16-4) into (A16-6)

$$d_{eff} = d\left(1 - \frac{L_c}{d}\right) \qquad \text{(A15-7)}$$

The effective aspect ratio is defined as:

$$\alpha_{eff} = \frac{h}{d_{eff}} = \frac{h}{d\left(1 - \frac{L_c}{d}\right)} = \sigma \frac{1}{\left(1 - \frac{L_c}{d}\right)} \qquad \text{(A16-8)}$$

The effective volume fraction is defined as:

$$\frac{V_{f \cdot eff}}{V_f} = \frac{d_{eff}}{d} = \left(1 - \frac{L_c}{d}\right) \quad \text{or} \quad V_{f \cdot eff} = V_f\left(1 - \frac{L_c}{d}\right) \qquad \text{(A16-9)}$$

Replace α and V_f in Eshelby's equation by α_{eff} and V_{f*eff}, then the equation becomes a function of α, V_f, d, and Lc. α, V_f, and d are given. Modulus of composites can be obtained experimentally. Thus Lc can be calculated, so as α_{eff}, V_{f*eff}, and d_{eff}.

Appendix A17

Modulus for Composite with Randomly Oriented Reinforcement

(2-Dimensional averaging of transversely isotropic composite system)

Consider a model composite in which a shot fiber is aligned in direction 1.

The stress-strain relation in 1-2 cordiation can be written as:

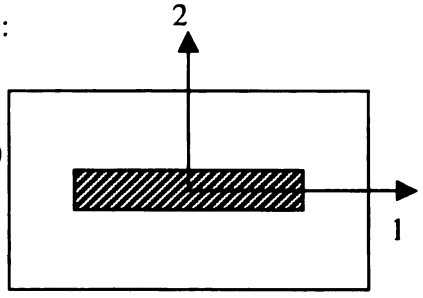

$$\begin{bmatrix}\sigma_{11}\\ \sigma_{22}\\ \tau_{12}\end{bmatrix} = Q\begin{bmatrix}\varepsilon_{11}\\ \varepsilon_{22}\\ \gamma_{12}\end{bmatrix} \quad \text{where} \quad Q_1 = \begin{bmatrix}Q_{11} & Q_{12} & 0\\ Q_{12} & Q_{22} & 0\\ 0 & 0 & Q_{66}\end{bmatrix} \quad \text{(A17-1)}$$

where σ is tensile stress, τ is shear stress, ε is tensile strain, and γ is shear strain. The subscripts mean the direction of each factor.

Now consider X-Y coordination, which has rotation angle ϕ from 1-2 coordination. The stress-strain relation in X-Y coordination is:

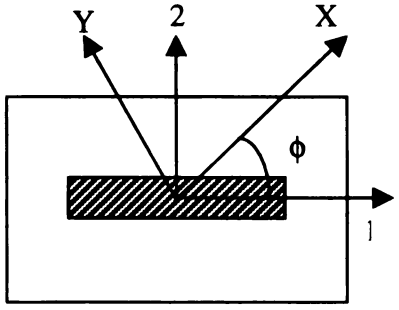

$$\begin{bmatrix}\sigma_{XX}\\ \sigma_{YY}\\ \tau_{XY}\end{bmatrix} = Q'\begin{bmatrix}\varepsilon_{XX}\\ \varepsilon_{YY}\\ \gamma_{XY}\end{bmatrix} \quad \text{where} \quad Q' = \begin{bmatrix}Q'_{11} & Q'_{12} & Q'_{16}\\ Q'_{12} & Q'_{22} & Q'_{26}\\ Q'_{16} & Q'_{26} & Q'_{66}\end{bmatrix} \quad \text{(A17-2)}$$

Since fiber is aligned off direction from X-Y axis, the shear strain affects tensile stress and vise versa.

Now Q'_{11} is a function of ϕ. Integrating Q'_{11} in the range from $\phi=0$ to $\phi=\pi$ and dividing the result by π gives the average value of Q'_{11}, which is the tensile modulus for composite with randomly oriented fiber.

Here, stresses in X-Y coordination can be related to those in 1-2 coordination, so as strains. Define T and T' as transformation tensor for each case, then:

$$\begin{bmatrix}\sigma_{XX}\\ \sigma_{YY}\\ \sigma_{XY}\end{bmatrix}=T\begin{bmatrix}\sigma_{11}\\ \sigma_{22}\\ \sigma_{12}\end{bmatrix},\qquad \begin{bmatrix}\varepsilon_{XX}\\ \varepsilon_{YY}\\ \tau_{XY}\end{bmatrix}=T'\begin{bmatrix}\varepsilon_{11}\\ \varepsilon_{22}\\ \tau_{12}\end{bmatrix} \tag{A17-3}$$

From (A16-1), (A16-2), and (A16-3), Q' can be calculated as:

$$Q'=T\cdot Q\cdot (T')^{-1} \tag{A17-4}$$

Here consider a transversely isotropic composite in 1-2 coordination. Assume the length of the composite in 1 and 2 direction are dp and dq respectively. Also assume the thickness of the composite in 3 (or Z) direction is unit, so that the calculation would be easier.

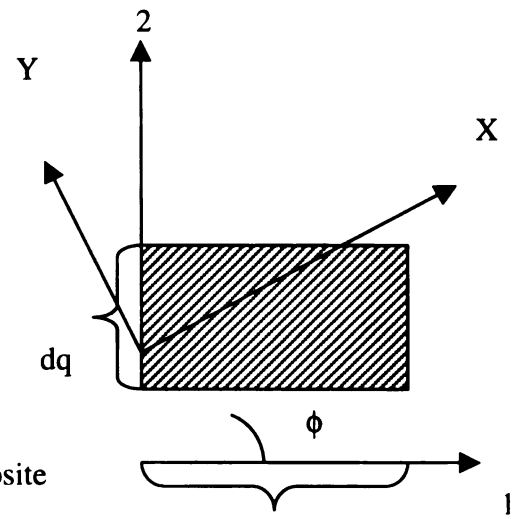

Set X axis as the diagonal direction of the composite so that ϕ can be related to dp and dq.

$$\tan\phi=\frac{dq}{dp},\quad \cos\phi=\frac{dp}{\left(dp^2+dq^2\right)^{1/2}},\quad \sin\phi=\frac{dq}{\left(dp^2+dq^2\right)^{1/2}} \tag{A17-5}$$

Now consider the half of the composite. Define tensile and shear stress on plane 1, 2, and 3 as shown in a right figure. Assume the system is in equilibrium condition. Define forces acting on plane 1, 2, and 3 as F1, F2, and F3 respectively. These forces can be written as:

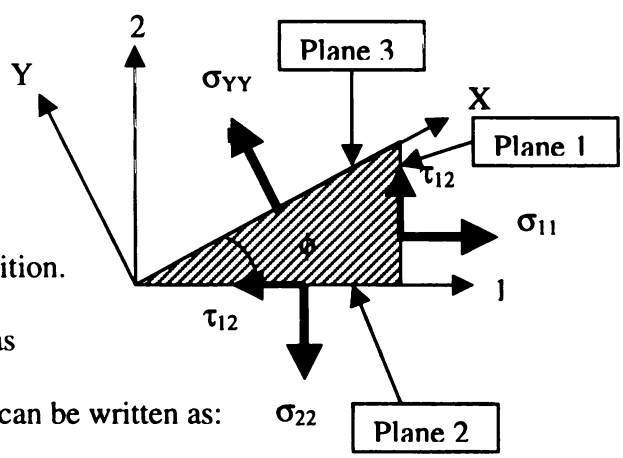

$$\left.\begin{aligned} F1&=\sigma_{11}\cdot dq\cdot 1-\tau_{12}\cdot dp\cdot 1\\ F2&=\sigma_{22}\cdot dp\cdot 1-\tau_{12}\cdot dq\cdot 1\\ F3&=\sigma_{YY}\left(dp^2+dq^2\right)^{1/2}\cdot 1\end{aligned}\right\} \tag{A17-6}$$

where 1 is the thickness in 3 or Z direction, which is defined as unit. In an equilibrium condition, F1, F2, and F3 can be related as:

$$F3 = F1 \cdot \sin\phi + F2 \cdot \cos\phi \qquad \text{(A17-7)}$$

Substitute (A17-6) into (A17-7) and summarize it in terms of sinϕ and sinϕ by using (A17-5).

$$\sigma_{YY} = \sin^2\phi \cdot \sigma_{11} + \cos^2\phi \cdot \sigma_{22} - 2\sin\phi \cdot \cos\phi \cdot \tau_{12} \qquad \text{(A17-8)}$$

In the same way, σ_{XX} and τ_{XY} can be obtained as:

$$\sigma_{XX} = \cos^2\phi \cdot \sigma_{11} + \sin^2\phi \cdot \sigma_{22} + 2\sin\phi \cdot \cos\phi \cdot \tau_{12} \qquad \text{(A17-9)}$$

$$\tau_{XY} = -\sin\phi\cos\phi \cdot \sigma_{11} + \sin\phi\cos\phi \cdot \sigma_{22} + \left(\cos^2\phi - \sin^2\phi\right)\tau_{12} \qquad \text{(A17-10)}$$

Thus, T can be expressed as:

$$T = \begin{bmatrix} \cos^2\phi & \sin^2\phi & 2\sin\phi\cos\phi \\ \sin^2\phi & \cos^2\phi & -2\sin\phi\cos\phi \\ -\sin\phi\cos\phi & \sin\phi\cos\phi & \cos^2\phi - \sin^2\phi \end{bmatrix} \qquad \text{(A17-11)}$$

Also, $(T')^{-1}$ can be expressed as:

$$(T')^{-1} = \begin{bmatrix} \cos^2\phi & \sin^2\phi & \sin\phi\cos\phi \\ \sin^2\phi & \cos^2\phi & -\sin\phi\cos\phi \\ -2\sin\phi\cos\phi & 2\sin\phi\cos\phi & \cos^2\phi - \sin^2\phi \end{bmatrix} \qquad \text{(A17-12)}$$

Substitute (A17-1), (A17-11), and (A17-12) into (A17-4):

$$Q' = \begin{bmatrix} \cos^2\phi & \sin^2\phi & 2\sin\phi\cos\phi \\ \sin^2\phi & \cos^2\phi & -2\sin\phi\cos\phi \\ -\sin\phi\cos\phi & \sin\phi\cos\phi & \cos^2\phi - \sin^2\phi \end{bmatrix} \begin{bmatrix} Q_{11} & Q_{12} & 0 \\ Q_{12} & Q_{22} & 0 \\ 0 & 0 & Q_{66} \end{bmatrix} \begin{bmatrix} \cos^2\phi & \sin^2\phi & \sin\phi\cos\phi \\ \sin^2\phi & \cos^2\phi & -\sin\phi\cos\phi \\ -2\sin\phi\cos\phi & 2\sin\phi\cos\phi & \cos^2\phi - \sin^2\phi \end{bmatrix}$$

(A17-13)

Thus, Q'_{11} can be calculated as:

$$Q'_{11} = \cos^4\phi \cdot Q_{11} + \sin^2\phi\cos^2\phi \cdot (Q_{12} + 2Q_{66}) + \sin^4 Q_{22} \qquad \text{(A17-14)}$$

Now calculate

$$Q_{random} = \frac{1}{\pi}\int_0^{\pi} Q'_{11}\, d\pi \qquad \text{(A17-15)}$$

Here use

$$\left.\begin{aligned} \int\sin^4\phi \cdot d\phi &= \frac{3}{8}\phi - \frac{1}{4}\sin 2\phi + \frac{1}{32}\sin 4\varphi \\ \int\cos^4\phi \cdot d\phi &= \frac{3}{8}\phi + \frac{1}{4}\sin 2\phi + \frac{1}{32}\sin 4\varphi \\ \int\sin^2\phi\cos^2\phi \cdot d\phi &= \frac{1}{8}\phi - \frac{1}{32}\sin 4\varphi \end{aligned}\right\} \qquad \text{(A17-16)}$$

Substitute (A17-14) and (A17-16) into (A17-15) and summarize it.

$$Q_{random} = \frac{1}{8}(3Q_{11} + 3Q_{22} + 2Q_{12} + 4Q_{66}) \qquad \text{(A17-17)}$$

In the case of transversely isotropic material, Q_{11}, Q_{22}, Q_{12}, and Q_{66} can be written by elastic constants E_{11}, E_{22}, ν_{12}, and ν_{21} where E and ν means tensile modulus and Poisson's ratio respectively. [Error! Reference source not found.]

Now Q_{random} can be written as:

$$Q_{random} = \frac{1}{8}(3E_{11} + 3E_{22} + 2\nu_{12}E_{22} + 4G_{12}) \qquad \text{(A17-18)}$$

Here recall equation (A14-25)

$$\frac{1}{G_{12}} = \frac{V_m}{G_m} + \frac{V_f}{G_f}$$

Assume $G_f >> G_m$.

$$\frac{1}{G_{12}} \cong \frac{V_m}{G_m} \quad \text{or} \quad G_{12} = \frac{G_m}{V_m} \tag{A17-19}$$

Now matrix is an isotropic material, then:

$$G_m = \frac{E_m}{2(1+\nu_m)} \tag{A17-20}$$

Substitute (A17-20) into (A17-19), then:

$$G_{12} = \frac{E_m}{V_m \cdot 2(1+\nu_m)} \tag{A17-21}$$

Here recall equation (A14-11).

$$\frac{1}{E_{22}} = \frac{V_m}{E_m} + \frac{V_f}{E_f}$$

Assume $E_f >> E_m$.

$$\frac{1}{E_{22}} \cong \frac{V_m}{E_m} \quad \text{or} \quad E_m = V_m \cdot E_{22} \tag{A17-22}$$

Substitute (A17-22) into (A17-21), then:

$$G_{12} = \frac{E_{22}}{2(1+\nu_m)} \tag{A17-23}$$

Substitute (A17-23) into (A17-18), then:

$$Q_{random} = \frac{1}{8}\left(3E_{11} + 3E_{22} + 2\nu_{12}E_{22} + \frac{2E_{22}}{(1+\nu_m)}\right) \tag{A17-24}$$

Now ν_m is around 0.28 to 0.38 for polymers while ν_f is around 0.22 to 0.35 for glass, carbon, and aramid fibers. Thus, it is reasonable to assume $\nu_m = \nu_{12} = 0.3$. Then:

$$Q_{random} \cong \frac{1}{8}(3E_{11} + 5E_{22}) \tag{A17-25}$$

Appendix A18

Stress-Strain Relation of Elastic Materials

[1] Isotropic Material

Mechanical properties of all directions are the same and only two engineering constants are independent. Now consider compliance matrix,

$$\begin{bmatrix} \varepsilon_{11} \\ \varepsilon_{22} \\ \varepsilon_{33} \\ \gamma_{23} \\ \gamma_{31} \\ \gamma_{12} \end{bmatrix} = \begin{bmatrix} S_{11} & S_{12} & S_{12} & 0 & 0 & 0 \\ S_{12} & S_{11} & S_{12} & 0 & 0 & 0 \\ S_{12} & S_{12} & S_{11} & 0 & 0 & 0 \\ 0 & 0 & 0 & S_{44} & 0 & 0 \\ 0 & 0 & 0 & 0 & S_{44} & 0 \\ 0 & 0 & 0 & 0 & 0 & S_{44} \end{bmatrix} \begin{bmatrix} \sigma_{11} \\ \sigma_{22} \\ \sigma_{33} \\ \tau_{23} \\ \tau_{31} \\ \tau_{12} \end{bmatrix} \quad \text{where}$$

$$S_{11} = \frac{1}{E},\ S_{12} = -\frac{\nu}{E},\ \text{and}\ S_{44} = 2(S_{11} - S_{12}) = \frac{1}{G} = \frac{2(1+\nu)}{E}. \qquad \text{(A18-1)}$$

Here ε is tensile strain, and γ is shear strain, σ is tensile stress, τ is shear stress, E is tensile mdulus, ν is poisson's ratio, and G is shear modulus.

Here consider stiffness matrix,

$$\begin{bmatrix} \sigma_{11} \\ \sigma_{22} \\ \sigma_{33} \\ \tau_{23} \\ \tau_{31} \\ \tau_{12} \end{bmatrix} = \begin{bmatrix} C_{11} & C_{12} & C_{12} & 0 & 0 & 0 \\ C_{12} & C_{11} & C_{12} & 0 & 0 & 0 \\ C_{12} & C_{12} & C_{11} & 0 & 0 & 0 \\ 0 & 0 & 0 & C_{44} & 0 & 0 \\ 0 & 0 & 0 & 0 & C_{44} & 0 \\ 0 & 0 & 0 & 0 & 0 & C_{44} \end{bmatrix} \begin{bmatrix} \varepsilon_{11} \\ \varepsilon_{22} \\ \varepsilon_{33} \\ \gamma_{23} \\ \gamma_{31} \\ \gamma_{12} \end{bmatrix} \quad \text{where } C_{ij} = S_{ij}^{-1}$$

and

$$C_{11} = \frac{(1-\nu)E}{(1+\nu)(1-2\nu)},\ C_{12} = \frac{\nu E}{(1+\nu)(1-2\nu)},\ \text{and}\ C_{44} = \frac{(C_{11} - C_{12})}{2} = G = \frac{E}{2(1+\nu)}$$

(A18-2)

[2] Orthotropic Material

Mechanical properties of direction 1 2, and 3 are all different and nine engineering constants are independent. Now consider compliance matrix,

$$\begin{bmatrix} \varepsilon_{11} \\ \varepsilon_{22} \\ \varepsilon_{33} \\ \gamma_{23} \\ \gamma_{31} \\ \gamma_{12} \end{bmatrix} = \begin{bmatrix} S_{11} & S_{12} & S_{13} & 0 & 0 & 0 \\ S_{12} & S_{22} & S_{23} & 0 & 0 & 0 \\ S_{13} & S_{23} & S_{33} & 0 & 0 & 0 \\ 0 & 0 & 0 & S_{44} & 0 & 0 \\ 0 & 0 & 0 & 0 & S_{55} & 0 \\ 0 & 0 & 0 & 0 & 0 & S_{66} \end{bmatrix} \begin{bmatrix} \sigma_{11} \\ \sigma_{22} \\ \sigma_{33} \\ \tau_{23} \\ \tau_{31} \\ \tau_{12} \end{bmatrix} \quad \text{where}$$

$$S_{11} = \frac{1}{E_{11}},\ S_{22} = \frac{1}{E_{22}},\ S_{33} = \frac{1}{E_{33}},$$

$$S_{12} = -\frac{\nu_{12}}{E_{11}},\ S_{13} = -\frac{\nu_{13}}{E_{11}},\ S_{23} = -\frac{\nu_{23}}{E_{22}}$$

$$S_{44} = \frac{1}{G_{23}},\ S_{55} = \frac{1}{G_{31}},\ \text{and}\ S_{66} = \frac{1}{G_{12}} \qquad \text{(A18-3)}$$

Here ε is tensile strain, and γ is shear strain, σ is tensile stress, τ is shear stress, E is tensile mdulus, ν is poisson's ratio, and G is shear modulus.

Here consider stiffness matrix,

$$\begin{bmatrix} \sigma_{11} \\ \sigma_{22} \\ \sigma_{33} \\ \tau_{23} \\ \tau_{31} \\ \tau_{12} \end{bmatrix} = \begin{bmatrix} C_{11} & C_{12} & C_{13} & 0 & 0 & 0 \\ C_{12} & C_{22} & C_{23} & 0 & 0 & 0 \\ C_{13} & C_{23} & C_{33} & 0 & 0 & 0 \\ 0 & 0 & 0 & C_{44} & 0 & 0 \\ 0 & 0 & 0 & 0 & C_{55} & 0 \\ 0 & 0 & 0 & 0 & 0 & C_{66} \end{bmatrix} \begin{bmatrix} \varepsilon_{11} \\ \varepsilon_{22} \\ \varepsilon_{33} \\ \gamma_{23} \\ \gamma_{31} \\ \gamma_{12} \end{bmatrix}$$

where

$$C_{ij} = S_{ij}^{-1} = \frac{1}{\Delta}\begin{bmatrix} \frac{1-\nu_{23}\nu_{32}}{E_{22}E_{33}} & \frac{\nu_{21}+\nu_{31}\nu_{23}}{E_{22}E_{33}} & \frac{\nu_{31}+\nu_{23}\nu_{32}}{E_{22}E_{33}} & 0 & 0 & 0 \\ \frac{\nu_{12}-\nu_{13}\nu_{31}}{E_{33}E_{11}} & \frac{1-\nu_{31}\nu_{13}}{E_{33}E_{11}} & \frac{\nu_{32}+\nu_{31}\nu_{12}}{E_{33}E_{11}} & 0 & 0 & 0 \\ \frac{\nu_{13}+\nu_{12}\nu_{23}}{E_{11}E_{22}} & \frac{\nu_{32}+\nu_{13}\nu_{23}}{E_{11}E_{22}} & \frac{1-\nu_{12}\nu_{23}}{E_{11}E_{22}} & 0 & 0 & 0 \\ 0 & 0 & 0 & G_{23} & 0 & 0 \\ 0 & 0 & 0 & 0 & G_{31} & 0 \\ 0 & 0 & 0 & 0 & 0 & G_{12} \end{bmatrix}$$

where $\Delta = \dfrac{1-\nu_{12}\nu_{21}-\nu_{23}\nu_{32}-\nu_{31}\nu_{13}-2\nu_{12}\nu_{23}\nu_{31}}{E_{11}E_{22}E_{33}}$ (A18-4)

[3] Transversely Isotropic Material

Assume direction 3 is the longitudinal direction and direction 1 and 2 are the transverse direction. Mechanical properties in direction 1 and 2 are the same, while those in direction 3 are different and 5 engineering constants are independent. Now consider compliance matrix,

$$\begin{bmatrix} \varepsilon_{11} \\ \varepsilon_{22} \\ \varepsilon_{33} \\ \gamma_{23} \\ \gamma_{31} \\ \gamma_{12} \end{bmatrix} = \begin{bmatrix} S_{11} & S_{12} & S_{13} & 0 & 0 & 0 \\ S_{12} & S_{11} & S_{13} & 0 & 0 & 0 \\ S_{13} & S_{13} & S_{33} & 0 & 0 & 0 \\ 0 & 0 & 0 & S_{44} & 0 & 0 \\ 0 & 0 & 0 & 0 & S_{44} & 0 \\ 0 & 0 & 0 & 0 & 0 & S_{66} \end{bmatrix} \begin{bmatrix} \sigma_{11} \\ \sigma_{22} \\ \sigma_{33} \\ \tau_{23} \\ \tau_{31} \\ \tau_{12} \end{bmatrix} \quad \text{where}$$

$$S_{11} = \frac{1}{E_{11}},\ S_{33} = \frac{1}{E_{33}},$$

$$S_{12} = -\frac{\nu_{12}}{E_{11}},\ S_{13} = -\frac{\nu_{31}}{E_{33}},$$

$$S_{44} = \frac{1}{G_{31}}, \text{ and } S_{66} = \frac{1}{G_{12}} = \frac{2(1+\nu_{12})}{E_{11}} \qquad \text{(A18-5)}$$

Here ε is tensile strain, and γ is shear strain, σ is tensile stress, τ is shear stress, E is temsile mdulus, ν is poisson's rati, and G is shear modulus.

Here consider stiffness matrix,

$$\begin{bmatrix} \sigma_{11} \\ \sigma_{22} \\ \sigma_{33} \\ \tau_{23} \\ \tau_{31} \\ \tau_{12} \end{bmatrix} = \begin{bmatrix} C_{11} & C_{12} & C_{13} & 0 & 0 & 0 \\ C_{12} & C_{11} & C_{13} & 0 & 0 & 0 \\ C_{13} & C_{13} & C_{33} & 0 & 0 & 0 \\ 0 & 0 & 0 & C_{44} & 0 & 0 \\ 0 & 0 & 0 & 0 & C_{44} & 0 \\ 0 & 0 & 0 & 0 & 0 & C_{66} \end{bmatrix} \begin{bmatrix} \varepsilon_{11} \\ \varepsilon_{22} \\ \varepsilon_{33} \\ \gamma_{23} \\ \gamma_{31} \\ \gamma_{12} \end{bmatrix}$$

where $C_{66} = \frac{1}{2}(C_{33} - C_{23})$, and

$$C_{ij} = S_{ij}^{-1} = \frac{1}{\Delta}\begin{bmatrix} \frac{1-\nu_{13}\nu_{31}}{E_{11}E_{33}} & \frac{\nu_{12}+\nu_{31}\nu_{13}}{E_{11}E_{33}} & \frac{\nu_{31}(1+\nu_{12})}{E_{11}E_{33}} & 0 & 0 & 0 \\ \frac{\nu_{12}-\nu_{13}\nu_{31}}{E_{33}E_{11}} & \frac{1-\nu_{31}\nu_{13}}{E_{33}E_{11}} & \frac{\nu_{31}(1+\nu_{12})}{E_{33}E_{11}} & 0 & 0 & 0 \\ \frac{\nu_{13}(1+\nu_{12})}{{E_{11}}^2} & \frac{\nu_{13}(1+\nu_{12})}{{E_{11}}^2} & \frac{1-{\nu_{12}}^2}{{E_{11}}^2} & 0 & 0 & 0 \\ 0 & 0 & 0 & G_{31} & 0 & 0 \\ 0 & 0 & 0 & 0 & G_{31} & 0 \\ 0 & 0 & 0 & 0 & 0 & \frac{E_{11}}{2(1+\nu_{12})} \end{bmatrix}$$

$$= \frac{1}{\Delta}\begin{bmatrix} \frac{1-\nu_{13}\nu_{31}}{E_{11}E_{33}} & \frac{\nu_{12}+\nu_{31}\nu_{13}}{E_{11}E_{33}} & \frac{\nu_{13}(1+\nu_{12})}{{E_{11}}^2} & 0 & 0 & 0 \\ \frac{\nu_{12}-\nu_{13}\nu_{31}}{E_{33}E_{11}} & \frac{1-\nu_{31}\nu_{13}}{E_{33}E_{11}} & \frac{\nu_{13}(1+\nu_{12})}{{E_{11}}^2} & 0 & 0 & 0 \\ \frac{\nu_{13}(1+\nu_{12})}{{E_{11}}^2} & \frac{\nu_{13}(1+\nu_{12})}{{E_{11}}^2} & \frac{1-{\nu_{12}}^2}{{E_{11}}^2} & 0 & 0 & 0 \\ 0 & 0 & 0 & G_{31} & 0 & 0 \\ 0 & 0 & 0 & 0 & G_{31} & 0 \\ 0 & 0 & 0 & 0 & 0 & \frac{E_{11}}{2(1+\nu_{12})} \end{bmatrix}$$

where $\Delta = \frac{1-{\nu_{12}}^2 - 2\nu_{13}\nu_{31} - 2\nu_{12}\nu_{13}\nu_{31}}{{E_{11}}^2 E_{33}} = \frac{(1+\nu_{12})(1-\nu_{12}-2\nu_{13}\nu_{31})}{{E_{11}}^2 E_{33}}$ (A18-6)

Appendix A19

Calculation of 5 Engineering Constants from Stiffness Matrix for Transversely Isotropic Material

Here consider direction3 is the longitudinal direction and the stiffness matrix for transversely isotropic material can be written as,

$$\begin{bmatrix} \sigma_{11} \\ \sigma_{22} \\ \sigma_{33} \\ \tau_{23} \\ \tau_{31} \\ \tau_{12} \end{bmatrix} = \begin{bmatrix} C_{11} & C_{12} & C_{13} & 0 & 0 & 0 \\ C_{12} & C_{11} & C_{13} & 0 & 0 & 0 \\ C_{13} & C_{13} & C_{33} & 0 & 0 & 0 \\ 0 & 0 & 0 & C_{44} & 0 & 0 \\ 0 & 0 & 0 & 0 & C_{44} & 0 \\ 0 & 0 & 0 & 0 & 0 & C_{66} \end{bmatrix} \begin{bmatrix} \varepsilon_{11} \\ \varepsilon_{22} \\ \varepsilon_{33} \\ \gamma_{23} \\ \gamma_{31} \\ \gamma_{12} \end{bmatrix} \quad \text{(A19-1)}$$

(1) Elastic Modulus (Young's Modulus) in direction 3, E_{33}

Now apply $\sigma_{33} \neq 0$. (other stresses are 0)

$$0 = C_{11}\varepsilon_{11} + C_{12}\varepsilon_{22} + C_{13}\varepsilon_{33} \quad \text{(A19-2)}$$

$$\sigma_{33} = C_{13}\varepsilon_{11} + C_{13}\varepsilon_{22} + C_{33}\varepsilon_{33} \quad \text{(A19-3)}$$

Because of its isotropy in direction 1 and 2,

$$\varepsilon_{11} = \varepsilon_{22} \quad \text{(A19-4)}$$

Substitute (A19-4) into (A19-2) and summarize it.

$$\varepsilon_{11} = \frac{-C_{13}}{C_{11} + C_{12}}\varepsilon_{33} \quad \text{(A19-5)}$$

Substitute (A19-5) into (A19-3) and summarize it.

$$\sigma_{33} = \left(C_{33} - \frac{2C_{13}^{\,2}}{C_{11} + C_{12}} \right)\varepsilon_{33} \quad \text{and} \quad E_{33} = \frac{\sigma_{33}}{\varepsilon_{33}} = \left(C_{33} - \frac{2C_{13}^{\,2}}{C_{11} + C_{12}} \right) \quad \text{(A19-6)}$$

(2) Elastic Modulus (Young's Modulus) in direction 1 or 2, $E_{11}=E_{22}$

Now apply $\sigma_{11} \neq 0$. (other stresses are 0)

$$\sigma_{11} = C_{11}\varepsilon_{11} + C_{12}\varepsilon_{22} + C_{13}\varepsilon_{33} \quad \text{(A19-7)}$$

$$0 = C_{12}\varepsilon_{11} + C_{11}\varepsilon_{22} + C_{13}\varepsilon_{33} \quad \text{(A19-8)}$$

$$0 = C_{13}\varepsilon_{11} + C_{13}\varepsilon_{22} + C_{33}\varepsilon_{33} \quad \text{(A19-9)}$$

(A19-7)-(A19-8) and summarize it.

$$\varepsilon_{22} = \frac{\sigma_{11}}{C_{12} - C_{11}} + \varepsilon_{11} \quad \text{(A19-10)}$$

Substitute (A19-10) into (A19-9) and summarize it.

$$\varepsilon_{33} = \frac{-C_{13}}{C_{33}(C_{12} - C_{11})}\sigma_{11} - \frac{2C_{13}}{C_{33}}\varepsilon_{11} \quad \text{(A19-11)}$$

Substitute (A19-10) and (A19-11) into (A19-7) and summarize it.

$$E_{11} = \frac{\sigma_{11}}{\varepsilon_{11}} = \frac{C_{33}\left(C_{11}{}^2 - C_{12}{}^2\right) - 2C_{13}{}^2(C_{11} - C_{12})}{C_{11}C_{33} - C_{12}{}^2} \quad \text{(A19-12)}$$

(3) Poisson's Ratio, $\nu_{31}=\nu_{32}$

Recall equation (A19-5), then;

$$\nu_{31} = \nu_{32} = -\frac{\varepsilon_{11}}{\varepsilon_{33}} = \frac{C_{13}}{C_{11} + C_{12}} \quad \text{(A19-13)}$$

(4) Shear Modulus, $G_{31}=G_{32}$

From definition, $G_{31} = G_{32} = C_{44}$ (A19-14)

(5) Shear Modulus, G_{12}

$$G_{12} = C_{66} = \frac{1}{2}(C_{33} - C_{13}) \quad \text{(A19-15)}$$

Appendix A20

Failure Mechanisms of Materials and Fracture Mechanics Theories

Category	Material	Mechanism	Theories
Yielding	Ductile	Plastic deformation	• Tresca, Maximum Shear Stress Theory • Saint-Venant Maximum Strain Theory • Beltrami-Haigh Total Strain Energy Theory • Huber, Hencky, von Mises Maximum Distortion Energy Theory
Fracture	Brittle (crack free)	Sudden catastrophic failure without plastic deformation on the macroscopic level	• Rankine, Lame Maximum Principal Stress Theory • Coulomb-Mohr Internal Friction Theory • Modified Internal Friction Theory
Fracture	Brittle (crack exists)	Crack growth due to applied stress	• Griffith Crack propagation criterion for an elliptical crack • Irwin Crack propagation criterion for a linear crack • Barenblatt, Dougdale Cohesive Crack Model • Carpinteri Brittleness Number Energy Number
Fatigue	Brittle (crack exists)	Slow crack growth due to repeatedly applied stress	• Crack Growth Rate
Excessive Elastic Deformation		Buckling or bending due to compression, twisting, vibration, etc	• Euler's Formula • Generalized Euler's Formula
Others		• Corrosion related fatigue • Wear failure-Complex surface related damage phenomena • Liquid erosion-Wear failure due to removal of material by liquid	

Appendix A21

Von Mises Criterion for Failure Analysis of Ductile Material

The von Mises yield criterion [143] is used to estimate the yield phenomena of ductile materials. This criterion states when the energy of distortion (effective energy) reaches the yield energy of the material, the failure of ductile material occurs. This relation is mathematically expressed as,

$$\sigma_{yield} \geq \sigma_{eff} = \frac{1}{\sqrt{2}}\left[(\sigma_1 - \sigma_2)^2 + (\sigma_2 - \sigma_3)^2 + (\sigma_3 - \sigma_1)^2\right]^{1/2} \qquad \text{(A21-1)}$$

where σ_{eff} is the effective energy of the material and $\sigma 1$, $\sigma 2$, and $\sigma 3$ are stresses in direction 1, 2, and 3. In the case of plane stress, only $\sigma 1$and $\sigma 2$ exist. So the equation becomes,

$$\sigma_{yield} \geq \sigma_{eff} = \left(\sigma_1^2 - \sigma_1\sigma_2 + \sigma_2^2\right)^{1/2} \qquad \text{(A21-2)}$$

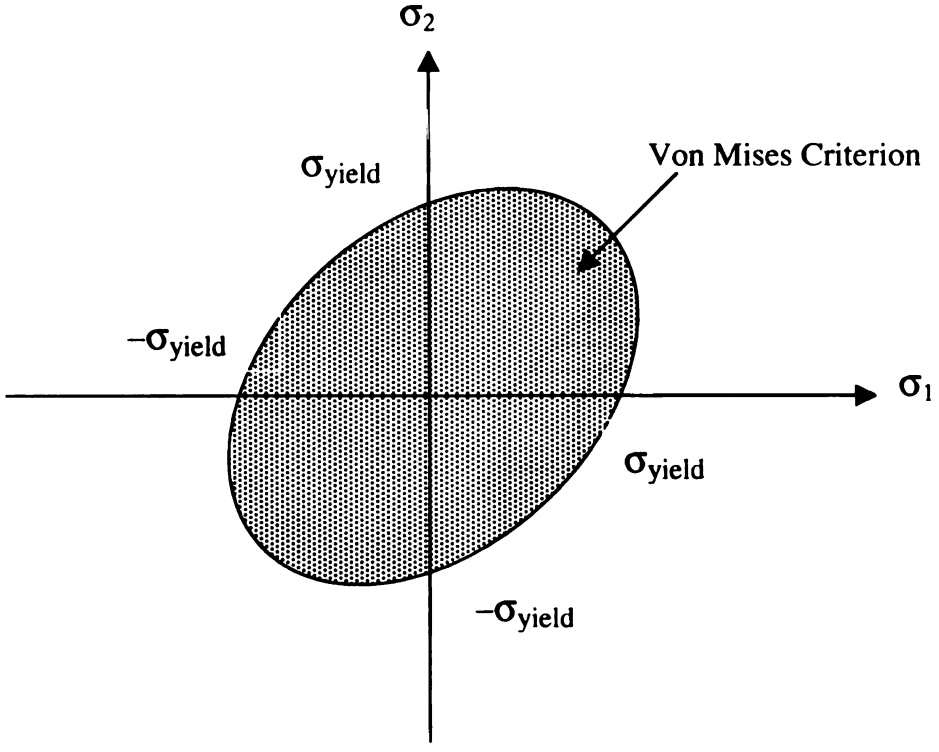

Appendix A22

Examples of Lattice Models for Percolation Theory

(1) 1-dimensional model

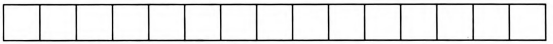

(2) 2-dmensional model

Honeycomb

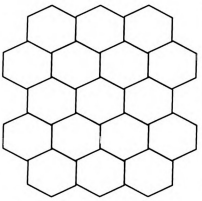

Square

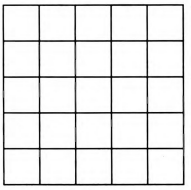

Triangular

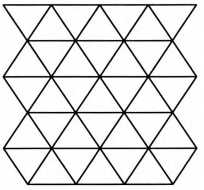

(3) 3-dimensional model

Diamond

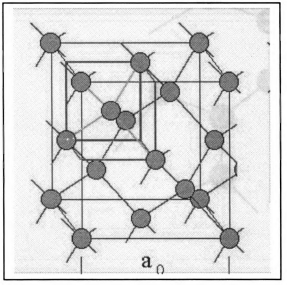

Simple Cubic

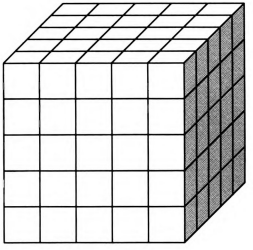

BCC
(Body Centered Cubic)

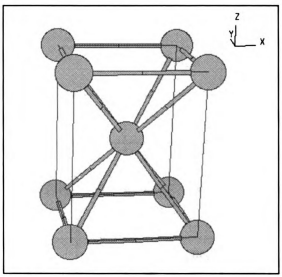

FCC
(Face Centered Cubic)

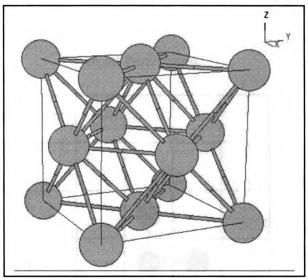

(4) Bethe Lattice (Infinite Dimensionality)

This figure shows a Bethe lattice with Z=3 (each site has 3 bonds), but Z can be 4, 5, 6, 7, ... Thus, the Bethe lattice is described as lattice with infinite dimensionality.

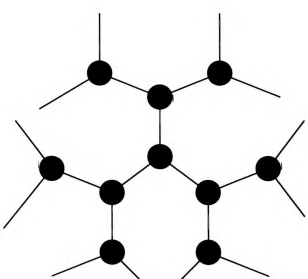

Appendix A23

Site Percolation and Bond Percolation

Site Percolation

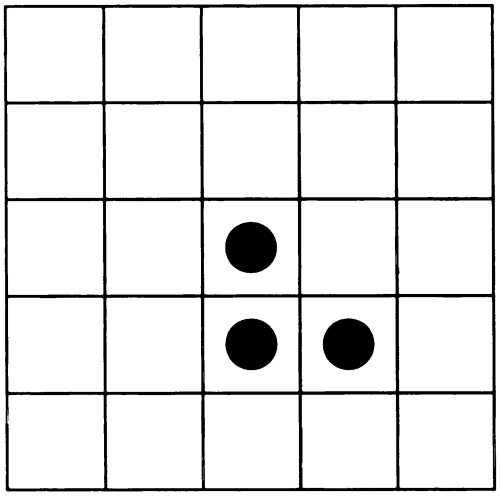

Size of Cluster = Number of sites involved

Bond Percolation

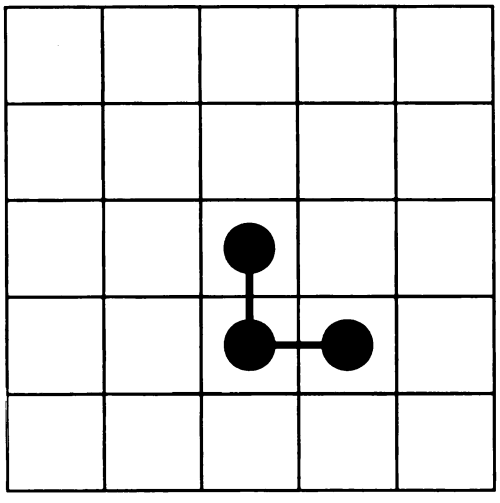

Size of Cluster = Number of bonds involved

Appendix A24

Complex Exponential Functions

It is inevitably necessary to use sinusoidal signals when handling the calculations of of AC circuit properties. Using trigonometric functions is straightforward, but it becomes very complex and often unmanageable when the AC circuit has multiple components. Instead, using complex exponential functions makes these calculations easy because summation, subtraction, multiplication, and division of complex functions are also complex functions, since rationalization can be used.

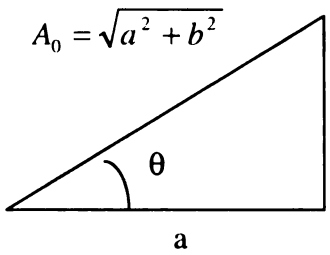

$$A = A_0 e^{i\theta} = A_0(\cos\theta + i\sin\theta) \qquad \text{(A24-1)}$$

where $A_0 = \sqrt{a^2 + b^2}$ and (A24-2)

$$\tan\theta = \frac{b}{a}, \sin\theta = \frac{b}{\sqrt{a^2 + b^2}}, \cos\theta = \frac{a}{\sqrt{a^2 + b^2}} \qquad \text{(A24-3)}$$

Substitute (A24-2) and (A24-3) into (A24-1) and summarize.

$$A = a + ib \quad \text{[Cartesian form]} \qquad \text{(A24-4)}$$

Here consider a sinusoidal voltage source with angular frequency of ω and a current response with phase delay ϕ in a AC circuit. These can be represented as:

$$V = V_0 \cos\omega t \quad \rightarrow \quad V = V_0 e^{i\omega t} \qquad \text{(A24-5)}$$

$$I = I_0 \cos(\omega t - \phi) \quad \rightarrow \quad I = I_0 e^{i(\omega t - \varphi)} \qquad \text{(A24-6)}$$

Thus, the impedance of the AC circuit, Z, can be written in complex form as;

$$Z = \frac{V}{I} = \frac{V_0}{I_0} e^{-i\phi} = \frac{V_0}{I_0} \frac{1}{\cos\phi + i\sin\phi} = \frac{V_0}{I_0}(\cos\phi - i\sin\phi) = Z' - iZ'' \qquad \text{(A24-7)}$$

where Z' is the real part of the impedance while Z" is the imaginary part.

Appendix A25

Circuit Models to represent Dielectric Properties of Gasses, Liquids, and Solids

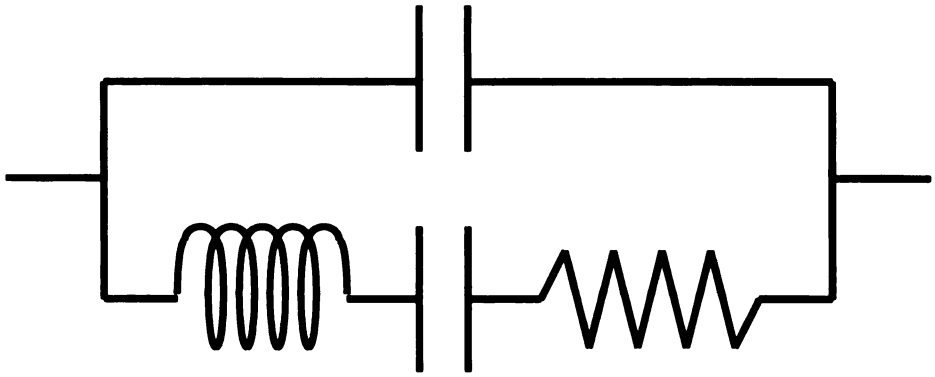

Figure A25-1. Model Circuit for Resonator Molecule (Gasses at low-pressure condition).

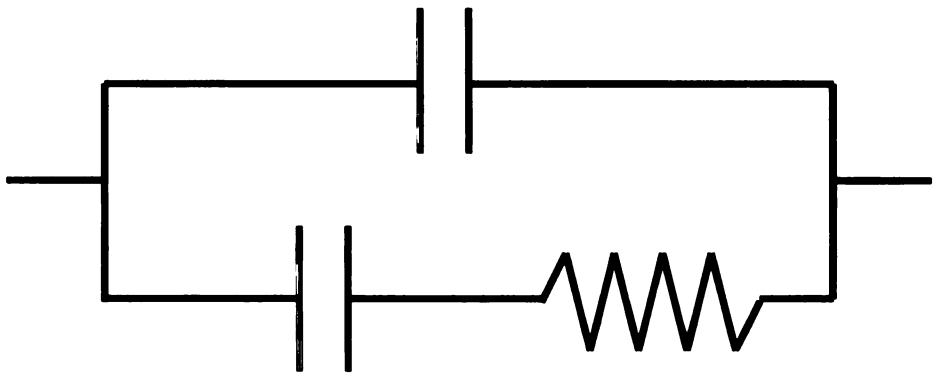

Figure A25-2. Model Circuit for Rotator Molecule in Condensed Condition (Solids, Liquids, and Gasses at high-pressure condition).

Appendix A26

Relation between Impedance data and Dielectric Constants

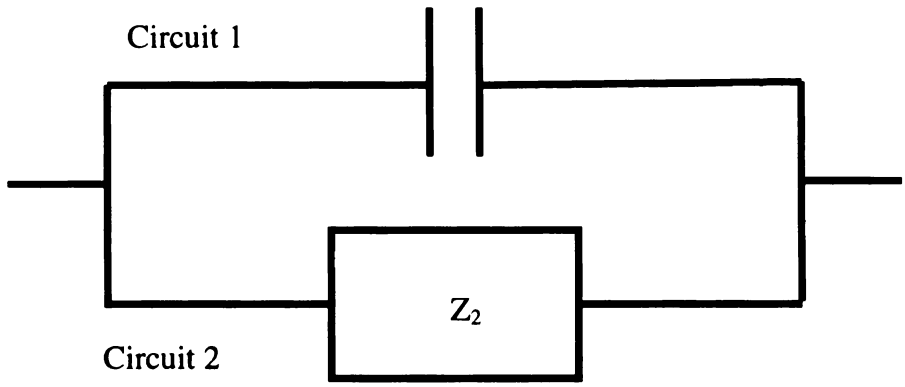

Here consider this circuit as a parallel combination of two circuits, 1 and 2. Circuit 2 can be RC or LRC circuit. The charging current of this whole system can be written as:

$$I_c = \frac{dQ}{dt} = i\varpi CV = i\varpi\varepsilon_r C_0 V \qquad \text{(A26-1)}$$

where C is the conductance factor of whole circuit, ε_r is relative pemittivity, C_0 is the permittivity of vacuum and V is the voltage applied to the system. Now the conductance term in AC circuit should represent not only migration of charge carriers, but also any other energy consuming process, including conduction loss (occurred in resistor part) and polarization loss. To express this loss current in addition to charging current, it is necessary to introduce complex relative permittivity. [**Appendix A24**]

$$\varepsilon_r^* = \varepsilon_r' - i\varepsilon_r'' \qquad \text{(A26-2)}$$

Now, the total current of this circuit can be written as;

$$I = \frac{dQ}{dt} = i\varpi CV = i\varpi\varepsilon_r^* C_0 V = i\varpi(\varepsilon_r' - i\varepsilon_r'')C_0 V = (\varpi\varepsilon_r'' + i\varpi\varepsilon_r')C_0 V \qquad \text{(A26-3)}$$

And the admittance of circuit becomes;

$$A = \frac{I}{V} = i\varpi\varepsilon_r * C_0 = \varpi\varepsilon_r'' C_0 + i\varpi\varepsilon_r' C_0 \qquad \text{(A26-4)}$$

Now assign the impedance of the whole circuit as Z*=Z'-iZ". Then the admittance can be written as;

$$A = \frac{1}{Z' - iZ''} = \frac{Z' + iZ''}{Z'^2 + Z''^2} \qquad \text{(A26-5)}$$

Compare (A26-4) to (A26-5), then we get;

$$\varepsilon_r'' = \frac{Z'}{\varpi C_0 (Z'^2 + Z''^2)} \quad \text{and} \quad \varepsilon_r' = \frac{Z''}{\varpi C_0 (Z'^2 + Z''^2)} \qquad \text{(A26-6)}$$

Z' and Z" can be obtained experimentally, then ε_r' and ε_r" can be calculated.

The real part of complex relative permittivity, ε_r', is called dielectric constant. This factor is related to the polarizability of the material. A material with high dielectric constant has lots of dopole moments including permanent dipolesdue to polar functional groups. The imaginary part, ε_r", is called (dielectric) loss factor, which is related to the energy loss (heat dissipation) in the circuit. Also loss tangent is defined as:

$$\tan\delta = \frac{\varepsilon_r''}{\varepsilon_r'} \qquad \text{(A26-7)}$$

where δ is the phase difference between input voltage and output current and can be determined experimentally. A material with large tanδ absorb energy and dissipate it as heat more efficiently.

Appendix A27

The Relaxation Spectrum: The interpretation of Dielectric Data by Molecular Mechanism of Polarization

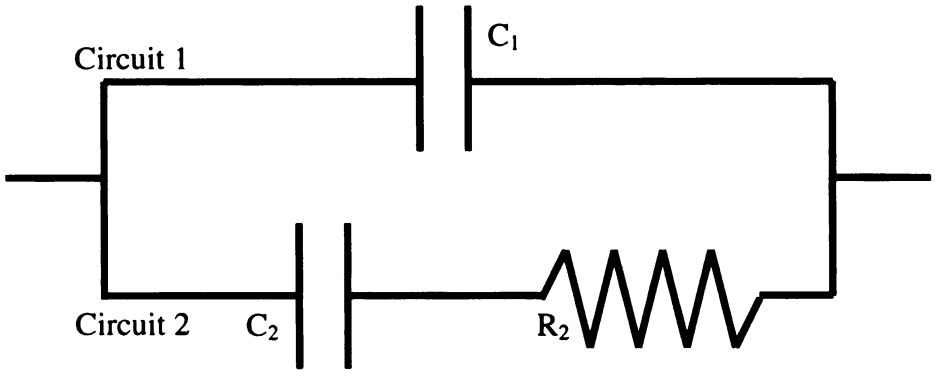

Now consider this circuit as a combination of circuit 1 and 2. Then the impedance, Z, and admittance, A,of each circuit can be written as:

The impedance of circuit 1: $$Z_1 = -\frac{i}{\varpi C_1} \quad \text{(A27-1)}$$

The admittance of circuit 1: $$A_1 = \frac{1}{Z_1} = -\frac{\varpi C_1}{i} = i\varpi C_1 \quad \text{(A27-2)}$$

The impedance of circuit 2: $$Z_2 = R_2 - \frac{i}{\varpi C_2} = R_2 + \frac{1}{i\varpi C_2} \quad \text{(A27-3)}$$

The admittance of circuit 1: $$A_2 = \frac{1}{Z_2} = \frac{1}{R_2 + \frac{1}{i\varpi C_2}} \quad \text{(A27-4)}$$

The total admittance of parallel circuit is the sum of the admittances of the components, thus, the total admittance of whole circuit, A_t can be written as;

$$A_t = A_1 + A_2 = i\varpi C_1 + \frac{1}{R_2 + \frac{1}{i\varpi C_2}} \quad \text{(A27-5)}$$

Now consider a circuit written below;

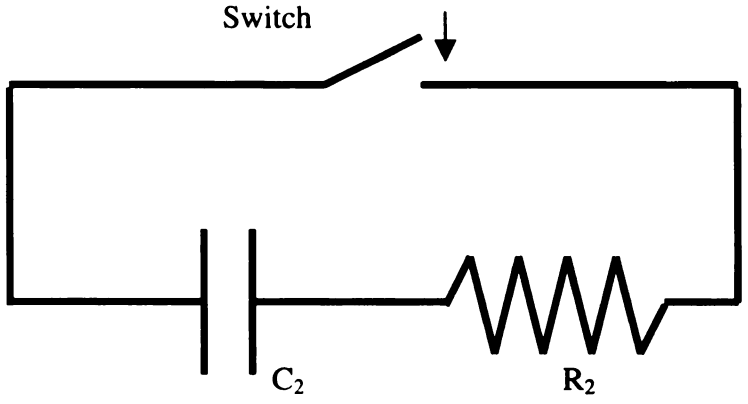

If C_2 is charged to voltage V_0 and then circuit is shorted by closing the switch, a transient voltage is observed. This voltage can be expressed by using a differential equation for charge, Q, ;

$$R_2 \frac{dQ}{dt} + \frac{Q}{C_2} = V_2 \quad \text{or} \quad R_2 C_2 \frac{dQ}{dt} + Q = C_2 V_2 \qquad \text{(A27-6)}$$

The solution of this equation is;

$$V_2 = V_0 e^{-\frac{1}{\tau}} \qquad \text{(A27-7)}$$

where relaxation time τ isexpressed as: $\tau = R_2 C_2$ or $R_2 = \frac{\tau}{C_2}$ (A27-8)

Now substitute (A27-8) into (A27-5) and summarize it.

$$A_t = i\varpi C_1 + \frac{1}{R_2 + \frac{1}{i\varpi C_2}} = i\varpi C_1 + \frac{1}{\frac{\tau}{C_2} + \frac{1}{i\varpi C_2}} = i\varpi \left(\frac{C_1}{C_0} + \frac{C_2}{C_0} \frac{1}{1 + i\varpi\tau} \right) C_0 \qquad \text{(A27-9)}$$

Here recall (A27-4): $A = \frac{I}{V} = i\varpi \varepsilon_r * C_0$ and compare this to (A27-9).

$$\varepsilon_r^* = \left(\frac{C_1}{C_0} + \frac{C_2}{C_0} \frac{1}{1 + i\varpi\tau} \right) \tag{A27-10}$$

Here define the static dielectric constant, ε_s', as ε_r^* when $\omega \rightarrow 0$, and optical dielectric constant, ε_∞', as ε_r^* when $\omega \rightarrow \infty$.

$$\varepsilon_s' = \frac{C_1}{C_0} + \frac{C_2}{C_0} \tag{A27-11}$$

$$\varepsilon_\infty' = \frac{C_1}{C_0} \tag{A27-12}$$

The physical meaning of the optical dielectric constant, ε_∞', is the permittivity according to the polarization only due to the induced dipoles (atomic polarization, **Appendix A28**), since under the condition of $\omega \rightarrow \infty$, the permanent dipoles don't have enough time to rotate and contribute to the dielectric constant. The static dielectric constant, ε_s', includes the polarization mechanisms due to both permanent and induced dipoles. Thus, $\varepsilon_s' - \varepsilon_\infty'$ should include the permittivity only due to permanent dipoles. If a material has a large $\varepsilon_s' - \varepsilon_\infty'$ value, it should have a lot of permanent dipoles or polar functional groups.

Now (A27-10) can be rewritten as:

$$\varepsilon_r^* = \left(\varepsilon_\infty' + \frac{\varepsilon_s' - \varepsilon_\infty'}{1 + i\varpi\tau} \right) \tag{A27-13}$$

This is called Debye equation, which gives the basic concept of relaxation spectrum of dielectric materials.

For condensed phase dielectric materials, the Debye equation should be modified because the local electric field of condensed phase should be different from the applied field. In this case, the equation becomes:

$$\varepsilon_r^* = \left(\varepsilon_\infty' + \frac{\varepsilon_s' - \varepsilon_\infty'}{1 + i\varpi\tau_e} \right) \tag{A27-14}$$

where τ_e is lengthened relaxation time due to modified local field.

Now the Debye equation for solids can be written as:

$$\varepsilon_r^* = \left(\varepsilon_\infty' + \frac{\varepsilon_s' - \varepsilon_\infty'}{1 + i\varpi\tau_e} \right) = \varepsilon_\infty' + \frac{\varepsilon_s' - \varepsilon_\infty'}{1 + \varpi^2\tau_e^2} - i\frac{(\varepsilon_s' - \varepsilon_\infty')\varpi\tau_e}{1 + \varpi^2\tau_e^2} \tag{A27-15}$$

Here compare this equation to (A26-2): $\varepsilon_r^* = \varepsilon_r' - i\varepsilon_r''$.

$$\varepsilon_r' = \varepsilon_\infty' + \frac{\varepsilon_s' - \varepsilon_\infty'}{1 + \varpi^2\tau_e^2} \tag{A27-16}$$

$$\varepsilon_r'' = \frac{(\varepsilon_s' - \varepsilon_\infty')\varpi\tau_e}{1 + \varpi^2\tau_e^2} \tag{A27-17}$$

Thus, the dielectric constant is related to polarization due to induced dipoles and relaxation movement of permanent dipoles, while the loss factor is due to the relaxation movement of permanent dipoles.

Now introduce a new variable X as:

$$e^X = \varpi\tau_e \tag{A27-18}$$

Substitute (A27-18) into (A27-16) and (A27-17) and summarize them.

$$\frac{\varepsilon_r' - \varepsilon_\infty'}{\varepsilon_s' - \varepsilon_\infty'} = \frac{e^{-X}}{e^X + e^{-X}} \tag{A27-19}$$

$$\frac{\varepsilon_r''}{\varepsilon_s' - \varepsilon_\infty'} = \frac{1}{e^X + e^{-X}} \tag{A24-20}$$

The curves of these functions are shown below.

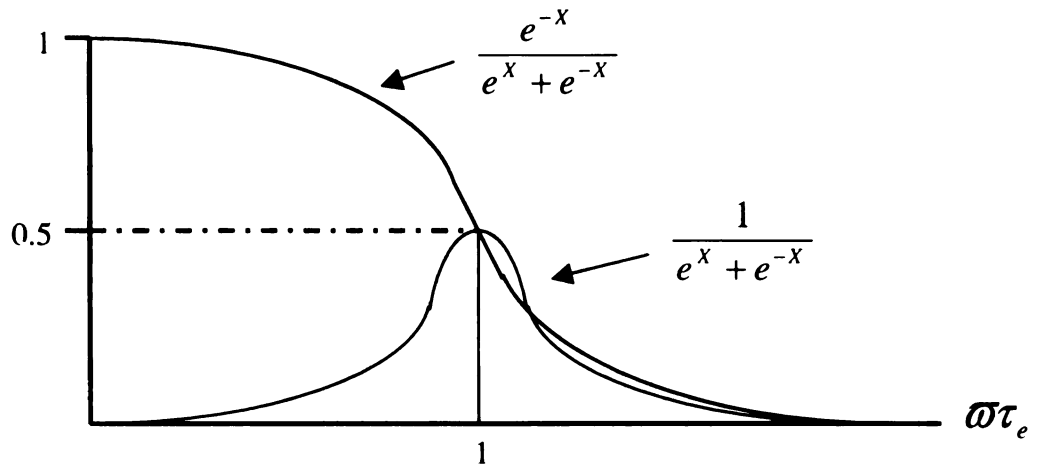

Thus, if the property of a dielectric material can be expressed by Debye equation, the relaxation spectrum of the materials should follow the shape of diagram shown below.

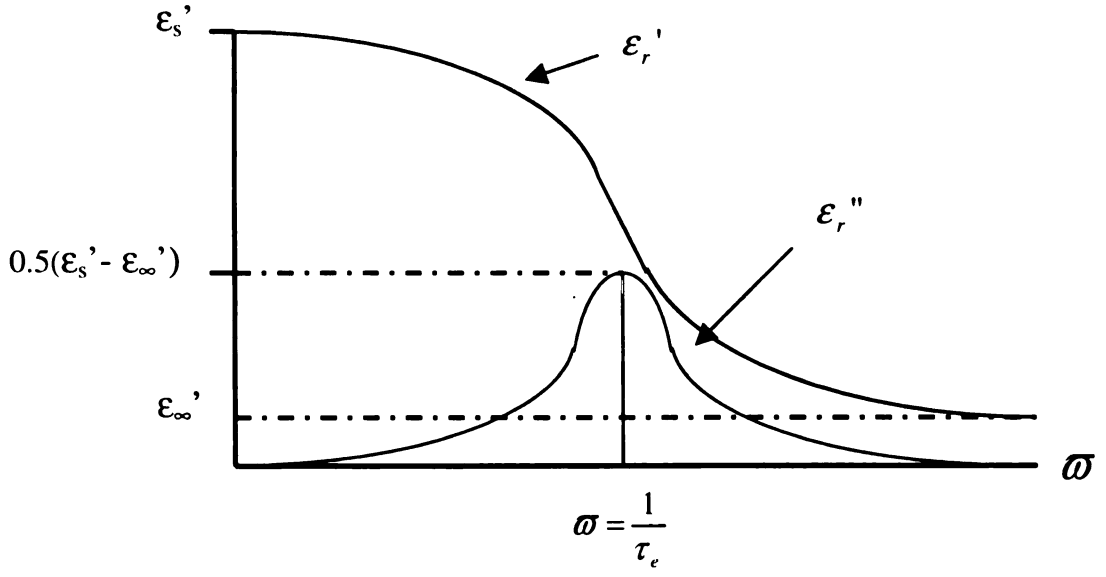

Appendix A28

Mechanisms of Polarization in Material

There are four types of mechanisms of polarization;

1. Electronic Polarization

A neutral atom has a positively charged nuclei surrounded by negatively charged electron cloud. The electron cloud has symmetric shape and there is no overall polarization. When an external electric field is applied, the electrons are displaced and form distorted electron cloud, causing mismatch between the center of electron cloud and the center of nuclei. Under this condition, an electric dipole is created. This is a first type of induced dipole. This is the dominant polarization mechanism at high frequency region, which is close to the ultraviolet range of electromagnetic spectrum. (10^{14} – 10^{16} Hz).

2. Atomic Polarization

When a molecule is made of two different kinds of atoms, usually they will not share electrons symmetrically because of the difference in electron-negativity of both atom. As a result, the electron cloud is displaced towards the atom(s) with higher electron-negativity, causing negative charge while the other atom(s) acquire positive charge. [Permanent dipole] An external electron field causes the extension, twisting, and bending motion of molecule, creating displacement of charged atoms. This is a second type of induced dipole. The atomic polarization occurs in the infra-red (10^{11} – 10^{13} Hz) or lower range of electromagnetic spectrum. Atomic polarization can occur in non-ionic materials, but ionic materials show a lot more atomic polarization.

3. Orientation Polarization

Permanent dipoles exist without external electric field, but usually they orient randomly so that the overall polarization is zero under normal condition. When an external field is applied, they experience torque and tend to orient in the field direction, causing overall polarization. This polarization occurs in microwave range ($3 \times 10^8 - 3 \times 10^{11}$ Hz) or lower frequency

4. Space Charge Polarization (Interfacial Polarization)

When a material has charge carriers, they can migrate and cause macroscopic polarization when an external field is applied. This occurs in radio frequency ($10^3 - 10^{10}$ Hz) or lower frequency range. This phenomena appears as an increase in the capacitance of the material and is the fundamental polarization mode in semiconductors.

Appendix A29

Cole-Cole Plot

If dielectric constant, ε_r', and loss factor, ε_r" obey the Debye equation, the plot ε_r" against ε_r" should show a semicircle. K. S. Cole and R. H. Cole first pointed it out in 1941. [Cole, K. S., and Cole, R. H., " ", J. Chem. Phys., 9, 341 (1941).] Here rewrite Debye equation as:

$$(\varepsilon_r{}^* - \varepsilon_\infty{}')+i(\varepsilon_r{}^* - \varepsilon_\infty{}')\varpi\tau_e = \varepsilon_s{}' - \varepsilon_\infty{}' \qquad \text{(A29-1)}$$

Here define u and v as:

$$u = (\varepsilon_r{}^* - \varepsilon_\infty{}') \qquad \text{(A29-2)}$$

$$v = (\varepsilon_r{}^* - \varepsilon_\infty{}')\varpi\tau_e \qquad \text{(A29-3)}$$